Configurable Input Devices for 3D Interaction using Optical Tracking

Cover design by Arjen van Rhijn.

Printed by Universiteitsdrukkerij Technische Universiteit Einhoven

CIP-DATA LIBRARY TECHNISCHE UNIVERSITEIT EINDHOVEN

Rhijn, Arjen Jacobus van

Configurable input devices for 3D interaction using optical tracking /
door Arjen Jacobus van Rhijn.
Eindhoven : Technische Universiteit Eindhoven, 2007.
Proefschrift. ISBN 90-386-0834-9. ISBN 978-90-386-0834-1
NUR 980
Subject headings: interactive computer graphics / tracking systems / computer vision / virtual reality
CR Subject Classification (1998) : I.3.7, I.4.8, H.5.2, I.3.6

Configurable Input Devices for 3D Interaction using Optical Tracking

PROEFSCHRIFT

ter verkrijging van de graad van doctor aan de
Technische Universiteit Eindhoven, op gezag van de
Rector Magnificus, prof.dr.ir. C.J. van Duijn, voor een
commissie aangewezen door het College voor
Promoties in het openbaar te verdedigen
op donderdag 18 januari 2007 om 16.00 uur

door

Arjen Jacobus van Rhijn

geboren te Diemen

Dit proefschrift is goedgekeurd door de promotoren:

prof.dr.ir. R. van Liere
en
prof.dr.ir. J.J. van Wijk

Copromotor:
dr. J.D. Mulder

The research reported in this thesis was carried out at CWI, the Dutch national research institute for Mathematics and Computer Science, within the theme Visualization and 3D User Interfaces, a subdivision of the research cluster Information Systems.

To Barbara, who carries my heart
To my parents, who gave me my heart
In memory of Mirjam, who will always be in my heart

Contents

Preface

"*The most beautiful thing we can experience is the mysterious. It is the source of all true art and all science. He to whom this emotion is a stranger, who can no longer pause to wonder and stand rapt in awe, is as good as dead: his eyes are closed.*"

Albert Einstein

The events leading up to this thesis began in 2001. After finishing my Master of Science in Electrical Engineering, I started working for a company where my daily routine consisted mostly of debugging existing software. Unfortunately, development work in this department was scarce. Some months later, when the economy was going downhill, rumors started circulating in the company that most of the personnel in my department had to go. Not wanting to wait for the outcome of these rumors, I started looking around for other work in November 2002.

Coincidentally, my close friend Alexander Scholten worked at the Center for Mathematics and Computer Science and told me about a Ph.D. position in the field of virtual reality. He got me into contact with Robert van Liere, who was leading the theme of visualization and 3D user interfaces, and I started working on my Ph.D. in March 2002. Ironically, I always considered myself more an engineer than a researcher. These events show that there is only so much a person can plan in his life.

This thesis is the result of several years of research, which would not have been possible without the help of many people. I would like to express my sincere gratitude to all who made this work possible and who contributed directly or indirectly.

First of all, many thanks go to my promotors Robert van Liere and Jack van Wijk, and to my co-promotor and daily supervisor Jurriaan Mulder. The brainstorm sessions with Jurriaan often shed new light on the matters at hand, and his knowledge, insights, and creativity have been a great stimulus during the course of the thesis. The monthly sessions with Jack always resulted in new ideas and approaches, and they provided a good evaluation of my own solutions. Jack's ability to identify problems and generate new and out of the box ideas has continuously amazed me. The same goes for Robert, who is a walking encyclopedia of virtual reality literature, who always has a clear vision about where virtual reality is going and where it should be going, and whose enthusiasm and ability to convey this enthusiasm is unparalleled.

Special thanks go out as well to the other members of the committee (prof. Berndt Fröhlich, prof. Ulrich Lang, prof. Jean-Bernard Martens, prof. Jos Roerdink) for their proofreading of the thesis and their valuable comments.

I would also like to thank my colleagues at the visualization and 3D user interfaces group for the many discussions, both professional and for fun: Breght Boschker, Alexander Broersen, Chris Kruszynski, Wojciech Burakiewicz, and Ferdi Smit. Furthermore, I would like to thank the test subjects who voluntarily participated in the user experiments, and Koos

van Rhijn and the Technische Verenfabriek De Merwede B.V. for construction help and supply of materials for the configurable interaction device.

I would like to thank the people that indirectly contributed to this thesis in my personal life, for their support and for keeping me going. I will always remember the weekly online sessions with George and Onno, the almost weekly games with Remco and Jen that are now unfortunately in the past, and the lunches and regular evenings of fun, and probably too much beer, with Alexander. I hope one day they will excuse me for neglecting them so much in the last months.

Finally, I especially thank my parents, brother, sister-in-law, and my nieces Tessa and Mieke, for their invaluable and unconditional support over the years. Last but definitely not least, I thank Barbara for her love and understanding during my work on this thesis. Thank you for keeping me sane, focussed, and believing in myself, and for all the beautiful moments, the joy, and the happiness.

Arjen van Rhijn

Woerden, November 2006

Chapter 1

Introduction

"*Interaction in three dimensions is not well understood. Users have difficulty controlling multiple degrees of freedom simultaneously, interacting in a volume rather than on a surface, and understanding 3D spatial relationships. These problems are magnified in an immersive virtual environment, because standard input devices such as mice and keyboards may not be usable...*"

Bowman, Johnson, and Hodges, 2001 [BJH01]

In 1965, Ivan Sutherland challenged researchers not to think of a computer monitor as a screen, but as a window through which one looks into a virtual environment in which the viewer is immersed [Sut65]. In this environment, users should be able to see, feel, and manipulate virtual objects as if they were real. Sutherland predicted that advances in computer science would eventually make it possible to engineer virtual experiences that were convincing to the human senses.

This vision has driven the field of virtual reality ever since. Advances in display hardware and software have significantly increased the realism in which virtual objects are presented to the user, increasing our ability to "see" in a virtual environment. However, increasing the ability to "feel" and "manipulate" virtual objects still poses a major challenge. In a survey on the state of the art in virtual reality in 1999, Brooks [Bro99] identified effective interaction with virtual objects as one of the most crucial issues that needs to be solved, in order to stimulate the growing success and speed of adoption of virtual reality in real world applications.

The research in this thesis focusses on 3D interaction in virtual environments. Although much research has been done on interaction techniques and design methodologies, truly intuitive and natural interaction in virtual environments is still uncommon, and as a result, user performance is often poor. The reason is that 3D interaction is difficult. As noted by Bowman et al. [BJH01], users have difficulties understanding 3D spatial relationships and manipulating 3D user interfaces. Conventional interaction paradigms known from the desktop computer, such as the use of interaction devices as the mouse and keyboard, are insufficient or even inappropriate for most 3D spatial interaction tasks.

The aim of the research in this thesis is to develop the technology that enables efficient development of new interaction devices, and which improves 3D user interaction by allowing interaction devices to be constructed such that their use is apparent from their structure. In the following sections, the background of the research in this thesis is first reviewed. Next, the scope is defined and the thesis objective is formulated.

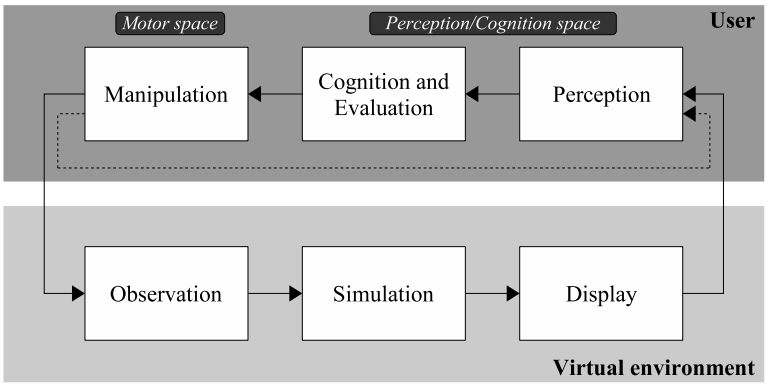

Figure 1.1: The interaction process can be modeled as a continuous feedback loop between a user and a virtual environment.

1.1 3D Interaction

Three-dimensional interaction is an essential part of a virtual environment. The goal of 3D interaction is to transfer information between a user and a virtual environment. In order to improve user performance in a virtual environment, interaction should be intuitive and natural, such that users can focus completely on the task at hand. Users should be able to perform basic interaction tasks, such as navigating through a 3D environment or selecting and manipulating virtual objects, as well as more complex tasks that require the manipulation of a large number of spatial parameters. In the following, we briefly review the 3D interaction cycle and the aspects that are involved from a cognitive psychology and ergonomics points of view, as well as from a design methodology and evaluation point of view. Furthermore, the main issues with 3D interaction are defined.

The Interaction Cycle

The interaction process can be modeled as a continuous cycle, which is symmetric between the user and the virtual environment. The interaction cycle is depicted in Figure 1.1, which is adapted from [Mei71]. The user and the virtual environment continuously observe the action of the other, process and evaluate the observed information, and present new information to the other party. The user presents information to the system by manipulating user interface entities, or input devices. The system observes the user's actions, changes its state as necessary, and defines an appropriate response. The response is fed back to the user by means of a display system. The user's perception and cognition system observes the system response, evaluates the information in the current context, and defines a new action. The user's context includes his goals, expectations, and knowledge of the system.

A user's expectations of the outcome of his actions are influenced by his knowledge about the system, his experiences with similar actions in the real world, active system feedback, and passive feedback such as tactile feedback, proprioception and kinesthesis. Proprioception and kinesthesis enables users to sense the locations and movements of the limbs relative to other parts of the body.

The main aim in designing 3D interaction is to provide a natural and intuitive interface

for the user. This problem has been widely studied in cognitive psychology and ergonomics. More natural and intuitive interaction can be achieved by minimizing the "gulf of execution" [HHN86]. The gulf of execution is the difference between a user's intentions and what the interaction device allows him to do and how well the system supports his actions. To minimize the gulf of execution, input devices should be designed such that they enable a user to perform the actions necessary to complete a task, while minimizing the psychological gap required to perform these actions.

In this thesis, the geometric arrangement of the degrees of freedom (DOFs) of an input device is referred to as its *spatial structure*. It comprises the geometric shape of the device and the direction of movement of the DOFs relative to the device. A degree of freedom is defined as the capability of motion in translation or rotation [RDB00]. The spatial structure of input devices may affect the effectiveness of interaction because of stimulus-response (S-R) compatibility. S-R compatibility can be defined as the degree to which a response matches a corresponding stimulus [WB98]. Stimuli and responses are regarded as compatible if they facilitate efficient action. Various researchers have studied the phenomenon [FS53, BG62, WB98]. A high level of S-R compatibility is believed to enhance human performance and reduce cognitive load.

Two aspects of S-R compatibility relate to the spatial structure of input devices: spatial and directional S-R compatibility. This can be defined as the degree of congruence between the position and orientation of a device or control and the direction of its motion, and that of the corresponding visual stimulus [WB98]. Stimulus-response compatibility can be increased by structuring interaction devices such that the user can fully concentrate on the task that needs to be performed, and not on the operation of the device. As such, an interaction device should be structured such that it reflects the task at hand. In this case, the structure of the perceptual and cognition space reflects the structure of the motor space [JS92]. The perception and cognition space arises from the output of the virtual environment and the user's expectations and goals, whereas the motor space involves the motor actions a user needs to perform to manipulate an interaction device.

Design and Development of Effective 3D Interfaces

The interaction process is characterized by three aspects, as depicted in Figure 1.2:

- *Interaction task*
  A piece of work that needs to be finished to accomplish a certain goal. The task depends on a user's observations of the virtual environment, his expectations, and the goal he tries to realize (see Figure 1.2). The goal depends on the type of application. For instance, the goal of applications as architectural design and scientific visualization may be to gain knowledge of or insight into 3D spatial structures and relationships. To realize such higher level goals, multiple smaller tasks generally need to be performed, such as selecting and moving virtual objects.

- *Interaction technique*
  A method by which a user performs a task in the virtual environment, by means of one or more interaction devices. An interaction technique may be as simple as clicking on a button, or as complex as performing a specific sequence of operations. An interaction technique provides a mapping of the functions of an interaction device to the parameters of the task to be performed, but is separate from the device. As such, it can be regarded as an abstraction of the device.

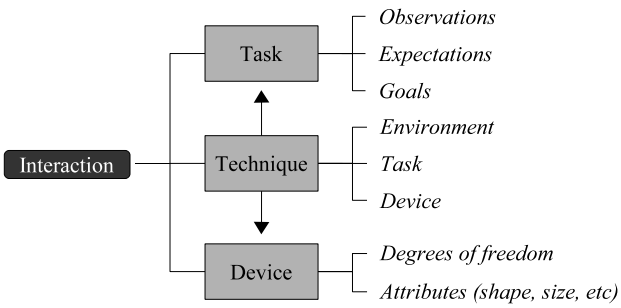

Figure 1.2: The interaction process is characterized by the interaction task, technique and device.

- *Interaction device*
  The hardware component that mediates input from the user to the virtual environment. Interaction devices can be simple desktop computer devices as keyboard and mouse, or more complex devices that allow for the manipulation of six or more degrees of freedom, such as a 3D mouse. Important design factors are the number of degrees of freedom that the device should support, as well as attributes as shape and size that influence the ergonomics.

Various researchers have addressed the question of how to design, develop, and evaluate 3D interfaces, such that the interaction process becomes more effective. Card et al. proposed a formal framework for the design and evaluation of 2D and 3D interaction devices [CMR90]. Bowman et al. provided a taxonomy of interaction techniques, which were divided into the main tasks of navigation, object selection and manipulation, and system control [BH99b, BJH01]. This taxonomy provided the basis of a design and evaluation methodology for 3D interaction techniques. Other researchers have performed experimental comparisons of input devices for certain tasks [ZM93, Zha98].

Although the development of design and evaluation methodologies for 3D interaction is very important, the driving vision in this thesis is that for effective and natural direct interaction the structure of an interaction device should be specifically tuned to the interaction task. Two aspects play a role in this vision:

- *Natural usage*
  Interaction devices should be structured such that the task-device mapping, provided by the interaction technique, is as direct and transparent as possible.

- *Efficient development*
  The underlying technology should allow developers to rapidly construct and evaluate new interaction devices, which can be structured appropriately for a given task.

In this thesis, the focus is on the development and application of the required underlying technology.

1.2 Related Work on 3D Interaction Devices

Three-dimensional interaction requires the manipulation of a number of input dimensions. This can be accomplished by using interaction devices that provide a number of degrees of freedom, which can be mapped to the input dimensions of the task by the use of an interaction technique. Interaction tasks can be divided into two categories, based on the number of input dimensions that need to be manipulated:

- *Low dimensional input:* Tasks that require the manipulation of up to six input dimensions.
- *High dimensional input:* Tasks that require the manipulation of more than six input dimensions.

Low Dimensional Input

In this thesis, low dimensional input tasks are defined as tasks that require the manipulation of up to six input dimensions. For instance, to change the 3D position and orientation of a virtual object, three positional and three rotational input dimensions need to be manipulated. There have been various approaches to designing interaction devices for such tasks. One approach is to use a standard 2D mouse to perform 3D interaction. However, a mouse has only two degrees of freedom that can be used to manipulate input dimensions. As such, positioning and rotating objects in 3D requires the use of an interaction technique that maps the two degrees of freedom of the mouse to six input dimensions, making interaction more difficult.

To support more direct 3D interaction, handheld devices have been developed that directly provide six degrees of freedom (DOFs). Such devices allow for the direct manipulation of the position and orientation of virtual objects, enabling a user to manipulate virtual objects as if he was really holding them in his hands.

Many six DOF input devices have been developed, based on different technologies. Examples of commercially available six DOF input devices are the SpaceBall and the Logitech 6D mouse. The SpaceBall is an input device developed by 3DConnexion [CNX]. It consists of a rubberized sphere mounted in a base, as illustrated in Figure 1.3(a). An optical sensor is used to measure six degrees of freedom. It is an isometric rate control device, similar to the standard desktop mouse. The Logitech 6D mouse is a desktop mouse that has been modified to provide six DOFs using ultrasonic tracking technology. It is a free flying handheld device providing direct control over position and orientation. These devices provide a direct and intuitive interface for controlling the 3D position and orientation of virtual objects.

High Dimensional Input

High dimensional input tasks are defined as tasks that require the manipulation of more than six input dimensions. For instance, a modeling application may require users to be able to position, rotate, and scale virtual objects, resulting in nine input parameters. Another example is a scientific visualization and data analysis application that allows a user to manipulate a data set and move one or more slicing planes through it. Such applications require complex spatial 3D interaction.

Two basic approaches for designing interaction devices for high dimensional input tasks can be distinguished:

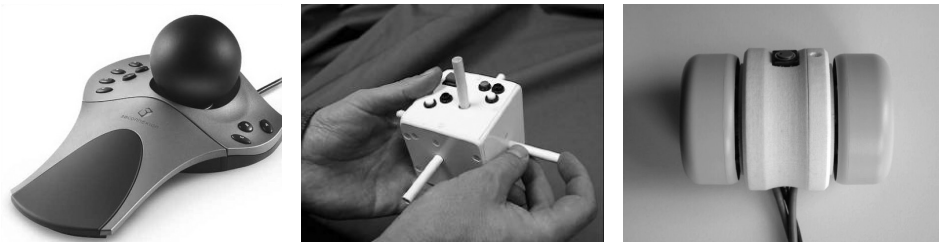

(a) (b) (c)

Figure 1.3: Interaction devices for 3D interaction (a) The SpaceBall by 3DConnexion [CNX], (b) The Cubic Mouse [FP00], (c) The YoYo [SF03].

- *Mode switching*
  A common approach is to use a device with a smaller number of degrees of freedom (DOFs) than the number of input dimensions, which can be put into different modes. Each mode is used to manipulate a certain set of input parameters. This mode switching may interrupt task flow and present an extra cognitive load on the user. Other options are to use multiple devices and assign different subtasks to each of them, or to use a device to manipulate control points that have different functions assigned to them. In these cases, mode switching is implicit in the selection of a device or a control point, and may present the same interruption of task flow.

  Jacob et al. [JSM+94] have shown that mode switching interfaces may be efficient for tasks that require the manipulation of application parameters, or attributes, that a user perceives as independent, such as the position and color of a virtual object. In case attributes are perceived as related, the attributes are manipulated in parallel. For instance, Jacob et al. found that the 2D position and scale of a virtual object were perceived as related. Consequently, input devices should be designed such that they allow for independent manipulation of attributes that are perceived as independent, and for parallel manipulation when attributes are perceived to be related.

- *Application specific devices*
  More recently, application specific devices have been designed to perform high dimensional interaction tasks. Such devices can be designed appropriate to the way a user perceives different attributes, and enable a user to directly control all required DOFs using bimanual interaction techniques. As such, the spatial structure of the device can reflect the interaction task at hand.

  An example of an application specific device that has been successfully used in high dimensional interaction scenarios is the Cubic Mouse, presented by Fröhlich et al. [FP00]. The cubic mouse is a handheld interaction device as depicted in Figure 1.3(b), designed for complex interaction tasks. It consists of a cubic case with three orthogonal rods passing though it. By pushing and pulling the rods, the motion of virtual objects can be controlled relative to the pose of the cube and constrained along the x, y, and z axes. The device is mostly used for scientific data visualization, where the cube corresponds to a 3D model, and the rods manipulate slicing planes using position control techniques. In a later version, the rods can also be rotated around their translation axes.

  Another example of a device for high dimensional interaction tasks is the YoYo, which

was proposed by Simon et al. [SF03]. The YoYo is depicted in Figure 1.3(c). It is a handheld interaction device, combining elastic force input and isotonic input in a single unit. The device consists of a cylindric centerpiece, with two rings attached on each side that can be moved relative to the centerpiece. The rings are used as elastic six DOF force sensors. The device basically enables a user to control three coordinate systems.

The advantage of developing application specific devices is that they can be designed appropriate to the way a user perceives different attributes, and that they enable users to directly control all required degrees of freedom using bimanual interaction. As such, the spatial structure of the device can reflect the interaction task at hand. In this case, somatosensory cues that a user receives during device manipulation, such as proprioception and kinesthesis, are consistent with the visual cues from the virtual environment. Kinesthesis enables users to feel the movements of their body and limbs, whereas proprioception allows users to sense the locations of the limbs relative to other parts of the body. The Cubic Mouse is a good example of a device where these principles are brought into practice.

However, constructing new input devices from scratch for different interaction tasks is inefficient and impractical. This issue could be solved by developing flexible interfaces that can easily be configured specifically for a given interaction task. In this thesis, the goal is to develop configurable interaction devices that allow a designer to rapidly construct and evaluate new configurations, given the requirements for effective interfaces as discussed in Section 1.1.

1.3 Scope

The research presented in this thesis was performed using the Personal Space Station (PSS^{TM}) [ML02, PST]. The PSS is a near-field desktop virtual reality system, which is developed at CWI. The system is depicted in Figure 1.4. In the PSS, a head tracked user looks into a mirror in which stereoscopic images are reflected, such that a 3D virtual environment is created behind the mirror. By using a mirror-based setup, a user can reach under the mirror and interact with 3D objects without blocking his own projection.

Three-dimensional spatial interaction is performed directly in the virtual environment with one or more tangible interaction devices. The interaction space is monitored by two or more cameras. Each camera is equipped with an infrared (IR) pass filter in front of the lens, and a ring of IR LEDs around the lens to illuminate the interaction space with IR light. Interaction devices are equipped with retro-reflective markers, which reflect the incoming IR light back to the cameras.

The PSS uses a model-based optical tracking system. Tracking refers to the process of measuring the degrees of freedom of an object that moves in a defined space, relative to a known source [RDB00]. The tracking system is used to recognize the marker configurations on each interaction device using the images from the cameras, and reconstruct the 3D position and orientation, or pose, of the devices. By equipping objects with markers, tangible, wireless input devices can be constructed and tracked in the environment.

The PSS has been used for applications in scientific visualization, and many interaction techniques have been developed to support these applications. Often, two-handed and high dimensional interaction is required within the small interaction volume of the PSS. As such, the PSS imposes the following requirements on the development and use of configurable interaction devices:

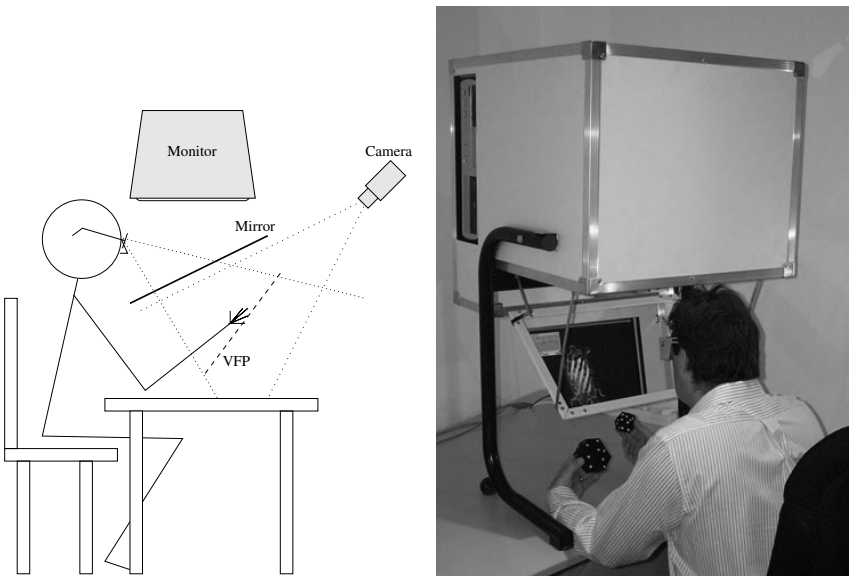

(a) (b)

Figure 1.4: (a) A schematic representation of the Personal Space Station (PSS^{TM}). A user reaches under a mirror into a virtual environment. The optical tracking system consists of two or more cameras that are directed to the interaction space. (b) The Personal Space Station^{TM}.

- *Small*
  Devices should be small enough to hold and manipulate comfortably within the interaction volume of the PSS.
- *Unobtrusive*
  The use of configurable interaction devices should be unobtrusive. Due to the bimanual interaction tasks in the small interaction volume of the PSS, this implies that devices operate without wires.
- *Suitable for two-handed interaction*
  Devices should be constructed such that two-handed interaction and proprioception can be exploited.

To determine the degrees of freedom of each input device, such as the 3D position and orientation, the optical tracking system of the PSS needs to be able to recognize which 2D markers belong to which input device, and estimate the values of the degrees of freedom. This is done by matching device models to the measured marker locations. These models describe the 3D configurations of markers on each device. The type of interaction tasks in the PSS puts the following requirements on a model-based optical tracking system:

- *Accurate*
  The resolution should be better than 1 mm in position and 1 degree in orientation [WF02].

- *Low latency*
  The tracking system should be fast enough to track multiple objects with a frame rate above 60 Hz and a latency below 33 ms. Latency is the effect that a virtual object lags behind the movements of an input device. Latencies above 33 ms reduce user performance and the sense of "being there" in the virtual environment [EYAE99, MRWB03].

- *Robust against occlusion*
  A consequence of optical tracking is that line of sight must be maintained. Many current optical tracking approaches fail to recognize an input device when one or more markers become occluded. An optical tracking system should be robust against partial occlusion of the marker sets.

- *Robust against error sources*
  An optical tracking system should be robust against various error sources. Error sources include image noise, small camera calibration errors, and errors in the device model. Undesired effects of error sources include jittering of the virtual object while keeping the interaction device stationary or failure to recognize an input device.

Additionally, the tracking system should meet the following requirements to allow for effective development of new interaction devices that are suitable for the high dimensional interaction tasks in the PSS:

- *Generic device shape*
  Various tracking approaches put constraints on the shape of the objects that can be tracked, for instance by requiring markers or patterns to be applied to planar surfaces (e.g. [LM03, KB99, Fia05]). An optical tracking system should be able to track objects of arbitrary shape.

- *Rapid development of devices*
  It should be easy for a developer to construct new interaction devices by equipping them with markers. This implies that the application of markers onto the surface of the device should be an easy procedure. Moreover, in order to construct a new input device, a developer needs to define a model that describes the 3D locations of markers relative to the device. Measuring such a model by hand is a tedious and time-consuming task, and only feasible for objects of simple shape. An optical tracking system should provide tools to automatically acquire such models.

- *Support for configurable interaction devices*
  Configurable interaction devices enable users to manipulate a large number of input dimensions. However, most previous tracking approaches focus on tracking standard six degree of freedom devices. A tracking system should provide tools to assist a developer in constructing new device configurations, and needs to support tracking of more than six degrees of freedom.

1.4 Research Objective

The goal of the research in this thesis is defined as follows:

> *The development and application of configurable input devices for direct 3D interaction in near-field virtual environments using optical tracking.*

The developed concepts and techniques were to be employed in the PSS, a desktop near-field virtual environment developed at the Center for Mathematics and Computer Science (CWI). The PSS uses an optical tracking system to measure the 3D position and orientation of handheld input devices. This system was to be extended to support configurable input devices and to provide more robust tracking. Although the focus is on desktop near-field VR, the developed techniques would have to be transferable to different types of virtual environments as well.

The configurable input devices should:

- Enable users to manipulate large numbers of application parameters with a single, compact device.
- Enable developers to structure devices such that they reflect application parameters, contributing to intuitive interfaces for high dimensional interaction tasks.
- Enable developers to rapidly develop new interaction techniques and test new configurations.

1.5 Thesis Outline

This thesis is organized as follows. First, a review of the optical tracking field is given in Chapter 2. The tracking pipeline is discussed, existing methods are reviewed, and improvement opportunities are identified.

In Chapters 3 and 4, we focus on the development of optical tracking techniques of rigid objects. The goal of the development of the tracking method presented in Chapter 3 is to reduce the occlusion problem. The method exploits projection invariant properties of line pencil markers, and the fact that line features only need to be partially visible. The approach is experimentally compared to a related solution, which is based on projection invariant properties of point markers.

In Chapter 4, the aim is to develop a tracking system that supports generic device shapes, and allows for rapid development of new interaction devices. The method is based on subgraph isomorphism to identify point clouds, and introduces an automatic model estimation method that can be used for the development of new devices in the virtual environment. An experimental comparison is performed to compare the method to a related tracking approach, which is based on matching 3D distances of point patterns.

Chapter 5 provides an analysis of three optical tracking systems based on different principles. The first system is based on an optimization that matches the 3D device model points to the 2D data points that are detected in the camera images. The other systems are the tracking methods as discussed in Chapters 3 and 4. The performance of the tracking methods is

analyzed, subject to a number of error sources. The accuracy of the methods is analytically estimated for each of these error sources and compared to experimentally obtained data.

An analysis of various filtering and prediction methods is given in Chapter 6. These techniques can be used to make the tracking system more robust against noise, and to reduce the latency problem.

Chapter 7 focusses on optical tracking of composite input devices, i.e., input devices that consist of multiple rigid parts that can have combinations of rotational and translational degrees of freedom with respect to each other. Techniques are developed to automatically generate a 3D model of a segmented input device by moving it in front of the cameras, and to use this model to track the device.

In Chapter 8, the presented techniques are combined to create a configurable input device, which supports direct and natural co-located interaction. In this chapter, the goal of the thesis is realized. The device can be configured such that its structure reflects the parameters of the interaction task. The interaction technique then becomes a transparent one-to-one mapping that directly mediates the functions of the device to the task.

In Chapter 9, the configurable interaction device is used to study the influence of spatial device structure with respect to the interaction task at hand. The driving vision of this thesis, that the spatial structure of an interaction device should match that of the task, is analyzed and evaluated by performing a user study.

Finally, in Chapter 10 conclusions are given and future research opportunities are discussed.

1.6 Publications from this Thesis

Most chapters in this thesis are based on separate publications, which appeared in the proceedings of international conferences. Chapters 3, 4, 6, 7, 8, and 9 appeared in:

- A. van Rhijn and J. D. Mulder
  Optical Tracking using Line Pencil Fiducials
  Proceedings of the Eurographics Symposium on Virtual Environments 2004, pp. 35-44. [RM04]

- A. van Rhijn and J. D. Mulder
  Optical Tracking and Calibration of Tangible Interaction Devices
  Proceedings of the Workshop on Virtual Environments 2005, pp. 41-50. [RM05]

- A. van Rhijn, R. van Liere, and J. D. Mulder
  An Analysis of Orientation Prediction and Filtering Methods for VR/AR
  Proceedings of the IEEE Virtual Reality Conference 2005, pp. 67-74. [RLM05]

- A. van Rhijn and J. D. Mulder
  Optical Tracking and Automatic Model Estimation of Composite Interaction Devices
  Proceedings of the IEEE Virtual Reality Conference 2006, pp. 135-142. [RM06b]

- A. van Rhijn and J. D. Mulder
  CID: An Optically Tracked Configurable Interaction Device
  Proceedings of Laval Virtual Reality International Conference 2006 [RM06a]

- A. van Rhijn and J. D. Mulder
  Spatial Input Device Structure and Bimanual Object Manipulation in Virtual Environments
  Accepted for publication at VRST 2006. [RM06c]

Chapter 5 is based on the following publication:

- R. van Liere and A. van Rhijn
  An Experimental Comparison of Three Optical Trackers for Model Based Pose Determination in Virtual Reality
  Proceedings of the Eurographics Symposium on Virtual Environments, pp. 25-34. [LR04]

During the research of this thesis, various related publications on optical tracking appeared in the proceedings of international conferences:

- R. van Liere and A. van Rhijn
  Search space reduction in optical tracking
  Proceedings of the workshop on Virtual environments 2003, pp. 207-214. [LR03]

- J. D. Mulder, J. Jansen, and A. van Rhijn
  An Affordable Optical Head Tracking System for Desktop VR/AR Systems
  Proceedings of the Workshop on Virtual Environments 2003, pp. 215-223. [MJR03]

- F. A. Smit, A. van Rhijn, and R. van Liere
  A Topology Projection Invariant Optical Tracker
  Proceedings of the Eurographics Symposium on Virtual Environments 2006, pp. 63-70. [SRL06]

Chapter 2

Model-based Optical Tracking

In virtual environments, accurate, fast and robust motion tracking of a user's actions is essential for smooth interaction with the system. Optical tracking has proved to be a valuable alternative to tracking systems based on other technologies, such as magnetic, acoustic, gyroscopic, and mechanical. Advantages of optical tracking include that it is less susceptible to noise, it allows for many objects to be tracked simultaneously, and interaction devices can be lightweight and wireless. As such, it allows for almost unhampered operation.

In this chapter, the current state of the art in model-based optical tracking is reviewed. After defining the aims and problems in optical tracking, various tracking approaches are discussed and solution strategies reviewed. This chapter focusses on tracking the three-dimensional position and orientation of rigid interaction devices. Optical tracking techniques for devices with more degrees of freedom are discussed in Chapter 7.

The chapter is organized as follows. In Sections 2.1 and 2.2, the optical tracking problem is defined, and a framework is presented that identifies the various steps involved in optical tracking. In Section 2.3, various concepts are discussed that are used to solve the optical tracking problem. Sections 2.4 and 2.5 review the most common recognition and pose estimation methods. A description of the tracking system of the Personal Space Station as developed at CWI is given in Section 2.6. Section 2.7 discusses strategies for the evaluation of tracking methods. Finally, Section 2.8 gives conclusions.

2.1 The Optical Tracking Problem

Optical tracking methods can be divided into two categories:

- *Feature-based*
  Feature-based tracking approaches are based on the detection of certain predefined features in the environment using imaging sensors. Features are prominent properties that can be detected in the tracking volume. For instance, colored markers or small light sources such as light-emitting diodes can be added to a scene. These markers are relatively easy to find, simplifying the image processing. A common approach is to use round markers, such that the features are defined by points.

- *Vision-based*
  Vision-based approaches try to identify real-life features by using advanced image processing. As such, no artificial features need to be introduced to the environment. Vision-based approaches are generally more computationally expensive than feature-based approaches. As a consequence, they operate at lower frequency and introduce higher latency.

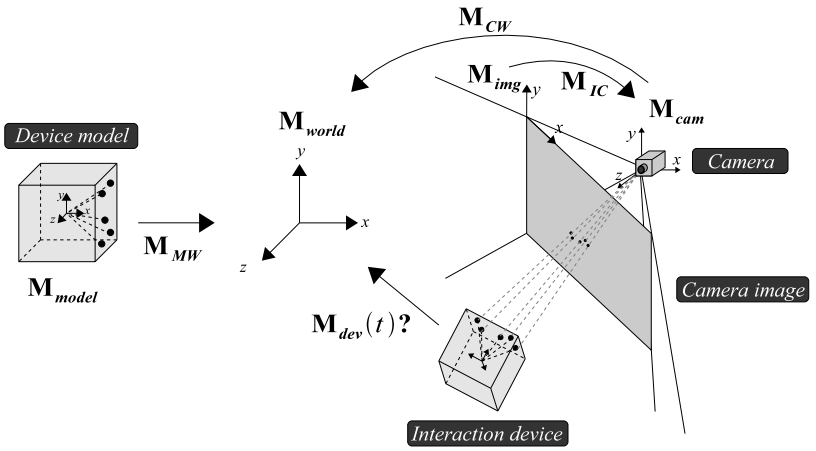

Figure 2.1: The coordinate systems involved in the tracking problem.

The research in this thesis focusses on feature-based optical tracking, due to its capability of achieving high frame rates and low latency.

2.1.1 Problem Statement

Optical tracking of rigid objects can be defined as the measurement of the 3D position and orientation, or pose, of one or more interaction devices that move in a defined space, relative to a known location [RDB00]. The tracking problem involves various frames of reference, as illustrated in Figure 2.1. A frame of reference is represented as a 4×4 homogeneous transformation matrix [Van94].

The world frame of reference $\mathbf{M}_{world}$ and the camera frame of reference $\mathbf{M}_{cam}$ are fixed at an arbitrary location in the tracking space. Features in the camera image are defined in the image frame of reference $\mathbf{M}_{img}$. The transformation $\mathbf{M}_{CW}$ that maps camera coordinates to world coordinates is defined by the extrinsic camera parameters, whereas the transformation $\mathbf{M}_{IC}$ that maps image coordinates to camera coordinates is defined by the intrinsic camera parameters. These parameters are determined by a camera calibration procedure, which is discussed in more detail in Section 2.3.1.

The 3D positions, and the orientations if appropriate, of the features on a device are defined by a *device model*, which expresses the features in a common model frame $\mathbf{M}_{model}$ that is placed at the origin and aligned with the axes of the interaction device. The model frame and the world frame are related by a transformation matrix $\mathbf{M}_{MW}$, that, for simplicity and without loss of generality, can be set to the identity matrix $\mathbf{I}$.

The optical tracking problem can now be formulated as follows:

> Determine the matrix $\mathbf{M}_{dev}(t)$ that transforms the 3D model features in $\mathbf{M}_{model}$ into the world frame $\mathbf{M}_{world}$, such that their projections onto the camera image planes match the detected 2D image features.

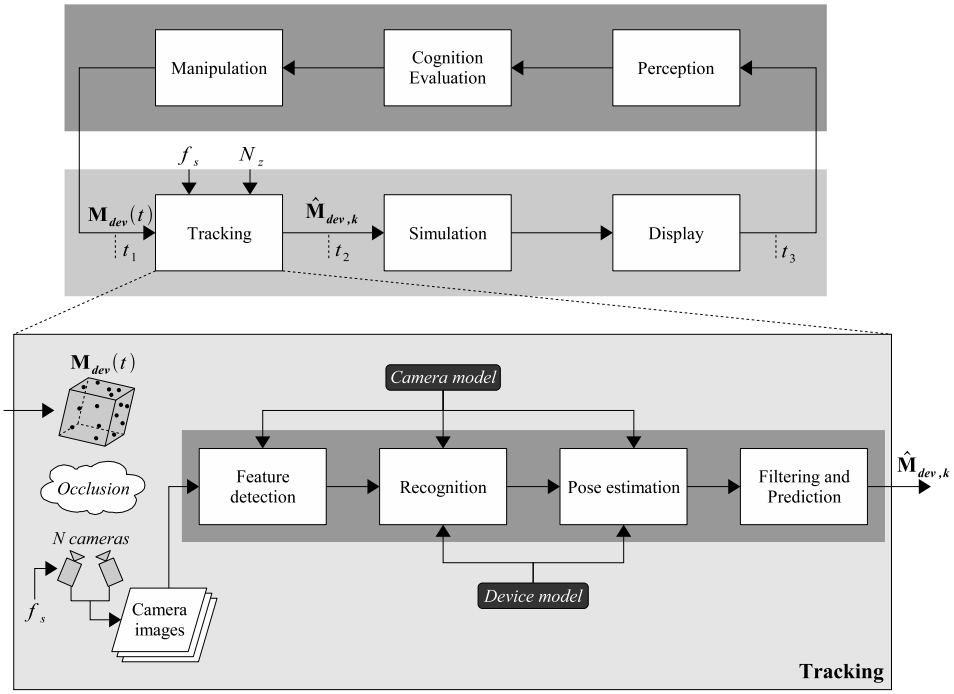

Figure 2.2: The tracking pipeline and its place in the interaction cycle. Tracking consists of four subproblems: feature detection, recognition, pose estimation, and filtering and prediction.

2.2 Optical Tracking Framework

In this section, a framework is presented that defines the subproblems that need to be addressed to solve the optical tracking problem, and how these steps fit within the interaction cycle as discussed in Chapter 1. The framework also identifies critical parameters that influence the performance of a tracking method, which are discussed in more detail in Section 2.7.

Figure 2.2 depicts the optical tracking framework and its relation with the interaction cycle as presented in Figure 1.1. A user performs an action with one or more interaction devices at time t_1. The position and orientation of an input device is represented as the 4×4 homogeneous transformation matrix $\mathbf{M}_{dev}(t)$. The user's actions are registered by a tracking system, which samples the tracking space with a frequency f_s and introduces measurement noise N_z. As a result, the tracking system obtains an estimate $\hat{\mathbf{M}}_{dev,k}$ at discrete time k of the actual pose. The pose estimates $\hat{\mathbf{M}}_{dev,k}$ are used by the virtual environment to update a simulation, and at time t_3 the display is updated accordingly. The time interval $t_3 - t_1$ is the end-to-end latency of the virtual environment.

The first step in optical tracking is feature detection, which involves the application of image processing techniques to detect the features in the camera images. For instance, if round markers are used, their 2D locations are detected in the images. Once these features have been found, the optical tracking problem can be solved in three steps:

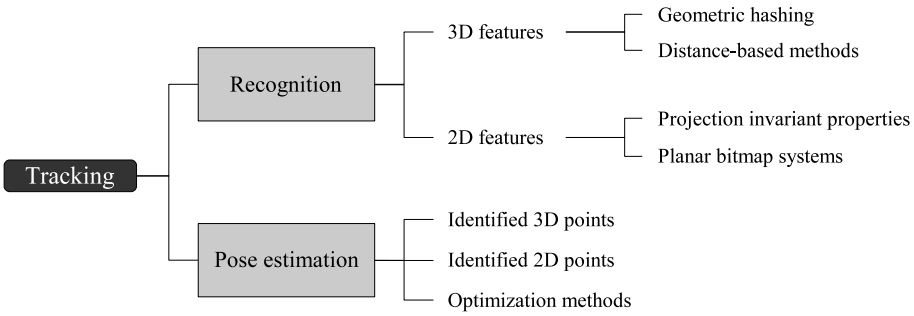

Figure 2.3: Taxonomy of recognition and pose estimation methods.

- *Recognition*
  Recognition involves determining the correspondence between the detected 2D image features and the 3D features in the device model.
- *Pose estimation*
  Pose estimation entails the calculation of the 3D position and orientation of each input device.
- *Filtering and prediction*
  The influence of the measurement noise N_z and the effects of latency can be reduced by the application of filtering and prediction techniques. Such techniques are analyzed in Chapter 6.

In the following, the recognition and pose estimation steps are discussed in more detail.

Recognition

The recognition problem is defined as the determination of the correspondence between the detected 2D image features and the 3D markers on the interaction device. This can be accomplished by matching the image features to a device model, which describes the 3D structure of the features on the device relative to the reference frame $\mathbf{M}_{model}$. Recognition methods can be divided into two categories, as illustrated in Figure 2.3:

- *Recognition using 3D features*
  Features from two or more cameras are first matched to each other to determine the feature parameters in 3D. The basic steps involve using stereo correspondence to relate features from one image to the features in a second images, transform these to 3D, and use a 3D recognition method to identify device features. These steps are discussed in more detail in Section 2.3.2.

  A common approach for recognition using 3D markers is to use point features, such that recognition can be accomplished in two ways. The first is the geometric hashing approach, which is discussed in Section 2.4.1. The second approach is based on matching the distances between markers with the distances stored in the device model.
- *Recognition using 2D features*
  Interaction devices are identified completely in 2D using a single camera image. Ex-

isting tracking methods generally fall into two categories. The first is to use feature properties that are invariant under perspective projection. The second approach is to encode information into planar bitmap patterns. The perspective distortion can easily be removed from such patterns, such that the encoded information can be retrieved for recognition.

Previous research that uses these recognition methods are discussed in Section 2.4.

Pose Estimation

Pose estimation is defined as the determination of the 3D position and orientation of the interaction device, given the correspondence between the data features and the device model obtained from the recognition step. The most common pose estimation approach is to extract a set of points from the device model, along with a corresponding set of points from the 2D image feature set. Three pose estimation approaches can be distinguished:

- *Pose estimation using identified 3D points*
  Points are identified in the recognition step and transformed to 3D space using two or more cameras. As a result, a set of 3D data points is constructed, along with the set of corresponding 3D model points. The pose is defined by the transformation that maps the 3D model points onto the 3D data points.

- *Pose estimation using identified 2D points*
  Points are identified in the recognition step, and a set of 2D data points and the set of corresponding 3D model points is constructed. The pose is defined by the transformation that changes the position of the 3D model points such that their projections onto the image plane match the 2D data points.

- *Pose estimation by optimization*
  In case features cannot be identified, optimization routines can be used to estimate a pose from the data. In this case, the pose of the input device is iteratively refined to match the data points to the model.

These approaches are discussed in more detail in Section 2.5.

2.3 Concepts

To solve the optical tracking problem as defined in Section 2.1, the relation between 2D image features and the world reference frame $\mathbf{M}_{world}$ needs to be determined. In this section, the underlying concepts that are needed to solve the optical tracking problem are reviewed.

2.3.1 Camera Model

A camera model defines a mapping between the 3D world and a 2D image. This section discusses the camera model that is used in the optical tracking techniques presented in this thesis.

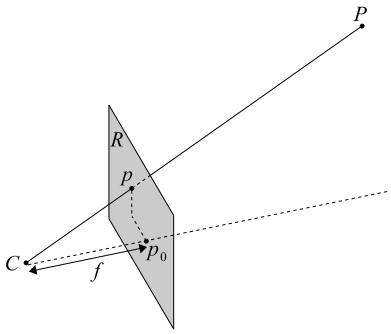

Figure 2.4: A pinhole camera model, described by its optical center C and its retinal plane $\mathcal{R}$.

The Pinhole Camera

We first review the most specialized and simple camera model, which is the basic pinhole camera model. This model is improved upon in the following sections.

A pinhole camera can be described by its optical center C and its retinal plane $\mathcal{R}$. The retinal plane (or image plane) represents the imaging sensor of the camera, which is generally a charge-coupled-device (CCD). A 3D point P is projected into an image point p, which is given by the intersection of the plane $\mathcal{R}$ with the line through C and P (see Figure 2.4). The line through C and the principal point p_0, which is orthogonal to $\mathcal{R}$, is called the optical axis. The distance between C and $\mathcal{R}$ is the focal length f.

The relation between a 3D point P and its projection p on the retinal plane $\mathcal{R}$ is defined by a perspective transformation, which is represented by a linear transformation in homogeneous coordinates. Let the 3D point P and its 2D projection p be expressed as homogeneous coordinates $P = (x, y, z, 1)$ and $p = (u, v, 1)$, respectively. The perspective transformation is given by

$$\begin{pmatrix} u' \\ v' \\ w' \end{pmatrix} = \mathbf{M}_{CI}\mathbf{M}_{WC} \begin{pmatrix} x \\ y \\ z \\ 1 \end{pmatrix} \tag{2.1}$$

$$u = \frac{u'}{w'}, \qquad v = \frac{v'}{w'} \tag{2.2}$$

In this equation, the matrix $\mathbf{M}_{CI}$ depends solely on intrinsic camera parameters. These are internal camera parameters, which do not change when adjusting the position and orientation of the camera, i.e., the principal point p_0, the pixel aspect ratio, and the focal length. The matrix $\mathbf{M}_{WC}$ models the extrinsic parameters, which model the position and orientation of the camera in an arbitrarily fixed world coordinate system.

The camera parameters can be modeled as follows:

- *Intrinsic Matrix*
  In the simplest case of perspective projection, the projection center C is placed at the origin of the world coordinates and the image plane is aligned with the xy plane, with the optical axis along the z-axis. This configuration is referred to as camera space.

The transformation from a 3D point $P = (x, y, z)$ to a 2D point $p = (u, v)$ in camera space is given by

$$\begin{pmatrix} u \\ v \end{pmatrix} = \begin{pmatrix} \frac{fx}{s_x z} + u_0 \\ \frac{fy}{s_y z} + v_0 \end{pmatrix} \tag{2.3}$$

where f is the focal length of the camera, $s = (s_x, s_y)$ represents the pixel size along the u and v axes, and $p_0 = (u_0, v_0)$ the principal point. In practice, the axes of a pixel are often not completely orthogonal, which is accounted for by a skew-factor α. The complete matrix $\mathbf{M}_{CI}$ from Equation 2.1 is then given by

$$\mathbf{M}_{CI} = \begin{pmatrix} \frac{f}{s_x} & \alpha & u_0 & 0 \\ 0 & \frac{f}{s_y} & v_0 & 0 \\ 0 & 0 & 1 & 0 \end{pmatrix} \tag{2.4}$$

- *Extrinsic Matrix*
  The perspective projection is completely described by the intrinsic matrix, as long as all coordinates are expressed in camera space. In case the projection center C is not placed at the origin of the world coordinates and the optical axis does not correspond to the z-axis, the extrinsic matrix $\mathbf{M}_{WC}$ is used to transform points from world space to camera space. The matrix is defined by a rotation and a translation

  $$\mathbf{M}_{WC} = \mathbf{TR} \tag{2.5}$$

  Therefore, it is independent of internal camera parameters, and defines the position and orientation of the camera in world coordinates.

  The translation of the world origin to the location of the projection point $C = (c_x, c_y, c_z)$ is defined by the transformation matrix

  $$\mathbf{T} = \begin{pmatrix} 1 & 0 & 0 & -c_x \\ 0 & 1 & 0 & -c_y \\ 0 & 0 & 1 & -c_z \\ 0 & 0 & 0 & 1 \end{pmatrix} \tag{2.6}$$

  The rotation matrix $\mathbf{R}$ rotates all points around the projection point to align the optical axis with the z-axis. If the axes of the camera coordinate system are known, this matrix is given by

  $$\mathbf{R} = \begin{pmatrix} N_x & N_y & N_z & 0 \\ U_x & U_y & U_z & 0 \\ V_x & V_y & V_z & 0 \\ 0 & 0 & 0 & 1 \end{pmatrix} \tag{2.7}$$

  where $V = (V_x, V_y, V_z)$ is the camera's viewing direction, $U = (U_x, U_y, U_z)$ the up vector, and $N = V \times U$.

Image Distortion

Real cameras deviate from the pinhole model in a few ways, adding non-linear components to the linear transformation defined by Equation 2.1:

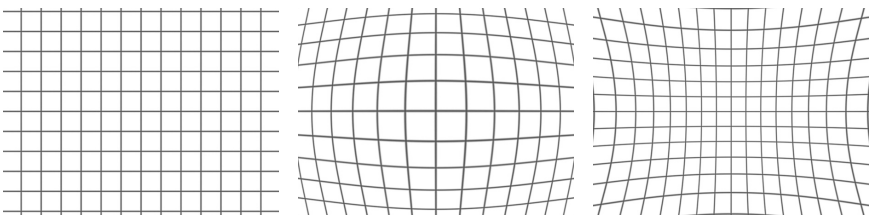

Figure 2.5: Illustration of image distortion. (a) The original image. (b) The image with barrel distortion. (c) The image with pincushion distortion.

- Real camera lenses have a limited depth of field. In order to collect enough light to expose the CCD, light is gathered across the surface of the lens. As a consequence, only a small plane in the tracking space is in perfect focus, resulting in a shallow depth of field. However, by choosing the lens aperture and shutter time appropriately, the depth of field can be sufficiently increased, such that this effect can be neglected.
- The second cause for deviations from the pinhole model is lens distortion. Due to various constraints in the lens manufacturing process, the projection of a straight line on the image plane of a real lens becomes somewhat curved. Since each lens element is practically radially symmetric, this distortion generally is radially symmetric. This radial distortion is the most present form of distortion.

Distortion effects can be observed in most cameras, and are generally stronger in wide-angle lenses. Two types of radial distortion can be distinguished:

- Barrel effect. This type of distortion causes images to appear curved outward from the center (see Figure 2.5(b)).
- Pincushion effect: this type of distortion causes images to appear pinched towards the center (see Figure 2.5(c)).

A second form of distortion of tangential distortion. This is due to imperfect centering of the lens components on the axis and other manufacturing defects.

Lens distortion can be accurately modeled by the sum of the radial and tangential distortions vectors [HS97]. The radial distortion vector is defined as

$$\begin{pmatrix} \hat{u} \\ \hat{v} \end{pmatrix} = \begin{pmatrix} u(k_1 r^2 + k_2 r^4 + \ldots) \\ v(k_1 r^2 + k_2 r^4 + \ldots) \end{pmatrix} \tag{2.8}$$

where u and v are image coordinates, $\hat{u}$ and $\hat{v}$ are distorted image coordinates, k_i are radial distortion coefficients, and $r = \sqrt{u^2 + v^2}$.

The tangential distortion vector is defined by

$$\begin{pmatrix} \hat{u} \\ \hat{v} \end{pmatrix} = \begin{pmatrix} 2p_1 uv + p_2(r^2 + 2u^2) \\ p_1(r^2 + 2v^2) + 2p_2 uv \end{pmatrix} \tag{2.9}$$

where p_1 and p_2 are tangential distortion coefficients.

These equations provide an accurate model to map image coordinates to their distorted counterparts. However, no analytic solution to the inverse mapping exists [HS97]. A number of approximative solution strategies exist. One option is to neglect the tangential distortion, and to invert the parameters of the radial distortion component. Clearly, this approach is not very accurate. Another option was proposed by Heikkiläs, which involves a non-linear search for implicit parameters to recover the real pixel coordinates from the distorted ones [HS97]. This approach is more accurate than neglecting tangential distortion completely, but is also more computationally expensive.

Calibration

Camera calibration involves determining the intrinsic and extrinsic camera parameters that are used in the camera model as discussed in the previous sections. Since the distortion parameters do not change when moving a camera, they are regarded as intrinsic parameters. The main idea in calibration is to obtain a number of matching relations between a 3D point P and its projection p, and use these in an optimization procedure to determine the camera parameters.

A number of calibration approaches exist, which can be categorized based on the dimensionality of the object used for calibration:

- *Three dimensional object calibration*
  Tsai's method for camera calibration recovers the intrinsic and extrinsic camera parameters that provide a best fit of the measured image points to a set of known 3D target points [Tsa86]. The procedure starts with a closed form least-squares estimate of some parameters, followed by an iterative non-linear optimization of all parameters simultaneously. The method works with objects spanning a volume or with coplanar objects.

- *Grid calibration*
  The most common calibration method uses a coplanar and predefined point grid that can be moved freely in front of the cameras [Zha00, Tsa86]. At least two images of the grid have to be taken at different positions and orientations. The main advantage of this method is that it is relatively easy to construct the calibration object.

- *Pointer calibration*
  Zhang proposed a method that uses a pointer shaped calibration object using collinear points [Zha02]. The method recovers intrinsic camera parameters. Constraints are that the object should rotate around a fixed point, and distortion parameters are not obtained.

- *Moving point calibration*
  In this case, it suffices to move a single point around in the interaction volume [LS00a]. Moving point calibration methods are intended to recover extrinsic parameters only. Although this is a limitation, a grid calibration method could be used to recover intrinsic parameters. Since these parameters remain constant when the camera placement is changed, extrinsic parameters can be determined using the more convenient moving point calibration method.

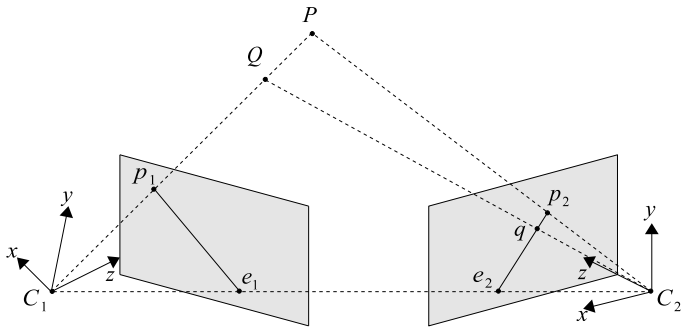

Figure 2.6: Stereo geometry: A 3D point P is projected onto the image planes of two pinhole cameras with optical centers C_1 and C_2.

2.3.2 Stereo Geometry

Many tracking approaches transform the detected image features to 3D by using stereo geometry. Using stereo geometry, features in two camera images can be matched to each other and transformed to 3D. This information can then be used to perform the recognition using 3D features.

Consider a stereo setup composed by two pinhole cameras, as illustrated in Figure 2.6. Let C_1 and C_2 be the optical centers of the left and right cameras respectively. A 3D point P is projected onto both image planes, resulting in the 2D point pair p_1 and p_2. Given p_1, its corresponding point in the right image is constrained to lie on a line called the epipolar line. The epipolar line is the projection of the optical ray through C_1 and p_1, and passes through p_2 and e_2. All epipolar lines in an image pass through a common point, e_1 for the left image and e_2 for the right. This common point is referred to as the epipole, and is the projection of the optical center of the other camera onto the image plane.

Given a point p_1 in one camera image, the search for a corresponding point p_2 in the other camera image is constrained to lie on the epipolar line. A special case is when all epipolar lines are parallel and horizontal. The search for a corresponding point p_2 is then reduced to a one-dimensional search. This situation occurs when the epipoles e_1 and e_2 of both images are at infinity, i.e., when the baseline (C_1, C_2) is contained in both focal planes. In this case, the retinal planes are parallel to the baseline. Any pair of images can be transformed such that the epipolar lines are parallel and horizontal in each image, as illustrated in Figure 2.7. This procedure is called rectification.

Rectification involves the following steps:

- Compute the intersection line between the original image planes.
- Compute the baseline (C_1, C_2).
- Compute the equation of the plane that is parallel to both lines.
- Rotate both cameras so they have a common orientation.

For a more detailed discussion on stereo geometry and rectification, the reader is referred to [FP02].

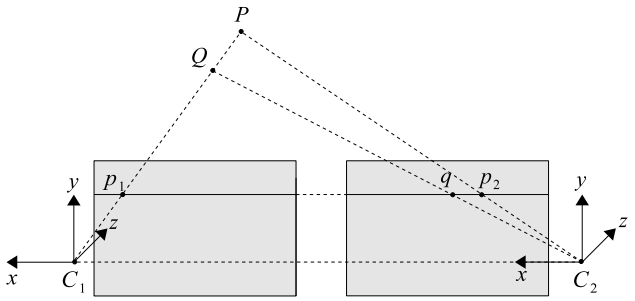

Figure 2.7: A stereo setup after rectification. The epipolar lines become horizontal, reducing the stereo correspondence problem to a one-dimensional search problem.

Stereo Correspondence

The stereo correspondence problem is defined as the determination of the correspondence between features in the left image and the features in the right image, such that each pair of features (p_1, p_2) originates from the same 3D feature. After rectification, stereo correspondence is reduced to a one-dimensional search problem. Given a feature p_1 in one image, its corresponding feature p_2 is constrained to lie on the corresponding horizontal epipolar line. This search is ambiguous, since multiple features in the right image may lie on the same epipolar line of a feature in the left image. For instance, in Figure 2.7 the corresponding feature of p_1 is constrained to lie on the epipolar line that passes through p_2 and q. As a result, the 3D point that corresponds to p_1 could be either P or Q.

To solve this ambiguity, other matching constraints can be exploited:

- *Similarity*
  Features in both images must have similar attributes and similar neighborhoods.
- *Uniqueness*
  A feature in one image can only correspond to one feature in the other image. An exception is the case where a feature lies in the same line of view as another feature, causing them to merge in the camera image.
- *Continuity*
  In case an object contains multiple 3D points relatively close together, the disparity of corresponding features of the device should vary smoothly. For instance, if a cube is equipped with markers, the disparity of the 2D projections of the markers on the same surface varies smoothly. This constraint fails at discontinuities of depth, which cause abrupt changes in disparity.
- *Ordering*
  If a point p_1 in the left image matches a point q_1 in the right, a point p_2 matches a point q_2, and p_1 is to the left of p_2, then q_1 should also be to the left of q_2. In other worlds, the ordering of features is preserved across images. This constraint can fail in scenes containing narrow foreground objects [YP84].

Much research has been done on stereo correspondence. Many researchers have addressed the problem of dense stereo correspondence [SS02], dealing with large numbers of

features. A common approach is to match features based on the similarity of the surrounding pixels [PMF85, Pil97, BT98]. Pilu [Pil97] uses an elegant and simple algorithm to incorporate the uniqueness and similarity constraints into the matching process. He uses a general correspondence method described by Scott and Longuet-Higgins [SLH91], and defines a similarity metric to match features, based on the distance between the 2D feature locations in the camera images, and the correlation of the surrounding pixels.

Another approach to solve the stereo correspondence problem is to use relaxation techniques. Such techniques use a global matching constraint to eliminate false matches. For instance, Barnard and Thompson [BT80] propose a relaxation technique that starts by assigning each candidate match a probability value. This value is based on the number of neighboring matches that have consistent disparity values with the candidate match. The probability value of each candidate match is iteratively updated until it is below a certain threshold, after which it is removed. The procedure stops when each candidate match has only one probability value left, i.e., when all features are in one-to-one correspondence.

Most stereo correspondence approaches use matching metrics such as the correlation of surrounding pixels or marker characteristics. However, the camera images from the infrared optical tracking system of the PSS (see Section 2.6), which uses features such as points and lines, do not contain enough information to use such characteristics. Point or line shaped markers will have practically identical characteristics in both images. In this case, other approaches need to be found to solve the stereo correspondence problem.

2.4 Recognition

In the following sections, previous work on recognition approaches as discussed in Section 2.2 is reviewed. This overview is not meant to be exhaustive, but rather to review the most important and practical approaches made in the field of optical tracking. For a more extensive discussion on optical tracking methods, the reader is referred to [LF05].

2.4.1 Recognition using 3D features

Given a set of 3D data features, the tracking problem can be divided into two steps: matching a subset of the 3D features to a subset of the features defined in a device model, and determining the pose of each recognized device. Most trackers based on 3D features use point shaped markers. These approaches can be divided into two categories:

- *Pattern-based methods*
  These methods subdivide a model into small unique patterns, and try to match complete patterns with the features found in the camera images. These methods are generally efficient in terms of computational and storage requirements, but fail to track an object when patterns are only partially visible.

- *Point-cloud based methods*
  In this case, all points of a model are considered as one whole, and a subset of the model is matched to the data.

Geometric Hashing

A well-known point-cloud based method is geometric hashing [LSW88]. It is based on a preprocessing stage to generate fast lookup tables. For each combination of three model points, a coordinate system is defined in which all remaining points are expressed. Next, the locations of these points are quantized to account for noise, and serve as addresses into a 3D hash table. The table stores pointers back to the model and the reference frame. During recognition, a combination of three data points is taken and a reference frame is determined. All other data points are expressed in this frame, and are used to address the hash table to generate votes for a model and reference frame. If a model receives enough votes, it is marked as identified. Since the repeated transformation of data points into a reference frame can be computationally expensive, the effectiveness of this method depends on the amount of candidates that need to be examined.

3D Distance Methods

Various researchers have used 3D distance fitting approaches for device recognition. An approach presented by Dorfmüller [Dor99] uses retro-reflective spherical markers on each input device, which are easily detected as 2D blobs in the camera images. Next, all possible 3D positions are calculated using stereo geometry. Devices are equipped with three markers to form a non-regular triangle, where all inter-marker distances are unique. A model of a triangle is then fitted to the 3D data positions by minimizing the sum of differences between the real markers distances and the measured distances.

Ribo et al. [RPF01] followed a similar approach and used two CCD cameras to track 25 markers in the scene at 30 Hz. The system used Zhang's calibration method [Zha00], linear prediction of targets in image space, and straightforward epipolar geometry to determine a list of candidate 3D marker locations.

Van Liere et al. [LR04] developed a distance-based recognition method that is a special case of the general Euclidean Distance Matrix completion problem [Lau01], and can be seen as a generalization of the method proposed by Dorfmüller [Dor99]. The method requires the definition of point patterns. For each pattern on a device, a distance matrix is constructed by measuring the 3D distance between each marker pair of the pattern. The recognition method first finds all the sub-matrices in the data distance matrix $\mathbf{D}$ that fit in the pattern distance matrix $\mathbf{P}$. Then, a least squares fitting metric is used to determine which sub-matrix of $\mathbf{D}$ best fits the pattern distance matrix $\mathbf{P}$.

2.4.2 Recognition using 2D Features

Projection Invariants

Some optical tracking methods use features with projection invariant properties, which are properties that remain constant under perspective projection. Features with such properties can be recognized in 2D using a single camera image. In the following, some important projection invariant properties that have been used for optical tracking are reviewed.

- *The Cross Ratio*
  Projective geometry preserves neither distances nor ratios of distances. However, it does preserve a property called the cross ratio, which is a ratio of ratios of distances. Given four collinear points, labeled as A, B, C, D (see Figure 2.8), the cross ratio is

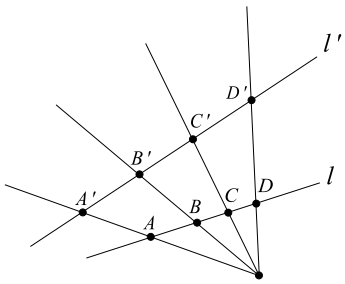

Figure 2.8: The cross ratio of four collinear points is invariant under perspective projections. As such, the cross ratio of points A, B, C, D equals the cross ratio of points A', B', C', D'.

the real number defined by:

$$C_r(A, B, C, D) = \frac{|AB|/|BD|}{|AC|/|CD|} \tag{2.10}$$

where $|AB|$ is the Euclidean distance between points A and B.

The cross ratio has been extended to five coplanar points. Van Liere et al. [LM03] have applied the cross ratio to construct patterns of four collinear or five coplanar points. Each device is augmented with one or more patterns, which are modeled and stored in a database. The model describes the 3D positions of markers on the device in a common coordinate system, along with the cross ratio of each pattern.

Recognition of patterns is performed by calculating the cross-ratio of each combination of four or five points detected in the camera image, and by comparing the obtained cross ratio with a certain range. This range is used to account for noise in the measured 2D marker locations, as the cross ratio is sensitive to noise. The cross ratio and its associated range of each pattern is obtained by a training procedure, during which a developer moves the pattern in front of the camera. The resulting values are stored in the device model.

The computation of the cross ratio depends on the order of the points. Van Liere et al. [LM03] use a permutation invariant introduced by Meer et al. [MLR98], resulting in a single cross ratio value, independent of ordering. After recognition, the correspondence between point patterns in the camera image and the 3D pattern information stored in the device model is known.

However, to reconstruct the pose of the device, the exact one-to-one correspondence between individual 2D points and the modeled 3D points has to be known. This correspondence is determined by transforming the points to 3D using stereo geometry, and calculate the 3D positions of the pattern points. Next, the inter-point distances are used to match data points to model points, using a least-squares fit metric. For patterns of five points, this results in a maximum of 25 combinations to test in order to obtain identified points.

- *Graph Topology*
  Another projection invariant property is graph topology: when projecting a graph structure its topology remains constant, as long as no parts of the graph become overlayed

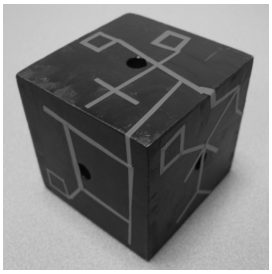

Figure 2.9: An example device augmented with a graph.

in the camera images. Recent work by Smit et al. [SRL06] exploits this property for single camera device recognition and pose estimation. Devices are augmented with a graph, as illustrated in Figure 2.9. This graph can be efficiently located in the camera images.

The method starts by an image processing stage to retrieve the graph structures in 2D. First, a thresholding method is applied to obtain a binary image. The connected regions are determined and processed using a morphology-based skeletization algorithm. Small parasitic edges are removed in the final phase. The result is a strictly 4-connected, single pixel width skeleton of the input blobs. The graph topology is obtained by performing a recursive walk method. Vertices are created when a pixel has more than two neighboring pixels.

The obtained graph topology is matched to a device model, which describes the topology and 3D positions of the graph vertices in a common device coordinate system. The matching is done by applying an error tolerant subgraph matching algorithm, which is a slight modification of the method by Cordella et al. [CFSV04]. The pose can be reconstructed using a single camera, although depth resolution is poor. Combining multiple cameras, a more accurate pose estimate can be obtained.

The approach can handle partial occlusion of the graph structure. Furthermore, recognition is performed entirely in 2D, and therefore no stereo correspondence is needed. As such, there are virtually no restrictions to camera placement.

- *Other projection invariant properties*
  Various other projection invariant properties have been identified and used for recognition. Verri et al. [VY86] discuss the use of points of zeros of curvature of curves as projection invariant properties. Mendlovic et al. [MKM90] have used a logarithmic harmonic filter for projection invariant pattern recognition of bitmap targets. Lui et al. [LPN+06] have used the projection invariant characteristics of NURBS for stereo matching.

  The applicability of these approaches for tracking in virtual environments, which require high accuracy and low latency object recognition, is the subject of further research. The use of logarithmic harmonics allows for bitmap patterns to be recognized, similar to the use of ARToolkit [KB99]. The use of curve shapes may be less suitable for rapid construction of new interaction devices, unless these curves can be arbitrarily drawn, printed out, and trained to be recognized by the system.

(a) (b)

Figure 2.10: (a) Two example ARToolkit bitmap patterns. (b) Two ARTag bitmap patterns including an error correcting code.

Planar Bitmap Pattern Systems

Planar bitmap pattern systems share ideas with projection invariant properties. They are based on encoding information into a bitmap that can easily be retrieved after perspective projection. Planar patterns are used so that the perspective distortion can be accurately removed from the bitmap and the encoded information can be retrieved.

A widely used framework for augmented reality is ARToolkit [KB99]. This system solves the recognition problem by detecting a square, planar bitmap pattern, using correlation techniques for pattern recognition. ARToolkit patterns are planar bitmaps and can easily be printed out and used by the system. Two example patterns are depicted in Figure 2.10(a). They are enclosed by a black border. Pattern recognition proceeds in two stages: recognition of the pattern boundaries, and correlation of the interior pattern with the patterns stored in a database.

The pattern borders are detected by finding connected groups of pixels below a certain threshold, finding their contours, and marking the contours consisting of four straight lines as potential patterns. The corners of the contours are used to remove the perspective distortion and transform the pattern into a canonical coordinate system. Next, an $N \times N$ grid is defined to sample the pattern. The samples are correlated with several reference grids stored in a pattern file.

The pattern file contains 12 reference grids, which are three versions of four possible rotation positions of a pattern. The three versions are intended to handle different lighting and distance conditions that influence the appearance of patterns. The system outputs a confidence factor, which is compared to a threshold to determine if a pattern is visible. In case a pattern has been found, the corners of the border are used to determine the 3D position and orientation of the pattern using a single camera.

Although ARToolkit is useful for many applications, it has a few disadvantages. First, it is sensitive to pattern occlusion. In case the border is occluded, the method fails to find potential patterns, whereas if part of the interior bitmap is occluded the correlation method fails. Second, the use of correlation methods to recognize patterns causes high false positive and inter pattern confusion rates.

Fiala [Fia05] reduced the occlusion problem by using an error correcting code as bitmap pattern in ARTag. It used an edge linking method to detect the pattern borders, instead of the contour of thresholded images as in ARToolkit. As a result, ARTag can still detect patterns if part of a border is occluded. The interior pattern is a digitally encoded, error correcting code, as illustrated in Figure 2.10(b). As a result, the pattern interior may be partially occluded,

and ARTag achieves lower false negative rates than ARToolkit, as well as, and more crucially, lower false positive rates. However, patterns are still required to be planar.

2.5 Pose Estimation

In the following sections, previous work on pose estimation is reviewed. Pose estimation involves determining the 3D position and orientation of the interaction device, given the data features and the device model. Pose estimation is usually performed by first extracting a set of points from the model and image features. In the following, three common approaches are discussed.

2.5.1 Pose Estimation using Identified 3D Points

If recognition results in identified 3D image points, pose estimation is reduced to the absolute orientation problem. The absolute orientation problem can be defined as the minimization of the mean squared error between two matched points sets under rigid-body transformations. Consider a set of N 3D data points p_i and the corresponding model points m_i. The goal is to find the rotation matrix $\mathbf{R}$ and translation T that maps m_i to p_i:

$$p_i = \mathbf{R}m_i + T \tag{2.11}$$

Due to various properties of quaternions that make them preferable over rotation matrices [Hor87], Equation 2.11 can be expressed as

$$p_i = qm_iq^{-1} + t \tag{2.12}$$

where q is the quaternion representation of $\mathbf{R}$. The absolute orientation problem can now be defined as finding the least-squares solution that minimizes the objective function

$$f(q,t) = \sum_{i=1}^{N} |p_i - qm_iq^{-1} - t|^2 \tag{2.13}$$

over all rotations q and translations t.

Horn [Hor87] derived a solution to the absolute orientation problem. The method can be summarized by the following steps:

- Calculate the centroids r_p and r_m of the point sets p_i and m_i, and subtract these from the data.
- For each pair of coordinates (p_i, m_i), calculate all possible products of the point coordinates $x_px_m, x_py_m, \ldots, z_pz_m$ and add these up to obtain $S_{xx}, S_{xy}, \ldots, S_{zz}$.
- Compute the elements of the symmetric matrix $\mathbf{N}$

$$\begin{bmatrix} S_{xx}+S_{yy}+S_{zz} & S_{yz}-S_{zy} & S_{zx}-S_{xz} & S_{xy}-S_{yx} \\ S_{yz}-S_{zy} & S_{xx}-S_{yy}-S_{zz} & S_{xy}+S_{yx} & S_{zx}+S_{xz} \\ S_{zx}-S_{xz} & S_{xy}+S_{yx} & -S_{xx}+S_{yy}-S_{zz} & S_{yz}+S_{zy} \\ S_{xy}-S_{yx} & S_{zx}+S_{xz} & S_{yz}+S_{zy} & -S_{xx}-S_{yy}+S_{zz} \end{bmatrix} \tag{2.14}$$

- The unit quaternion that minimizes Equation 2.12 is given by the eigenvector that corresponds to the most positive eigenvalue of **N**.

The translation is then given by the difference between the centroid r_p and the rotated centroid r'_m. For the complete derivation of the above procedure, the reader is referred to [Hor87].

2.5.2 Pose Estimation using Identified 2D Points

If recognition results in identified 2D image points, the device pose can be reconstructed using Quan's method [QL99]. The idea is to first determine the 3D point locations that correspond to the 3D model points, given the 2D image points and the camera positions. Next, the pose estimation problem reduces to the absolute orientation problem as defined in the previous section, which can be solved efficiently using Horn's method [Hor87]. The method for determining the 3D point locations is briefly discussed below.

Given camera calibration matrices $\mathbf{M}_{CI}$ and $\mathbf{M}_{WC}$, the camera positions C_i, a set of 2D image points u_i, and a set of corresponding 3D device model points m_i, the problem is to determine the 3D positions p_i. Since all p_i reside in a different frame of reference as the device model $\mathbf{M}_{model}$, only the inter-point distances can be used. Each image point u_i can be expressed as a 3D point in the focal plane in world coordinates using the transformation matrices $\mathbf{M}_{IC}$ and $\mathbf{M}_{CW}$, yielding 3D image coordinates $\tilde{u}_i$. Each 3D point p_i is restricted to lie on the line through the 3D image point $\tilde{u}_i$ and the camera location C_i. The line L_i of point $\tilde{u}_i$ is described by its parametric form $C_i + t_i D_i$, with $D_i = \tilde{u}_i - C_i$. To determine the 3D points that match the model points m_i, the distance between each pair of points in the model (m_i, m_j) should match the distance between the corresponding pair of 3D points (p_i, p_j), such that

$$d_{ij} = ||m_i - m_j||^2 = ||(C_i + t_i D_i) - (C_j + t_j D_j)||^2 \tag{2.15}$$

Algebraic manipulation of this equation results in a polynomial in two unknowns (t_i, t_j)

$$\begin{aligned} f_{ij}(t_i, t_j) \quad = \quad & -d_{ij} + (C_{ij} \cdot C_{ij}) - 2(D_j \cdot C_{ij})t_j + (D_j \cdot D_j)t_j^2 \\ & + 2(D_i \cdot C_{ij})t_i - 2(D_i \cdot D_j)t_i t_j + (D_i \cdot D_i)t_i^2 = 0 \end{aligned} \tag{2.16}$$

where $C_{ij} = C_i - C_j$. The polynomial can be further simplified by normalizing the line directions D_i, such that $D_i \cdot D_i = 1$, and by translating all cameras to the origin, such that $C_{ij} = 0$. As a result, the following polynomial is obtained

$$f_{ij}(t_i, t_j) = t_i^2 + t_j^2 - 2(D_i \cdot D_j)t_i t_j - d_{ij} = 0 \tag{2.17}$$

Each pair of points leads to an equation of this form. Therefore, given N points, there are $\binom{N}{2}$ constraining equations. Using three equations P_{ij}, P_{ik}, and P_{jk}, a fourth degree polynomial in t_i^2 can be constructed by variable elimination. Given N points, $\binom{N-1}{2}$ fourth degree polynomials in one variable $t = t_i^2$ can be constructed. For $N > 5$ this system is an over-determined homogeneous linear equation system in $(1, t, \ldots, t^4)$, which can be solved in a least-squares fashion by using the singular value decomposition on the $\binom{N-1}{2} \times 5$ coefficient matrix. In case of $N = 4$ the linear system is under-determined, but can still be solved (see [QL99] for more details). Therefore, a minimum of four image points u_i and its corresponding model points m_i is required to reconstruct the 3D points p_i. After calculating t_i, the position of the 3D point p_i can be determined using the line equation $C_i + t_i D_i$.

After the 3D points p_i have been reconstructed, the transformation matrix that maps p_i onto the corresponding 3D model points m_i can be determined using Horn's method [Hor87].

2.5.3 Pose Estimation by Optimization

In case the one-to-one correspondence between the image points and the device model points cannot be obtained by recognition, the pose of an input device can still be estimated from the data by using the iterative closest point algorithm.

The iterative closest point (ICP) algorithm was introduced in 1992 by Besl and McKay, [BM92]. It is a general purpose, representation-independent method for registering three-dimensional shapes. The ICP algorithm is designed to match a set of data points to the points in a model. The ICP algorithm can be applied to pose estimation using either N 2D image points u_i and the model points m_i, or, in case the image points can be first transformed to the 3D points p_i, it can be adapted to function completely in 3D.

Given a device pose $\hat{\mathbf{M}}_{dev}$, a distance function is used to determine how well the data points fit the model points. An optimization procedure is used to minimize this distance function. Using only 2D image features, the distance function can be defined as the sum of minimum distances between the set S' of projected model points m'_i and the 2D image points u_j. In 3D, the distance function is simply defined as the sum of minimum distances between the set S of model points m_i and the 3D points p_j. The distance function D is defined as follows:

$$D = \frac{1}{N} \sum_{j}^{N} ||u_j - \mathcal{C}_{cp}(u_j, S')||^2 \tag{2.18}$$

in case of 2D pose estimation, or as

$$D = \frac{1}{N} \sum_{j}^{N} ||p_j - \mathcal{C}_{cp}(p_j, S)||^2 \tag{2.19}$$

in case of 3D pose estimation. The function $\mathcal{C}_{cp}$ is the closest point operator defined as

$$\mathcal{C}_{cp}(\underline{a}, \zeta) = \arg\min_{\underline{x} \in \zeta} ||\underline{x} - \underline{a}|| \tag{2.20}$$

The ICP algorithm iteratively minimizes the distance metric D. The ICP method can be formulated as an optimization problem in which the distance function produces an erratic multi-dimensional landscape with many local minima. A six DOF device results in a six dimensional space. The ICP method can easily be extended for multiple devices, where each device has its own device transformation matrix $\hat{\mathbf{M}}_{dev}$.

The main problem with the ICP method is that it requires a reasonable initial estimate of the device pose in order to complete efficiently. If an initial pose is unknown, a number of positions and orientations can be generated and used as input to ICP. However, this makes the method computationally expensive. The advantage of the method is that it is more robust against partial occlusion than most pattern-based approaches. Only a small subset of the device points needs to be visible in the cameras.

2.6 The Tracking System of the Personal Space Station

The research in this thesis was performed using the Personal Space Station, a near-field virtual environment developed at CWI. The PSS uses an optical tracking system. In the following, this system is discussed in more detail.

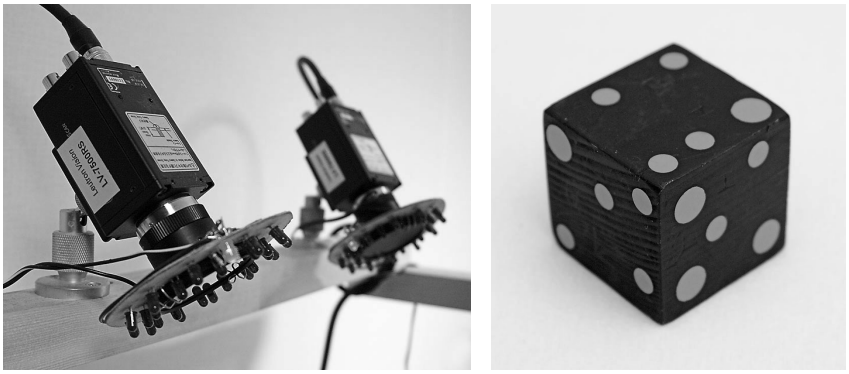

(a) (b)

Figure 2.11: (a) The cameras of the PSS are equipped with infrared-pass filters and a ring of IR LEDs illuminating the interaction space. (b) An example interaction device. The device is equipped with retro-reflective markers, which reflect incoming infrared light.

Tracking Setup

The Personal Space Station uses a marker-based optical tracking system. The tracking system consists of a set of cameras that face the interaction space, as illustrated in Figure 2.11(a). The PSS uses Leutron Vision LV-7500 progressive scan CCD cameras, operating at a frequency of 60 Hz. They are connected to a computer, equipped with Leutron Vision PicPort H4D frame grabbers for synchronized image capturing. More recent versions of the PSS use IEEE 1394 FireWire cameras to reduce the cost of the system.

The interaction space is illuminated by infrared (IR) light using a ring of light-emitting diodes (LEDs) mounted around the camera lenses. Interaction devices are equipped with retro-reflective markers, which reflect the incoming IR light back to the cameras. An example interaction device is given in Figure 2.11(b), where a small wooden cube is shown. By equipping the lenses with IR-pass filters, the resulting camera images contain the IR light reflected by interaction device markers, while blocking out most of the background. As a result, the images contain white blobs corresponding to the markers, which can be located using simple image processing techniques.

Feature Detection

Feature detection is accomplished by first transforming the camera images to a binary image using a dynamic threshold. Blob candidates are created by finding all distinguishable connected components using a flood fill method. Next, the center of each blob candidate is determined using a weighted average of the connected pixels, which is returned as its 2D position.

Distortion Correction

Distortion correction in the PSS is performed according to the method described by [Rey03]. The approach involves the pre-computation of a 2D lookup table which maps distorted image coordinates to undistorted coordinates. The lookup table has more pixels than the camera

images to account for the barrel distortion effect. The idea is then to use bilinear interpolation to map a distorted point $(\hat{u}, \hat{v})$ to a corrected point (u', v'). For more details, the reader is referred to [Rey03].

Calibration

For camera calibration in the PSS, the method of Zhang is used [Zha00]. The method uses a 2D grid of markers to compute six extrinsic camera parameters (position and orientation), and eight intrinsic parameters (focal length, aspect ratio, the image center, and two radial and tangential distortion coefficients).

2.7 Evaluating Tracking Methods

The performance of an optical tracking method can be defined as a combination of three different factors:

- *Accuracy*
  The accuracy of a tracking method is determined by the difference between the estimated device pose $\hat{\mathbf{M}}_{dev,k}$ and the real pose $\mathbf{M}_{dev}(t)$.

- *Latency*
  The latency of a tracking method is defined as the time required for image capturing, feature detection, recognition, and pose estimation, i.e. $t_2 - t_1$ in Figure 2.2.

- *Robustness*
  A tracking method is regarded robust if it satisfies the following properties. First, no false negatives should occur. Every time the cameras capture an image of an interaction device, the tracking method should be able to recognize the device and estimate its pose. Second, no false positives should be reported by the tracking method. If an interaction device is not located within the interaction volume at a certain time, the tracking method should not falsely report it. Third, the system should not report an invalid pose.

The performance of an optical tracking method depends on the reliability of its input parameters. From the framework defined in Figure 2.2, four sources of errors can be identified that influence the input to the tracking methods:

- *Lighting conditions*
  Camera image processing is very sensitive to the lighting conditions. This can lead to inaccurate parameter values of the detected 2D features, such as inaccurate point positions or line directions. As a consequence, the device pose estimate exhibits jitter.

- *Camera calibration*
  Inaccurate camera parameters influence the tracking methods in many ways. For example, incorrect camera parameters influence stereo geometry computations and the accuracy of back-projected features, and inaccurate image distortion parameters influence the geometry of the 2D features.

- *Device models*
  Inaccurate device models influence the recognition and pose estimation procedures, resulting in a systematic pose estimation error.

- *Occlusion*
  Occlusion of features can lead to failure to track an interaction device. Additionally, partially occluded image features may lead to inaccurate feature parameters, leading to inaccurate device pose estimates.

The performance of optical tracking methods can be evaluated and compared, subject to each of these error sources. Two evaluation strategies can be distinguished: analytical and experimental.

An analytical evaluation requires a mathematical analysis of the influence of each of the steps in the tracking pipeline on the performance metrics, subject to each error source. This involves creating an accurate model of the lighting conditions, occlusion, camera calibration errors, and errors in the device model. Next, the accuracy, latency, and robustness of the complete tracking pipeline have to be mathematically analyzed. This involves performing an analysis of all parameters that are involved in the feature detection, recognition and pose estimation methods. A complete analytical evaluation of a tracking method is very complex and almost infeasible, given the large number of parameters and conditions to be modeled and analyzed.

An experimental evaluation of tracking methods is less complicated. Two methods can be experimentally compared under controlled, identical circumstances. There are two approaches to obtain the device motion sequence that serves as input to the tracking methods. The first approach is to use a controlled and known motion (e.g. by using a pendulum). The advantage of this method is that all characteristics of the resulting input signal are known. However, building a setup with accurately defined motion with respect to the cameras is tedious. Furthermore, the resulting motion may be too simple and repetitive to model a realistic range of motion characteristics, such as the ones encountered in normal interaction scenarios.

The second approach is to let users perform normal interaction tasks. A set of different motion sequences can be recorded, in which various input parameters to the tracking methods are varied. Next, accuracy, latency, and robustness metrics can be derived from the data sets. The disadvantage of experimental evaluations is that it is difficult to control all parameters that influence the tracking setup, and that trackers may have different relative performance for different motion sequences. However, by recording a typical interaction task, motion sequences can be created that feature a variety of motion characteristics to test the tracking methods. In this thesis, most proposed tracking techniques are evaluated experimentally by comparing them to a related approach.

2.8 Conclusion

Optical tracking is a powerful method to determine the 3D position and orientation of interaction devices. This chapter defined the optical tracking problem and reviewed the state of the art in object recognition and pose estimation using optical tracking. However, none of these methods provides the optimal tracking solution.

Given the previous work on optical tracking, four requirements of an optical tracking system as defined in Chapter 1 need more attention:

- *Robustness against occlusion*
  Most pattern-based methods require an entire pattern to be visible in order to recognize an object and determine its pose. Point-cloud based methods are better suited to handle

partial occlusion, but are generally less efficient in terms of computational and storage requirements.

- *Generic device shape*
  Many previous approaches require the application of patterns onto planar surfaces. However, the development and application of configurable interaction devices requires that the optical tracking system is able to track objects of arbitrary shape.

- *Rapid development of devices*
  It should be easy for a developer to construct new interaction devices. Some previous approaches require manual definition of device models, which make it infeasible to rapidly construct interaction devices of complex shape.

- *Support for configurable interaction devices*
  An optical tracking system should support the use of configurable interaction devices, which require the tracking of more than six degrees of freedom. Furthermore, the system needs to provide tools to assist a developer in constructing such devices and applying them in the virtual environment.

Chapter 3

Projection Invariant Tracking using Line Pencils

The previous chapter identified various challenges that should be addressed to make optical tracking more practical. One of the most limiting properties of optical tracking is that it requires line-of-sight. In this chapter, the goal is to develop a practical optical tracking system that is less sensitive to occlusion than conventional point-based tracking methods. The method is based on projection invariant properties of line pencils, and is experimentally compared to a related solution using projection invariant properties of point shaped markers.

3.1 Overview

Most conventional point-based optical tracking methods are sensitive to occlusion. If a point is not visible, the input device often cannot be recognized. Algorithms such as iterative closest point (ICP) [BM92] and geometric hashing [LSW88] are better suited to handle occlusion. However, geometric hashing generally has large memory requirements and can be too computationally expensive to satisfy the low latency requirement of a practical optical tracking system as defined in Section 1.3 (objects should be tracked with a frame rate above 60 Hz and a latency below 33 ms), whereas ICP relies on a good initial estimate for the device pose.

The occlusion problem can be reduced using various strategies:

- Allowing partial occlusion of patterns or marker sets. Various tracking approaches require a pattern to be visible completely, and cannot combine the information of multiple partially visible patterns.
- Not requiring individual features to be visible in multiple cameras simultaneously. If features are required to be visible in multiple cameras, the cameras are required to be placed close to each other. This may not be optimal with respect to occlusion. Lifting this restriction results in a tracking method that is better suited to handle occlusion since less information is needed for recognition and pose estimation, while the cameras can be placed in a more optimal configuration.
- Using more cameras. Increasing the number of cameras used for recognition and pose estimation allows for more occlusion per camera. The use of more cameras is more effective when features do not have to be visible in multiple cameras simultaneously.

In this chapter, the idea is to include these occlusion reduction strategies by relying on patterns of line features, rather than the more common point features. If a line feature becomes

Figure 3.1: An example 7×7×7 cm input device with line pencil markers.

partially occluded, in most cases there is still enough information to determine a point on the line and its direction, such that it is completely described. This property of lines is exploited to develop an optical tracking method that allows for partial occlusion of the patterns, and which does not require the same feature to be visible in multiple cameras. The approach is based on the recognition of patterns consisting of line markers. Each pattern represents a *pencil*, i.e. four lines intersecting in one point. Input devices are augmented by one or more of these pencils. Figure 3.1 shows an example of a cube-shaped input device with line pencil markers.

The tracking system uses a model that describes the 3D position and direction of each line that is attached to the input device. Pattern recognition is accomplished using a projective invariant property of line pencils, the cross ratio, such that it operates completely in 2D. During the recognition stage the one-to-one correspondence between each individual 2D image line and its associated 3D line stored in the device model is determined. This allows for single camera orientation estimation by using a technique called line-to-plane correspondences. The final pose estimate is derived by combining the results from multiple cameras.

This chapter is organized as follows. Section 3.2 describes the concepts on which the method is based: the cross ratio of line pencils and line-to-plane correspondences. Section 3.3 describes the method that is used for recognition and pose estimation. Section 3.4 presents the results of an evaluation of the proposed optical tracking method, comparing accuracy and latency with a related point-based optical tracking method. Section 3.5 provides a discussion of the results and an analysis of the advantages and disadvantages of our method compared to previous approaches. Section 3.6 provides conclusions.

3.2 Concepts

In this section, two concepts on which the optical tracking method is based are discussed: The cross ratio of line pencils, which is used for the recognition stage, and line-to-plane correspondences, which are used for single camera orientation estimation.

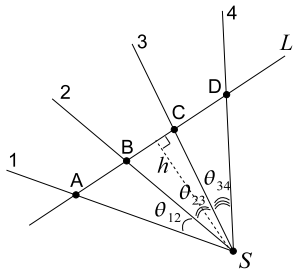

Figure 3.2: The cross ratio of four collinear points is dual to the cross ratio of four intersecting lines.

3.2.1 Cross Ratio of Line Pencils

Projective geometry preserves neither distances nor ratios of distances. However, the cross ratio [FP02], which is a ratio of ratios of distances, remains constant under projective transformations, and can be used to solve the recognition problem in 2D (see Chapter 2).

Figure 3.2 illustrates that the cross ratio of a pencil of four lines is dual to the cross ratio of four collinear points. It follows from the projection invariant property that the cross ratio of the intersection points of any arbitrary line L and the lines in the pencil is constant.

The relation between the cross ratio of a pencil of lines and four collinear points can be obtained as follows. Consider a pencil of four lines passing through an intersection point S. An arbitrary line L that does not intersect S results in four intersection points A, B, C, and D. The area of the triangles SAB, SAC, SBD, and SCD can be written as

$$h|AB|/2 = |SA||SB|\sin\theta_{12}/2 \quad (3.1)$$
$$h|AC|/2 = |SA||SC|\sin\theta_{13}/2 \quad (3.2)$$
$$h|BD|/2 = |SB||SD|\sin\theta_{24}/2 \quad (3.3)$$
$$h|CD|/2 = |SC||SD|\sin\theta_{34}/2 \quad (3.4)$$

where h is the height of the triangles with respect to L, and θ_{ij} is the angle between lines i and j. Substituting these equations into the cross ratio Equation 2.10 results in

$$C_r(\theta_{12},\theta_{13},\theta_{34},\theta_{24}) = \frac{\sin\theta_{12}/\sin\theta_{24}}{\sin\theta_{13}/\sin\theta_{34}} \quad (3.5)$$

yielding an expression for the cross ratio of a line pencil as a function of the angles between the lines.

From Equations 2.10 and 3.5 some important symmetry properties of the cross ratio can be derived. These properties imply that a different order of the points (or lines) may result in the same cross ratio. For example, $C_r(A,B,C,D) = C_r(D,C,B,A) = C_r(B,A,C,D)$. Furthermore, a uniform scaling of the distances between the points has no influence on the cross ratio. The consequence of such properties is that there exist pencil configurations with the same cross ratio.

The cross ratio can be used to identify pencils of four lines in a 2D image, allowing for single-camera pattern recognition.

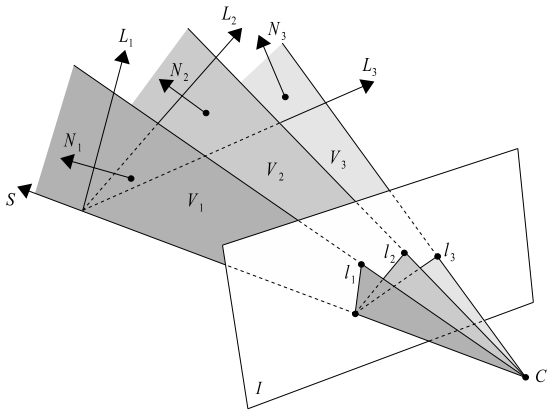

Figure 3.3: 3D lines L_i and their projections l_i on the image plane I, and the resulting 3D planes with normals vector N_i.

3.2.2 Line-to-plane Correspondences

Given a 2D line pencil in a camera image and its corresponding 3D pencil model, the geometric transformation that maps the model onto the 2D image features can be determined. The situation is illustrated in Figure 3.3. In the figure, a pencil of 3D lines L_i is projected onto a pencil of 2D lines l_i in the image plane I. Note that line-to-plane correspondence only needs three lines in a pencil, whereas the recognition method uses four. A line L_i is represented by its parametric equation $L_i = O_i + tD_i$, where O_i represents a point on the line, and D_i its direction. The camera's center of projection C and the line projections l_i define a sheaf of planes V_i in 3D, with normal vectors N_i.

After recognition, the problem is to determine the full pose of an input device, given the center of projection C, the image plane I, the pencil projection l_i, and the 3D model lines L_i. To accomplish this, the affine transformation matrix $\mathbf{M}$ has to be determined that transforms the model lines into the corresponding planes V_i (see Figure 3.4). This is generally known as the line-to-plane correspondence problem, and has been addressed by various researchers, e.g. [CH99, Che91].

The line-to-plane correspondence problem consists of two subproblems: determining position and determining orientation. The position of the 3D lines must lie on the intersection line S of the sheaf of planes. The exact position on S cannot be determined from a single pattern, unless an extra line is used. As such, four unknown degrees of freedom remain: one translational DOF along line S, and three rotational DOFs. The remaining translational DOF can be determined using the method described in Section 3.3.2.

To estimate the rotational degrees of freedom, the problem is to find a rotation matrix $\mathbf{R}$ applied to the 3D model lines L_i, such that the directions D_i are transformed into the corresponding planes with normals N_i, i.e.

$$N_i^T \mathbf{R} D_i = 0 \tag{3.6}$$

Chen [Che91] has addressed the line-to-plane correspondence problem in the general case. He identified degenerate configurations of lines and planes, for which no solution can be determined. For valid configurations, he found a closed form solution in the case of three

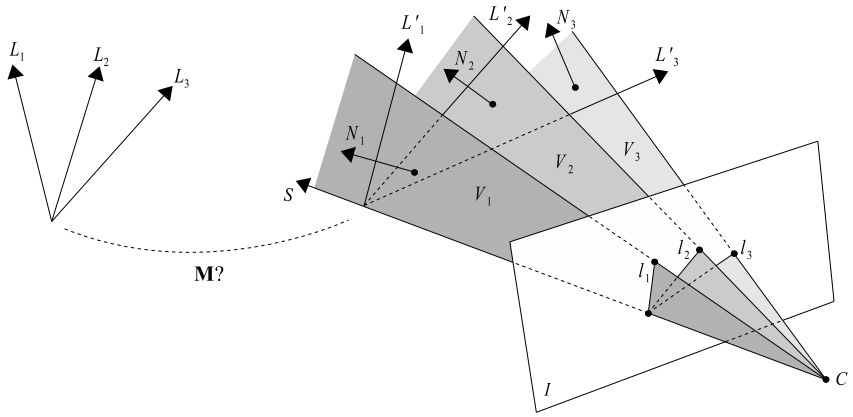

Figure 3.4: The line-to-plane correspondence problem: derive the affine transformation matrix $\mathbf{M}$ that transforms the 3D model lines L_i into the corresponding planes V_i, given the center of projection C, the image plane I, and the pencil projection l_i.

line-to-plane correspondences, resulting in an eight degree polynomial in one unknown.

Chen's Line-to-plane Correspondence Method

The key of Chen's method is to first rotate the model lines such that the transformed line L'_1 lies inside the first plane V_1, as illustrated in Figure 3.5. In the resulting configuration, the line direction D'_1 is perpendicular to the plane normal N_1, and therefore only two rotational degrees of freedom are left. Chen provides a general solution method to find the remaining degrees of freedom. In the following, Chen's method is described in more detail. Next, the simplifications are given that can be made for configurations of planar line pencils and sheafs of planes. This leads to an efficient method for determining the orientation of an input device using a recognized pencil in a single camera.

The first step is to rotate the model lines around axis $E = N_1 \times D_1$ over an angle ϕ. The resulting configuration has two rotational degrees of freedom left around the new axes D'_1 and N_1, since these axes have to stay perpendicular. Axis E forms a coordinate system with N_1 and $D'_1 = E \times N_1$, which can be defined to be the x, y, and z axes of a coordinate frame in which the normals and rotated model lines are expressed. After rotating the lines to this canonical configuration, the remaining rotation can be written as

$$\mathbf{R}(N_1, \theta)\mathbf{R}(\hat{D}_1, \phi) = \begin{bmatrix} \cos\theta & 0 & \sin\theta \\ 0 & 1 & 0 \\ -\sin\theta & 0 & \cos\theta \end{bmatrix} \begin{bmatrix} \cos\phi & -\sin\phi & 0 \\ \sin\phi & \cos\phi & 0 \\ 0 & 0 & 1 \end{bmatrix} \tag{3.7}$$

Substituting Equation 3.7 into 3.6 gives a system of equations in $\cos\theta$, $\sin\theta$, $\cos\phi$, and $\sin\phi$. This system can be solved using various algebraic manipulations and the fact that $\cos^2\theta + \sin^2\theta = 1$. The result is the polynomial in the unknown $\cos\phi$

$$P(\phi) = \sum_{i=0}^{8} \sigma_i \cos^i \phi = 0 \tag{3.8}$$

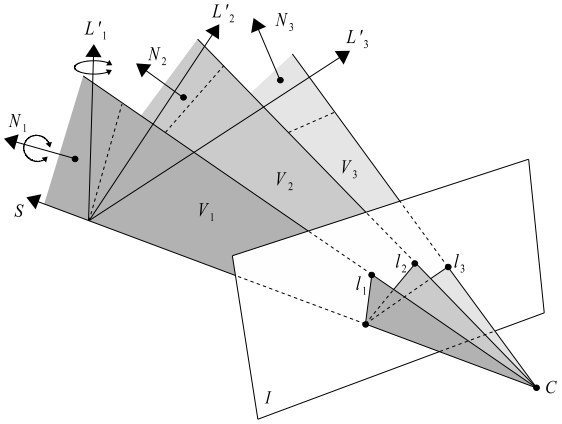

Figure 3.5: The model lines are rotated such that L'_1 lies inside plane V_1. In this configuration, two unknown rotations remain: one rotation around L'_1, and one rotation around N_1.

where the coefficients σ_i are functions of the components of D_2, N_2, D_3, and N_3. The full derivation of this equation and the coefficients σ_i are given in [Che91].

Line-to-plane Correspondence for Pencils

In case of line pencils, the lines share an intersection point and are coplanar, and thus the directions $D_i = (x_i, y_i, z_i)$ and the normals $N_i = (\bar{x}_i, \bar{y}_i, \bar{z}_i)$ of the corresponding planes are both in a coplanar configuration. A canonical configuration is then easily obtained by applying a rotation $\mathbf{R}_D$ to orient the lines such that the line directions D_i in the yz plane, such that $D_1 = (0, 0, 1)$, and a rotation $\mathbf{R}_N$ to orient the normals N_i in the yz plane, such that $N_1 = (0, 1, 0)$. In the canonical configuration, all x-components of D_i and N_i are zero and cancel out the σ_i coefficients in Equation 3.8. It can be shown that the resulting polynomial can be written as

$$\begin{aligned} P(\phi) = {} & \alpha_3^4 - 2\alpha_3^2(\alpha_1^2 + \alpha_2^2 + \alpha_3^2)\cos^2\phi \\ & + (2\alpha_1^2\alpha_3^2 + (\alpha_1^2 + \alpha_2^2 + \alpha_3^2)^2)\cos^4\phi \\ & - 2\alpha_1^2(\alpha_1^2 + \alpha_2^2 + \alpha_3^2)\cos^6\phi + \alpha_1^4\cos^8\phi \end{aligned} \tag{3.9}$$

where

$$\begin{aligned} \alpha_1 &= -y_2\bar{y}_2\bar{z}_3y_3 + y_2\bar{z}_2\bar{y}_3y_3 \\ \alpha_2 &= y_2\bar{y}_2\bar{z}_3z_3 - z_2\bar{z}_2\bar{y}_3y_3 \\ \alpha_3 &= -y_2\bar{z}_2\bar{z}_3z_3 + z_2\bar{z}_2\bar{z}_3y_3 \end{aligned} \tag{3.10}$$

Equation 3.9 can be written as a square of fourth-degree polynomials with only a second and fourth order term. The roots are given by

$$\cos\phi = \pm\sqrt{\frac{B \pm \sqrt{B^2 - 4\alpha_1^2\alpha_3^2}}{2\alpha_1^2}} \tag{3.11}$$

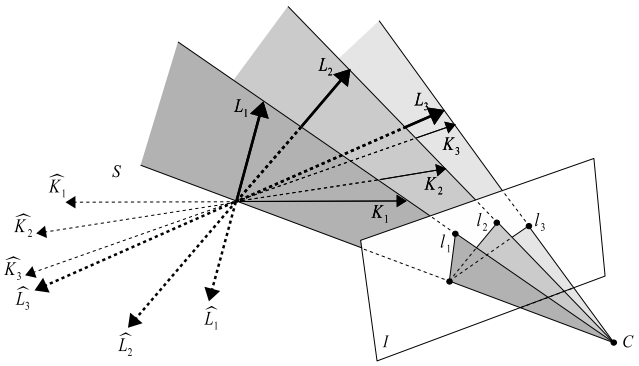

Figure 3.6: The line-to-plane correspondence problem always has four real solutions for the pencil case. Two solutions are mirrored versions of the others.

where $B = \alpha_1^2 + \alpha_2^2 + \alpha_3^2$.

It is worth noting that Equation 3.9 always has four real solutions, since $B^2 - 4\alpha_1^2\alpha_3^2 = 2\alpha_2^2(\alpha_1^2 + \alpha_3^2) + (\alpha_1^2 - \alpha_3^2)^2 + \alpha_2^2 > 0$, and $B - \sqrt{B^2 - 4\alpha_1^2\alpha_3^2} > 0$ since $B^2 > 4\alpha_1^2\alpha_3^2 > 0$. Therefore, in case the line directions are corrupted by noise, the method is still able to find a solution. The four solutions are illustrated in Figure 3.6. There are two solutions, L_i and K_i, that lie within the planes bounded by the 2D pencil lines l_i and the intersection line S. The other solutions, $\hat{L}_i$ and $\hat{K}_i$, are the reflected pencils that are found since the line-to-plane correspondence method assumes infinite planes.

After determining $\cos\phi$ and $\sin\phi = \pm\sqrt{1 - \cos^2\phi}$, $\cos\theta$ and $\sin\theta$ can be found by substituting the solutions back into the system of equations defined by 3.7 and 3.6, resulting in

$$\cos\theta = \frac{\alpha_1 \cos\phi \sin\phi}{\alpha_3 \sin\phi} \tag{3.12}$$

$$\sin\theta = \frac{\alpha_2 \cos\phi}{\alpha_3 \sin\phi} \tag{3.13}$$

The final rotation $\mathbf{R}_{tot}$ is then given by

$$\mathbf{R}_{tot} = \mathbf{R}_N \mathbf{R}(N_1, \theta) \mathbf{R}(\hat{D}_1, \phi) \mathbf{R}_D^T \tag{3.14}$$

3.3 Method

The optical tracking method is based on line pencils. Line pencils are applied to the surface of each input device, as illustrated in Figure 3.1. The method comprises three stages: recognition, pose estimation, and pose refinement. The tracking pipeline is depicted in Figure 3.7.

The method takes a list of 2D line features detected in a camera image as input, and proceeds in the following steps:

- Detect all possible pencils of four lines.

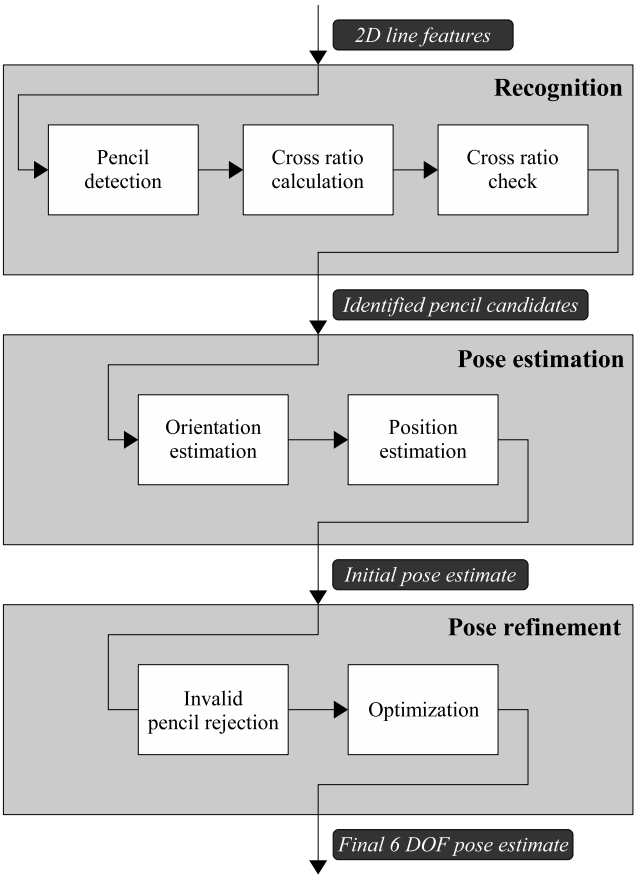

Figure 3.7: Overview of the tracking pipeline.

- Calculate the cross ratio of each pencil using Equation 3.5.
- Compare the cross ratios to those stored in the device model, and create a list of candidate matches.
- Estimate the orientation of the input device using line-to-plane correspondences.
- Estimate the position of the input device from multiple cameras.
- Optimize the pose estimate with respect to all identified pencils.

The 2D line features are detected in the camera images using a straightforward line detection method. Lines are detected by using a dynamic threshold to determine possible line pixels, after which a flood fill algorithm is performed to detect groups of connected pixels. Each group of connected pixels defines a possible line. This is similar to the procedure to detect point features in the camera images, as described in Chapter 2. A 2D line can be described by its parametric equation

$$l_i = p_i + t d_i \tag{3.15}$$

where p_i represent a position on the line, and d_i its direction. A position p_i is defined by the center of the connected pixels. The direction d_i is found by performing a least squares fit of the line equation to the group of connected pixels, such that the orthogonal distances of the pixels in the group to the line equation is minimized. If a line is interrupted in the image, for instance due to occlusion, the line detector return these line segments separately.

3.3.1 Recognition

The recognition stage involves determining the correspondence between the lines detected in the images and the lines stored in a model database. The model database consists of a list of pattern models for each input device. Each pattern model consists of four line directions and the location of the intersection point of the pencil. In the following, each step of the recognition stage is described in detail.

Pencil Detection

A list of candidate pencils is generated by calculating all line-line intersections, and finding the intersection points through which at least four lines pass. Intersection points of more than four lines generate $\binom{N}{4}$ possible pencil combinations. All these combinations are considered valid candidate pencils until they are invalidated at a later stage.

Cross Ratio Calculation

The cross ratio of each line pencil that has been detected in the camera images is calculated according to Equation 3.5. The computation of the cross ratio depends on the order of the four lines. Since the directions of the lines with respect to their intersection point are known, the lines are ordered in a clockwise fashion to prevent ambiguities in line order. This results in only one possible cross ratio for every pencil. The line order is a projection invariant property, and can be determined by sorting the lines such that

$$d_i \times d_j > 0 \qquad \forall i, j \in [0, 3], i < j \tag{3.16}$$

where d_i represents the line's direction, and $d_i \times d_j$ represents the two-dimensional cross product. After recognition, the line order can be used to obtain identified lines. If the line order is not used, recognition would only result in the correspondence between patterns of 2D lines and the associated pattern in the device model, rather than the one-to-one correspondence between the 3D model lines and the 2D image lines. This would result in $4! = 24$ possible one-to-one correspondences.

Cross Ratio Check

Changing light conditions, varying illumination of the retro-reflective markers, and miscalibrations all add to image noise, resulting in small variations of the 2D line directions in each pencil. As the cross ratio function is very sensitive to noise (see [ÅM95, May95] for probabilistic analyses of the cross ratio), a training session is included to determine the interval of the cross ratio of each pattern. A device developer moves a pattern around in the workspace, while the system determines a mean cross ratio and its range of deviations. The obtained cross ratio of each pattern and its associated range are stored in the model database. During recognition, all pencils outside the range are not considered candidates for the given

pattern. During the training session, colliding ranges of cross ratios are detected to give a developer feedback on the patterns of the input devices. Typical cross ratio ranges in the PSS are $C_r \pm 0.025$, with C_r the mean cross ratio value obtained during the training session.

3.3.2 Pose Estimation

The pose estimation stage involves calculating the position and orientation of the input device that has been found in the images.

Orientation Estimation

After recognition, each identified pattern is used to obtain an orientation estimate of the associated input device. Line-to-plane correspondences are used to calculate possible rotations of the pattern model, generally resulting in four solutions (see Section 3.2.2). Two of these solutions can be eliminated, since they fall outside the planes bounded by the 2D pencil lines l_i and the intersection line S, as illustrated in Figure 3.6. A valid solution results in the lines L_i, whereas the corresponding invalid solution results in the mirrored lines $\hat{L}_i$.

The two remaining rotation solutions can be disambiguated as follows. First, each detected pencil is used to estimate an orientation using line-to-plane correspondences. Next, the orientation mismatch between each possible pair of pencils in different cameras is determined. The orientation mismatch follows from the definition of the quaternion as [Sho85]

$$\epsilon = 2\cos^{-1}((q_1 \cdot q_2^{-1})_w) \tag{3.17}$$

where q_1, q_2 are quaternions representing solutions of a pencil pair, and where q_w represents the w-component of q. As final device rotation matrix $\mathbf{R}_\mathrm{d}$, the solution with the smallest orientation mismatch is selected.

Determining Device Position

The position of a device is determined using two recognized patterns. For this, the two patterns with the smallest orientation mismatch are used, i.e., the patterns used to derive the final orientation estimate. First, the vector between the intersection points of these patterns is determined in model coordinates (see Figure 3.8). This vector is transformed by the rotation matrix $\mathbf{R}_\mathrm{d}$, as determined by the line-to-plane correspondence method, giving the vector $W = P_1 - P_2$. Next, the line S_2 is translated over vector W to S_2', such that its origin is located at C_2'. The position P_1 is then given by the intersection point of lines S_1 and S_2'.

3.3.3 Pose Refinement

Pose estimation based on line-to-plane correspondences can produce some jitter in the device pose, due to noise in the images and thus in the detected 2D line directions. To reduce this problem, the estimated pose is used as an initial estimate for an optimization procedure.

Pose refinement proceeds in two steps. First, invalid candidate pencils are detected. Second, all valid candidate pencils are used in an optimization procedure. The position and orientation of the input device are optimized, such that the angle and distance between the 3D planes of each identified pencil and the corresponding transformed model lines is minimized.

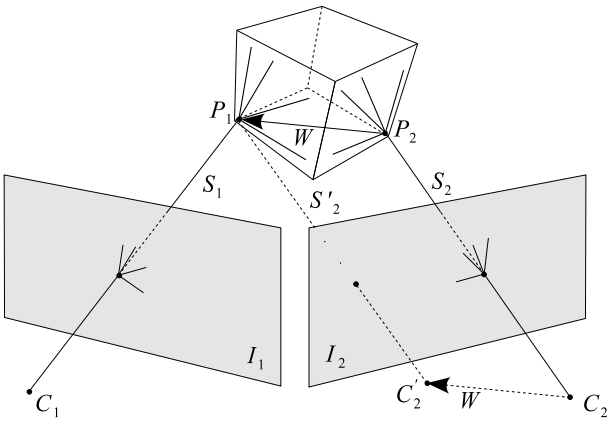

Figure 3.8: Determining device position.

Invalid Candidate Pattern Detection

After the complete pose of each device is determined, all invalid candidate patterns are identified from the candidates obtained during recognition. Invalid candidate patterns are detected by estimating the orientation mismatch between the rotations of each candidate pattern, and examining the pose estimate of the associated device. If the difference in orientation is larger than a threshold value, the candidate is invalidated.

Optimization

The pose is optimized to all identified pencils using the downhill simplex method [Chv83]. The downhill simplex method is a commonly used nonlinear optimization algorithm. It is due to Nelder and Mead [NM65] and is a numerical method for minimizing an objective function in a multi-dimensional space. It is a direct search, which does not rely on derivative information, but uses only function evaluations. Given an N dimensional problem, it constructs a geometric figure consisting of $N + 1$ points, which define a simplex. It evaluates a cost function at the vertices of this simplex, and then iteratively shrinks the simplex as better solutions are found, until some desired bound is obtained. The method requires a reasonable initial estimate of the solution.

Note that there are various numeric optimization methods. Although the downhill simplex method is not the most efficient in terms of the number of function evaluations that it requires, it is relatively robust and numerically less complicated than most alternatives, and it generally is able to find reasonably good solutions quickly. Since the initial pose is accurate, this procedure completes fast.

3.3.4 Tracking Multiple Devices

The tracking method as discussed in the previous sections can be used to track multiple input devices simultaneously. However, lines from one device may form a pencil with lines from a second device during recognition. Consequently, many unnecessary candidates are introduced, such that computational requirements are increased and there is a higher likelihood of

false pencil matches.

A simple clustering method is performed to reduce the list of candidates. The clustering method is based on the distance between lines. It assigns lines of different input devices into separate clusters, unless the devices are very close together with respect to the viewing direction of the camera. During pencil detection, only lines within a cluster can generate candidate pencils.

3.4 Results

The pencil-based tracking method has been implemented and evaluated using the PSS. The accuracy and latency of the method was compared to the point-based tracking method as presented by [LM03]. This method uses the cross ratio of point patterns for recognition, and exploits stereo geometry to transform recognized patterns to 3D for pose estimation. Each pattern consists of 5 coplanar points, applied to the sides of a cubic shaped input device. The method is described in more detail in Section 2.4.2. For both methods flat retro-reflective material was used. The point markers have a diameter of 5 mm, whereas the line markers are approximately 2×45 mm. Both input devices are 7×7×7 cm.

3.4.1 Accuracy

Method

An absolute accuracy study of an optical tracker is a time-consuming and tedious task. The tracking volume has to be divided into a grid of sufficient resolution. Next, the input device has to be positioned and oriented accurately at each grid position, after which the pose estimate from the tracker can be compared to the grid.

The approach of Mulder et al. [MJR03] was followed to obtain a fast indication of the accuracy. Their approach entails moving the input device over three planes, and collecting the position measurements from the tracker. Next, for each data set, the measurements are fit to a plane by minimizing the root-mean-square distance to this plane. The average and maximum distance of the measurements to the fitted plane give an indication of the positional accuracy of the tracker.

This approach was extended by including rotation. When moving the input device over the planes, both position and orientation measurements were collected. Next, the mean angle between the input device and the fitted plane is determined. The average and maximum angular deviation of the orientation measurements to the mean angle can then be determined to give an indication of orientation accuracy.

Results

Figure 3.9 shows the position measurements of both tracking methods for three orthogonal planes, corresponding to movements of the input device in the xy, xz, and yz planes. The cameras are placed above the tracking volume, facing down in the direction of the z-axis. The movement range and speed was similar for both data recordings.

The distance of the measurements to the planes was statistically analyzed to verify that the data could be approximated by a Gaussian distribution. The t-distribution was used to determine a 95% confidence interval for the average measurement-to-plane distance [DS98]. Figure 3.10(a) and Table 3.1 summarize the results.

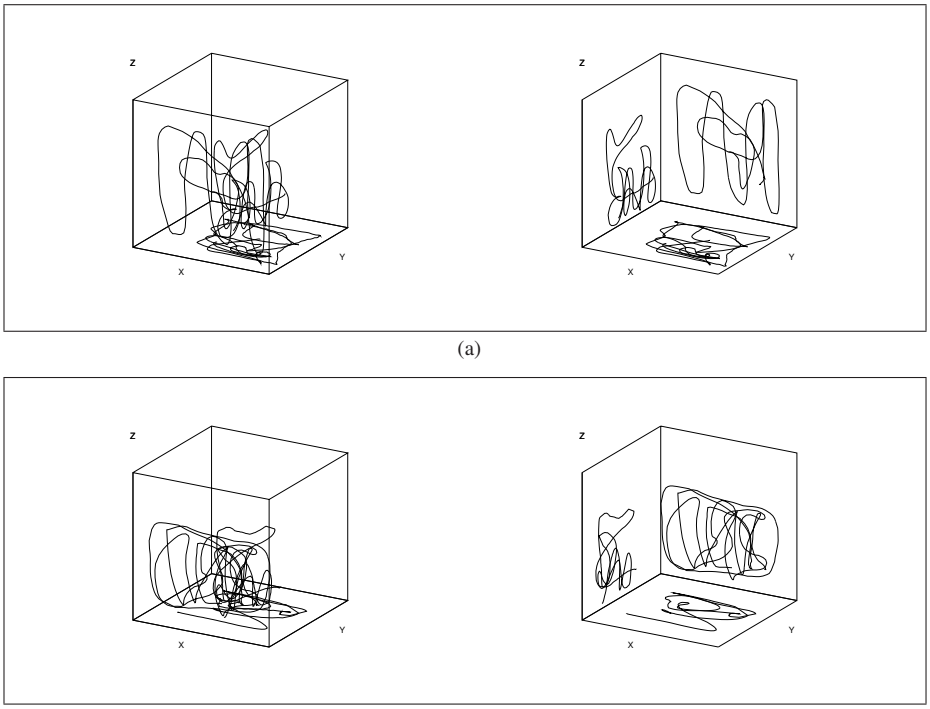

Figure 3.9: The 3D data recordings in the xy, xz, and yz planes. Depicted are the recordings in the tracking volume and the 2D projections of each recording onto its corresponding plane. (a) Recordings of the tracker based on line patterns. (b) Recordings for the tracker based on point patterns.

For orientation, the average angular deviation of the measurements with respect to the mean angle between the input device and the plane is analyzed analogous to the distance of the measurements to the plane. Figure 3.10(b) and Table 3.2 give the results of the angular deviations with the 95% confidence intervals.

From these results can be derived that both tracking methods have good accuracy, satisfying the 1 mm positional and 1 degree angular accuracy requirements as defined in Chapter 1. An analysis of variance (ANOVA) was performed on the data to indicate statistical significance between the tracking methods in the different planes. It was found that the point-based tracker performs significantly better than the line-based tracker in the xy-plane ($F(1,480) = 71.33$, $p < 0.01$). In the xz and yz planes, the line-based tracker performs significantly better than the point-based tracker ($F(1,580) = 17.05$, $p < 0.01$ in the xz-plane, and $F(1,666) = 119.31$, $p < 0.01$ in the yz-plane). The line-based tracker performs better in orientation in all cases ($F(1,480) = 17.34$, $p < 0.01$ in the xy-plane, $F(1,580) = 99.51$, $p < 0.01$ in the xz-plane, and $F(1,666) = 2372.28$, $p < 0.01$ in the yz-plane). These results suggest that the line-based tracker has better accuracy in the z-direction (i.e. higher depth resolution) than the point-based tracking, resulting in better performance in the xz and yz planes.

There are various sources of accuracy differences between both tracking approaches. First, both methods rely on a model description of each input device. Inaccuracies in these

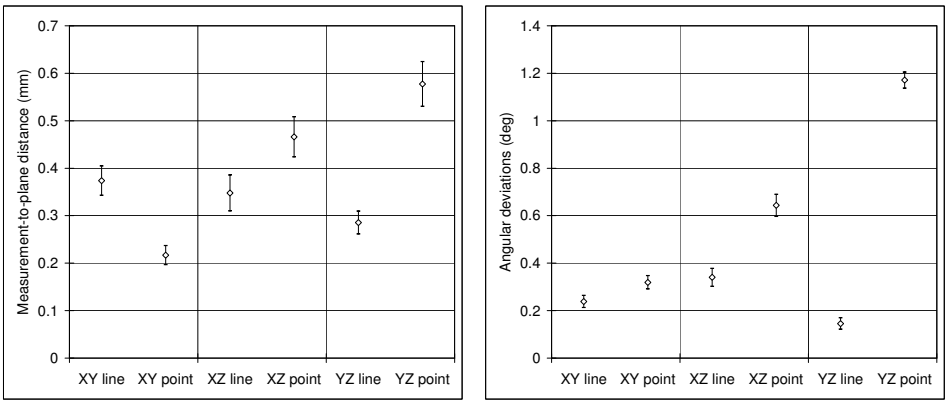

(a) (b)

Figure 3.10: Translational and rotational errors for the line-based tracker versus the point-based tracker. (a) Average measurement-to-plane distances with 95% confidence intervals. (b) Angular deviations in degrees with 95% confidence intervals.

	xy		xz		yz	
	Mean	95%	Mean	95%	Mean	95%
Line	0.37	0.06	0.35	0.08	0.29	0.05
Point	0.22	0.04	0.47	0.08	0.58	0.09

Table 3.1: Measurement-to-plane distances in millimeters with 95% confidence intervals.

	xy		xz		yz	
	Mean	95%	Mean	95%	Mean	95%
Line	0.24	0.05	0.34	0.07	0.15	0.04
Point	0.32	0.05	0.64	0.09	1.17	0.07

Table 3.2: Angular deviations in degrees with 95% confidence intervals.

model descriptions translate directly to inaccuracies in the estimated pose. Second, the 2D features detected from the camera images are different. As the data used for recognition and pose estimation is different, both methods yield different results in accuracy. As a result, the use of differently sized point or line markers gives different results.

3.4.2 Latency

The frame rate of both tracking methods was recorded as a function of the number of features present in two camera images. Frame rates were measured on a system with a 2.2 GHz Pentium IV CPU and 1 Gb RAM. Both trackers searched for two devices. Figure 3.11 summarizes the results. For both trackers, features were randomly added to the scene and placed relatively close together, in order to test the worst case situation where no clustering is performed. An example of a resulting camera image is shown in Figure 3.12. In the figure, 28 lines have been detected in the image. The recognition stage correctly identified

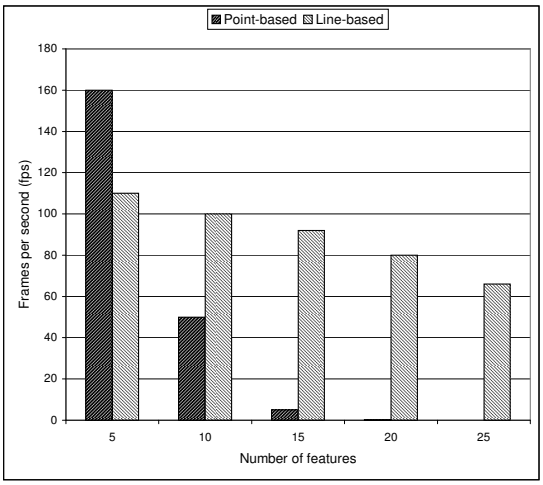

Figure 3.11: Frame rate measurements of the line-based tracker versus the point-based tracker, as a function of the number of 2D image features N. Measured using two cameras.

4 pencil patterns. The frame rate for this situation was 67 fps. The frame rate represents the total tracking time, including detection of 2D features in both camera images. Point and line detection in the camera images took about 7-9 ms of the total tracking time. The extra computational cost of line detection compared to point detection is approximately 2 ms.

From Figure 3.11 can be derived that the point-based method becomes infeasible for more than 15 features, a relatively low number. In contrast, the performance of the line-based method almost decreases linearly with the number of features and maintains high frame rates.

The performance issues of the point-based tracker are due to the following. First, the line tracker can reject combinations of four lines that do not form a pencil at a very early stage. However, the point tracker has to test each combination of five points, and has to use stereo geometry to transform an identified pattern to 3D, before testing whether the combination of points is planar. Second, the point tracker can only determine the correspondence between a pattern of 2D points and the associated pattern in the device model after recognition, whereas the line tracker has the exact one-to-one correspondence of each data line and its associated line in the device model. In the point-based tracker, pose estimation is performed by first transforming the points of the identified pattern to 3D using stereo geometry. Next, the convex hull of the pattern points is determined, which are matches to the modeled pattern points using a least squares 3D distance fit metric. For patterns of five points, this results in a maximum of 25 possible matches.

3.4.3 Occlusion

One of the main advantages of the pencil-based tracking method is its ability to handle considerable amounts of occlusion. Figure 3.13 shows an example of a user handling an input device, causing occlusion with his fingers. The tracking method only requires four valid line directions, which can still be determined in the camera images. Therefore, the tracking system is able to correctly identify the input device and estimate its pose. A similar amount of occlusion in case of an input device with point patterns generally leads to tracking failure.

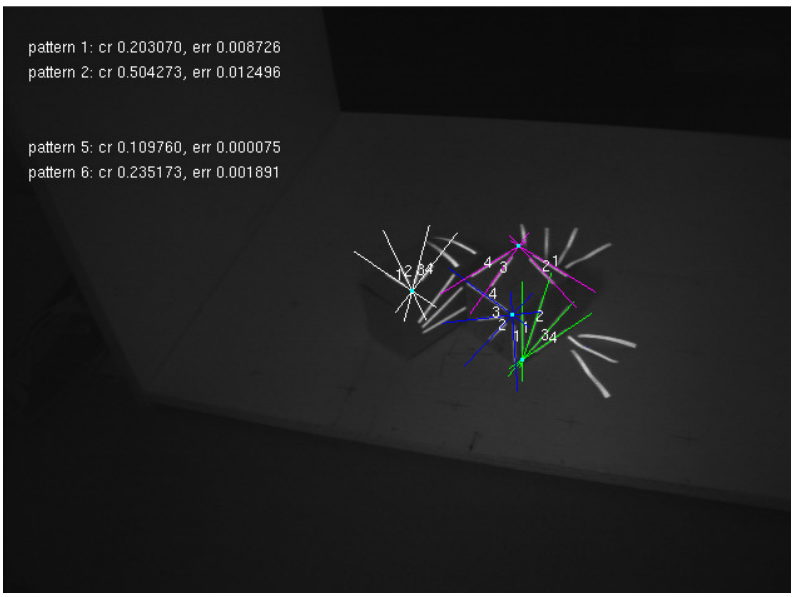

Figure 3.12: A snapshot of a camera image for the line tracker. Recognized patterns are drawn in different colors.

(a) (b)

Figure 3.13: An example of occlusion: (a) A user occludes part of the pencil pattern. (b) A snapshot from the camera of the same view. The tracking system identified the correct pattern.

This is further investigated in Chapter 5, where three tracking methods are analyzed with respect to occlusion, noise, and camera calibration errors.

3.5 Discussion

In the previous sections a method was described for the recognition of marker patterns based on projective invariant properties of lines, and pose estimation based on line-to-plane correspondences. We now discuss some advantages and disadvantages of the recognition and pose estimation stages of the method.

3.5.1 Recognition

Accuracy

The 2D features are subject to noise due to changing lighting conditions and camera properties. Smaller variations of the detected cross ratio's were experienced than for the point-based tracker (an average range of 0.05 for the line-tracker compared to 0.08 for the point-based tracker). This indicates that for the devices included in this comparison, the calculation of line directions from a 2D image is more accurate than the calculation of marker positions.

Latency

The latency of the line-based tracking approach increases linearly with the number of lines in the camera images. There are several points that make the tracker efficient. First, the ordering of pencil lines can be determined in 2D, such that there are no ambiguities due to cross ratio permutations. Second, since the line ordering is known, lines are fully identified after recognition. The point-based tracker only establishes the correspondence between a collection of 2D points and the associated collection of 3D model points during recognition, and has to test 25 combinations of 5 3D points in two cameras for pose estimation. Third, all combinations of 4 lines that do not result in a pencil in 2D can be quickly identified. The point-based tracker needs to consider each combination of 5 points during recognition, resulting in $\binom{N}{5}$ possibilities.

The complexity of the recognition stage depends on the number of detected line features. The worst case performance is obtained when all lines in the camera image intersect at one point, resulting in $\binom{N}{4}$ pencils, with N the number of detected line features in the camera images. Therefore, the complexity of the recognition stage $O(N^4)$. However, in practice the number of pencils is low and the recognition stage efficient.

The recognition procedure can be sped up by applying the search space reduction techniques of [LR03]. In this case, the location of the 2D line features can be predicted based on previous measurements, and these predicted locations can be compared to the data.

Occlusion

The main motivation for using lines instead of points as pattern features is that it allows for significant amounts of occlusion. With points, depending on the method used, one missing point can be enough for the tracker to fail. For instance, the point-based tracker used in the evaluation requires all points in a pattern to be visible. Although for the line-based tracker all lines in a pattern also need to be visible, it is no problem if part of a line is occluded, as long

as its direction can be determined (see Figure 3.13). For the point-based tracker, the occlusion problem could be reduced by adding more points to each surface, but the computational cost would increase considerably.

Robustness

During testing of the line-based tracker, it was found that in some cases the tracker cannot find a valid pattern, leading to tracking failure. In all investigated cases, this problem was caused by the line detector used to extract the line directions from the camera images. In some cases, the light reflected from the retro-reflective markers back into the cameras is not enough in order distinguish a line. In other cases the line detector could not differentiate between different lines.

Since these tracking failures are caused by blob detection problems, the tracking method itself is robust. To make the tracking system more practical, the line detector could be extended to handle connecting lines. A popular and robust technique for line detection is the Hough Transform [DH72]. However, without modifications this technique is not yet suitable for realtime tracking.

Pattern Constraints

Designing patterns for input devices is subject to some constraints. First, patterns have to consist of 4 lines intersecting in a common point, and have to be planar. This implies that interaction devices should contain planar surfaces to accommodate the patterns. Currently, if two patterns each have one completely occluded line, information of both patterns cannot be used in the recognition stage. More work is needed to examine the possibility of using projective invariants of non-coplanar lines (see e.g. [Sug94]).

Second, due to the sensitivity of the cross ratio to noise, only a limited number of patterns is possible. The cross ratio of each pattern has to be unique in its range. Moreover, the cross ratio function is symmetric and scalable, resulting in duplicate pencil configurations. Due to the average cross ratio range of approximately 0.05, it is estimated that 20 distinguishable patterns can be created. This is sufficient to track at least two six degree of freedom input devices simultaneously.

Currently, a user equips a device with patterns and can train the tracking system to recognize the different patterns. An alternative would be to let the computer generate a set of distinguishable patterns, print these out, and apply them to the input device. More work is needed to further develop this approach.

3.5.2 Pose Estimation

Accuracy

The pose estimation method is sensitive to noise in the 2D line directions. Small variations in the 2D lines are amplified in the 3D plane normal vectors. This results in a small amount of jitter in the final pose estimate. Another possible source of pose estimate errors is the device model. The model contains a description of the 3D location and direction of each pencil line with respect to the input device. Measurement errors in this model manifest themselves as systematic errors in the pose estimate for each pencil. However, different pencils introduce different errors, which can result in jitter in the device pose as pencils appear and disappear in the camera images.

It is possible to reduce these jittering effects by including a subsequent filtering step. Various filtering strategies are discussed and evaluated in Chapter 6.

Latency

The experimental results show that the method is quite fast, maintaining frame rates of over 60 Hz with 25 line features visible in two cameras. Since the exact line correspondence is known from the recognition stage, the pose estimation step is efficient.

The complexity of the pose estimation stage depends on the number of patterns detected. For each detected pattern, two possible rotations are calculated. Next, each pattern pair is checked and the best pair is selected. This makes the complexity $O(N^2)$, where N represents the number of detected patterns.

Camera Placement

The pose estimation method based on line-to-plane correspondences is more flexible than the more common pose estimation methods based on stereo geometry with respect to camera placement. Stereo geometry requires the same pattern to be visible in two cameras. Therefore, cameras need to be placed relatively close together. However, the accuracy of the pose estimate depends on the spacing between the cameras. A smaller camera spacing results in a lower depth resolution.

In the case of line-to-plane correspondences, camera restrictions are relaxed and the cameras can be placed more optimally with respect to occlusion and accuracy.

Generality

Line-to-plane correspondences are used to obtain an orientation estimate of the input device for each pattern. Although the line-to-plane correspondence method works with a single camera, it yields two valid orientation solutions. Therefore, a second camera is needed to derive the correct solution. It is possible to use an extra line for each pattern to disambiguate the two orientation solutions, and to determine the position from one camera. This line should intersect the lines in a different point than the pencil intersection point. However, position estimates would be inaccurate due to the low resolution in the viewing direction of the camera. Since an extra camera is needed for an accurate position estimate, and extra lines would clutter the images and produce more candidates during recognition, the decision was made to disambiguate the two pattern orientation solutions using this extra camera.

Note that if better line detection is used, it is advantageous to use an extra feature on each pattern. This would give more information to determine the orientation, and would give five points per pattern to determine position. A mathematical analysis of the influence of the number of features on accuracy is given in Chapter 5. It is shown that accuracy is expected to improve if more features can be used for pose estimation. However, accuracy is comparable to a point-based method, and extra lines would clutter the camera images more and generate more candidate pencils.

3.6 Conclusion

In this chapter, an optical tracking algorithm based on line pencils was presented. Patterns are recognized using the cross ratio of line pencils. The cross ratio is a projective invariant

property and thus allows for single camera recognition. An orientation estimate is obtained by using single camera line-to-plane correspondences. Translation is derived from multiple cameras.

Results show that the method has lower latency and a comparable accuracy compared to a related point-based tracking method. This is due to several properties of line pencils, which allow for rejection of feature combinations at an early stage in the algorithm.

An important advantage of line markers is that only part of the marker needs to be visible in order to detect a position on the line and its direction. Therefore, the tracking method allows for significant amounts of occlusion. Furthermore, the method relieves the restrictions on camera placement that are imposed by stereo-based methods. A disadvantage of line markers is that they require more complex image processing than point features.

Chapter 4

Tracking using Subgraph Isomorphisms

In Chapter 3 an optical tracking method was presented that uses line features to reduce the occlusion problem. Although the method is able to successfully handle partial occlusion, the method requires more complex image processing techniques than point-based tracking approaches. Moreover, it requires the application of planar pencil patterns, which limits the possible shapes of interaction devices, and makes the construction of new devices more difficult.

In this chapter, an alternative method for tracking rigid objects is presented, which is based on point features. The focus is on the development of a method that satisfies the generic shape and rapid development requirements as defined in Chapter 1. As such, the goal of the tracking techniques presented in this chapter is to enable a developer to rapidly construct new interaction devices of arbitrary shape, while keeping the system robust against partial occlusion. An automatic model estimation procedure is used to obtain a 3D device model that describes the 3D marker locations with respect to the device. The tracking system is based on finding subgraph isomorphisms between the 3D data points and the device model. The method is experimentally compared to a related 3D distance-based method, which is based on grouping markers into patterns.

4.1 Overview

An important property of point-based optical tracking is that it allows for rapid development of interaction devices. Since the tracking system only requires information about the locations of the markers on a device, developers are able to construct new interaction devices by equipping objects with retro-reflective markers and defining a model for the tracking system. However, creating such a model by hand is a tedious and error prone task, and is only feasible for simple shaped objects.

In this chapter, a system for model-based optical tracking and automatic real-time model estimation is presented. The system supports:

- Model estimation and tracking of rigid objects of arbitrary shape.
- Model estimation and tracking of multiple objects simultaneously.
- High frame rates during both model estimation and tracking.

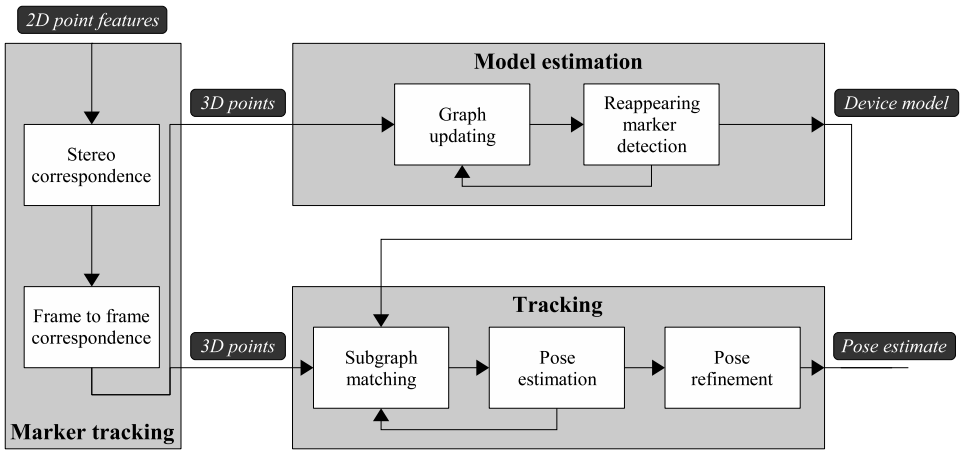

Figure 4.1: The tracking and model estimation system.

- Handling of partial occlusion.
- Robustness against noise and spurious markers.

The system allows a developer to simply equip an object with retro-reflective markers, and move the object in front of the cameras during the model estimation stage. The system automatically estimates a 3D model of the object, which the tracking system uses to identify the object and determine its pose.

The design of the tracking system developed in this chapter is depicted in Figure 4.1. It consists of three components:

- *Marker tracking*
  The goal of marker tracking is to determine the 3D marker locations from the 2D blobs in the camera images, and assign a unique identifier to each marker during the time it is visible. To transform the 2D blobs to 3D, *stereo correspondence* is used. *Frame-to-frame correspondence* can then be exploited to track the markers through time and label each with a unique identifier. A robust stereo correspondence method is proposed, which can also be used to obtain frame-to-frame correspondence.

- *Model estimation*
  To track an input device, a model is needed that describes the 3D locations of the markers attached to an object. As an example, Figure 4.2 shows three objects, along with the corresponding models as determined by the model estimation method. During model estimation, a developer moves a device in front of the cameras to show the system all markers. The model estimation system incrementally updates a model and provides instant feedback to the developer of the acquired object model. This enables him to detect model estimation errors at an early stage, and provides feedback about the required movement speed and when model estimation is completed.

  An object model is described by a graph G, where a vertex represents a 3D marker, and an edge represents the (static) distance between two markers. An edge is only present if the two markers can be seen simultaneously. Subsequently, the system can distinguish

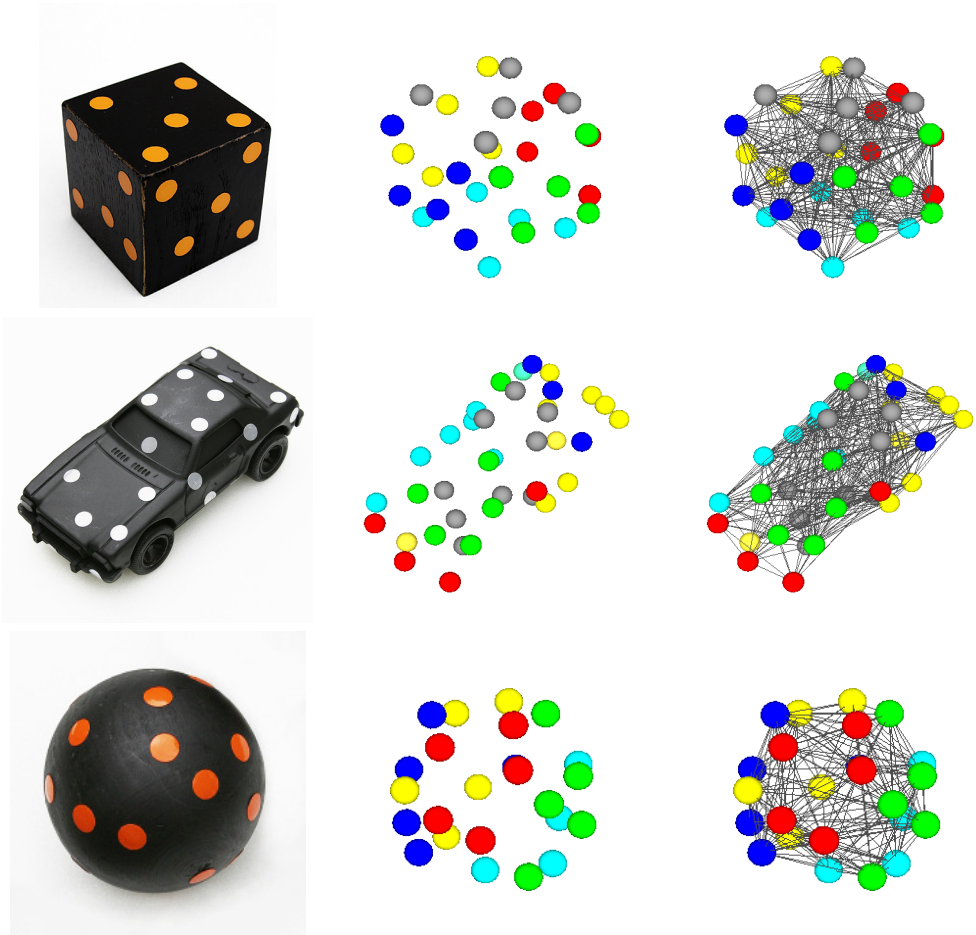

(a) (b) (c)

Figure 4.2: (a) Three example objects. The cube contains 30 markers, the toy car contains 38 markers, and the sphere contains 24 markers. (b) The corresponding models with the 3D marker locations, and (c) the complete model graphs, including edges.

between marker belonging to an object, and spurious markers that may be present in the tracking volume.

Since not all markers may be visible at the same time due to occlusion caused by the object itself and by the developer's hands, the system needs to detect reappearing markers. This is accomplished by calculating the transformation that maps the 3D marker locations to a common coordinate system, and predicting occluded marker locations. Furthermore, clustering techniques are used to allow a developer to train multiple rigid objects simultaneously and makes the system more robust against other spurious markers within the tracking volume.

- *Object tracking*
  The third component provides the object tracking. The tracking system uses the device models obtained from the model estimation procedure to determine the pose of the devices. This model-based tracking system uses a minimum subset of markers needed to unambiguously determine the pose. This minimum number of markers can be determined during model estimation. The tracking method is based on subgraph isomorphisms to recognize input devices, and determines the position and orientation of each device by a pose estimation step.

The chapter is organized as follows. Section 4.2 proposes a marker tracking approach, which is used to track markers through time and label each with a unique identifier. In Section 4.3, the model estimation method is discussed. The tracking method based on subgraph isomorphism is presented in Section 4.4. In Section 4.5, results are given on the tracking and model estimation methods. Section 4.6 provides a discussion of the proposed methods, and in Section 4.7 conclusions are given.

4.2 Marker Tracking

To track markers in 3D, two subproblems need to be solved: the 2D blob locations have to be transformed to 3D marker locations, and the 3D markers need to be tracked through time. These problems are solved using stereo and frame-to-frame correspondence. In the following sections, these techniques are discussed in more detail.

4.2.1 Stereo Correspondence

The first step in the developed tracking system is to find the blobs in the camera images, corresponding to the markers attached to an interaction device. The location of these blobs can be found by the image processing techniques discussed in Chapter 2. To determine the 3D locations of the 2D blobs, pairs of blobs in two (or more) camera images have to be found such that each pair corresponds to one device marker. This is known as the stereo correspondence problem. When correspondence has been established, the 3D location of each marker can be determined using triangulation.

For the model estimation approach presented in this chapter, reliable 3D marker locations are required. A standard stereo correspondence approach that only includes the epipolar constraint is not sufficient, as this results in the creation of many false 3D locations, depending on the number of features on the same epipolar line, and the uniqueness constraint is not fulfilled (see Section 2.4.1). Pilu [Pil97] presented an elegant and simple algorithm to incorporate the

uniqueness and similarity constraints into the matching process. He uses the correspondence method described by Scott and Longuet-Higgins [SLH91], and defines a similarity metric for matching points (i, j) based on the correlation of the surrounding pixels intensities and the distance between the 2D locations of the points in the camera images.

However, the optical tracking system of the PSS illuminates the scene with infrared lighting and uses cameras with IR filters. As a result, the images contain round blobs with practically identical properties. This makes a correlation metric of surrounding pixel intensities meaningless. Furthermore, using the 2D distance of blob locations requires the disparity between blobs in both images to be small, or at least a known constant. However, the disparity of a marker moving in the workspace of the PSS varies greatly with the position of the object.

The method proposed by Pilu can be adapted for stereo correspondence of calibrated IR camera images by including the epipolar constraint and defining a correlation function of surrounding markers in the rectified images. Using the matching method of Scott and Longuet-Higgins [SLH91] as a method to find a correspondence between two sets of points, both stereo and frame-to-frame correspondence can be solved using the same method by defining appropriate matching functions.

The Scott and Longuet-Higgins Matching Method

Scott and Longuet-Higgins [SLH91] proposed a general method to determine the correspondence between two sets of points. The method is founded on an eigenvector solution, which involves no explicit iterations. The algorithm is briefly described below.

Let I and J be two images, containing m points I_i $(i = 1, \ldots, m)$ and n points J_j $(j = 1, \ldots, n)$, respectively, which are to be put into one-to-one correspondence. For instance, these points could come from two consecutive frames of a moving object, or from different views of the same object. The method starts by defining a proximity matrix $\mathbf{G}$ of the two sets of points, where each element G_{ij} is a Gaussian-weighted similarity measure between points I_i and J_j

$$G_{ij} = e^{-r_{ij}^2/2\sigma} \tag{4.1}$$

where $r_{ij} = ||I_i - J_j||$ is their Euclidean distance, where the images are assumed to be overlaid in the same coordinate system. The proximity matrix $\mathbf{G}$ is positive definite and G_{ij} decreases monotonically from 1 to 0 with distance. Parameter σ controls the degree of interaction between the two sets of points, where a higher value permits a more global interaction.
The second step is to perform the singular value decomposition (SVD) on $\mathbf{G}$

$$\mathbf{G} = \mathbf{U}\mathbf{D}\mathbf{V}^T \tag{4.2}$$

where $\mathbf{U}$ is an $m \times m$ orthogonal matrix and $\mathbf{V}$ is an $n \times n$ orthogonal matrix. The diagonal matrix $\mathbf{D}$ is $m \times n$, and contains the positive singular values along its diagonal elements D_{ii} in descending order. Matrix $\mathbf{D}$ is converted to a new matrix $\mathbf{E}$ by replacing all singular values with one. This matrix is used to compute a new matrix

$$\mathbf{P} = \mathbf{U}\mathbf{E}\mathbf{V}^T \tag{4.3}$$

As shown in [SLH91], a one-to-one mapping between points I_i and I_j is found if P_{ij} is both the greatest element in its row and in its column.

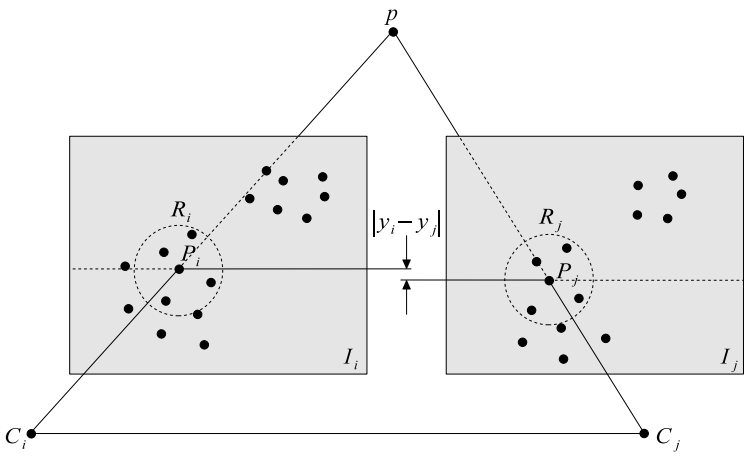

Figure 4.3: The stereo correspondence method uses the epipolar constraint and the distribution of neighboring points as similarity constraint.

Point-based Stereo Correspondence

The method of Scott and Longuet-Higgins can be applied to stereo correspondence by defining a metric that exploits the epipolar and similarity constraints. Note that the uniqueness constraint is automatically included in the matching method of Scott and Longuet-Higgins. The basic idea is that for two points to match, they should lie on the same epipolar line, and their neighboring points should be distributed similarly in the rectified images, as illustrated in Figure 4.3.

The epipolar constraint is included into the proximity matrix $\mathbf{G}$ by

$$g_{ep}(i,j) = e^{-|P_i.y - P_j.y|^2/2\sigma_{ep}^2} \tag{4.4}$$

where P_i denotes the rectified image coordinates of point I_i, and σ_{ep} is a tuning parameter which should reflect the expected error in epipolar geometry.

The similarity constraint is included by defining a region R around the rectified points P_i and P_j. All points in the regions R_i and R_j are translated such that P_i and P_j are in O. Next, the mean of minimum distances is calculated as

$$d_{md}(S_1, S_2) = \frac{1}{N} \sum_{P \in S_1} ||P_i - \mathcal{C}_{cp}(P_i, S_2)|| \tag{4.5}$$

where S_1 denotes the smallest set of points, N denotes the size of set S_1, and S_2 is the larger set of points. The function $\mathcal{C}_{cp}$ is the closest point operator as defined by Equation 2.20. The similarity constraint is included into the proximity matrix $\mathbf{G}$ by

$$g_{md}(i,j) = e^{-d_{md}(R_i,R_j)^2/2\sigma_{md}^2} \tag{4.6}$$

where σ_{md} should reflect the expected similarity error. The total proximity matrix is given by

$$G_{ij} = g_{ep}(i,j) g_{md}(i,j) \tag{4.7}$$

4.2.2 Frame-to-frame Correspondence

Frame-to-frame correspondence can be obtained by application of the correspondence method of Scott and Longuet-Higgins [SLH91] with a different proximity metric. Since the distance a marker travels in a frame is relatively small compared to the distance between markers, the Euclidean distance is minimized. As such, the matrix $\mathbf{G}$ is defined by the Euclidean distance between 3D marker locations of the frames at time t and $t - \Delta t$:

$$G_{ij} = e^{-||p_i(t)-p_j(t-\Delta t)||^2/2\sigma_f^2} \tag{4.8}$$

where $p_i(t)$ is the 3D location of a marker at time t, and σ_f a parameter defining the expected error. To improve the robustness of the frame-to-frame correspondence in case of multiple objects moving independently and in case of fast movements, a simple linear prediction of each 3D marker location is included

$$p_i(t) = p_i(t - \Delta t) + v(t)\Delta t \tag{4.9}$$

where $v(t)$ represents the measured speed of the point at time t. As a result, σ_f can be chosen small.

Note that frame-to-frame correspondence may fail in case of a low sampling rate or fast and erratic device motion. As such, a developer is required to move the device in front of the cameras with limited velocity. To make sure these motion restrictions do not apply during normal interaction, the tracking method does not require frame-to-frame correspondence.

4.3 Model Estimation

Obtaining a model of an object by moving it in front of the cameras is closely related to motion segmentation in long image sequences. A common approach is to track markers using a Kalman filter, and to group markers together if they have similar kinematic parameters. Zhang and Faugeras [ZF92] track 3D line markers and estimate their motion using an extended Kalman filter, grouping together markers with similar motion. Occlusion is handled by predicting the location of disappearing features using the Kalman filter. This assumes short-term occlusions. Smith [Smi95] uses a similar approach, but uses 2D point markers.

Mills [MN00] and Hornung [HSDK05] use alternative approaches. They maintain a graph, where each node represents a marker, and an edge represents a rigid relation between markers. As markers are moved, edges are updated, and when the distance between markers varies too much, the edge is deleted. The approaches differ in how occlusion is handled. However, both approaches suffer from problems which limit their applicability, as discussed in more detail in Section 4.3.3.

The model estimation approach presented in this section shares ideas with the work of Mills. However, it differs in the way occlusion is handled and how the model is maintained, making it more robust to long-term occlusion.

4.3.1 Model Definition

The model of a rigid interaction device, that is to be obtained by the model estimation procedure, is defined by a graph $G = (V, L, E)$, where

- V is the set of vertices v_i representing markers.

- $L \subseteq V$ is the set of 3D locations, where l_i assigns a 3D location to vertex v_i in a common frame of reference.
- $E \subseteq V \times V$ is the set of edges, where $\delta(e_{ij})$ represents the average Euclidean distance between vertices v_i and v_j. An edge e_{ij} is only present if during model estimation the distance between the markers associated with vertices v_i and v_j remains static. In this case, the markers associated with v_i and v_j are said to have a *rigid relation*.

4.3.2 Graph Updating

The basis of model estimation is to use frame-to-frame correspondence to track markers through time, assigning each an age and a unique identifier (ID), and to maintain a graph G as defined in Section 4.3.1. Initially, all visible markers are added to G as vertices, and edges are created between them. As markers are moved around, the euclidian distance between each marker pair (v_i, v_j) is examined and compared to the distance $\delta(e_{ij})$ associated with the corresponding edge e_{ij} in the graph G

$$|||v_j - v_i|| - \delta(e_{ij})| < \epsilon \tag{4.10}$$

If the difference in distances exceeds a threshold ϵ, the edge is deleted. In order to deal with noise and measurement errors, a running average distance (with equal weights) between markers over the last N frames is maintained, and compared with the edge distance. This has the effect of making edges somewhat elastic.

Problems arise when markers enter the scene for which no frame-to-frame correspondence can be established, i.e. markers of age zero. A marker with age zero can be a new marker not yet part of the model, or a previously occluded marker that reappears. The system needs to distinguish between both cases, and in the case of a reappearing marker assign the original ID and age to this marker. New markers are assigned new IDs, added to G, and connected to all other visible markers.

4.3.3 Reappearing Marker Detection

To detect reappearing markers, new markers need to be compared to occluded markers. A marker is new if no frame-to-frame correspondence can be determined for it, i.e. its age is zero. Other (older) visible markers are referred to as identified points.

Hornung [HSDK05] detects reappearing markers by comparing the distances between new markers and identified markers to the distances between occluded markers which have an edge to identified markers. When all distances match, the new marker is considered to be a reappearing marker. However, this approach fails for occluded markers which do not (yet) have an edge with the identified markers. Figure 4.4 illustrates the problem: during model estimation of a cube, a side may reappear with markers that have no edges with the markers on the side of the cube that is visible.

A better approach to detect reappearing markers is to directly predict the location of occluded markers, as followed by Mills [MN00]. The idea is to cluster the graph G into rigid substructures, and to calculate the rigid body transform of these rigid substructures to predict occluded markers.

Rigid substructures form cliques in G. A clique in an undirected graph G is a set of vertices V such that for every two vertices in V, there exists an edge connecting them. However,

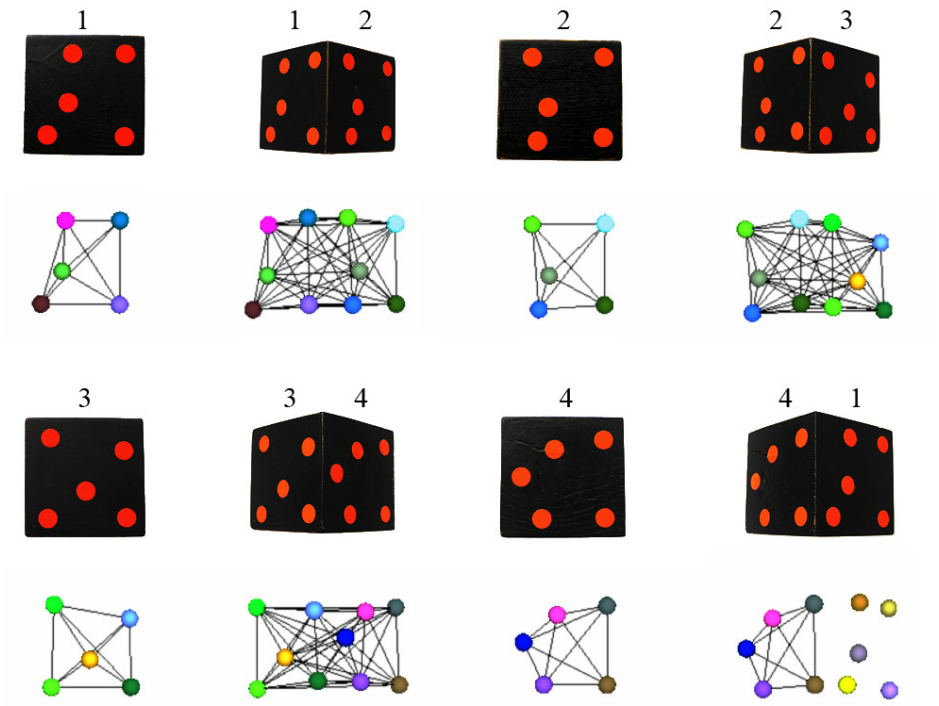

Figure 4.4: A cube being rotated during model estimation. The model estimation system determines the relation between sides $(1, 2)$, $(2, 3)$, and $(3, 4)$. When side 4 is visible and side 1 reappears, there is no direct relation between sides 4 and 1, and so matching the (reappearing) markers of side 1 directly to the other visible markers fails.

as clique finding in graphs is computationally expensive, Mills proposes a triangle-based clustering, where markers are only assigned to the same cluster if they are both part of a triangle with a shared edge. However, this method can falsely classify structures as rigid, as illustrated in Figure 4.5(a). The vertices v_1 and v_2 of two connected triangles, which are adjacent to the connected vertices v_3 and v_4, are free to rotate around axis A without changing any of the distances d_{ij} for which there exists and edge in the graph. Consequently, the distance d_{12} is not required to be constant.

Misclassification of markers of different objects into one rigid structure can have adverse effects on the model estimation procedure. Consider for example the graph of Figure 4.6. As all triangles in this graph share edges with at least one other triangle, a triangle-based clustering method would produce one rigid body, while in reality the graph contains two rigid object graphs G_1 and G_2. Any rotation of G_1 around axis AB does not remove any edges in the graph, and therefore the complete graph is incorrectly classified as rigid. Since edges are somewhat elastic, this situation may occur quite frequently in practice. Subsequently, all markers are used to calculate the rigid body transform of the model, resulting in incorrect predicted locations of occluded markers.

The situation can be corrected by classifying markers to different objects using a clus-

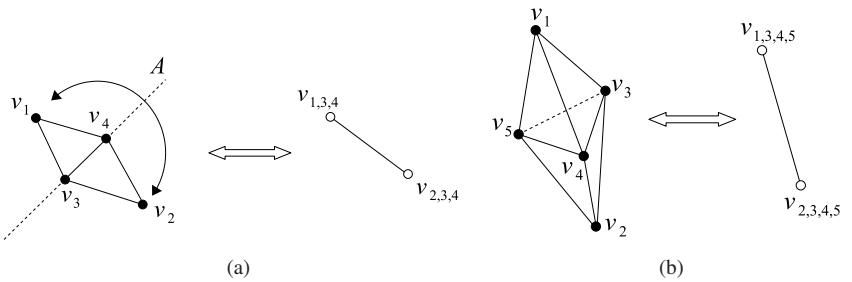

Figure 4.5: Comparing the triangle-based clustering (a) to the pyramid-based clustering (b). The triangle-based clustering allows for a rotational degree of freedom of vertices v_1 and v_2 around axis A, whereas the pyramid-based clustering guarantees points of the same rigid substructure.

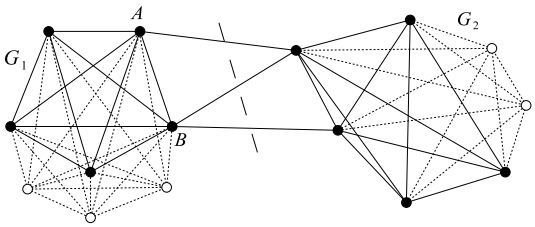

Figure 4.6: A sample graph. A triangle-based clustering would produce one rigid body, whereas a pyramid-based clustering produces subgraphs G_1 and G_2. Since rotations around axis AB have no effect on the graph, prediction of occluded markers (denoted by white dots) is inaccurate if the complete graph is classified as rigid.

tering method that is based on connected pyramids or 4-cliques. Furthermore, a graph is maintained for each detected object G_O, rather than one graph G for all data. This ensures that markers assigned to different objects are not reconnected at a later stage by new markers appearing, increasing both the accuracy and efficiency of occlusion prediction.

A pyramid is a rigid substructure consisting of four vertices, where each pair of vertices has an edge. Two pyramids are connected if and only if they share a triangle. The clustering is defined by the connected components of the pyramid graph, which can be efficiently computed by running a depth-first search from each node. Although connected pyramids do not necessarily form a clique, markers within a cluster are part of the same rigid structure. Figure 4.5(b) illustrates that there exists no transformation of vertices v_1 and v_2 that changes the distance d_{12} between these vertices, while keeping the distances d_{ij} for which there exists an edge constant (apart from a reflection in the plane defined by the shared triangle).

A pyramid-based clustering can be efficiently computed by determining all triangles in a graph, and connecting triangles if and only if they both share an edge and if there is an edge between the adjacent vertices, i.e., if they form a pyramid. Triangles in a given graph can be efficiently determined using the triangle listing algorithms presented in [SW01].

The object graph G_O also stores a model of all 3D object marker locations in a normalized coordinate system, giving the set L. Marker locations are averaged over all frames to reduce inaccuracies due to noise and outliers. The locations can be determined by calculating the

rigid body transform that maps the identified markers to the corresponding model markers in a least-squares manner [Hor87]. This transform is used to predict the locations of occluded markers. When a marker is found for which no frame-to-frame correspondence could be established, its location is compared to the predicted occluded marker locations. If the error of the rigid body transform is too large, a combination of the given points is used to obtain a new transform. This procedure is repeated until all combinations are tried, or a combination is found that results in an accurate rigid body transform.

4.3.4 Model Estimation Summary

Given the 2D blob locations, the following steps are performed:

1. *Marker tracking*
   The 3D locations of the 2D blobs detected in the camera images are determined using stereo correspondence, as described in Section 4.2. Markers are associated with the markers in the previous frame by frame-to-frame correspondence, such that each marker has a unique ID that stays constant during the time it is visible.

2. *Edge updating*
   For each object graph G_O, the edges between visible markers within the model are updated. If the distance between two visible markers remains constant, the average distance is updated. Otherwise, the edge is removed.

3. *Invalid marker removal*
   In certain circumstances, the blob detector may find blobs that do not correspond to valid markers. For instance, these blobs may come from objects in the workspace that reflect incoming infrared lighting. If these undesired blobs are present in multiple camera images, this may result in false 3D marker positions. However, these markers are usually only visible for a short period of time or are located far from the input device. These markers are therefore easily detected and removed from the object graphs by checking their age and by using distance-based clustering techniques.

4. *Graph clustering*
   Each object graph G_O is split into new object graphs if necessary, by performing the pyramid-based graph clustering technique.

5. *Occluded marker prediction*
   The rigid body transform of each object is calculated and the locations of its occluded markers are predicted. Next, all markers for which no frame-to-frame correspondence could be established are compared to these occluded markers, and if they are close enough to each other, the marker is recognized as a reappearing marker. Its ID and age are updated with those of the occluded marker. Note that only markers that are considered reliable are used to compute the rigid body transform.

6. *New marker insertion*
   New markers that have not been recognized as reappearing markers are inserted into all object graphs.

4.4 Model-based Object Tracking

The input to the tracking system is an estimated model graph $G_m = (V, L, E)$ as defined in Section 4.3.1. The tracking system needs to identify a subset of this graph in the image points. This is closely related to the double subgraph isomorphism problem. A subgraph G_1 is isomorphic to another subgraph G_2 if there is a one-to-one correspondence between their vertices and there is an edge between two vertices of G_1 if and only if there is an edge between the corresponding vertices in G_2. As this problem is known to be NP-complete [AF98], the problem is simplified by defining a minimum size S_{min} of a subgraph of G_m which needs to be present in a data graph G_d, with the constraint that this subgraph is a clique. Parameter S_{min} defines how many markers are needed to unambiguously identify a model graph, and each set of S_{min} markers that can be visible simultaneously is by definition fully connected. Note that S_{min} can be determined during model estimation.

Tracking Method

The first step is to preprocess the model graph G_m. A hash table is constructed which indexes each distance between vertices v_i and v_j for which there exists an edge e_{ij}. The table stores pointers back to the model and the vertices v_i and v_j. The tracking method proceeds as follows.

- A data point p is chosen, and the distance $d = ||p - p_j||$ between p and all other data points p_j is indexed into the hash table.
- Each vertex v_k in G_m maintains a list of possible matching data and model point pairs (p_j, v_l). Therefore, a set of candidates is created for each v_k, for which $||p - p_j|| = ||v_k - v_l||$.
- If p matches v_k, there must be a combination of matches between data points p_j and model points v_l which is fully connected and for which the remaining distances are correct, since by definition each set of S_{min} matching points must form a clique. As such, each combination of three points of each candidate is checked for the remaining distances with the model. If these match, a subgraph isomorphism of size four has been found.
- The rigid body transform matching the model to the data graph is found by least-squares [Hor87].
- All data points are transformed to the model coordinate system, and compared to the model points. If at least S_{min} matching points are found, the tracking system can mark the model as identified and stop the search for this model. However, to increase robustness, all candidates are examined and the one that matches the image points best is selected. This best fit is found by minimizing the sum of distances between model and transformed data points defined by

$$F = \frac{1}{N} \sum_{i=1}^{N} ||p_j - \hat{\mathbf{M}}_{dev} v_i|| \tag{4.11}$$

where $\hat{\mathbf{M}}_{dev}$ is the transform that maps the model points to the data points, v_i denotes a recognized model point, and p_j is its corresponding data point.

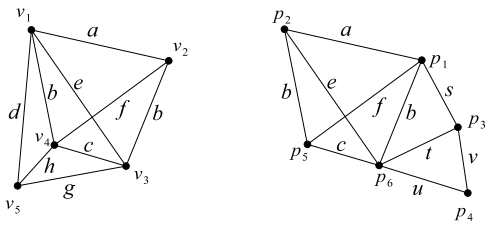

Figure 4.7: (Left) An example model graph G_m with vertices v_i and distances $a, \ldots, i$. (Right) A data graph G_d with points p_i, which has a double subgraph isomorphism with G_m

- Chapter 5 includes a mathematical analysis on the influence of the number of features used during pose estimation on accuracy. Since accuracy is shown to be a function of the number of features, the pose estimation is refined using the downhill simplex method as discussed in Section 3.3.3, which uses all detected data points. The function to be minimized is the sum of minimum distances between the N matching data points, transformed to the model coordinate system, and the corresponding model points.

Note that the tracking method implicitly exploits the fact that an edge is only present if the two markers can be simultaneously visible, thus greatly reducing the number of candidates.

Optimizations

The tracking procedure can exploit frame-to-frame correspondence in order to speed up the matching process. When the tracking system has identified an interaction device at a certain time t, and frame-to-frame correspondence results in enough identified points at time $t + \Delta t$ that correspond to points at time t, the pose of the device is directly derived from these points. In this case, the complete search procedure is skipped. In case frame-to-frame correspondence results in only one or two identified points, these points can be used as starting points for the search.

Tracking Example

As an example of the tracking procedure, consider the model and data graphs of Figure 4.7. This situation could occur when model point v_5 is occluded, v_2 and v_5 cannot be visible simultaneously, and data points p_3 and p_4 represent spurious markers.

The method first determines the distance matrix of the data graph G_d and the hash table $\mathbf{H}$ of the model. The distance matrix of the data graph G_d is given by

$$\mathbf{M_d} = \begin{pmatrix} 0 & a & s & 0 & f & b \\ a & 0 & d & 0 & b & e \\ s & d & 0 & v & 0 & t \\ 0 & 0 & v & 0 & 0 & u \\ f & b & 0 & 0 & 0 & c \\ b & e & t & u & c & 0 \end{pmatrix}$$

The hash table $\mathbf{H}$ of G_m, omitting model pointers, is given by

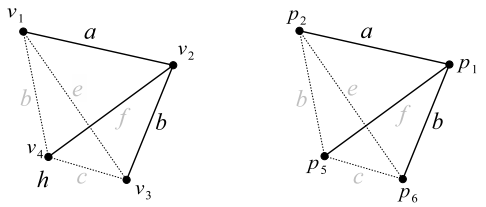

Figure 4.8: Vertex v_2 has three candidate matches for data point p_1. At this point, a set of model and data points with a common vertex has been found. A double subgraph isomorphism is found if the remaining distances match.

a	b	c	d	e	f	g	h
(v_1, v_2)	(v_2, v_3) (v_1, v_4)	(v_3, v_4)	(v_1, v_5)	(v_1, v_3)	(v_2, v_4)	(v_3, v_5)	(v_4, v_5)

The tracking method hashes all distances $||p_1 - p_i||$, $i = 2, \ldots, 6$, i.e. the first row of $\mathbf{M_d}$, into $\mathbf{H}$. The resulting list of matching distances can be expressed as follows.

(p_1, p_2)	(p_1, p_3)	(p_1, p_4)	(p_1, p_5)	(p_1, p_6)
(v_1, v_2)			(v_2, v_4)	(v_2, v_3) (v_1, v_4)

which can be rewritten as a list of candidate matches between data points p_i and model points v_j.

(p_1, v_1)	(p_1, v_2)	(p_1, v_3)	(p_1, v_4)
(p_2, v_2) (p_6, v_4)	(p_2, v_1) (p_5, v_4) (p_6, v_3)	(p_6, v_2)	(p_5, v_1) (p_6, v_1)

Next, all vertices v_i with at least three matches are taken as a candidate for point p_1, which in this case is only v_2. At this point, a set of model and data points with a common vertex match in distance, i.e. $||p_1 - p_j|| = ||v_2 - v_l||$, where $j = 2, 5, 6$ and $l = 1, 4, 3$ (see Figure 4.8). In order for these points to form a double subgraph isomorphism of size four, the remaining distances

$$\begin{aligned} ||v_1 - v_4|| &= ||p_2 - p_5|| \\ ||v_1 - v_3|| &= ||p_2 - p_6|| \\ ||v_3 - v_4|| &= ||p_6 - p_5|| \end{aligned}$$

should match. Since these match, a double subgraph isomorphism has been found as (v_1, p_2), (v_2, p_1), (v_3, p_6), (v_4, p_5). The system can determine a rigid body transform to find other matching data points, and accepts the match if the fit is good enough and S_{min} points are found.

4.5 Results

The marker tracking, model estimation, and model-based tracking techniques have been implemented and evaluated using the PSS. In the following subsections, the stereo correspon-

dence method is compared to an approach using only the epipolar constraint, and the robustness and performance of the model estimation and tracking methods are evaluated.

4.5.1 Stereo Correspondence

A straightforward method for stereo correspondence is to match all pairs of points in two camera images that are within a certain epipolar distance of each other. However, this method generates many false matches when multiple points are close to the same epipolar line. Figure 4.9 illustrates the difference between this approach and the SVD-based matching approach. Figure 4.9(a) shows three objects in the tracking volume, from a point of view

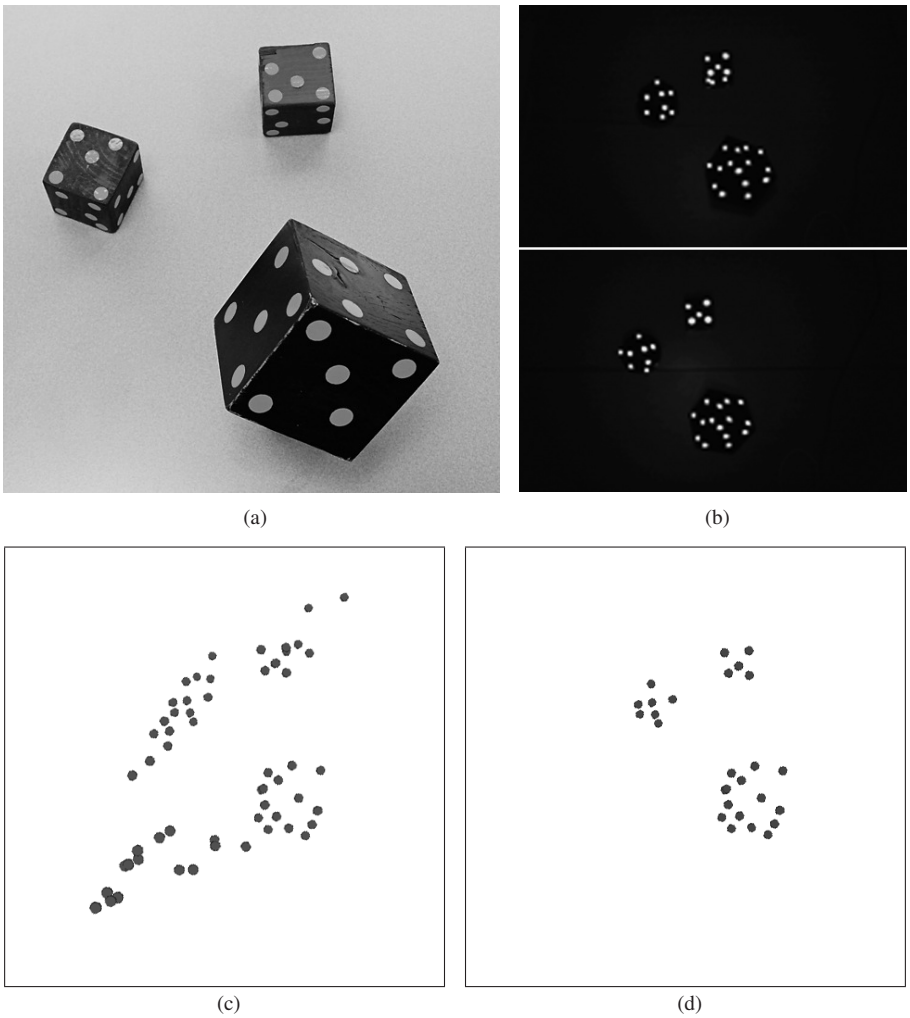

Figure 4.9: Stereo correspondence. (a) Three devices in the workspace. (b) The corresponding camera images. (c) Resulting 3D marker locations of stereo matching by epipolar constraint only. (d) Resulting 3D marker locations of the SVD-based stereo correspondence.

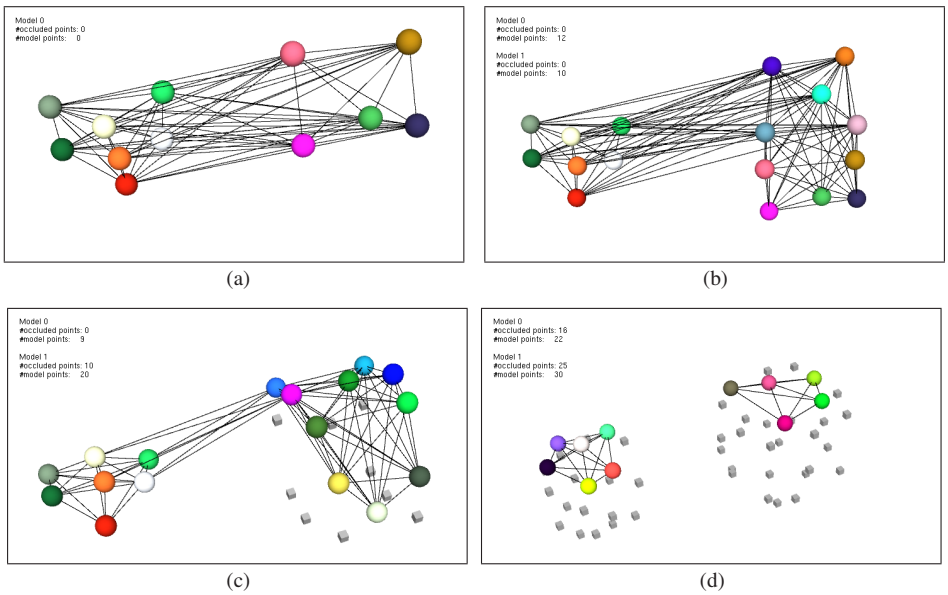

Figure 4.10: Four frames during simultaneous model estimation of the cubical and spherical objects of Figure 4.2. The colored spheres represent the visible markers of the model, where the colors encode the unique marker identifiers. (a) Initially, all points are regarded as one object. (b) After some movement, edges are removed and the system correctly identifies two objects. (c) During model estimation, occluded point locations are predicted and drawn with grey cubes. (d) The system correctly modeled the two objects.

from the cameras. Figure 4.9(b) shows the blobs in the corresponding camera images, while Figures 4.9(c) and (d) depict the output of stereo correspondence by epipolar matching, and stereo correspondence by SVD matching, respectively. The SVD-based correspondence successfully identifies the correct 3D marker locations, whereas the epipolar matching generates too many additional false matches for reliable model estimation.

4.5.2 Model Estimation

Figure 4.10 depicts three frames of a data sequence of 2200 frames (36 seconds), where a spherical object of diameter 7 cm and a cubical object of 7×7×7 cm are trained simultaneously (see Figure 4.2). These objects are equipped with 24 and 30 markers, respectively. The figure shows that initially, all points are regarded as a single object. In the second frame, after some movement, connections between new points and previously identified points are created, and connections between points not rigidly attached are removed. At this point, the model estimation system correctly identified two objects. Note that a triangle-based clustering of this graph would result in only one object. In the last frame, after a data sequence of only 36 seconds, the system correctly identified two objects and created a model of all markers attached to the objects. Creating these models by hand is obviously a very difficult and time consuming task.

Figure 4.11 gives the total computation time the model estimation procedure requires for

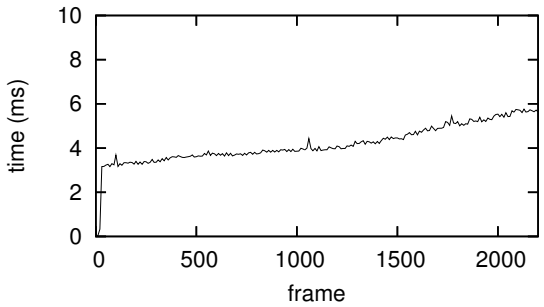

Figure 4.11: Computational time of simultaneous model estimation of a spherical and cubical object of 30 and 24 markers.

each frame for the same data sequence as Figure 4.10, excluding image grabbing and blob detection. Frame rates were measured using a system with a 2.2 GHz Pentium IV CPU and 1 Gb RAM. The computation time slowly increases while the objects are being moved, as more points appear and the models get more complex. Most of the time is spent in the graph clustering procedure (less than 1 ms is spent on stereo correspondence). The figure shows that the time required to update the models is well below 10 ms. This implies that two objects with a total of 54 markers can be trained with a frame rate of 60 Hz, which is limited by the speed of the cameras. Therefore, the model estimation system provides instant feedback to the developer of the acquired object model, such that model estimation errors are detected at an early stage, and feedback is given about model completion.

4.5.3 Tracking

The performance of the tracking method presented in this chapter is compared with a pattern-based tracker based on matching distances, as described in [LR04] (see Chapter 2 for more details). The tracking method based on finding subgraph isomorphisms is referred to as the subgraph tracker. Two wooden cubes of sizes 7×7×7 cm and 5×5×5 cm were used as interaction devices. For each cube, 6 patterns of 5 points were defined for the pattern tracker, and the object was trained for the subgraph tracker. Next, a data set was recorded, where both cubes were manipulated simultaneously with both slow motions, and faster, more erratic movements. For both trackers, the computational time required by the tracking method was examined, excluding image grabbing and blob detection. Blob detection takes approximately 8 ms on average. Both trackers examine all candidate matches, and select the one with the lowest distance metric as defined by Equation 4.11. This results in comparable accuracy of both trackers.

The miss and hit rates of both tracking method were determined for an object exploration task using two input devices, i.e., the number of frames the cubes could not be found (misses) versus the number of frames the cubes were identified (hits). Table 4.1 shows the performance of both trackers in terms of hits and misses. The table indicates that the pattern-based tracker does not handle partial occlusion as well as the subgraph tracker. This can be attributed to the fact that the pattern-based tracker does not deal with multiple partially visible patterns, while in these situations the subgraph tracker has enough information to correctly identify the device and its pose. Both trackers perform well for the noise levels introduced by the optical

Tracker	*Cube 1*			*Cube 2*		
Method	*hits*	*misses*	*rel.*	*hits*	*misses*	*rel.*
Subgraph	2165	83	96.3%	2127	121	94.6%
Pattern	1994	254	88.7%	1862	386	82.8%

Table 4.1: Hits and misses for a data sequence of two cubic interaction devices, for the subgraph tracker vs. a pattern tracker

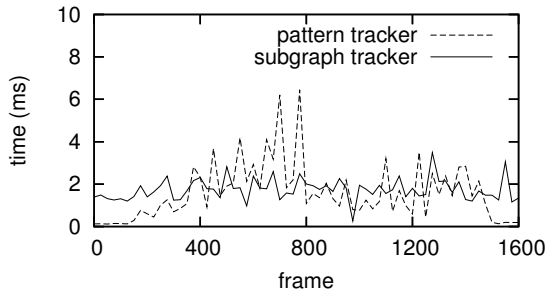

Figure 4.12: Computational time of the subgraph tracker vs. a pattern-based tracker (excluding image grabbing and blob detection). The data set contains the movements of two cubes being manipulated simultaneously.

tracking setup of the PSS, as closer inspection of the results reveals that most misses of the subgraph tracker are due to either failed blob detection, or that one cube occludes the other.

Figure 4.12 gives the computational performance for both methods on the same data set. The figure shows that both methods are competitive and able to track both cubes with more than 60 Hz (processing time < 16.6 ms).

4.6 Discussion

In this chapter, a method was presented for the automatic estimation of object models of arbitrary shape, and the use of these models in a subgraph tracking system. Objects are equipped with retro-reflective markers, and used as interaction devices in the virtual environment. We now discuss some advantages and disadvantages of the model estimation and tracking techniques.

4.6.1 Marker Tracking

The stereo correspondence method presented in this chapter can be used to obtain reliable 3D marker locations from camera images. The method incorporates the epipolar, uniqueness, and similarity constraints. Each marker is assigned a unique identifier that remains constant during the time the marker is visible using frame-to-frame correspondence.

The stereo correspondence method has three tuning parameters: the expected error in epipolar geometry σ_{ep}, the expected similarity error σ_{md}, and the region size S. It was found that the method is sensitive to these parameters, and that the optimum values depend on camera placement, calibration, and on the size of the interaction device and its position in

the workspace. To further increase the robustness of the stereo correspondence method, these parameters could be estimated adaptively.

4.6.2 Model Estimation

The model estimation method can handle virtually any shape, as long as at least three non-collinear points are visible and recognized, in order to establish a relation with new points. Short-term occlusion is handled by predicting the location of occluded markers. The method can estimate multiple object models with a moderate amount of markers simultaneously. Since objects that are identified as separate clusters are never reconnected, the graph clustering method never needs to handle more points than are on a device, making the complexity practically linear in the number of devices. The worst case performance of the clustering method occurs when the graph is fully connected. A fully connected graph has $\binom{N}{3} = O(N^3)$ triangles, where each triangle forms a pyramid with $3(N-3)/2$ other triangles. Therefore, the worst case computational complexity is $O(N^4)$, which could be improved by updating the pyramid graph incrementally. In practice, three objects of 30 markers can be trained with high frame rates.

The model estimation method assumes that motions are slow and smooth, and that the 3D data is reasonably reliable. This means that mistakes in marker tracking or blob detection (e.g. multiple blobs that become one when they are aligned during rotation), may result in model errors. In order to support faster and more erratic motions, the following strategies can be applied. First, a predictive filtering technique can be used to estimate 3D marker locations, so that outliers and jittering can be reduced. The filter can also be used to predict marker locations more accurately, resulting in more reliable frame-to-frame correspondence. Second, the robustness of the blob detection can be increased by incorporating marker quality metrics. For instance, the roundness of a blob can be checked, so that two markers forming one blob in a camera image can be rejected. Third, in case frame-to-frame correspondence is completely lost, the tracking method can be applied using the model acquired so far, until a known part of the model is found again. This occurs when less than three non-collinear markers remain visible. This would also enable a developer to completely remove an object from the workspace during model estimation, and insert it at a later time, or even to completely stop the model estimation procedure to resume it at a later time.

4.6.3 Model-based Tracking

The tracking method treats the markers on an interaction device as one point-cloud, and does not require markers to be grouped into patterns. This makes the system more flexible compared to pattern-based approaches. For instance, in the situation illustrated in Figure 4.13, two sides of a cube are partially occluded. The pattern-based approach using points would fail to recognize the object even though seven markers are visible, whereas the subgraph tracker correctly identifies the cube and its pose.

Results show the method is competitive with a pattern-based approach in terms of computational efficiency, and more robust against occlusion. Although it would be possible to use a pattern-based tracker with a trained device model by generating all patterns from the model, this would require a prohibitive amount of patterns. For instance, an object with 30 markers would require $\binom{30}{5} = 142506$ patterns. Although this number can be decreased by using visibility information, the number of patterns required is clearly too large for realtime tracking.

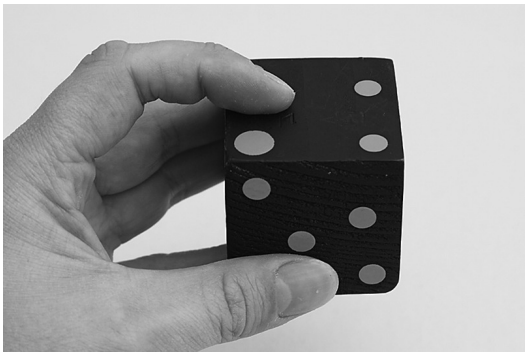

Figure 4.13: A partially occluded cube. A pattern-based tracking approach would fail to recognize the object, as the two visible sides are partially occluded by the user's hand. The subgraph tracker correctly identifies the object and determines its pose.

There is a tradeoff between tracking speed and the allowed noise levels in marker distance. Higher noise levels mean that more distances are indexed into the same location in the hash table, and generate more candidates. In the implemented tracking system, noise levels were set so that the distance error could not exceed 4 mm. In this case, two objects of each 30 markers can be tracked with over 60 Hz. With a much larger number of markers, performance degrades.

The accuracy of the tracking method is identical to pattern-based approaches that optimize the pose estimate by performing a fit on all data, minimizing Equation 4.11. Accuracy depends on the size of the object, where a smaller object results in more jitter in the pose, and on the quality of the blob detection, which is related to the distance of the object to the cameras and lighting conditions.

4.7 Conclusion

In this chapter, an optical tracking system has been presented, which is capable of automatic model estimation and tracking of objects of arbitrary shape. The system is marker-based, allowing a developer to equip an object with retro-reflective markers, and train the system to recognize the object by moving it in front of the cameras. The tracking method is based on subgraph matching, finding a subset of the model graph in the data.

Results show that the system is robust against partial occlusion, noise, and outliers in the data, and maintains frame rates of 60 Hz while performing model estimation or tracking of two objects of 30 markers simultaneously.

The system can be extended to support fast and erratic motions during model estimation. This can be achieved by incorporating the tracking method into the model estimation procedure in case of loss of frame-to-frame correspondence.

Chapter 5

Analysis of Tracking Methods

In Chapters 3 and 4, two optical tracking methods were proposed for pose estimation of input devices. The approaches are based on different principles: one performs object recognition completely in 2D, whereas the other transforms detected image features to 3D and performs 3D subgraph matching for recognition. Each method was compared to a related tracking approach.

The goal of this chapter is to analyze the behavior of tracking methods that are based on different principles, subject to the error sources as defined in Chapter 2. Three tracking methods are selected: the method based on projection invariant properties as presented in Chapter 3; the method based on finding subgraph isomorphisms in 3D as presented in Chapter 4; and a method based on pose estimation by optimization as discussed in Section 2.5.3.

This chapter presents an experimental evaluation of these tracking methods to study the effects of each error source on the accuracy, latency, and robustness of each method. Furthermore, an error model for accuracy is presented, which is used to analyze the influence of the different error sources, and compared to experimentally obtained data. Results show that each of the tracking methods has its own advantages and disadvantages, and that none of the tested methods is robust to every error source. Furthermore, the accuracy model is shown to result in reasonable predictions of the accuracy of the tracking methods for a given error source value.

The chapter is organized as follows. In Section 5.1, the evaluation method is described. Next, the test setup and performance metrics are discussed. Section 5.2 provides an accuracy model of optical tracking methods, subject to different error sources. In Section 5.3, the results are presented. Section 5.4 provides a discussion of the results. Finally, in Section 5.5 conclusions are given.

5.1 Method

The fundamental problem in model-based optical tracking is to match the data features obtained from camera images to a device model, and to obtain a pose estimate of each interaction device. As discussed in Chapter 2, optical tracking methods can be divided into categories based on how recognition and pose estimation is performed.

In this chapter, three tracking solutions are compared that are based on different principles:

- *The pencil tracker*
  The pencil tracker, as presented in Chapter 3, is based on 2D recognition using projection invariant properties of line pencils. The approach outperforms a related approach based on point features with respect to occlusion and efficiency.

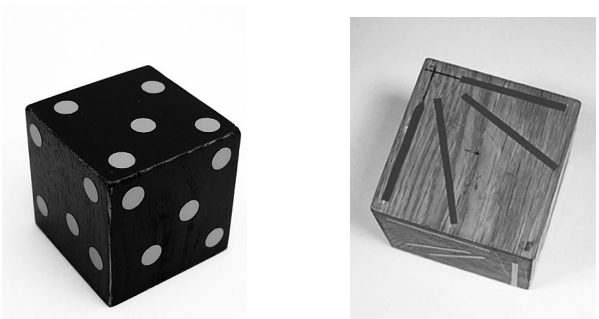

(a) (b)

Figure 5.1: Cubic devices with (a) point patterns and (b) line pencils.

- *The subgraph tracker*
  The subgraph tracker is presented in Chapter 4. It uses stereo correspondence to transform 2D image points to 3D, and uses a 3D recognition method based on subgraph isomorphisms for point identification. It is demonstrated in Chapter 4 that this method outperforms a related pattern-based approach with respect to occlusion and generic device shape.

- *The iterative closest point (ICP) tracker*
  The ICP tracker, as discussed in Section 2.5.3, is based on projecting the model points of a device back into the camera images, given a device pose. A fitting procedure is performed to refine the pose, matching the projected device features to the 2D image features.

The performance of the tracking methods is experimentally compared, subject to the following error sources (see Chapter 2): lighting conditions, the amount of occlusion, and the camera parameters determined by calibration.

5.1.1 Test Setup

Environment

For the experimental evaluation of tracking methods, simple wooden cubes were used as input devices. For the subgraph and ICP trackers, which use point features, retro-reflective markers were attached to a cube, and a model was trained using the model estimation techniques presented in Chapter 4. For the pencil tracker, a cube was equipped with six pencils, one for each side of the cube. A model of this cube was obtained by training the pencils using the techniques presented in Chapter 3, and by measuring the location of each pencil on the device by hand. Figure 5.1 shows the devices used in this study.

The experiments were conducted in the PSS. The tracking setup is discussed in Section 2.6. The experiments were performed on an AMD Athlon XP 2700+ with 1 Gb RAM.

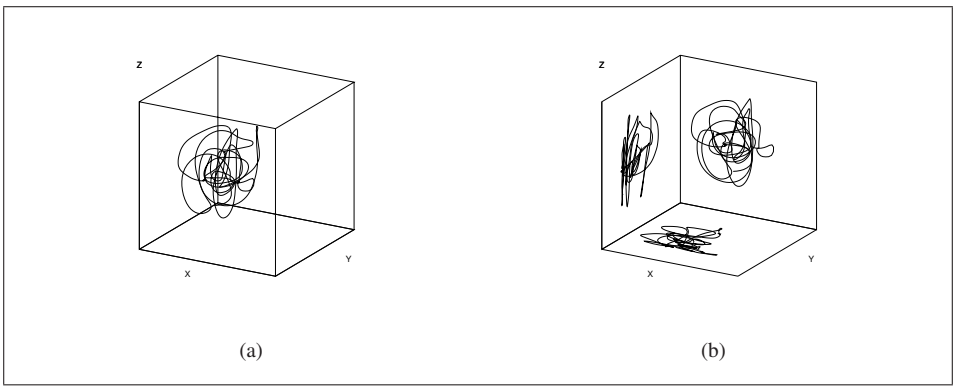

Figure 5.2: The 3D data recordings in the xy, xz, and yz planes. Depicted are (a) the recordings in the interaction volume, and (b) the 2D projections of each recording onto its corresponding plane.

Data Set Generation

To compare different tracking methods with respect to accuracy, a data set is required. The data set was created by recording an interactive session of a user exploring a virtual object using the tracking system, and storing the pose of the interaction device on disk. This sequence of poses provides a "ground truth", which is used to determine the performance of each of the tracking methods. Figure 5.2 shows the trajectories of the device frames during the interactive session. The recorded data set consists of 700 frames.

The data set is used to generate synthetic camera images for the tracking methods. The camera images are generated such that the effect of occlusion on each tracking method can be determined. Occlusion is added by blocking out certain regions in the camera images.

The pinhole camera model as discussed in Chapter 2 is used to project the 3D model features back to the camera images, given a pose in the data set. This process generates the ideal images: no image distortion or image noise is added, and all error sources are zero. By varying the error sources defined in Section 2.7, the accuracy of the tracking methods can be compared.

The images were generated by using OpenGL drawing routines. The device model used by the subgraph and ICP trackers, which describes the 3D marker locations on the input device, was used to draw white blobs with a diameter of 4.2 pixels with subpixel accuracy. Similarly, the model used by the pencil tracker, which describes the 3D line pencils on the input device, was used to draw white lines with a thickness of 3 pixels and a 3D length of 7 cm. These values correspond to the actual imagery obtained by the cameras.

Parameter Perturbation

The error sources were varied as follows:

- *Lighting conditions*
  To simulate changing lighting conditions, the data set was projected using the ideal camera parameters, and adding zero mean Gaussian noise with variance $\sigma_p^2 = 0.2$ and $\sigma_p^2 = 0.5$ pixels^2 to the coordinates of each 2D data feature. For the subgraph and ICP

(a) (b)

Figure 5.3: Moving black lines are drawn to the synthetic images in order to simulate occlusion. The line thickness is varied to control the level of occlusion. (a) The generated images for the subgraph and ICP trackers, containing the white blobs corresponding to the markers on the device. (b) The generated images for the pencil tracker, containing the white lines that correspond to the 3D line pencils on the device.

trackers this was accomplished by adding this noise to each coordinate of the generated blob position. The lines of the pencil tracker were perturbed by adding the noise to the endpoints of the line, such that the direction is changed.

- *Occlusion*
  Occlusion is simulated by drawing two moving black lines in the generated image sequences. The lines could correspond to a user's fingers that block parts of the interaction device during manipulation. To study the effect of varying amounts of occlusion, the line thickness is chosen as 2, 4, 6, or 10 pixels. Since the trackers use different types of features, simply removing a number of features for each generated camera image is inappropriate. Figure 5.3 gives an example of the camera images generated for the different tracking methods, subject to an occlusion level of 4 pixels.

- *Camera calibration*
  To simulate errors arising from inaccurate camera calibration, the intrinsic and extrinsic parameters of the ideal camera description are perturbed. The intrinsic parameters are changed by perturbing the focal length by 1%, 1.5%, and 2%. For the extrinsic parameters, the camera position is translated by 0.5, 1, and 2.5 mm in the xy plane. Additionally, the camera orientation is changed by rotating the camera around its "line of sight axis", i.e., the z-axis, by 0.1, 0.5, and 1 degrees. These extrinsic parameter perturbations give an indication of the influence of camera calibration inaccuracies, while keeping the number of test scenarios relatively small.

5.1.2 Performance Metrics

- *Accuracy*
  The accuracy of a tracking method is determined by calculating the difference between the device poses of the data set and the pose estimates obtained by the tracking method.

The accuracy of a pose estimate is divided into the positional and angular accuracy.

The positional accuracy is defined as the root mean square error (RMSE) of the difference in position between the poses of the data set and the pose estimates from the tracking method, as defined by

$$RMSE_t = \sqrt{\frac{1}{N}\sum_{i=1}^{N} ||T_i^{ref} - T_i^{est}||^2} \tag{5.1}$$

where N is the number of frames in the motion sequence, T_i^{ref} is the device position of the data set, and T_i^{est} represents the estimated device position at frame i. Similarly, the rotational accuracy is defined as the root mean square error of the difference in orientation between the poses of the data set and the pose estimates

$$RMSE_r = \sqrt{\frac{1}{N}\sum_{i=1}^{N} (\frac{360}{\pi} \cos^{-1}((q_{r_i} \cdot q_{e_i}^{-1})_w))^2} \tag{5.2}$$

where q_e is the quaternion representing the estimated orientation, q_r represents the reference signal, and q_w represents the w-component of quaternion q.

- *Latency*
  The latency of a tracking method is defined as the time required for image capturing, feature detection, recognition, and pose estimation. In the tracking framework of Figure 2.2, this time is given by $t_2 - t_1$. Although this is not the complete end-to-end latency of the system, it is a good and convenient metric to compare different tracking methods.

- *Robustness*
  The robustness of each method is determined by counting the number of frames in which the tracking method fails to recognize the input device and estimate its pose. This number of misses determines if a method is robust: if a device cannot be found for a certain parameter perturbation, the method is not considered to be robust with respect to this parameter. For instance, a method might fail due to partial occlusion or small inaccuracies in the camera parameters. The number of misses gives an indication of the sensitivity of a tracking method with respect to different error sources.

5.2 Accuracy Model

This section provides an error model of accuracy, which is used to analyze the influence of the different error sources. This analysis is used to predict the accuracy of optical tracking methods under different circumstances. The obtained data is compared to the experimentally obtained data in Section 5.3.

5.2.1 Image Noise

To model image noise, a stereo camera setup is assumed, where point features are detected in each camera image. Figure 5.4 illustrates a parallel stereo camera setup with cameras C_1

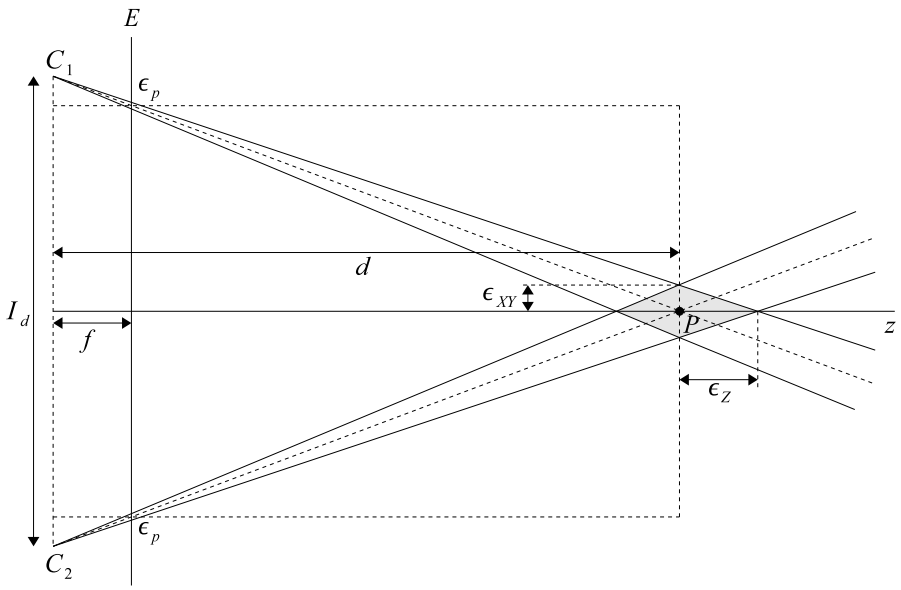

Figure 5.4: The expected error of a reconstructed 3D point P in a stereo camera setup, given its noisy 2D image projections.

and C_2, a focal length f, and an image plane E. A 3D point P with a depth d to the baseline of the cameras is projected onto E. Assuming the errors in the 2D point projections follow a Gaussian distribution with standard deviation ϵ_p, the reconstructed 3D point P lies within the region illustrated in the figure (see also [CS00]).

Expected Single Point Reconstruction Error

The region S can be described by the expected error ϵ_{xy} in the xy-direction, and ϵ_z in the z-direction. The expected error ϵ_{xy} follows directly from Figure 5.4 by similar triangles as

$$\frac{\epsilon_{xy}}{d} = \frac{\epsilon_p s_p}{f} \tag{5.3}$$

$$\epsilon_{xy} = \frac{d\epsilon_p s_p}{f} \tag{5.4}$$

where ϵ_p is the standard deviation of the Gaussian image noise in pixels, and s_p represents the pixel size in meters. Similarly, the expected error ϵ_z follows from similar triangles as

$$\frac{\epsilon_{xy}}{\epsilon_z} = \frac{\frac{I_d}{2}}{d + \epsilon_z} \tag{5.5}$$

where I_d is the distance between the cameras. This equation can be simplified by substituting Equation 5.4, which results in

$$\epsilon_z = \frac{2d^2\epsilon_p s_p}{I_d f - 2d\epsilon_p s_p} \tag{5.6}$$

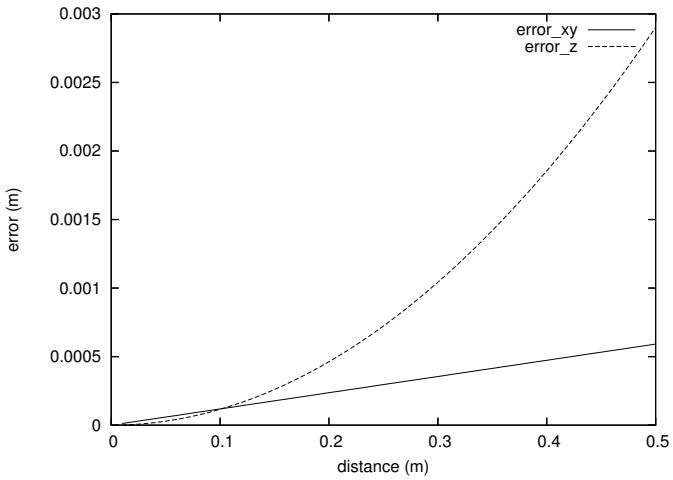

Figure 5.5: Reconstruction error versus distance.

Note that if $d > \frac{I_d f}{2f+2\epsilon_p s_p}$, ϵ_z is larger than ϵ_{xy}. In most stereo setups, $I_d \gg f > \epsilon_p s_p$, such that

$$\frac{I_d f}{2f + 2\epsilon_p s_p} \approx \frac{I_d}{2} \tag{5.7}$$

In other words, if the distance d to the baseline of the cameras is larger than half the distance between the cameras, the error in the reconstructed 3D point P is largest in the z-direction.

The total expected error of the 3D reconstruction of a single point P from its 2D image projections is given by

$$\epsilon_t = \sqrt{\epsilon_{xy}^2 + \epsilon_z^2} \tag{5.8}$$

Figure 5.5 plots the expected errors of a single 3D point reconstruction for a noise level $\epsilon_p^2 = 0.2$, as a function of the distance d to the cameras. The focal length f set to $3.74{\cdot}10^{-3}$ m, I_d was set to 0.205 m, and s_p to $9.9 \cdot 10^{-6}$ m, which corresponds to the values found during calibration of the camera setup of the PSS. These values are also used in the experimental evaluation. The expected error ϵ_{xy} in the xy-direction and ϵ_z in the z-direction are graphed. It can be seen that ϵ_z becomes larger than ϵ_{xy} for $d > \frac{I_d}{2}$. Furthermore, the error in z-direction increases more rapidly with distance than the error in the xy-direction. The larger the distance to the cameras, the more the error is dominated by ϵ_z.

Expected Device Position Error

The position of an input device is determined from N points, which should result in a lower error than using a single point. Assuming the noise in the point positions is independent and Gaussian, Equation 5.8 can be extended to N points as

$$\epsilon_t^N = \frac{1}{\sqrt{N}}\epsilon_t \tag{5.9}$$

Equations 5.8 and 5.9 show that the expected 3D reconstruction error decreases in all directions when more points are visible to the cameras.

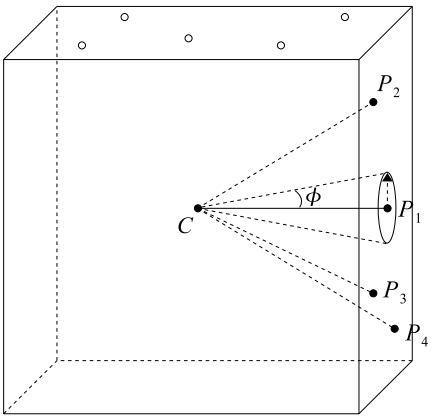

Figure 5.6: The maximum orientation error.

Expected Device Orientation Error

The expected error in the estimated device orientation can be estimated as follows. Consider a set of points P_i, which are shifted in relation to the device, for instance due to noise (see Figure 5.6). Using the expected position error ϵ_t, the maximum orientation error can be written as

$$\phi = \frac{180}{\pi\sqrt{N}} \tan^{-1} \frac{\epsilon_t}{0.5v} \tag{5.10}$$

where v represents the average distance from device points P_i to the center C of the device.

5.2.2 Camera Calibration Errors

Errors in the camera calibration are divided into two categories: errors in the intrinsic camera parameters, and errors in the extrinsic camera parameters. In this study, errors in the intrinsic camera parameters are modeled by focal length perturbations. The errors in the extrinsic camera parameters are modeled by deviations in the camera position and orientation.

Focal Length

Errors in the focal length are modeled according to Figure 5.7. The figure depicts a stereo setup with cameras C_1 and C_2. A 3D point P is projected onto the image plane E. The cameras have a true focal length f. A deviation Δf in the focal length causes the image plane to be shifted, which shifts the location of the reconstructed 3D point to $\hat{P}$. The effect is equivalent to the situation illustrated in Figure 5.7, where the camera positions are shifted away from the image plane over a distance of Δf. Similar triangles directly give the expected error ϵ_f

$$\frac{\epsilon_f + d + \Delta f}{I_d} = \frac{\epsilon_f + d - f}{l} \tag{5.11}$$

$$\epsilon_f = \frac{l(d + \Delta f) - I_d(d - f)}{I_d - l} \tag{5.12}$$

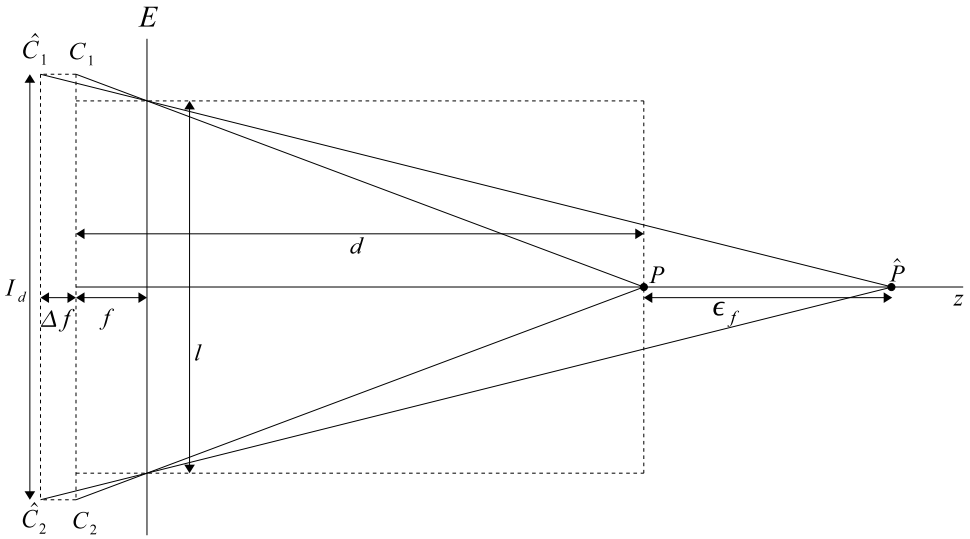

Figure 5.7: The expected error of a reconstructed 3D point P, given its 2D image projections and an error in focal length.

where l represents the distance between the projected 2D image points.

Note that l can be written as a function of the depth of point P, the focal length, and the distance between the cameras. The result is obtained from Figure 5.7 as

$$l = \frac{I_d(d - f)}{d} \tag{5.13}$$

Equation 5.12 gives the expected error of the reconstruction of a single point when the focal length is inaccurate. When more than one point is used for determining the device position, the exact expected error depends on the position and orientation of the device with respect to the cameras. If N points lie in a plane parallel to the image plane E, the expected error of the device position is equal to the expected error of a single point. Equation 5.12 serves as a maximum value of the reconstruction error.

Figure 5.8 illustrates how four points are transformed if the focal length is changed. The 3D reconstructed points are stretched in the z-direction. When multiple reconstructed 3D points are used in an optimization procedure to match the reconstructed points to the device model points, model points may be matched to incorrect reconstructed data points. This may cause errors in both the device position and orientation.

Camera Position

The effects of errors in the camera position on the accuracy of the reconstructed 3D point can be determined as follows. Consider a parallel stereo camera setup with cameras C_1 and C_2, as illustrated in Figure 5.9. A 3D point P with a depth d to the baseline of the cameras is projected onto E. A positional error ΔC of camera C_2 in the xy plane gives a 3D reconstruction error of $\epsilon_{c_{xy}}$ in the xy-direction and ϵ_{c_z} in the z-direction. Similar triangles

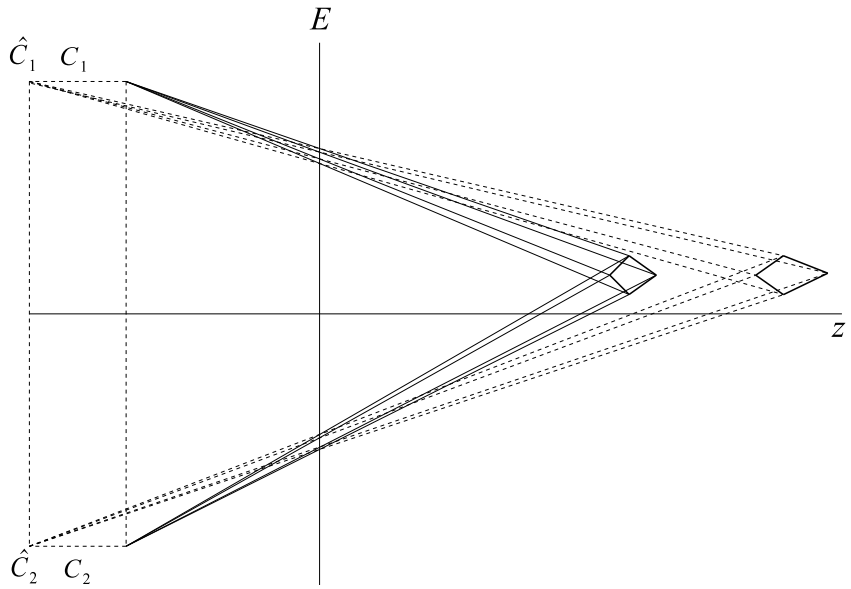

Figure 5.8: The reconstruction of device points is stretched in the z-direction for changing focal length.

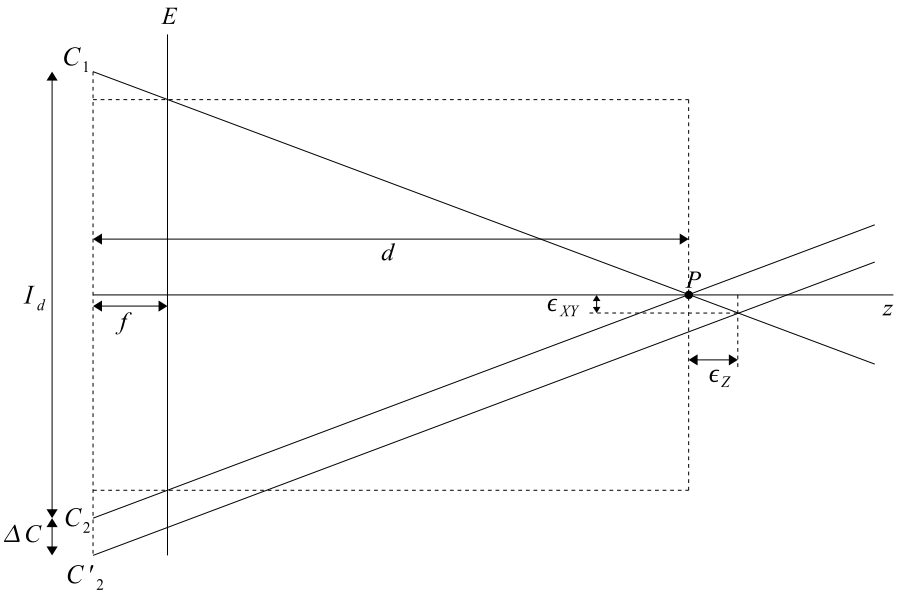

Figure 5.9: The expected error of a reconstructed 3D point P, given its 2D image projections and an error ΔC in camera position.

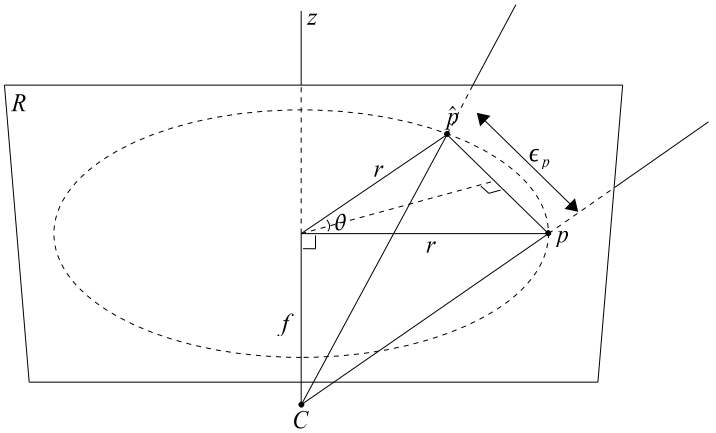

Figure 5.10: The expected error of a reconstructed 3D point P, given its 2D image projections and an error in camera orientation.

give the maximum reconstruction error:

$$\epsilon_{c_{xy}} = \frac{\Delta C}{2} \tag{5.14}$$

$$\epsilon_{c_z} = \frac{d\Delta C}{I_d} \tag{5.15}$$

$$\epsilon_c = \sqrt{\epsilon_{c_{xy}}^2 + \epsilon_{c_z}^2} \tag{5.16}$$

Camera Orientation

A rotation of one of the cameras around the z-axis will result in an error in the reconstructed 3D point. The situation is depicted in Figure 5.10. A point P is projected onto the image plane R of a camera C, resulting in the 2D projection p. Because of an error in the calibration of the camera orientation, the 2D projected point is rotated around the z-axis to point $\hat{p}$. The resulting error ϵ_{pr} in pixel position can be written as

$$\epsilon_{pr} = 2r\sin\frac{\phi}{2} \tag{5.17}$$

The expected error ϵ_r in device position can be obtained by substituting the result of Equation 5.17 into Equation 5.8.

5.3 Results

The tracking methods were applied to the data set for each of the error sources. The following sections present the results of the accuracy model and the experimental evaluation in terms of the performance metrics as defined in Section 5.1.2.

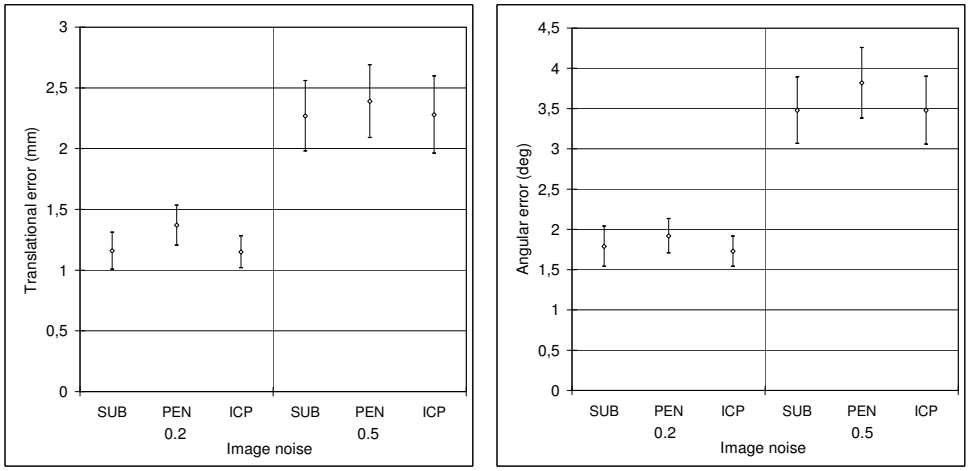

(a) (b)

Figure 5.11: Translational and rotational errors for image noise levels of $\sigma_p^2 = 0.2, 0.5$. (a) Translational errors in millimeters with 95% confidence intervals. (b) Rotational errors in degrees with 95% confidence intervals.

5.3.1 Accuracy

Image Noise

It was found that the translational and rotational errors could be approximated well by a Gaussian distribution. The t-distribution was used to determine 95% confidence intervals for the average errors [DS98]. Figure 5.11 depicts the results for noise levels $\sigma_p^2 = 0.2, 0.5$. Tables 5.1 and 5.2 list the translational and angular RMSE. The noise levels represent the variance of the Gaussian noise added to the data set.

Table 5.1 also lists the expected translational error as obtained from Equation 5.9. The parameters of the equation were obtained from the setup of the PSS. The distance d to the cameras was determined to be approximately 0.5 m, the distance between the cameras I_d was 0.205 m, the focal length f of the cameras was $3.74{\cdot}10^{-3}$ m, and the pixel size was $9.9 \cdot 10^{-6}$ m. The number of features N that were used in the pose estimation was determined to be an average of five features for the subgraph and ICP trackers. The pencil tracker uses four line features to determine the position of a pencil intersection and for pose estimation, and therefore N was set to four in this case.

Table 5.2 includes the expected orientation error as determined by Equation 5.10. The average distance v was set to 3.5 cm (the cube size is 7 cm). The values listed in Table 5.1 were used as noise levels ϵ_t in Equation 5.10.

The following observations can be made from Figure 5.11 and Tables 5.1 and 5.2:

- The pencil tracker is slightly less accurate than the subgraph and ICP trackers, although the difference becomes statistically insignificant for $\sigma_p^2 = 0.2$ or 0.5. A possible cause for accuracy differences is that the pencil tracker uses only four features per pattern to determine a pose, whereas the subgraph and ICP trackers use a minimum of five features.

	Subgraph		Pencil		ICP	
Noise	Measured	*Analytic*	Measured	*Analytic*	Measured	*Analytic*
0.0	0.16	*0.00*	0.25	*0.00*	0.16	*0.00*
0.2	1.16	*1.32*	1.37	*1.48*	1.15	*1.32*
0.5	2.27	*2.10*	2.39	*2.35*	2.28	*2.10*

Table 5.1: Positional RMSE in millimeters, for image noise levels of $\sigma_p^2 = 0.0, 0.2, 0.5$.

	Subgraph		Pencil		ICP	
Noise	Measured	*Analytic*	Measured	*Analytic*	Measured	*Analytic*
0.0	0.24	*0.00*	0.33	*0.00*	0.27	*0.00*
0.2	1.79	*1.89*	1.92	*2.24*	1.73	*1.89*
0.5	3.48	*3.69*	3.82	*3.89*	3.48	*3.69*

Table 5.2: Angular RMSE in degrees, for image noise levels of $\sigma_p^2 = 0.0, 0.2, 0.5$.

The accuracy of the device pose computed with the subgraph tracker is very similar to the one determined by the ICP tracker. This can be attributed to the nature of the algorithms. Both trackers use all available data to determine the pose, and perform an iterative optimization procedure to match the model points to the data points. The ICP tracker projects the 3D device model points back to the 2D camera images, given a device pose. It then iteratively refines this pose to fit the projected model points onto the 2D data points. The subgraph tracker first transforms the 2D data points to 3D space, and performs a similar iterative pose optimization procedure to match the 3D model points to the 3D data points. Since both approaches use all available data, the accuracy is very similar.

- The analytically determined values are reasonable estimations of the experimentally obtained results. The standard deviation as obtained from Equation 5.9 is a minimum value of the RMSE. However, in some cases the analytically determined values are slightly lower than the measured values. This can be attributed to quantization errors in the point and line detection methods that precede the recognition and pose estimation stages. These quantization effects are apparent from the fact that if no noise is added to the data set, i.e., σ_p^2 is set to zero, the measured position errors are not zero.

  The size of the quantization errors can be estimated as follows. The RMSE of the subgraph tracker for $\sigma_p^2 = 0$ is 0.16 mm. Substituting this error back into Equations 5.9, 5.4, and 5.6, a single point detection error with a variance of approximately 0.00295 pixel is obtained. This illustrates how very small errors during point detection can have significant effects on the accuracy of pose estimation.

  A better error estimate can be obtained by correcting the results from Equation 5.9 with the expected quantization error.

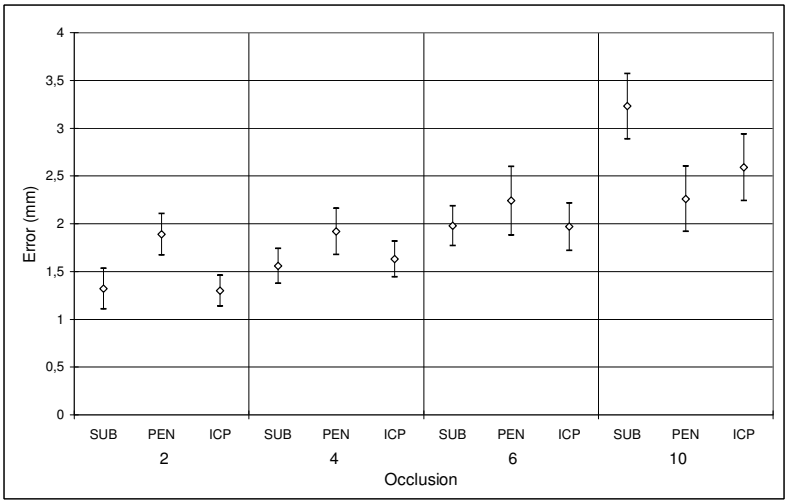

Figure 5.12: Positional errors with 95% confidence intervals of each tracking method for the cases a pose estimate could be obtained, subject to an occlusion level of 2, 4, 6, and 10 pixels.

Occlusion

The effect of occlusion on the accuracy of the pose estimate is illustrated in Figure 5.12. The figure shows the error in the pose estimate with 95% confidence intervals, as a function of the amount of occlusion in the camera images.

The figure demonstrates that all tracking methods become less accurate as occlusion is increased. The reason for this phenomenon can be found in the nature of the point and line detection methods. If an image point is only partially visible, its center is shifted. A relatively small perturbation of the center from its true value can have substantial effects on accuracy. Similarly, a partially visible line can result in small deviations of the line parameters. Comparing

The figure shows that the pencil tracker is slightly less accurate than the subgraph and ICP trackers for occlusion level 2. Due to the nature of the pose estimation method used by the pencil tracker, it is sensitive to small perturbations of the line parameters. Furthermore, on average less features are used to estimate the pose.

Camera Calibration Errors

Table 5.3 lists the positional accuracy of each tracking method, subject to different camera calibration errors. The analytic values of the expected errors were obtained from Equations 5.12 and 5.17. Figure 5.13 visualizes the most important data, including 95% confidence intervals. The figure demonstrates that for the cases all trackers are able to find pose estimates, there are no statistically significant accuracy differences.

If the focal length is perturbed by only 1%, each tracking method has a positional RMSE of over 3.5 mm, whereas the RMSE of the data set was below 0.3 mm. This illustrates the sensitivity of each of the tracking methods to focal length perturbations.

The analytically obtained error estimates for varying focal lengths provide an upper error bound. Due to the non-linear stretching of 3D points for focal length perturbations, and the

Parameter		Accuracy			
Type	Value	Subgraph	Pencil	ICP	Analytic
intrinsic	1.0%	3.76	4.25	3.82	4.96
focal	1.5%	5.57	6.01	5.49	7.44
length	2.0%	6.12	7.76	-	9.93
extrinsic	0.5	0.97	1.08	0.95	1.24
camera	1.0	1.98	2.21	1.96	2.49
translation	2.5	5.23	5.49	5.24	6.22
extrinsic	0.1	0.23	0.39	0.23	0.23
camera	0.5	1.13	1.37	1.14	1.17
rotation	1.0	0.39	2.54	-	2.40

Table 5.3: Positional errors of each tracking method in millimeters, subject to perturbations of intrinsic and extrinsic camera parameters.

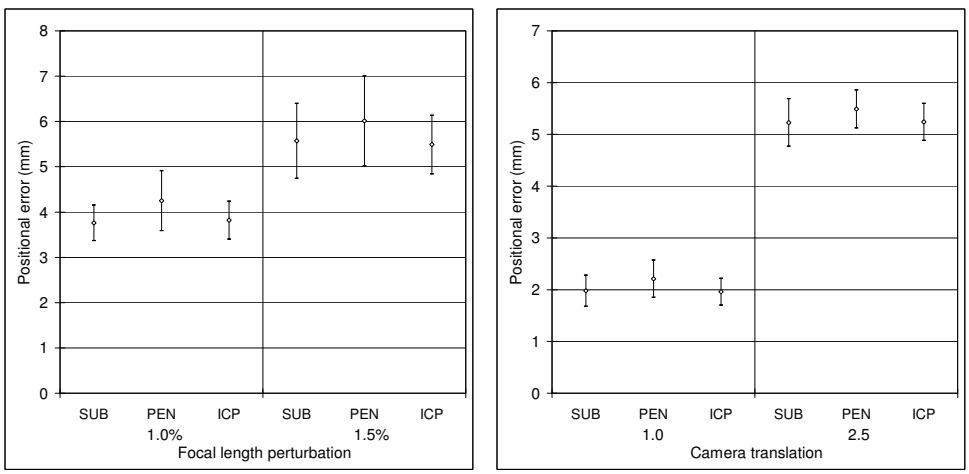

(a) (b)

Figure 5.13: Positional errors with 95% confidence intervals of each tracking method for: (a) Focal length perturbations of 1 and 1.5%. (b) Camera translation of 1 and 2.5 mm.

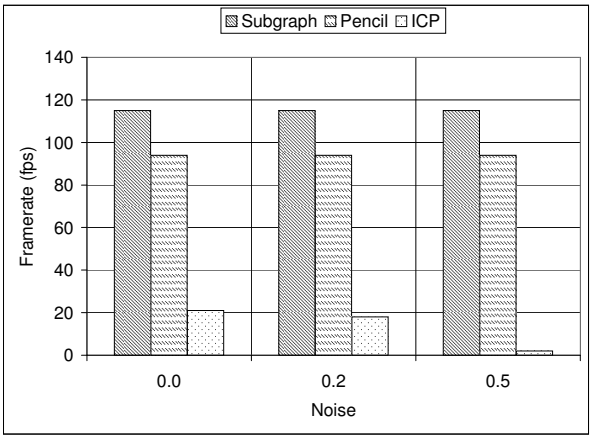

Figure 5.14: Average frame rates for each tracking method, subject to noise levels $\sigma_p^2 = 0, 0.2, 0.5$.

fact that each tracking method uses an optimization procedure to match the model features to the data features, the values are lower in practice.

It was found that the ICP method is sensitive to camera calibration errors. Since the method iteratively projects the model points back to 2D given a pose estimate and matches these points to the data points, it relies on an accurate camera description. The table shows that for a focal length perturbation of 2%, ICP is not able to determine a pose for all image frames. Similarly, ICP fails to find a pose if the camera orientation is perturbed by one degree. Although the subgraph and pencil trackers are able to find pose estimates under these circumstances, large camera calibration errors result in inaccurate estimates.

5.3.2 Latency

Figure 5.14 depicts the average frame rate of each tracking method, subject to different noise levels. The subgraph and pencil trackers are clearly faster than the ICP method. Also, it can be seen that the performance of the subgraph and pencil trackers is not sensitive to noise, whereas the ICP method becomes slower as noise increases. As more noise is added, the likelihood of an occasional miss is increased. If the ICP tracker is not able to obtain a reasonable initial pose estimate based on the pose of the previous frames, the method requires many optimizations to find a good pose estimate near the global minimum.

Figure 5.15 plots the accumulative latency of each tracking method for the data set. The slopes of the subgraph and pencil plots are practically constant. The slope of the ICP plot often remains constant, but suffers from a number of large discontinuities. In these cases, the initial pose estimate needed by the ICP method was not determined accurately enough.

In Chapter 1, the requirements for an optical tracking system were defined, with a minimum frame rate of 60 Hz and a maximum latency of 33 ms. It is evident from the data that the ICP method is in fact capable of reaching frame rates of around 60 Hz. However, the discontinuities in the latency bring the average frame rate below the required 60 Hz, such that the method is less suitable for real-time tracking.

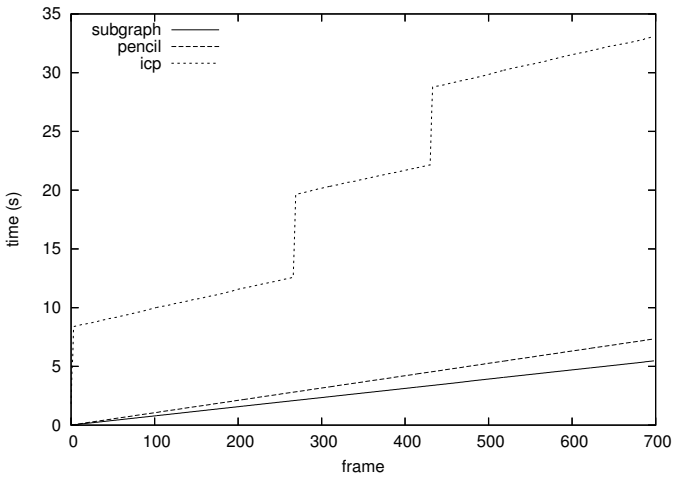

Figure 5.15: Accumulative time for the tracking methods for the data set.

5.3.3 Robustness

Table 5.4 tabulates the robustness of each method, subject to different image noise levels, occlusion, and camera parameter perturbations. The following observations can be made:

- *Image noise*
  The ICP tracker is more robust against image noise than the subgraph and pencil trackers. The subgraph tracker uses stereo correspondence, which relies on epipolar geometry. Errors in the epipolar geometry result in noisy 3D data points, resulting in a noisy pose estimate. If the noise becomes larger, the epipolar distance between an image point from one camera and a point in the other camera may exceed a certain threshold. In this case, the two image points are not considered as possible matches, and the 3D point cannot be determined correctly.

  The pencil tracker uses the detected lines in a camera image to detect an interaction device directly in 2D. Although image noise influences the cross ratio, the intervals in which the cross ratios may lie are chosen relatively large (the range was set to 0.08). As such, image noise has less influence on the device recognition, although larger cross ratio intervals result in a smaller number of distinguishable pencils.

  The ICP tracker uses a prediction of the device pose as an initial estimate, and iteratively refines this pose by projecting the model points to 2D and fitting these to the data points. As such, noisy data points have less influence on the ICP method.

- *Occlusion*
  The subgraph tracker suffers most from occlusion. Although in Chapter 4 the method was shown to be more robust than a related tracking method using 3D pattern recognition, the ICP and pencil trackers perform significantly better when features become occluded. The reason is that the subgraph tracker requires points to be visible in two cameras simultaneously in order to transform the point to 3D.

  On the other hand, the ICP method can handle situations where different device points

Parameter		Misses		
Type	Value	Subgraph	Pencil	ICP
Image noise	0.0	0	0	3
	0.2	10	3	4
	0.5	253	143	56
occlusion	2	121	12	78
	6	249	28	101
	10	386	100	298
focal length	1%	0	0	3
	2%	208	0	700
camera translation	0.5	0	0	3
	2.5	53	0	189
camera rotation	0.1	0	0	3
	1.0	670	0	700

Table 5.4: The number of misses of each tracking method in a motion sequence of 700 frames for varying noise levels, occlusion, and intrinsic and extrinsic camera parameters.

are visible in different cameras. As such, occlusion has less influence. However, the computational requirements of the ICP method depend on the number of misses, making the subgraph tracker preferable over ICP in practice.

The pencil tracker is the most robust against occlusion, due to the nature of the line features. Since only an arbitrary point on the line and its direction is required for the tracking method, only a small part of the line needs to be visible.

- *Camera calibration*
  The ICP tracker strongly relies on an accurate description of the camera parameters. If the focal length is miscalibrated by more than 1.5% of the reference focal length, the method is unable to correctly determine the pose of the device. In this case, the subgraph tracker is also not robust. If the camera translation is miscalibrated by 2.5 mm or more, or when the camera orientation is miscalibrated by 1 degree or more, the subgraph and ICP trackers are not robust.

  The pencil tracker is able to determine a device pose in all cases, and is the least sensitive to calibration errors. Although miscalibrations have an effect on its accuracy, it is the only method that is able to obtain a pose estimate in each of the tested camera parameter perturbations.

5.4 Discussion

In the previous sections, three model-based optical tracking methods have been compared, and their performance was evaluated analytically. The results are summarized by the three performance criteria as defined in Section 5.1.2:

- *Accuracy*
  The experimental data shows that the relative accuracy of the subgraph and ICP trackers is better than the pencil tracker. A possible cause for this would be the number of

features used during pose estimation. On average, the subgraph and ICP trackers use more features to determine a pose estimate. The pose estimation procedure of the pencil tracker could also be more sensitive to noise in the line directions. For instance, it was observed that the pencil tracker is quite sensitive to the length of the generated image lines.

The results show that the accuracy model developed in Section 5.2 gives a good indication of the worst case accuracy of the tracking methods, subject to image noise and camera calibration errors.

Occlusion has a significant effect on the accuracy of each of the tracking methods. If the level of occlusion is increased, the accuracy of the tracking methods decreases. This can be attributed to the nature of the point and line detection methods. If a point or line feature is partially occluded in the camera images, the center and line directions can become distorted.

Focal length was demonstrated to have a large effect on the accuracy of each tracker, increasing the positional RMSE of the subgraph tracker from its nominal value of 0.3 mm to more than 3.5 mm if the focal length is perturbed by just 1% of its reference value. Perturbations in the extrinsic camera parameters were found to have a smaller influence on accuracy.

- *Latency*
  The data shows that the subgraph and pencil trackers have a lower latency than the ICP tracker. The reason is that the ICP method is an optimization method that requires a reasonable initial estimate of the solution. In cases where this initial estimate cannot be obtained, or is not accurate enough, the procedure requires many optimizations to find an estimate close to the global minimum. Figure 5.15 illustrates that the ICP tracker is competitive with the other tracker if the initial estimate can be chosen near the global minimum. However, ICP suffers from large performance penalties in case this initial estimate cannot be determined accurately, for instance due to increased image noise, occlusion or camera calibration errors.

  The latency of a tracking method depends on the number of detected data features. The computational complexity of a tracking method can be used to get an idea of how well a method scales when the number of data features is increased.

  The worst case computational complexity of the recognition step of the pencil tracker is obtained when all lines in the camera image intersect at one point, resulting in $\binom{N}{4}$ pencils, where N is the number of detected line features. This results in a computational complexity of $O(N^4)$.

  The worst case computational complexity of the recognition step of the subgraph tracker is obtained when all data and model points have the same distance, and the best match is searched. In this case, the number of hashing collisions for a given data point is $O(N^2)$, resulting in a candidate list of N data point matches for every model point. Next, $O(N^3)$ distance checks need to be performed, resulting in a worst case complexity of $O(N^6)$.

  The worst case complexity of the ICP method depends on the method used as optimization procedure. In this thesis, the downhill simplex method from Nelder and Mead [Chv83] was used. Since no proof of convergence exists for this method, a complexity analysis is not possible.

Although the worst case computational complexity of the tracking methods are relatively high, it was found that in practice the worst case computational complexities are not reached. The pencil and subgraph trackers are capable of tracking two interaction devices with each 30 features with a latency below 16 ms.

- *Robustness*
  The results show that the subgraph tracker is less robust against image noise than the ICP and pencil trackers. The subgraph tracker uses stereo correspondence to transform the 2D image points to 3D, requiring features corresponding to the same 3D marker to be visible in both cameras. The pencil tracker is able to recognize line pencils in 2D, making it less sensitive to occlusion. The ICP method iteratively refines an initial pose estimate by projecting the model points to 2D and fitting these to the data points. As such, noisy data points have the least influence on the robustness of the method.

  For the same reasons, the subgraph tracker suffers most from occlusion. The pencil tracker is significantly more robust against occlusion than the ICP tracker. The line features used by the pencil tracker can be partially occluded, as long as an arbitrary point on the line and its direction can still be obtained. Note that occlusion robustness of the ICP and pencil trackers depends on camera placement. Since the cameras were placed close together to allow the subgraph tracker to use stereo correspondence, the ICP and pencil trackers did not benefit from the fact that they do not require the same feature to be visible in multiple cameras. As such, the differences between the subgraph tracker and the other trackers are expected to increase for different camera placement.

  The data shows that the influence of camera calibration errors is largest for the ICP tracker. This method relies on an accurate description of the camera parameters for back-projection. The subgraph and ICP trackers are not robust against focal length perturbations of more than 1.5% of its nominal value. Similarly, if the extrinsic parameters are perturbed by more than 1 degree for camera orientation or 2.5 mm for camera position, the subgraph and ICP trackers are not robust.

Choosing a Tracking Method

Each of the tracking methods investigated in this chapter behaves differently under given circumstances. Each method has its own advantages and disadvantages. The choice of a tracking method depends on a number of factors, and the importance of these factors depends on the virtual environment and the types of objects that are to be tracked. In Chapter 1, the following requirements for an optical tracking system for rigid interaction devices were defined:

- *Accuracy*
  Results show that the subgraph and ICP trackers provide more accurate pose estimates than the pencil tracker. However, if the image noise is low and camera calibration is accurate, the pencil tracker also provides reasonably accurate results.

- *Latency*
  The subgraph and pencil tracker both maintain frame rates of over 90 fps. The ICP tracker is able to reach frame rates of 60 fps, but suffers from large discontinuities in cases when a reasonable initial pose cannot be determined. This makes the ICP tracker impractical for use as an optical tracking method in a virtual environment.

	Subgraph	Pencil	ICP
Accuracy	++	+	++
Latency	++	++	--
Robustness	-	++	--
Generic shape	++	--	++
Rapid development	++	--	++

Table 5.5: A summary of the characteristics of different tracking methods.

- *Robustness*
  The pencil tracker is significantly more robust against image noise, occlusion, and camera calibration errors than the other tracking methods.
- *Generic device shape*
  The pencil tracker does not allow for devices of arbitrary shape to be tracked, as it requires planar pencils to be attached to the input device. The subgraph and ICP trackers can handle arbitrary shaped objects.
- *Rapid development of devices*
  Devices for use with the pencil tracker are more difficult to construct than the devices for the subgraph and ICP trackers. The markers have to be accurately attached to a device surface, such that the lines of a pencil intersect at a common point. On the other hand, the markers of devices for the subgraph and ICP trackers can be easily attached.

Table 5.5 summarizes the results of each tracking method with respect to the tracking criteria. It can be seen that the subgraph tracker performs best when all categories are considered. However, it depends on the virtual environment how much weight should be given to each factor.

Since the aim of the research in this thesis is to develop an optically tracked configurable interaction device, generic device shape and rapid development are important factors. The subgraph tracker is the most flexible tracking approach, providing easy construction of input devices of arbitrary shape, while being accurate and fast. Although the other trackers are more robust against partial occlusion, this problem could be reduced by adding more markers to the device or using more cameras.

5.5 Conclusion

In this chapter, three model-based optical tracking methods were compared. It was demonstrated how different error sources influence the relative accuracy, latency, and robustness of each method. Furthermore, an error model for accuracy was developed, which can be used to analyze the influence of the error sources.

The results show that each of the methods has its advantages and disadvantages. The subgraph tracker is fast and accurate, but suffers more from occlusion than the ICP and pencil trackers, and is sensitive to camera calibration errors. However, the method is more robust against partial occlusion than pattern-based approaches that need to be able to see a complete pattern.

The ICP tracker is better suited to handle partial occlusion than the subgraph tracker, but is slow and more sensitive to camera calibration errors. The pencil tracker is most robust against camera calibration errors and occlusion, but is slightly less accurate and less flexible with respect to rapid development of devices and the device shape.

Since none of the approaches provides an ideal tracking solution, the choice of tracking method depends on which factors are considered most important for a given virtual environment.

Chapter 6

Analysis of Orientation Filtering and Prediction

"*In my opinion, end-to-end system latency is still the most serious technical shortcoming of today's VR systems.*"

Frederick P. Brooks, Jr., 1999 [Bro99]

The previous chapters described and evaluated various optical tracking methods to determine the pose of interaction devices. As discussed in Chapters 2 and 5, two commonly encountered effects in a virtual environment are noise and latency. Any tracking technology introduces measurement noise in the pose estimate. This generally results in visible jitter in the virtual representation of a tracked object. Latency, or lag, is defined as the difference in time between a user performing an action and the feedback of the system reaching the user. This results in a virtual representation lagging in position compared to a tracked object.

Predictive filtering is a common approach to reduce noise and predict the position and orientation of rigid objects in order to compensate for latency in a VR system. Various prediction algorithms have been proposed [AB94, WO00]. However, most previous work only compares the proposed method to doing no prediction at all and only test limited combinations of parameters. How to choose a suitable prediction method for a given virtual environment is a problem that has not received much attention. There is no guideline that identifies the parameters that influence a filter's performance, the extent of this influence, and that evaluates the performance of different filtering methods within a VR/AR context.

In this chapter, a framework for predictive filtering algorithms is presented, which is an extension to the interaction cycle presented in Chapter 1. The framework is used to identify the parameters that influence filter performance. Using this framework, a systematic evaluation and comparison of various predictive filtering methods is performed, and the effect of each of these parameters is studied. The parameters that are studied are measurement noise, sampling frequency, motion model, prediction time, and input signal characteristics. The input signals were chosen from various common hand manipulation tasks and synthetic signals. The study focusses on filtering of orientation data, since these require filtering methods suited for non-linear motion models. Filtering position data can be achieved using a linear kinematics model, for which the Kalman filter provides the optimal Bayesian filtering solution [May79].

This chapter is organized as follows. In Section 6.1, related work on filtering and prediction in virtual reality is reviewed. Section 6.2 presents a framework that is used to identify critical filtering parameters, and discusses the motion models used for prediction. In Sections 6.3 and 6.4, the filtering methods included in the analysis are discussed, as well as the methods used for tuning the filtering parameters. Section 6.5 describes the test procedure.

In Section 6.6, the results of the analysis are given. Finally, Sections 6.7 and 6.8 provide a discussion and conclusions.

6.1 Previous Comparisons

Predictive tracking has received much attention in VR and AR. However, comparison studies are more limited, and so far have only studied a subset of the parameters involved.

Azuma and Bishop [AB94] developed a tracking system using inertial sensors mounted on a Head Mounted Display. They used an extended Kalman filter (EKF) and compare two motion and measurement models, with and without inertial measurements. Most parameters that influence prediction performance were fixed. They reported inertial measurements improved accuracy up to three times.

Wu and Ouhyoung [WO00] compared three prediction algorithms for head motions, using the same data sets as [AB94]. They did not include inertial measurements and performed their analysis using two prediction times. The algorithms in the comparison were an EKF, an extrapolator and a grey system theory-based predictor. They found that the EKF and grey system theory-based predictor performed significantly better than a method with no prediction.

A comparison between an EKF and an unscented Kalman filter (UKF) for orientation prediction was made by LaViola [LaV03]. The prediction time and sampling frequency was varied, no inertial measurements were included and the measurement noise was not varied. Two data sets were used: a hand and a head motion data set. No significant performance differences between the EKF and UKF were found.

Chai et al. [CNHV99] compared a multi-modal approach with a standard EKF. Multi-modal approaches involve using various system models and selecting the best one or calculating the best combination for a more accurate estimate. They used two models for the system dynamics and select the best one, allowing for variations in the expected motion characteristics. They reported a modest performance improvement over the best non-adaptive estimator.

Emura et al. [ET98] suggested two methods for latency compensation, by integrating a magnetic tracker and a gyro sensor, and compare both methods. They reported an accuracy improvement using the hybrid approach.

The goal of this chapter is to supplement these results by comparing relevant filtering methods for a wide spectrum of parameters, using both experimental and synthetic data sets.

6.2 Filter Parameters

6.2.1 Framework

In this section, a framework for comparing predictive filtering algorithms in a VR/AR setting is presented, which is an extension of the interaction cycle as presented in Chapter 1 (see Figure 1.1). It only applies to Bayesian filters, and its purpose is to identify critical parameters, rather than to provide a complete framework for filtering in general.

A general, two-layered framework of predictive filtering is used, as shown in Figure 6.1. The top layer shows a similar model of end-to-end delays as presented in [Min93] and used in Chapter 5. In the model, a user performs an action at time t_1, which is described by a

state vector $\mathbf{x}_k$. The user's action is registered by a tracking system, which samples with a frequency f_s and introduces measurement noise N_z. This results in an approximation of the true signal $\mathbf{x}_k$, to which is referred as the measurement $\mathbf{z}_k$. Next, the system analyzes and evaluates the data, calculates an appropriate response, and updates simulation tasks. The result is fed back to the user through a display system at time t_2. Time $t_2 - t_1$ is the end-to-end delay or latency of the system, for which is to be compensated by prediction.

The second layer in Figure 6.1 shows the filtering and prediction stage, which takes place in the interaction cycle between the tracking and evaluation stages. Filtering consists of three stages. First, the state estimate of the last frame $\hat{\mathbf{x}}_{k-1}$ is propagated in time using a motion model and sampling time $\frac{1}{f_s}$. Second, this initial estimate of the state $\tilde{\mathbf{x}}_k$ is related to an estimate of the measurement $\tilde{\mathbf{z}}_k$ by means of a measurement model. Finally, the measurement estimate $\tilde{\mathbf{z}}_k$ and the actual measurement $\mathbf{z}_k$ are used to obtain a correction of the initial state estimate, which results in the final state estimate $\hat{\mathbf{x}}_k$. The last stage is then to predict the state at time $t_k + t_{pred}$, where ideally t_{pred} should be equal to the end-to-end delay of the system $t_2 - t_1$. In this work, this delay is considered to be a parameter. In the next sections, these parameters are discussed in more detail.

6.2.2 Bayesian Filter Parameters

The most practical and most widely used class of stochastic filters is the class of Bayesian filters. Bayesian filters are based on the assumption that the signal and noise have certain stochastic characteristics, and are usually theoretically optimal in a sense of minimizing a cost function, under a set of assumptions about the system properties.

Bayesian filters are based on propagating the probability density in a recursive manner through the application of Bayes' rule. The object dynamics are modeled as a Markov process, which means that

$$p(\mathbf{x}_k|\mathbf{x}_{1:k-1}) = p(\mathbf{x}_k|\mathbf{x}_{k-1}) \tag{6.1}$$

where $\mathbf{x}_{1:k-1} = (\mathbf{x}_1, \mathbf{x}_2, \ldots, \mathbf{x}_{k-1})$. In other words, the process state is conditioned only on the previous state and independent of earlier history. This allows for a state representation of the process by means of a *motion model*

$$\mathbf{x}_k = \mathbf{f}_k(\mathbf{x}_{k-1}, \mathbf{w}_{k-1}) \tag{6.2}$$

where $\mathbf{x}_k$ is the process state at time t_k, $\mathbf{f}_k$ is a (linear or non-linear) function mapping the previous state to the current state, and $\mathbf{w}_k$ represents the process noise. To relate the system state to the measurement generated by the tracking system, a *measurement model* is used, which is given by

$$\mathbf{z}_k = \mathbf{h}_k(\mathbf{x}_k, \mathbf{v}_k) \tag{6.3}$$

where $\mathbf{z}_k$ is the measured state of the process at time t_k, $\mathbf{h}_k$ is a function mapping the state of the system $\mathbf{x}_k$ to the measured state $\mathbf{z}_k$, and $\mathbf{v}_k$ represents the measurement noise. The motion model basically models the user's action, whereas the measurement model is used to model the tracking stage. The combination of motion and measurement models is denoted as *system model*. The noise parameters $\mathbf{w}_k$ and $\mathbf{v}_k$ in Equations 6.2 and 6.3 are tuning parameters. These parameters determine how much the filter 'trusts' the motion model compared to the measurements.

The goal of filtering can be stated as finding estimates $\hat{\mathbf{x}}_k$ of the original states $\mathbf{x}_k$ given $\mathbf{z}_{1:k}$, the set of measurements up to time t_k. This requires the calculation of the probability

State Vectors		Parameters			
		Input		**System**	
$\mathbf{z}_k$	*Measurement*	$\mathbf{x}_t$	*Input signal*	t_{pred}	*Prediction time*
$\tilde{\mathbf{x}}_k$	*Initial state estimate*	**Filter**		f_s	*Sampling frequency*
$\tilde{\mathbf{z}}_k$	*Measurement estimate*	F_k	*Motion model*	N_z	*Measurement noise*
$\hat{\mathbf{x}}_k$	*State estimate*	H_k	*Measurement model*		
$\hat{\mathbf{x}}_{t_k+t_{pred}}$	*Predicted state estimate*	$Pred_i$	*Predictive filtering algorithm*		

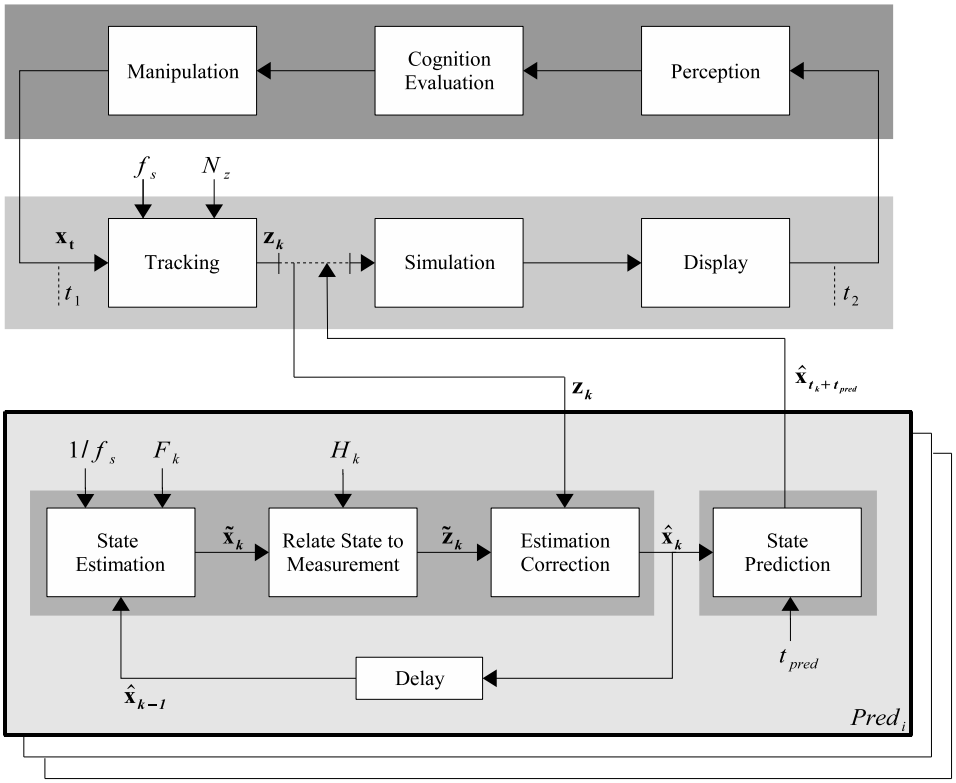

Figure 6.1: Framework for Bayesian predictive filtering algorithms in VR/AR. Defines critical parameters that affect performance.

density function $p(\mathbf{x}_k|\mathbf{z}_{1:k})$. Given a Markov chain with independent measurements, the probability density at time t_{k-1} is defined by $p(\mathbf{x}_{k-1}|\mathbf{z}_{1:k-1})$. This value can be propagated using

$$p(\mathbf{x}_k|\mathbf{z}_{1:k}) = c_k\, p(\mathbf{z}_k|\mathbf{x}_k)\, p(\mathbf{x}_k|\mathbf{z}_{1:k-1}) \tag{6.4}$$

where $c_k = 1/p(\mathbf{z}_k|\mathbf{z}_{1:k-1})$ is a normalization constant independent of $\mathbf{x}_k$ and

$$p(\mathbf{x}_k|\mathbf{z}_{1:k-1}) = \int p(\mathbf{x}_k|\mathbf{x}_{k-1})\, p(\mathbf{x}_{k-1}|\mathbf{z}_{k-1}) d\mathbf{x}_{k-1} \tag{6.5}$$

Here, $p(\mathbf{x}_k|\mathbf{z}_{1:k})$ is commonly referred to as the posterior density, $p(\mathbf{x}_k|\mathbf{z}_{1:k-1})$ as the prior density, $p(\mathbf{z}_k|\mathbf{x}_k)$ as the likelihood, and $p(\mathbf{x}_k|\mathbf{x}_{k-1})$ as the transition density. Equations 6.4 and 6.5 are an application of Bayes' law and give a recursive way to propagate the posterior density. Bayesian filtering can thus be seen as a two-stage process, a *prediction step* of the new state by the system model defined by Equations 6.2 and 6.3, and an *update step* where the prediction is modified by the new measurement, using Equations 6.4 and 6.5.

Generally however, no analytical solution exists for this optimal Bayesian filtering problem. For a more extensive introduction to Bayesian filtering, the interested reader is referred to [May79].

6.2.3 Motion Models

Consider a pose estimate expressed in Euler angles θ_i (yaw, pitch, roll). The time rate of change of the Euler angles can be modeled using the differential equations

$$\dot{\theta} = \begin{bmatrix} 0 & \sin\theta_3 \tan\theta_2 & \cos\theta_3 \tan\theta_2 \\ 0 & \cos\theta_3 & -\sin\theta_3 \\ 1 & \sin\theta_3 \sec\theta_2 & \cos\theta_3 \sec\theta_2 \end{bmatrix} \begin{bmatrix} \omega_1 \\ \omega_2 \\ \omega_3 \end{bmatrix} \tag{6.6}$$

where $\sec\theta_2 = \frac{1}{\cos\theta_2}$, and ω_i represents the angular velocity. This equation makes it possible to integrate the Euler angles as functions of time. However, the term $\sec\theta_2$ becomes infinite at $\theta_2 = \{\pi/2, 3\pi/2\}$, which is usually referred to as a kinematic singularity. Although it is possible to circumvent this problem, a more convenient approach is to express orientation by using a quaternion representation. The equivalent of Equation 6.6 that computes the derivative of the quaternion q used to represent orientation becomes

$$\dot{q} = \frac{1}{2}(q\omega) \tag{6.7}$$

The orientation state vector is expressed as

$$\mathbf{x}_k = \{q_w, q_x, q_y, q_z, \omega_1, \omega_2, \omega_3\} \tag{6.8}$$

where $q = \{q_w, q_x, q_y, q_z\}$ represents the orientation, and the quaternion $\omega = \{0, \omega_1, \omega_2, \omega_3\}$ represents angular velocity. By assuming a constant angular acceleration $\dot{\omega}$, the solution to this differential equation can be found as

$$q(t_1) = q(t_0)\exp(\Omega) \tag{6.9}$$

where the exp function denotes the quaternion exponentiation, and Ω is the time integral of ω, $\Omega = \{0, \frac{1}{2}\Omega_1, \frac{1}{2}\Omega_2, \frac{1}{2}\Omega_3\}$, where

$$\Omega_k = \int_{t_0}^{t_1} \omega_k dt = \omega_k(t_0)\Delta t + \frac{1}{2}\dot{\omega}_k(t_0)\Delta t^2 \qquad \text{for } k \in \{1, 2, 3\} \tag{6.10}$$

Note that if angular acceleration measurements cannot be obtained, the term after $\omega_k(t_0)\Delta t$ can be neglected.

Equation 6.9 shows that the system model for orientation is nonlinear. Since the nonlinear Bayesian filters have different assumptions, it is unclear which is most suitable for orientation filtering and prediction. Whether one filter has better performance than another depends on the noise characteristics and on how well a user's motions lend themselves to linearization.

Two system models are included in the analysis

- Motion model based on orientation measurements only (MM).
- Motion model using orientation and angular velocity measurements (MMI).

Since the MM model only incorporates orientation measurements, the state vector $\mathbf{x}_k$ only contains quaternion and angular velocity components (the term after $\omega(t_0)\Delta t$ in Equation 6.9 is ignored). The MMI model also includes angular velocity measurements from inertial sensors, which results in a state vector $\mathbf{x}_k$ extended with angular acceleration components. The measurement equation is simply a normalization of the quaternion part of the state vector $\mathbf{x}_k$, leaving out the highest derivative for both models.

6.3 Filter Methods

In this section, the various filters included in the analysis are described in more detail.

LTI Filter

Linear time-invariant (LTI) filtering is a fundamental technique in signal processing and has been used in a wide range of applications. It can be used to perform low-pass filtering that suppresses Gaussian noise, based on the implicit assumption that the signal and noise occupy separate frequency bands, although some overlap is allowed.

An important class of LTI filters is derived from the binomial distribution. These filters are low-pass finite impulse response filters that suppress Gaussian noise. The odd-sized filter of length N is described by

$$y(n) = \sum_{k=0}^{N-1} c_k x(n-k) \tag{6.11}$$

where the filter coefficients c_k are given by

$$c_k = \frac{1}{2^{N-1}} \binom{N-1}{k} = \frac{1}{2^{N-1}} \frac{(N-1)!}{(N-k-1)!k!} \tag{6.12}$$

Note that these factors are binomial coefficients. Since for large N the binomial distribution is a close approximation of the Gaussian distribution, the binomial coefficients are often used to approximate the ideal Gaussian filter.

The main problem with the design of an LTI filter for orientation filtering is that the orientation data should be transformed to a linear vector space. In this case, a conventional filter mask may be applied to the vector data, and the resulting vector can be transformed

back into orientation space. This scheme is described in detail in [LS00b]. The key is to express orientations as quaternions, and to define a three-dimensional vector

$$\omega_i = \log(q_i^{-1} q_{i+1}) \tag{6.13}$$

which represents the angular velocity of the motion that starts at q_i towards q_{i+1} [Sho85].

The resulting filtering algorithm is as follows:

1. Compute

$$a_k = \begin{cases} -\sum_{i=0}^{k} c_i & 0 \leq k \leq M \\ \sum_{i=k+1}^{N-1} c_i & M < k < N-1 \end{cases} \tag{6.14}$$

   where $M = \frac{N-1}{2}$, and c_i are the conventional filter coefficients.

2. Compute the filter response

$$y(n) = q_n \exp(\sum_{k=0}^{N-1} a_k \omega_{n+k-M}) \tag{6.15}$$

   where the exp function denotes the quaternion exponentiation and where ω_i is obtained from Equation 6.13.

An orientation filter that performs well in practice [LS00b] is obtained by using the Binomial filter coefficients given in Equation 6.12. Setting N to 5, the resulting filter kernel is given by $c_k = (\frac{1}{16}, \frac{4}{16}, \frac{6}{16}, \frac{4}{16}, \frac{1}{16})$. Substituting these values into Equation 6.14, the orientation LTI filter is derived from Equation 6.15 as

$$y(n) = q_n \exp(\frac{1}{16}(-\omega_{n-2} - 5\omega_{n-1} + 5\omega_n + \omega_{n+1})) \tag{6.16}$$

The LTI filter is adapted for prediction by adding a subsequent prediction step, which uses the same motion model as used by the Bayesian filters. Note that the filter itself introduces extra lag. This lag is compensated by predicting an extra time interval. The angular velocity is estimated by running an averaging filter over the filtered quaternions, with the history length as a tuning parameter. Advantages of the LTI filter with respect to the Bayesian filters are that it does not require complicated tuning procedures and it is easier to implement.

Non-Linear Kalman Filters

A filter that has received wide attention and has been applied in a large number of fields with great success is the Kalman filter. The Kalman filter calculates the optimal Bayesian filtering solution by minimizing the expected minimum square error, given certain assumptions. The first assumption is that the process to be filtered is a linear process, which implies that the functions $\mathbf{f}_k(\mathbf{x}_{k-1}, \mathbf{w}_{k-1})$ and $\mathbf{h}_k(\mathbf{x}_k, \mathbf{v}_k)$ in Equations 6.2 and 6.3 are linear functions. The second assumption is that the process and measurement noise $\mathbf{w}_k$ and $\mathbf{v}_k$ are gaussian and white and the posterior density is Gaussian at every time step. As a consequence, $p(\mathbf{x}_k|\mathbf{z}_{1:k-1})$ and $p(\mathbf{x}_k|\mathbf{z}_{1:k})$ can be fully described by their mean and covariance.

The most common algorithm for orientation prediction in VR is the extended Kalman filter (EKF) [AB94]. It is an extension to the Kalman filter to handle non-linear system models.

The EKF represents the state distribution by a Gaussian random variable and propagates it analytically through a first-order linearization of the system model Equations 6.2 and 6.3 about the current mean and covariance. The linearization is obtained using the Taylor expansion of the non-linear functions $\mathbf{f}_k$ and $\mathbf{h}_k$.

Using this formulation, the extended Kalman filter becomes a trivial variation of the standard Kalman filter. Although successful, it's a crude method where the distributions of the random variables are no longer gaussian after the linearization, and it provides only a first-order linearization of the system model. This can introduce errors in the true posterior mean and covariance of the state distribution, such that the EKF may be suboptimal and may even diverge.

Julier and Uhlman [JU97] have proposed the unscented Kalman filter (UKF), which represents the Gaussian random variable used for the state distribution by a set of carefully chosen sample points. These sample points completely describe the mean and covariance of the Gaussian random variable. After propagation through the system model equations, the sample points give a posterior mean and covariance accurate to the 3rd order. To analyze the effect of the first-order linearization of the EKF, the UKF is also included in the analysis.

Particle Filter

All Kalman-based filters assume that the posterior density $p(\mathbf{x}_k|\mathbf{z}_{1:k})$ can be described by a Gaussian random variable. For systems with non-Gaussian noise, a popular and relatively new method is particle filtering, which is a sequential Monte Carlo technique.

The idea is to approximate the posterior density function $p(\mathbf{x}_k|\mathbf{z}_{1:k})$ as a finite number of samples and propagate these over time, in contrast to the assumption of the Kalman filters that the probability density is gaussian and only propagate the mean and covariance. Since generally the posterior density cannot be sampled directly, every time step samples are taken from a proposal distribution $\pi(\mathbf{x}_k^i|\mathbf{x}_{k-1}^i, \mathbf{z}_{1:k})$. The posterior density can then be represented by $(\mathbf{x}_k^i, \omega_k^i)$, i=1, ..., N, where the weights ω_k^i are calculated as

$$\omega_k^i = \omega_{k-1}^i \frac{p(\mathbf{z}_k|\mathbf{x}_k^i)\, p(\mathbf{x}_k^i|\mathbf{x}_{k-1}^i)}{\pi(\mathbf{x}_k^i|\mathbf{x}_{k-1}^i, \mathbf{z}_{1:k})} \tag{6.17}$$

and normalized by

$$\omega_k^i = \frac{\omega_k^i}{\sum_{j=1}^N \omega_k^i} \tag{6.18}$$

The estimate is then evaluated using

$$E[f(\mathbf{x}_k)] = \sum_{i=1}^{N} \omega_k^i f(\mathbf{x}_k^i) \tag{6.19}$$

where $f(x) = x$ if one is interested in the mean state.

The choice of the importance sampling function $\pi(\mathbf{x}_k^i|\mathbf{x}_{k-1}^i, \mathbf{z}_{1:k})$ is crucial to the performance of the particle filter algorithm, and a poor choice of this function leads to poor performance. Indeed, the best choice for the importance sampling function would be the posterior distribution itself. Many variants of particle filtering exist and the choice of the importance sampling function is still an active topic in research. One proposition is the optimal

proposal distribution [DGK01], which minimizes the variance of the weights ω_k^i. In practice, however, finding the optimal proposal is complicated if not impossible. Other methods include the auxiliary particle filter [PS99] and the use of a separate unscented Kalman filter for each particle to generate and propagate the Gaussian proposal distribution [MDFW00]. An alternative choice for the importance sampling function is to simply use the prior, i.e. $\pi(\mathbf{x}_k^i|\mathbf{x}_{k-1}^i, \mathbf{z}_{1:k}) = p(\mathbf{x}_k|\mathbf{x}_{k-1}^i)$. This has the advantage that the importance weights are easily evaluated and therefore the importance density is easily sampled, but the function does not include information about the measurements and can therefore be inefficient and sensitive to outliers. However, its simplicity makes it a popular choice of importance sampling function. This approach is followed by for instance the condensation algorithm [IB98]. For more information on particle filtering, the reader is referred to [GSS93, AMGC02, Dou98].

The main drawback of particle filtering techniques is the computational cost. As any Monte Carlo technique, it requires a large number of samples to perform well, making it computationally expensive.

The particle filter is included in the analysis as a benchmark filter, which theoretically should provide the best results given identical system models. The distribution of each particle is approximated as a Gaussian and a non-linear Kalman filter for their propagation is used. For propagation of the particle distribution, both an EKF and an UKF were used, resulting in an extended and unscented particle filter [MFDW01].

Other Filters

A well-known filter that falls into the category of probabilistic filters is the Wiener filter, which is optimal under the assumptions that the signal and noise are stationary random processes, the filter is a time-invariant linear device operating on an infinite amount of data, and the criterium for optimality is the minimum mean square error [Wie49].

The Wiener filter can be shown to be equivalent to the steady state Kalman filter in the case of a time-invariant system model and stationary noise [May79]. Although the Wiener filter has been extended to lift its original restrictions, the computational requirements become high. As such, the Wiener filter has not been included in this analysis.

Other filters such as grid-based filters are not very useful for a virtual reality environment. Grid-based filters can lead to accurate results, but are complex in implementation and too computationally expensive to be of practical use in a VR environment.

6.4 Filter Tuning

The Bayesian filters have two tuning parameters: the characteristics of the measurement noise v_k and the process noise w_k (see Section 6.2.2). These are modeled as Gaussian noise, such that v_k and w_k can be described by $\mathcal{N}(0, R_k)$ and $\mathcal{N}(0, Q_k)$, respectively. By assuming a time-invariant system, R and Q become time-invariant, such that they can be determined off-line.

6.4.1 Measurement Noise Analysis

The measurement noise covariance R is determined as follows. First, an interaction device is placed at a stationary location within the tracking volume. The tracking system collects samples of the pose of the device. Next, R is determined by measuring the variance of these

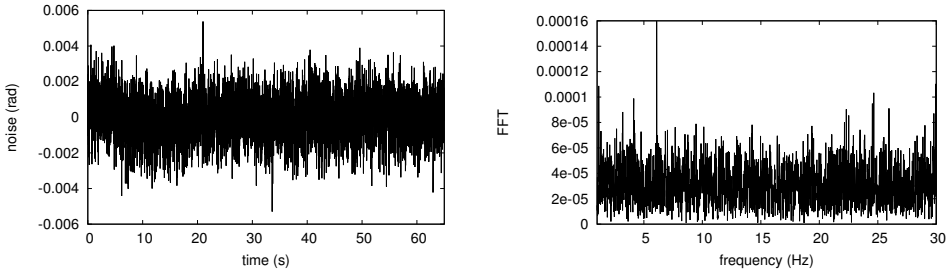

(a) (b)

Figure 6.2: Measurement noise analysis. (a) Quaternion component of the orientation measurement noise, with the interaction device at a stationary location, (b) The corresponding frequency spectrum.

samples from their mean. The noise characteristics can be verified to be white and Gaussian. This can be done by performing a Fast Fourier Transform (FFT) to determine the frequency spectrum, and by comparing the cumulative distribution function (cdf) of the measurement noise by the ideal cdf of a Gaussian random variable with deviation R.

This analysis has been performed for the measurement noise of the optical tracking method of the PSS as presented by [LM03] (see Section 2.4.2). As an example, Figure 6.2(a) depicts the measurement noise of one of the quaternion components of the orientation. The variance was determined to be approximately $1 \cdot 10^{-6}$. Figure 6.2(b) gives the corresponding frequency spectrum as determined by the FFT. It can be seen that the measurement noise is approximately white.

The orientation measurement noise of Figure 6.2 was verified to be Gaussian by determining its cdf. The result is plotted in Figure 6.3. The figure compares the measured cdf with the ideal cdf of a Gaussian random variable with deviation R. Clearly, the measurement noise can be accurately represented by a Gaussian random variable. Similar results were obtained for the other quaternion components and for the position measurement noise.

The noise characteristics in this analysis may not be accurate for a non-stationary device. For an optical tracker, the amount of noise depends on the distance of the device to the cameras. A moving device may result in motion blur and quantization effects that influence noise characteristics. An analysis of these effects is beyond the scope of this work.

6.4.2 Process Noise Analysis

The process noise covariance Q models the uncertainty in the motion model and the user's intentions. Prediction of the future position and orientation of an interaction device can only be made over relatively short time periods. Determining the process noise covariance Q is generally more difficult than determining the measurement noise covariance R as it is impossible to directly observe the process that is to be estimated. Any technology used to measure the motions of a user introduces measurement noise.

In practice, tuning Q is typically performed in an off-line procedure. Often the assumption is made that the components of the state vector are independent, such that the process

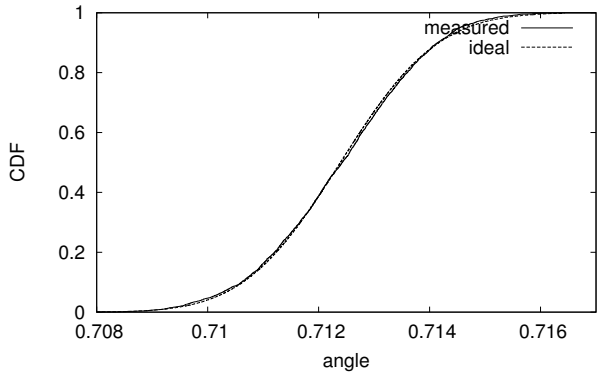

Figure 6.3: Cumulative distribution function of the orientation measurement noise.

noise covariance matrix Q is diagonal. For the orientation state vector of Equation 6.8 this implies that orientation and angular velocity must be independent. In this case, Q can be described by 7 parameters, which can be further reduced to 2 parameters by assuming that the quaternion components and the angular velocity components are identical.

In case the process to be estimated can be observed directly such that a reference signal can be obtained, the process noise covariance Q can be determined using a non-linear optimization routine that optimizes the filter's output to match the reference signal.

6.5 Test Procedure

6.5.1 Signal characteristics

Experimental versus Synthetic Motion Data

A filter and prediction comparison can be performed on experimental or synthetic motion data. Since the goal of this work is to evaluate performance in a VR context, motion data of typical VR tasks is needed. The easiest way to obtain such data is through a series of experiments, where users are asked to perform some task while their movements are recorded. The main problem with this approach is that the original signal is unknown, as only noisy measurement data is available. It is possible to clean up the data to some extent and use this as a reference signal, but this needs great care to avoid introducing false signal characteristics or removing true ones.

An alternative would be to use a setup that can generate a known and controllable motion. For instance, a pendulum could be used to generate a motion with accurately known characteristics. By equipping this pendulum with markers, filtered pose estimates from the tracking system can be compared to the motion of the pendulum. However, the resulting motion characteristics do not model hand motions in VR tasks. Furthermore, they are highly repetitive, such that the Bayesian filtering methods converge towards steady-state.

Another approach would be to use synthetic signals. However, it is extremely difficult to model the exact characteristics of hand motions encountered in VR tasks. A filter comparison, using synthetic signals that have little in common with the signals encountered during a typical VR interactive session, would say little about performance in a VR context.

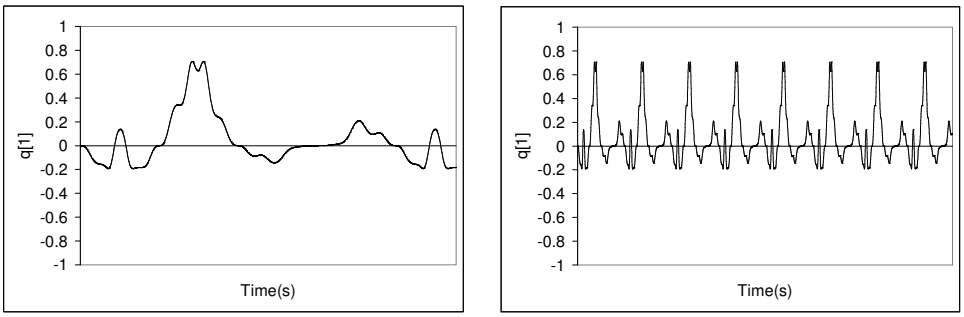

Figure 6.4: Synthetic signals, (a) $\omega = 0.3$. (b) $\omega = 2$.

As neither of these approaches is perfect, both analyses are performed and related to each other.

Synthetic Study

The synthetic signals should contain the most important characteristics of the data sets in the experimental study. Analyzing these characteristics accurately requires an extensive study on human hand anatomy, muscle capabilities and response times, VR tasks, and so on. Analyzing experimental data revealed that the hand motion data contains either smooth orientation changes or comprises two stages: a high angular velocity stage where the object is roughly placed into the correct orientation, and a higher precision low velocity stage. These two important characteristics have been incorporated into the synthetic signals. The resulting signal is given (in degrees) by

$$\begin{aligned} A &= 40\sin(\frac{1}{2}\omega t) + 40 \\ S &= A(\sin(\omega t) - \frac{1}{3}\sin(3\omega t) + \frac{1}{5}\sin(5\omega t) - \frac{1}{7}\sin(7\omega t)) \end{aligned} \tag{6.20}$$

where A represents a simple amplitude modulation. Parameter ω controls the speed of the motions, and is chosen as 0.3, 2, and 10. These values are chosen such that the angular velocities and velocity changes roughly match the ones from the docking and object exploration tasks ($\omega = .3$ and 2) as defined in the next section, and a much faster signal to test the filters under more complex circumstances ($\omega = 10$). The signals are interpreted as Euler angles and converted to quaternion reference signals. Figure 6.4 shows a plot of the x-components of the quaternions of the synthetic signals for $\omega = 0.3$ and 2.

Experimental Study

The signals for the experimental study are obtained by performing a number of representative VR/AR hand manipulation tasks. Head movements have already been studied by others, e.g. [AB94, WO00]. The optical tracking system of the PSS was used to record the experiments. The tracking method that is based on projection invariant properties of point patterns was used, as presented by van Liere et al. [LM03] (see Section 2.4.2). The experiments were

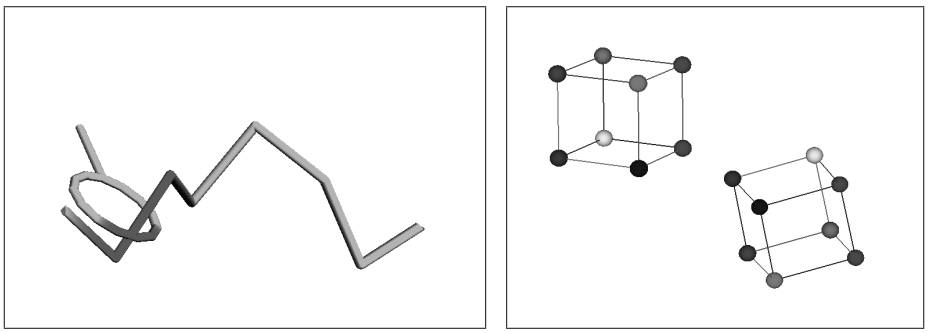

(a) (b)

Figure 6.5: Screenshot of two experiments. (a) Tracing task. The goal is to trace the contour with the ring, without the contour and ring colliding at any point. The ring is manipulated using a cube-shaped interaction device. (b) Docking task. The goals is to dock the left cube, which is manipulated using the same interaction device, into the target cube on the right.

performed using a cubic interactive device. In order to obtain angular velocity measurements, the device was also equipped with an inertial measurement unit, the Xsens MT9 [XSE]. The unit communicates through RS-232 and provides access to its gyroscopes.

Complex hand manipulation tasks are commonly regarded as combinations of four basic tasks [BKLP01]: selection, manipulation, navigation and system control. The following hand tasks were performed, which represent the motions of the basic tasks:

- *Selection*
  A target sphere is drawn at a random location. At the location of a cubic-shaped interaction device a source sphere is drawn. The goal is to place the source sphere over the target sphere. If the task is completed, the target is highlighted, after which the user presses a pedal to repeat the experiment.

- *Tracing*
  A contour is plotted and the user controls a ring with the interaction device. The user has to trace the contour with the ring, without the ring and contour colliding. This experiment is shown in Figure 6.5(a).

- *Docking*
  A target box is drawn with a random orientation. The box is drawn with differently colored spheres at the corners. An identical box is drawn with the same position and orientation as the interaction device. The goal is to align the source and target boxes. If the task is completed, the target is highlighted and the user presses a pedal to repeat the experiment. A screenshot of this experiment is given in Figure 6.5(b).

- *Object exploration*
  A cube is drawn with the same position and orientation of the input device. Each side of the cube has a different color. The goal is to orient the cube such that the side with a randomly given color faces the user, after which a pedal is pressed and the experiment repeated.

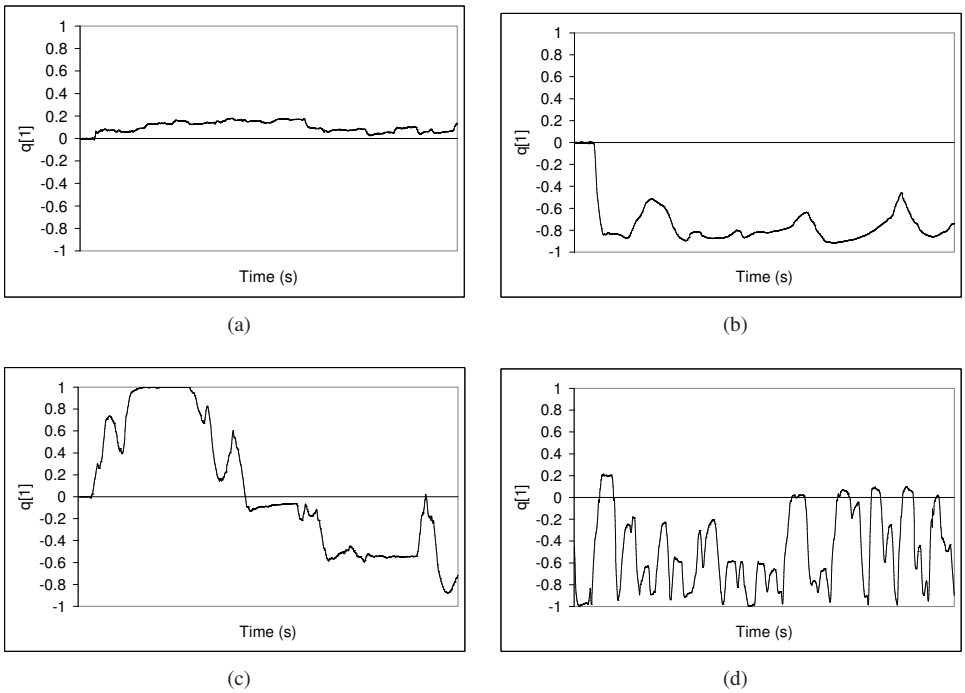

Figure 6.6: Experimental input signals. (a) selection, (b) tracing, (c) docking, (d) object exploration.

Each task was performed a number of times by one user with VR experience. Since the resulting signals are used as input to the filters, task completion times and success rates are not relevant. Each data set is cut to 50 seconds in length. As an example, the x-components of the quaternions are shown in Figure 6.6. The selection task produces a signal with a small range of orientations, where the orientation changes fast when changing selections and is practically constant in between. The tracing task produces a slightly more complex signal with a larger range of orientations and angular velocities. The docking task produces the entire range of orientations and a mix of high and low angular velocities. The signal clearly demonstrates a fast initial orientation change, followed by the slow more precise task of the final docking procedure. The object exploration task also shows the entire range of orientations and the largest angular velocities and accelerations. Comparing these signals with the head motion data sets from [AB94], it can be concluded that these hand tasks result in a larger range of signal characteristics.

Obtaining a Reference Signal

To be able to compare the performance of the prediction methods, the true signal is needed. Since this signal is not available for an experimental study, the approach of Azuma was followed [Azu95]: a high order non-causal low-pass filter was applied to the measured signal to obtain a reference or "ground truth" signal. The filter is carefully tuned to filter out most of the measurement noise, while keeping the original signal characteristics in tact. It was

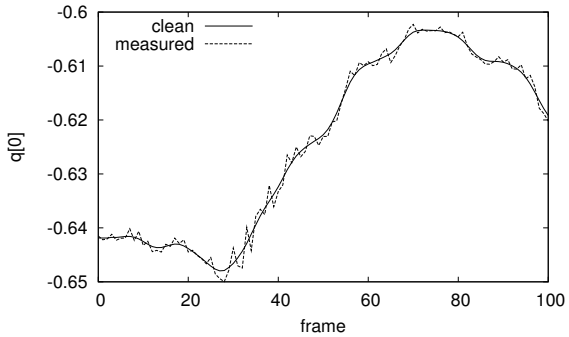

Figure 6.7: Results of the non-causal low-pass filter that is used to obtain a reference signal.

informally observed that higher frequency components in the original signal practically never exceed 10 Hz. Although the resulting reference signal may still contain a small amount of sensor noise, this noise is brought to a minimum. Moreover, it is virtually impossible to discriminate between lower frequency sensor noise and normal hand jittering. To examine the influence of noise on the relative performance of the filter methods, artificial noise was added to the reference signal of different magnitudes. The result of running the non-causal low-pass filter on motion data is shown in Figure 6.7. The figure illustrates the cleaning capability of the filter, without introducing extra lag or overshoot.

The tasks defined in Section 6.5.1 were recorded a number of times, and the ones that contained a minimal amount of measurement errors were selected. Measurement errors were found by inspection of the generated signals. Recordings with invalid spikes were rejected. These precautions minimize the number of false characteristics introduced to the true signal. A possible constant measurement bias does not really affect the characteristics of the original signal. Since each filter is tuned so that its output maximally matches the reference signal, such a bias has no influence on this relative performance study. For an absolute performance study of a filter, these arguments do not apply.

6.5.2 Performance Metrics

The accuracy of a filtering method is defined as the root mean square error (RMSE) of the difference in orientation between the filtered and reference signal in degrees

$$RMSE = \sqrt{\frac{1}{N}\sum_{i=1}^{N}\left(\frac{360}{\pi}\cos^{-1}((q_{c_i}\cdot q_{e_i}^{-1})_w)\right)^2} \tag{6.21}$$

where q_e is the quaternion representing the estimated orientation, q_c represents the reference signal, and q_w represents the w-component of quaternion q. Since the RMSE only gives an idea of the accuracy of a filter over the entire length of the data set, the peak error of the orientation mismatch in degrees is also analyzed. Large peak errors can be very disturbing in VR/AR environments and therefore are an important error metric.

Furthermore, an improvement factor is defined, which indicates how effective the use of

a filtering method is, compared to directly using the measurements:

$$\text{Improvement factor} = \frac{RMSE_{no\ filtering}}{RMSE_{filtered}} \tag{6.22}$$

6.5.3 System Parameters

The tracking system introduces various parameters that influence the performance of prediction schemes. The first system parameter is the sampling frequency f_s. The optical tracking system operates at a frequency $f_s = 60$ Hz. Since many popular tracking sensors, such as the Polhemus, the Logitech Acoustical tracker, and many optical tracking systems, operate at comparable or lower frequencies, f_s is only lowered by downsampling the data set. Although upsampling is possible to obtain higher sampling frequencies, characteristics of the true signal that may have been missed by sampling at 60 Hz cannot be added reliably without exact knowledge of this signal. The synthetic signal is also sampled at 60 Hz. All data sets are sampled at 60, 30, 20, and 15 Hz.

The second system parameter is the measurement noise N_z. The variances of the steady-state orientation and angular velocity measurement noise components were obtained as described in Section 6.4, which are approximations of the true measurement noise. The obtained values are $\sigma^2 = 10^{-6}$ and $\sigma^2 = 9 \cdot 10^{-4}$, respectively. Gaussian random noise was then added to the reference data sets, of magnitudes 1, 10, and 100 times the orientation measurement noise (renormalizing the resulting quaternion), and 1, 3, and 9 times the angular velocity measurement noise. Although the measurement noise of the optical tracker depends on the distance to the cameras and is far less in the center of the workspace, these values were regarded as constant and identical, since this study is a relative filter performance study. Absolute filter performance can be increased by a more accurate noise model.

The last parameter is the prediction time t_{pred}. This parameter is directly related to the end-to-end delay of the system, $t_2 - t_1$ in Figure 6.1. The prediction time was varied from 0 (i.e. only filtering) to 100 ms in steps of 33 ms. The errors at higher prediction times generally become too large for practical use [AB94].

6.6 Results

6.6.1 Synthetic Study

The EKF, UKF and LTI filters were applied to the synthetic signals. In Section 6.5.3, the settings of the parameters are defined. The filters were ran on each parameter combination, using the motion model including inertial measurements. The particle filters were ran on a subset of the parameter space for faster simulation. The most important results of the experiments are presented below.

- *Filtering and measurement noise*
  The improvement factor of each filter method for increasing measurement noise is graphed in Figure 6.8(a), where $t_{pred} = 0$ ms and $\omega = 2$ (see Equation 6.20). The improvement factor versus task is depicted in Figure 6.8(b).

- *Prediction time*
  The results of increasing the prediction time are graphed in Figure 6.9. Here, the RMSE and peek error are plotted versus prediction time, for $\omega = 2$.

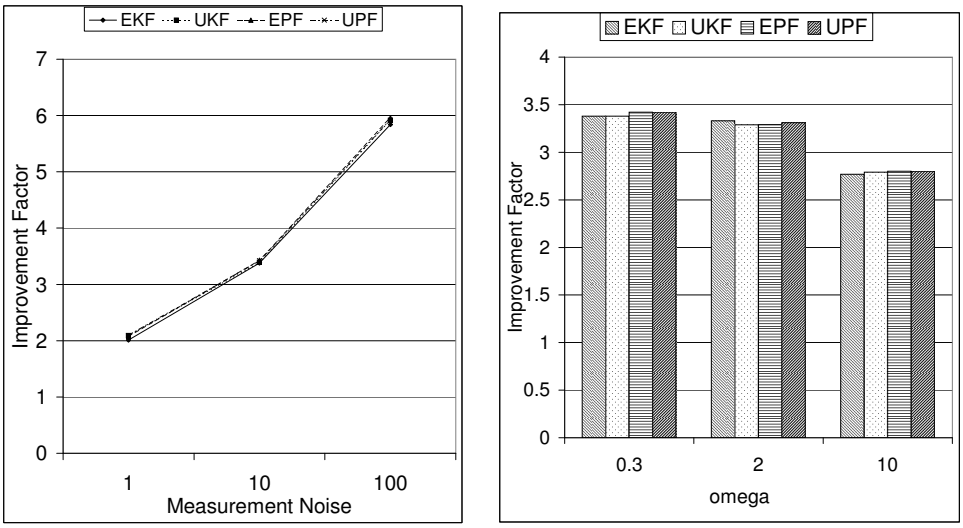

(a) (b)

Figure 6.8: Synthetic results for filtering ($t_{pred} = 0$): (a) Improvement factor vs. measurement noise ($\omega = 2$). (b) Improvement factor vs. omega for 10 times N_z.

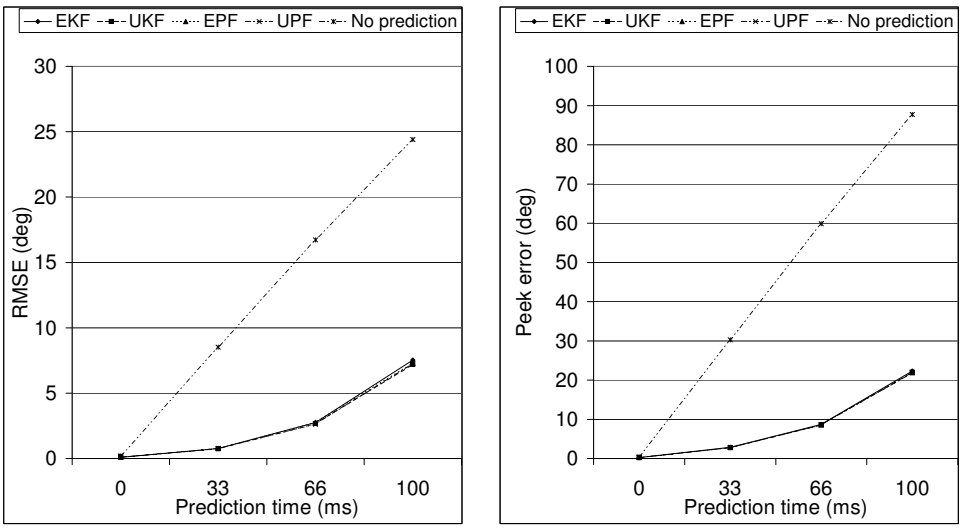

(a) (b)

Figure 6.9: Synthetic results for prediction ($\omega = 2$): (a) RMSE vs. prediction time. (b) Peek error vs. prediction time.

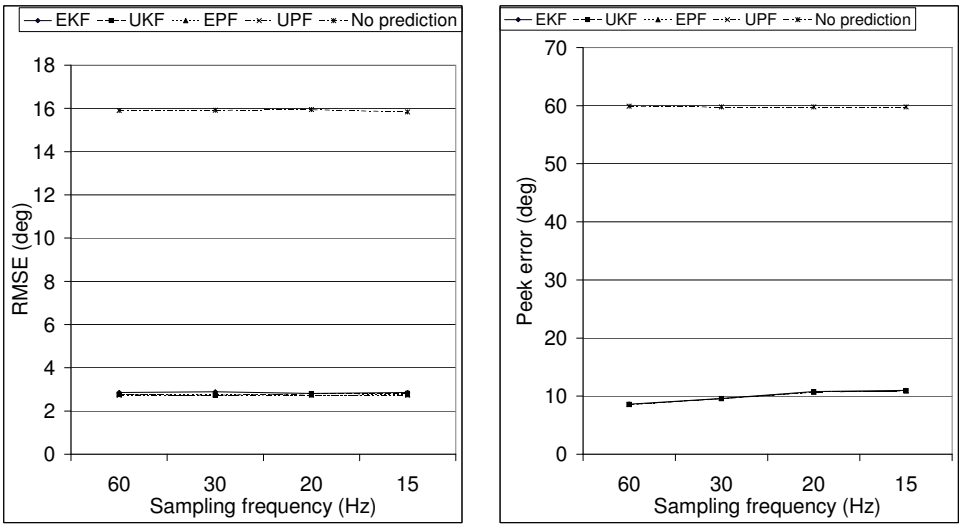

(a) (b)

Figure 6.10: Synthetic results for sampling frequency ($\omega = 0.3$): (a) RMSE vs. sampling frequency. (b) Peek error vs. sampling frequency.

- *Sampling frequency*
  The sampling frequency versus RMSE and peek error is shown in Figure 6.10. The figure shows the results for $\omega = 0.3$, a prediction time of 66 ms, and the measurement noise at its nominal value. The influence of f_s on the peak error is similar to the RMSE.

- *Relative filter performance*
  The performance results of the predictive methods are graphed in Figure 6.11. Here, the prediction time is 66 ms, the sampling frequency 60 Hz, and the measurement noise 10 and 3 times its nominal values. The results are shown for ω at 0.3, 2, and 10. The particle filters each used 50 particles.

6.6.2 Experimental Study

For the experimental study the same analysis was performed as in the synthetic, except both motion models are used. This results in 384 combinations for each filter. The most important results are given below, which are very similar to the synthetic case.

- *Filtering and measurement noise*
  The results of filtering (i.e. $t_{pred} = 0$ ms) are graphed in Figure 6.12. Figure 6.12(a) shows the improvement factor of each filter for increasing measurement noise, using the docking task and the MM model. Figure 6.12(b) shows the improvement factor of each filter for each task, with a measurement noise of 10 times its nominal value. The peak error shows similar behavior as the RMSE, where the exploration and docking tasks give slightly higher values than no filtering, with the measurement noise at both nominal and 10.

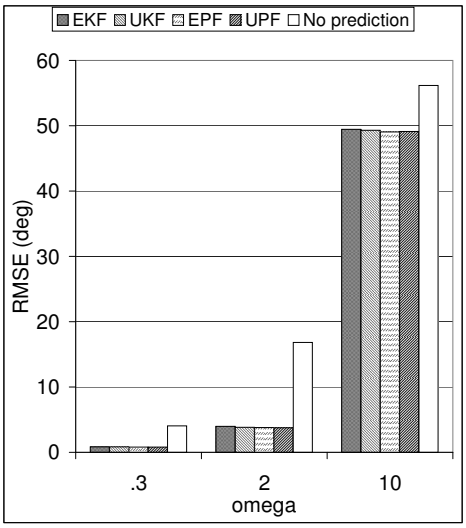

Figure 6.11: Synthetic results: Filter comparison for $t_{pred} = 66$ ms, $f_s = 60$ Hz, N_z 10 and 3 times the nominal orientation and angular velocity measurement noise.

- *Prediction time*
  The results of increasing the prediction time are graphed in Figure 6.13. Figure 6.13(a) plots the RMSE versus prediction time using the docking task, whereas Figure 6.13(b) depicts the peek error versus prediction time. Figure 6.14 shows the improvement factor using the object exploration task. The results are for the MM model.

- *Sampling frequency*
  The effects of changing the sampling frequency f_s are shown in Figure 6.15. The figure shows the results of the docking task for the prediction time at 66 ms and the measurement noise at its nominal value, using the MM model. The influence of f_s on the peak error is similar to the RMSE.

- *Relative filter performance*
  The performance results of the predictive filtering methods are given for the prediction time at 66 ms, the sampling frequency at 60 Hz, and the measurement noise as 10 and 3 times the nominal value of the orientation and angular velocity measurement noise, respectively. Figure 6.16 shows the RMSE values for each task, using both system models. The particle filters each used 50 particles. Larger numbers of particles gave no further improvement.

6.7 Discussion

Filtering and Measurement Noise

The experimental results in Figure 6.12 show that for increasing measurement noise N_z, the improvement factor of each filter relative to no filtering increases. The EKF and UKF have similar performance, while the LTI only gives an improvement over no prediction when N_z

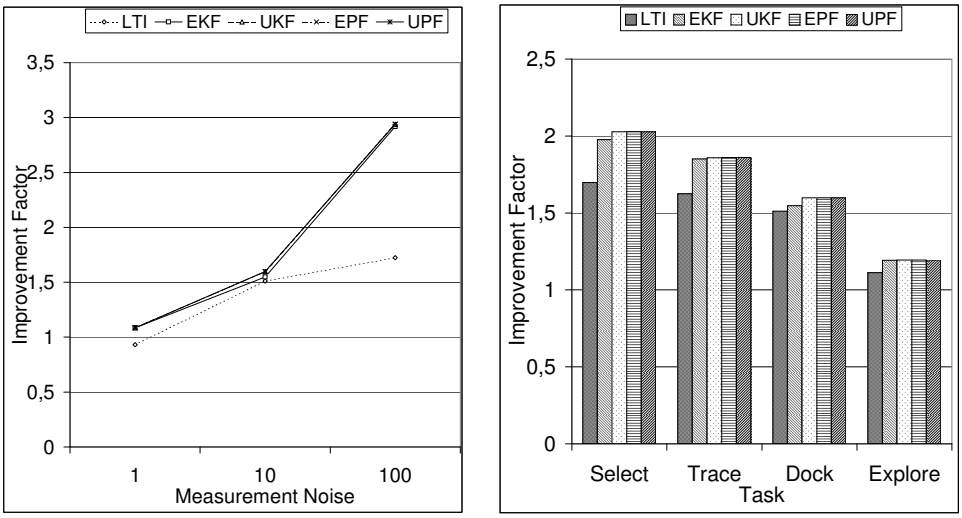

(a) (b)

Figure 6.12: Filter results: (a) Improvement factor vs. measurement noise (docking task). (b) Improvement factor vs. task for 10 times N_z.

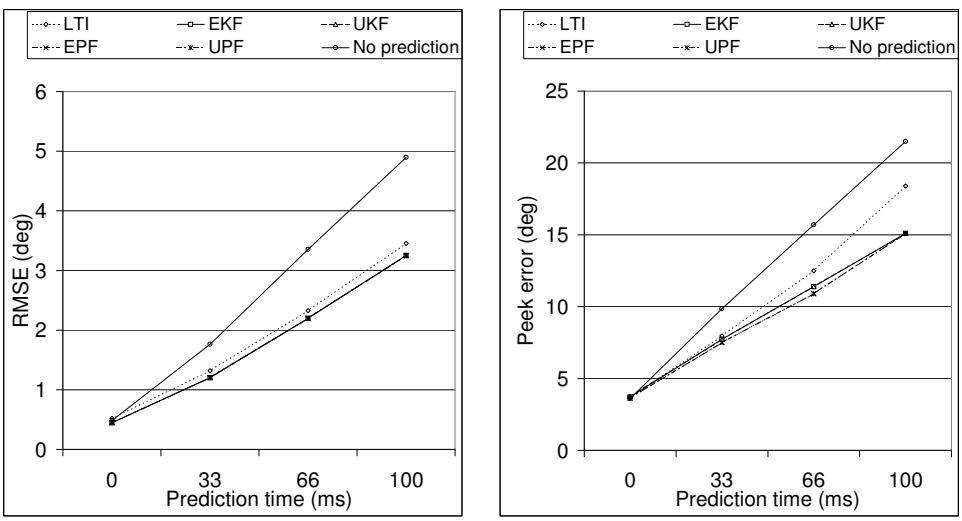

(a) (b)

Figure 6.13: Prediction results (docking task): (a) RMSE vs. prediction time. (b) Peek error vs. prediction time.

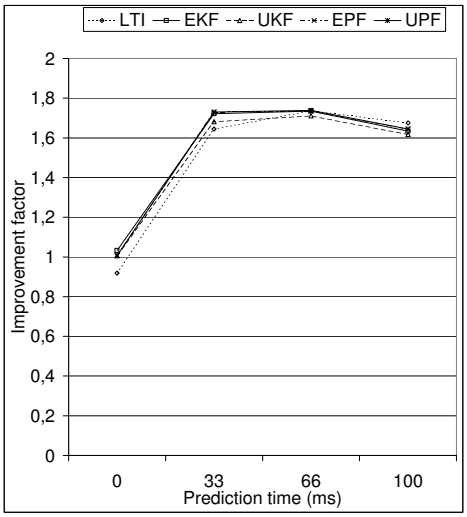

Figure 6.14: Prediction results (docking task): Improvement factor vs. prediction time (exploration task)

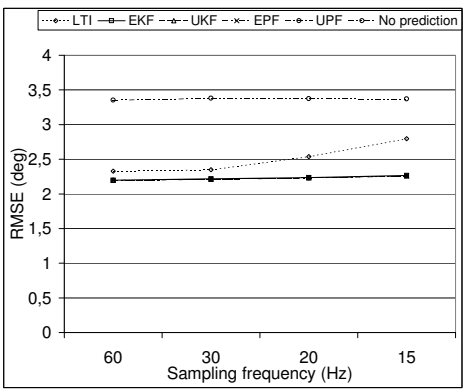

(a)

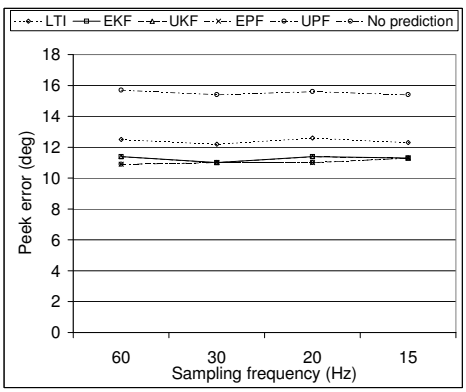

(b)

Figure 6.15: RMSE and peek error vs. sampling frequency for $t_{pred} = 66$ ms, N_z nominal.

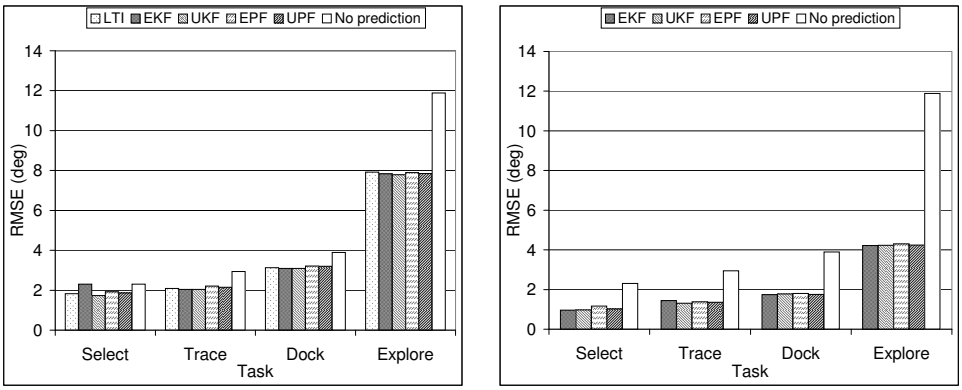

Figure 6.16: Filter comparison for $t_{pred} = 66$ ms, $f_s = 60$ Hz, N_z 10 and 3 times the nominal orientation and angular velocity measurement noise, respectively, using (a) only orientation measurements (MM), and (b) including inertial measurements (MMI).

is sufficiently high. For a measurement noise 100 times its nominal value, the LTI performs significantly worse than the EKF and UKF. This is caused by the small filter kernel. It might be solved using a slightly larger filter kernel, but this also introduces more lag which needs to be compensated.

Figure 6.12(b) suggests that as a signal's complexity increases, using a filtering method becomes less effective. This is likely the result of the process model being less accurate for more erratic motions.

Figure 6.8(a) confirms the results of the experimental study, showing that the effectiveness of the Bayesian filtering methods increases with measurement noise.

Prediction Time

Figure 6.13 shows a practically linear dependency between the RMSE and the prediction time for $t_{pred} \geq 33$ ms. The peek error shows similar characteristics. This implies that the system latency $t_2 - t_1$ (see Figure 6.1) should be kept as small as possible. The performance of the EKF and UKF are similar, while the LTI scores only slightly less. The figure further suggests that the improvement factor reaches an optimal value for a prediction time between 33 and 66 ms, and decreases as the prediction time is further increased. Application of a predictive filtering method is about 1.7 times less effective for a prediction time of 0 ms, compared to 33 ms.

Figure 6.8(b) shows that the RMSE increases fast with increasing prediction time, much worse than the almost linear dependency of Figure 6.14. The uncertainty of the motion model increases with prediction time, which is reflected in a much higher process noise. It is to be expected that at a certain prediction time, the process noise becomes so large that the filters regard the measurements to be more accurate, and the improvement factor converges to 1.

Sampling Frequency

Figure 6.11 shows that the RMSE and peek error of the EKF, UKF, and no prediction remain practically constant while lowering the sampling frequency. The Nyquist criterion states that in order to accurately reconstruct a signal of n Hz, a sampling frequency $\geq 2n$ Hz is needed. This suggests that most information content of the signal is located below 7.5 Hz.

The sampling frequency does have some influence on the performance of the LTI. The results of the other tasks indicate that its influence becomes larger for more complex input signals, as the effect on the RMSE is highest for the object exploration task and practically zero for the selection task. The reason is that the lag inherent to the LTI filter becomes larger as f_s decreases. This adds to the amount of time the filter has to predict.

The results of the synthetic study are the same as those of the experimental study. This is not surprising as the highest frequency component of the synthetic signals is 0.36, 2.39, and 11.94 Hz for $\omega = 0.3$, 2, and 10, respectively. For $\omega = 10$, this frequency component lies above the 7.5 Hz boundary, but the effects of lowering sampling frequency are small, as the highest frequency component is also the smallest and filter performance is already low for this signal.

Relative Filter Performance

In Figure 6.16, the performance of the LTI, EKF, UKF, EPF, and UPF are compared. From the figure and our other simulations follows that the EKF and UKF have a negligible performance difference in RMSE, for orientation prediction and filtering. This indicates that the input signals lend themselves well to linearization, as also suggested by [LaV03]. The particle filters both produce comparable RMSE values to the Kalman filters, where the UPF consistently scores slightly below the EPF. This indicates that the posterior distribution $p(\mathbf{x}_k|\mathbf{z}_{1:k})$ can be accurately represented by a Gaussian random variable, which also follows from the fact that the signals lend themselves well to linearization, since a linearized model with Gaussian noise has a Gaussian posterior distribution.

Comparing the experimental results of Figure 6.16(b) with the synthetic results of Figure 6.10, combined with the similar results for different parameter combinations, it can be concluded that the synthetic signal with $\omega = 0.3$ has similar characteristics as the docking task, and with $\omega = 2$ similar characteristics as the object exploration task. For a faster signal ($\omega = 10$), the effectiveness of the prediction methods becomes very small, and none of the filters are able to provide accurate estimates.

Since neither the UKF nor the particle filters gave much improvement compared to the EKF, it is very unlikely other Bayesian filters, e.g. the iterated extended Kalman filter [BC93], give further improvements for VR interaction tasks.

It was found that using inertial measurements gave a performance improvement of 1.3 to 3 over no inertial measurements. This confirms the work of Azuma and Bishop [AB94], and extends the results to different parameter combinations.

Runtime Performance

The average computation time of each filter is shown in Table 6.1. Running times were measured on an Athlon 1.4 GHz with 512 Mb RAM. Using inertial measurements is found to be about twice as costly.

The LTI is computationally efficient and has quite good performance in cases where the

	LTI	EKF	UKF	EPF	UPF
MM	13 μs	47 μs	215 μs	2.05 ms	11.7 ms
MMI	-	77 μs	392 μs	4.1 ms	21.4 ms

Table 6.1: Average running times per frame

measurement noise is not too high, and sampling frequency is sufficiently high. However, it is far more sensitive to measurement noise and sampling frequency than the Bayesian filters. Moreover, the prediction time to compensate for its lag and the length of the history used to calculate the angular velocity were optimized for each specific simulation. These tuning parameters depend on the characteristics of the input signal and the parameters involved, and may need to be adaptive. Alternatively, quaternion-based extrapolation techniques may prove to be effective for prediction.

The EKF requires the derivation of Jacobian matrices which generally makes its implementation more complex. Although the UKF does not require this derivation, the algorithm is somewhat more complex, requiring the calculation of a matrix square root (which can be calculated through a Cholesky factorization). As the derivation of the Jacobian matrices is a simple task for the motion model in this work, the EKF is easier to implement. Given its lower computation time and the fact that the computationally more expensive particle filters do not give more accurate results, the use of an EKF is sufficient for orientation prediction under the given circumstances.

Parameter Determination

As discussed in Section 6.5, the filters were tuned specifically for each simulation. Testing showed that the tuning parameters for the motion model F_k in Figure 6.1 vary significantly between input signals and different filter parameters. Incorrect parameters can lead to worse performance than using no filtering or prediction at all, and may even lead to completely 'loosing track'. Adaptive or self-tuning approaches, such as multimodal filtering, residual whitening and dual extended Kalman filtering [CNHV99, May79] may be promising techniques to improve filter performance and its application in practice.

RMSE versus Covariance

For this relative performance RMSE was chosen as performance measure. An alternative method to examine filter performance is the use of the covariance matrices generated by the filters. The diagonal terms of the covariance matrices represent the variances of the estimation errors of the state. For non-linear systems these only approximate the actual estimation error covariance. Since the covariance matrices still give a good indication of the general trend of the estimation error variances of the state, they were included in the analysis.

Figure 6.17 plots the trace of the covariance matrix generated by the EKF versus the MSE as a function of time, for the docking task, $t_{pred} = 66$ ms, $f_s = 60$ Hz and N_z 10. Other runs and filters gave similar results. Visually comparing both figures shows that the estimation error computed by the covariance matrix is correlated with the RMSE. A better approach to compare both figures would be to perform a correlation analysis, however, this will give similar results. Filter consistency has been confirmed by normalized innovation and state estimation error tests, as described in [BSF88].

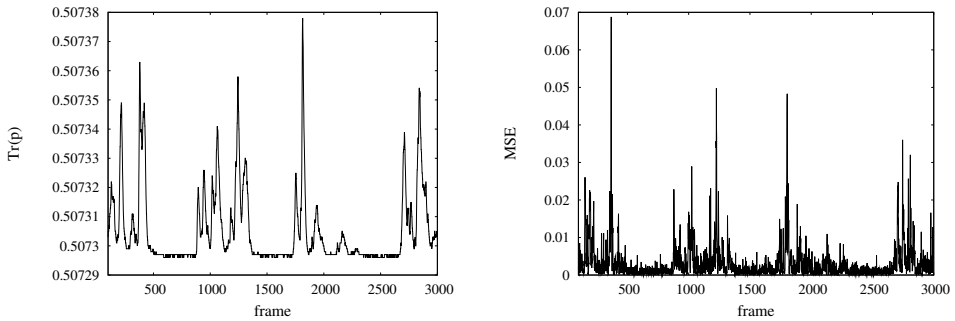

Figure 6.17: (a) Trace of the covariance matrix of the EKF as function of time. (b) MSE of the EKF as function of time, both for the docking task with $t_{pred} = 66$ ms, $f_s = 60$ Hz and N_z 10.

It should be noted however that for an absolute performance study of a filter, using the RMSE is generally not possible, and other performance analysis techniques are necessary (see e.g. [HV00, ET98]).

The motion model essentially models the actions of a user. Obviously, the performance of a filter depends on the accuracy of its ability to predict the new state, and therefore depends directly on the accuracy of the motion model. In this work, the most common motion models in VR are used. For a specific application, it may be possible to find a more accurate motion model. However, this generally means the model is less useful for other applications, and more likely to be susceptible to "losing lock" [Azu95].

6.8 Conclusion

In this chapter, a study of predictive filtering methods for orientation prediction in VR/AR was presented, using various hand tasks and synthetic signals. A framework was presented to identify critical parameters that influence these methods. A performance analysis was conducted using a linear time-invariant filter, an extended and unscented Kalman filter, and an extended and unscented particle filter. Parameters included in the analysis were prediction time, measurement noise, sampling frequency, motion model (with and without inertial measurements) and input signal characteristics.

It was found that the EKF, UKF and particle filters have similar performance for orientation prediction and filtering. The fact that even the particle filters gave no significant improvement suggests that the signals produced in typical VR/AR manipulation and selection tasks lend themselves well to linearization, and that the posterior density $p(\mathbf{x}_k|\mathbf{z}_{1:k})$ can be accurately represented by a Gaussian random variable. The LTI filter performs close to the Bayesian filters in cases where measurement noise is not too high (so that the filter kernel can be small), and sampling frequency is sufficiently high (so that the lag introduced by the filter remains small). In cases where angular velocity measurements are unavailable, the LTI may be sufficient.

The sampling frequency did not influence the performance of the Bayesian filters, which suggests that most of the signal content of selection and manipulation tasks in VR/AR is

located below 7.5 Hz. This does not mean a sampling rate of 15 Hz is sufficient, as the human perception system perceives an update rate of 15 Hz to be 'jerky'. Moreover, Azuma and Bishop have shown [AB94] that the prediction time must in fact be kept below 80 ms, since predicted output signals have more energy in higher frequency bands, increasing perceived jittering.

Further conclusions are that the application of a filtering method is most effective for a prediction time between 33 and 66 ms, and becomes less effective for higher prediction times. The improvement factor over no filtering increases as measurement noise increases and shows a dependency with the complexity of the input signal.

The tuning parameters of the filters varied significantly with changing input signals and filter parameters as prediction time. In practice, parameters as prediction time and sampling frequency are fixed, and the most significant influence on tuning parameters is the type of task. Adaptive filtering may provide a solution to this problem, such that the tuning parameters are automatically adjusted. One approach is to use multiple motion models, which are tuned to different types of motions [CNHV99]. Another possibility would be to control the tuning parameters based on the task a user is performing in the application. Consequently, high-level interaction information would be exploited in a low-level filtering and prediction method.

In these studies, measurement noise was modeled as additive Gaussian noise. Although the steady state noise of the optical tracking system was confirmed to be additive Gaussian, the measurement noise depends on the position of the input device relative to the cameras. Measurement noise increases as a function of the distance to the cameras. In case of an optical tracking system, a more accurate way to model the measurement process would be to include the steps used to calculate an orientation from 2D marker positions. However, since highly accurate measurement models are not available for all tracking systems, the measurement model was simplified. More accurate modeling of the measurement process and the measurement noise can further increase filter and prediction performance.

More research is needed to accurately model hand motion characteristics in a VR environment. Such a model can be used to create synthetic signals that act as a performance benchmark for filter and prediction performance evaluation, and to develop more accurate motion models for the filtering techniques.

Chapter 7

Tracking and Model Estimation of Composite Interaction Devices

Chapters 3 and 4 focussed on tracking and model estimation of rigid interaction devices. Chapter 6 aimed at improving the pose estimate provided by these tracking techniques with respect to noise and latency. Although rigid devices are applicable in a number of areas, some tasks require the manipulation of a larger number of dimensions. Consider for instance a modeling application, which includes spatial manipulation tasks as positioning, orienting, and scaling. In case of uniform scaling, the number of input dimensions is 7, while this number increases to 9 in case of non-uniform scaling. A six degree of freedom input device does not provide enough dimensions to perform such tasks without mode switching. An alternative approach would be to use an interaction device that supports the manipulation of a larger number of input dimensions.

The goal of this chapter is to develop a tracking system that allows a developer to rapidly construct and apply composite interaction devices. Composite interaction devices consist of linked segments with degrees of freedom with respect to each other. An example composite interaction device would be a glove, where the palm of the hand defines a six degree of freedom reference frame, and where each segment corresponds to a finger segment with rotational degrees of freedom with respect to each other. Composite interaction devices open up new perspectives on interaction in VR, as well as being applicable in a number of related research areas, such as medical research, animation, and rehabilitation.

The difficulty in tracking composite interaction devices is that each segment needs to be recognized. A simple approach would be to equip each segment with enough markers to be able to use the tracking techniques of Chapters 3 or 4 to recognize each segment separately. However, the resulting interaction devices would be prohibitively large for use in a desktop virtual environment such as the PSS.

In this chapter, a model-based optical tracking and automatic model estimation system for composite interaction devices is developed. Composite interaction devices are defined as objects that consist of a hierarchy of linked segments, where each segment can have degrees of freedom (DOFs) relative to a parent segment. Devices consist of one reference segment that is equipped with multiple markers, while other segments can contain only a single marker. This keeps the devices compact and easy to handle. The goal of this chapter is to develop tracking techniques for such devices and model estimation techniques to automatically derive the skeleton structure of these devices from motion data, along with the DOFs of each segment relative to its parent.

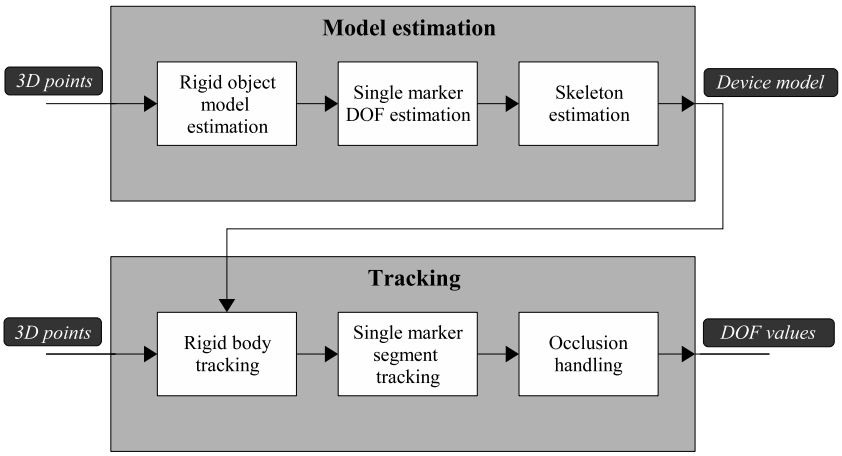

Figure 7.1: The tracking and model estimation system for composite interaction devices.

7.1 Overview

In this chapter, a model-based optical tracking and automatic model estimation system for composite interaction devices is presented. The system is designed to support a low number of markers attached to each segment, such that small interaction devices can be used in the virtual environment. Furthermore, the system is able to automatically estimate a hierarchical model of the interaction device from motion capture data, describing the DOF relations between segments, their ranges, and the geometric skeleton structure defining how these segments are connected. The optical tracking system is able to use the obtained models to identify the devices, and to determine all DOF parameters describing the pose of each segment.

Most previous work on model estimation of composite interaction devices has focussed on the human body. Each limb is either equipped with at least three markers (e.g. [HSDK05]), or models need to be pre-defined. By giving each segment a unique configuration of three or more markers, segments can be easily identified and a full coordinate system can be derived from the marker configuration. Examining the relation between segments is then reduced to examining the relation between moving coordinate systems. Clearly, this approach does not work when segments are allowed to contain less than three markers. Many VR systems, and desktop virtual environments in particular, work with interaction devices much smaller than the human body. As a result, segments of the interaction device may not provide enough room to accommodate multiple markers.

For the model estimation techniques presented in this chapter, it is assumed that stereo and frame-to-frame correspondence have been performed, resulting in labeled 3D marker locations. The techniques to achieve this are described in Chapter 4. The model estimation and tracking system for composite interaction devices is outlined in Figure 7.1.

Model estimation works in three steps:

- First, rigid objects are identified. These are objects that are equipped with three or more markers. A model of such objects is obtained using the model estimation techniques described in Chapter 4.

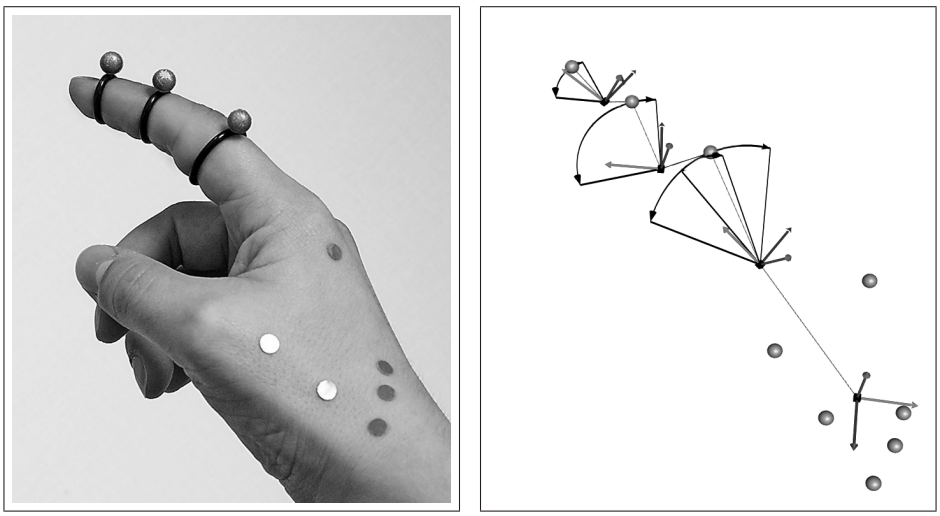

(a) (b)

Figure 7.2: (a) An example composite interaction device. The hand consists of a reference segment with 6 markers, followed by single marker segments with rotational DOFs. (b) The corresponding model with the 3D marker locations, skeleton structure, DOF relations and ranges, and reference frames.

- A model of single marker segments is obtained, which describes the DOFs and their ranges of each segment, relative to a frame of reference. This procedure is based on examining the geometric shape that the moving marker describes. For instance, a marker on a segment with one rotational DOF with respect to a parent segment results in a 3D circle arc. A set of fitting routines is applied to determine the geometric shape which best describes the motion of a single marker. Next, the parameters describing this geometric shape are mapped to the parameters of the corresponding DOF model. A new local coordinate system is constructed in the single marker segment, according to the determined DOF relation. This coordinate system functions as a new reference coordinate system to find other relations.
- After all possible DOF relations between segments are determined, a skeleton estimation procedure is used to derive the final hierarchical structure of the segments of the device.

As an example, Figure 7.2 shows a finger, along with the model as determined by the model estimation method. The finger features four segments, one used as a six DOF reference coordinate system (the palm), followed by a single marker segment with two rotational DOFs (the proximal phalanx) and two segments with each one rotational DOF (the middle and distal phalanges). During model estimation, the user moves the various parts of the composite interaction device in front of the cameras, such that all markers can be seen. Markers that are occluded for a short period of time are handled during frame-to-frame correspondence by predicting occluded markers locations (see Chapter 4). Long-term partial occlusion is only allowed in segments with more than three markers.

The tracking system is based on the following steps:

- The model obtained from the model estimation techniques is used to determine the pose of the interaction device, using the rigid body tracking techniques presented in Chapter 4.
- Markers are mapped to model segments, and the DOF parameters of each segment are determined by single marker tracking. The tracker is basically an exhaustive search that matches markers to model segments, and prunes the search space using a backtracking approach. To determine if there is a possible correspondence between a marker and a model segment, the point is first expressed in the coordinate system of the parent segment. Next, its DOFs are determined according to the model. If the DOFs are within the ranges stored in the model, a possible correspondence has been found.
- If the parent of a segment cannot be found, for instance due to occlusion, the tracking system uses extra relations stored during model estimation that are not part of the skeleton structure.

This chapter is organized as follows. In Section 7.2, related work is briefly reviewed. Sections 7.3 and 7.4 present the model estimation and tracking methods. Section 7.5 presents results of the proposed techniques and provides a discussion of these results. Finally, in Section 7.6 conclusions are given.

7.2 Related Work

Research on model estimation of composite interaction devices has mainly focussed on clique-based methods. These methods rely on sets of markers on each segment that form fully connected graphs, such that the (6 DOF) pose of each segment can easily be determined.

Silaghi et al. [SPB+98] developed a method that matches a template model to motion capture data, and estimates rotation centers of markers and their associated segments. O'Brien et al. [OBBH00] used magnetic sensors to determine the full pose of each segment, and presented a least squares solution to determine joint rotation centers of segments. The skeleton structure is estimated using a minimum spanning tree for the graph connecting all segments. Kurihara et al. [KHYN02] presented a method that matches a predefined model to motion capture data, but the technique relies on carefully chosen marker positions. Ringer et al. [RL02] presented a clique-based model estimation system, where each clique is assigned to a segment, and require markers not to be occluded. Zordan et al. [ZH03] presented a physical model to map optical motion capture data to a pre-defined skeleton model.

More recently, Hornung et al. [HSDK05] extended the work of O'Brien et al. for optical tracking and model estimation. Each segment of a composite object is equipped with multiple markers. The system first determines which markers maintain a rigid relation during movements of the object. Each marker is assigned to a clique, and markers within a clique are associated with a segment. Each clique defines a local coordinate system of a segment, and using the results of [OBBH00], the skeleton structure of the composite interaction device can be determined. The system does not provide a higher level analysis of the degrees of freedom of each segments, i.e. a high level DOF model. This makes it difficult to map the data from the tracking system to interaction techniques.

An important limitation of these clique-based approaches is that they require enough markers attached to each segment to be able to uniquely determine a coordinate system. Since markers cannot be arbitrarily small, this requires each segment to be large enough to

accommodate at least four markers. For instance, creating an optically tracked glove would be impossible due to the amount of markers required on each finger segment. In contrast, the Vicon [VIC] system supports model estimation of composite interaction devices with single markers on segments, but requires pre-defined models.

A related modeling and tracking approach is the use of Point Distribution Models (PDMs) [CTCG95]. The principle behind the PDM is that the shape and deformation of an object can then be learned through statistical analysis. The resulting model can be used for object localization and tracking. However, PDMs assume linear models, making them less suitable for expressing rotations. Although PDMs have been extended to support non-linear models [SCTM95], the method is slow and does not provide a high level DOF description.

Other related work in computer vision literature is the modeling of joint limits using quaternion field boundaries [HUHF03]. Although this provides a technique to model the limits of joint movements, it does not address the issue of automatically determining a skeleton structure. Parallel to the work presented in this chapter, Yan et al. presented a technique to automatically determine a kinematic chain from motion data [YP06]. The method is based on analyzing motion subspaces. Joints can be a point or an axis. The method deals with many features on segments. The authors do not address the use of the acquired model in a realtime tracking system, nor does the approach result in a model with constraints on the DOFs.

In this chapter, a model estimation method is presented which allows for single marker segments, and does not rely on a pre-defined model. As opposed to previous work, the method automatically derives the skeleton structure of the composite interaction device, along with the degrees of freedom between (single marker) segments and the ranges on these DOFs. It handles combinations of rotational and translational DOFs.

7.3 Model Estimation

Given labeled 3D marker locations, model estimation is solved in three steps.

- *Rigid object model estimation*
  All segments that contain three or more markers are identified from the motion capture data. The system constructs a model of the 3D marker locations of such segments using the model estimation techniques for rigid objects, as described in Chapter 4.

- *Single marker DOF relation estimation*
  The DOF relations of all markers not part of rigid segments are determined. The DOF relations of single marker segments are defined relative to the reference coordinate systems defined by the segments with three or more markers. When a DOF relation is found, the system determines a local coordinate system in the marker position, moving according to its DOFs. These local coordinate systems serve as reference frames for other single marker segments.

- *Skeleton estimation*
  The underlying skeleton structure of the segments is determined, such that the skeleton reflects how the segments are connected on the physical interaction device.

A marker moving according to a DOF relation results in a time series of 3D locations. This series of locations can be interpreted as a geometric shape. The model estimation method is based on mapping the DOF relation between a moving marker and a reference frame onto such a geometric shape. For instance, the trajectory of a point moving along an axis and

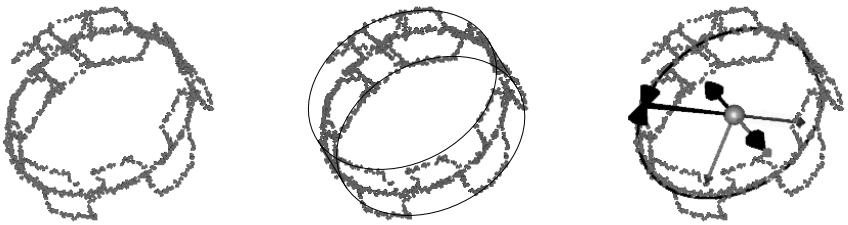

(a) (b) (c)

Figure 7.3: (a) A moving marker results in a time series of 3D locations. (b) The marker's trajectory can be interpreted as a cylinder. (c) The cylinder parameters are translated to a DOF model with a translational and a rotational degree of freedom.

rotating around it can be described by a 3D cylinder (see Figure 7.3). The parameters that describe this cylinder are then mapped to a model with one rotational and one translational degree of freedom. A set of common DOF relations is defined, and the corresponding geometric shapes are derived. When a relation between a point and a reference frame has been determined, a new local coordinate system can be constructed in this point. Other points can be expressed in this new coordinate system to discover relations between single markers.

In Section 7.3.1 the specification of the model is given, as it should be obtained by the model estimation procedure. Section 7.3.2 describes the mapping between DOFs and geometric shapes to find the DOF relations between single points and reference coordinate systems. Section 7.3.3 describes how these techniques are combined to estimate the complete skeleton structure of the composite object.

7.3.1 Model Definition

The formal definition of the model, which is to be obtained by the model estimation procedure and used by the tracking system, is as follows. The model of a composite interaction device is defined by a tree, i.e., a connected graph G with no cycles, $G = (V, P, D, \Psi)$, where

- V is the set of vertices v_i representing segments.
- $P \subseteq V$ is the set of parents, where P_{v_i} assigns a parent to segment v_i.
- D is the set of degree of freedom (DOF) relations, where D_{v_i} assigns a DOF relation to segment v_i relative to its parent segment P_{v_i}.
- Ψ is the set of 3D locations that correspond to the markers attached to the interaction device.

Each segment v_i holds a subset S of the 3D marker locations Ψ, $S \subseteq \Psi$, such that each pair $(p_i, p_j) \in S$ has zero degrees of freedom with respect to each other (i.e. the distance remains static), or S contains only one point. In other words, the subset defines a rigid subsection S of the marker positions Ψ.

If a DOF relation of segment v_i with respect to segment v_j has been found, then P_{v_i} is set to v_j, and D_{v_i} contains the determined DOF relation. A DOF relation D_{v_i} is defined by

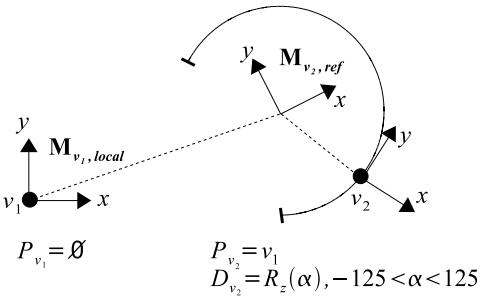

Figure 7.4: An example model graph, consisting of two vertices. Vertex v_1 is a root vertex, such that $P_{v_1} = \varnothing$. Vertex v_2 has one rotational DOF D_{v_2} with respect to its parent $P_{v_2} = v_1$. The reference frame $\mathbf{M}_{v_2,ref}$ defines the frame in which the DOF D_{v_2} is expressed, and is defined with respect to parent frame $\mathbf{M}_{v_1,local}$.

the parameters describing the DOFs, along with a reference frame $\mathbf{M}_{v_{ref}}$ given relative to the local coordinate frame $\mathbf{M}_{u_{local}}$ defined by the parent vertex $u = P_{v_i}$. An example model graph G is shown in Figure 7.4.

7.3.2 Single Marker DOF Relation Estimation

Model estimation is based on repeatedly determining the DOF relation of a single marker segment relative to a reference coordinate system. Reference coordinate systems are defined by segments with three or more markers, or by segments with single markers for which a DOF relation already has been found. Segments with three or more markers are trained using the rigid body model estimation techniques described in Chapter 4.

A moving marker expressed in a reference coordinate system results in a time series of 3D marker positions, denoted as a point set. To determine the DOF relation between a marker and a reference coordinate system, the geometric shape of this point set is examined. This geometric shape can be mapped to a DOF model. For instance, a marker on a segment with one translational DOF relative to a coordinate system results in a 3D line, whereas a marker on a segment with two rotational DOFs results in a sphere.

When a DOF relation of a single marker has been found, under certain conditions a local coordinate system can be constructed at its location. These conditions are only fulfilled when each point of the geometric shape maps uniquely to DOF parameters. For instance, the location on a sphere can be uniquely expressed by azimuth, elevation, and radius parameters, as long as the poles are excluded (when the elevation is 0 or π, the azimuth angle is ambiguous). Similarly, the roll of a single point on a sphere is ambiguous.

Three DOF models have been implemented, which are listed in Table 7.1. Note that this list is not intended to be complete, but to support the most commonly found DOF models.

DOF model	Geometric shape	#DOFs
Translation	Box	3
Azimuth, Elevation, Radius (AER)	Spherical Shell	3
Translation, Rotation	Cylinder	2

Table 7.1: Geometric shapes and their corresponding DOFs

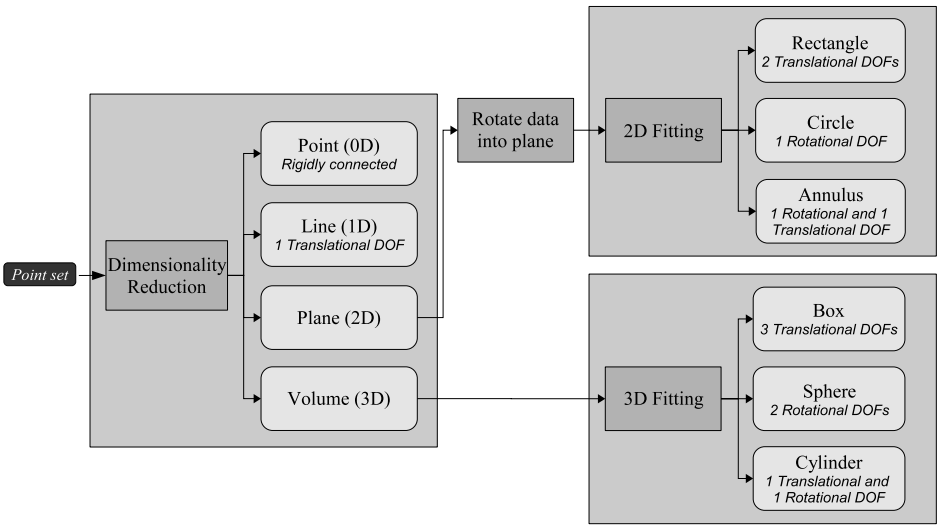

Figure 7.5: The fitting procedure.

Adding more DOF models does not change the techniques presented in this chapter.

Fitting routines are generally more efficient and more accurate for lower dimensions. Therefore, the geometric shapes corresponding to each DOF model of Table 7.1 are divided into simpler cases, and the corresponding geometric fitting routines are implemented. The complete procedure of finding a single marker DOF relation relative to a coordinate system is outlined in Figure 7.5. The fitting procedure is based on performing a Principal Component Analysis to find the dimensionality of the point set. If the point set can be reduced to zero dimensions, the data can be described by a single 3D point. In this case, a rigid relation between two single marker segments is found. If the point set can be described by one dimension, the data lies on a 3D line, such that the relation between two segments can be described by one translational DOF. In case the point set can be described by two dimensions, 2D fitting routines are applied to find the geometric shape that best describes the data. If the point set lies within a volume, 3D fitting routines are used. The fitting procedure and its implementation is discussed in more detail in the following sections.

Dimensionality Reduction

The first step of the fitting procedure is to find the dimensionality of the point set, i.e., to check if the point set can be described by a single 3D point, a line, a plane, or a volume. This is accomplished by performing a Principal Component Analysis (PCA) [Jol02]. Principal component analysis (PCA) is a powerful mathematical procedure that transforms a number of (possibly) correlated variables into a smaller number of uncorrelated variables, which are called principal components. The principal components are orthogonal, and are ordered descending in terms of how much they account for the variability in the data. The PCA is a popular technique to reduce the dimensionality of a data set or to detect structure in the relationships between variables. It re-expresses a data set as a linear combination of its base vectors. Consider a data set consisting of M measurements, where each measurement is represented by an L-dimensional vector v_i, $0 \leq i < M$. The PCA can be performed by the

following steps:

1. Subtract the mean of each variable from each measurement

$$\hat{v}_i = v_i - \frac{1}{M}\sum_{j=1}^{M} v_j \tag{7.1}$$

2. Organize the resulting data set as an $L \times M$ matrix $\mathbf{X}$

3. Compute the $L \times L$ covariance matrix $\mathbf{C}$

$$\mathbf{C} = \frac{1}{M-1}\mathbf{X}\mathbf{X}^T \tag{7.2}$$

4. Calculate the eigenvectors V of $\mathbf{C}$ and sort by decreasing eigenvalue D.

$$\mathbf{C}V = VD \tag{7.3}$$

The eigenvectors define the set of principal components $\hat{v}_i$, whereas the eigenvalues correspond to the principal values λ_i, such that the (centered) data set can be expressed by

$$\lambda_i \hat{v}_i \tag{7.4}$$

The PCA can also be performed by calculating a Singular Value Decomposition (SVD) on matrix $\mathbf{X}$

$$\mathbf{X} = \mathbf{U}\Sigma\mathbf{V}^T \tag{7.5}$$

where the columns of $\mathbf{V}$ are the principal components of $\mathbf{X}$. The SVD serves as a one-step function to perform PCA, without the need to explicitly compute the covariance matrix $\mathbf{C}$.

Performing the PCA on a 3D point set results in three principal components. The first component has the largest principal value, meaning it is a 3D vector in the direction that represents the largest variability in the data. To test if the point set can be described by one translational DOF, a line is constructed through the mean of the point set C and in the direction D of the principal component with the largest principal value. This corresponds to a least squares line approximation, where the orthogonal distance of the point set to the line is minimized [Sha98]. The mean square error (MSE) of the orthogonal distances of the point set to the line is used to determine if the point set can be accurately represented by a line

$$MSE = \sum_{i=1}^{M} |L \times (p_i - P)|^2 \tag{7.6}$$

where p_i is a 3D point, P a point on the line, M the size of the point set, and L the normalized line direction. If the MSE is below a specified threshold ϵ, it is concluded that the point set can be accurately described by a line. The threshold ϵ depends on the measurement noise introduced by the optical tracking system. If the geometric shape of the point set is determined to be a line, a translational DOF has been found. The translation range is determined by projecting the point set onto the line, using

$$(p_i - P) \cdot L \tag{7.7}$$

If the range is below ϵ, the data is regarded as a single 3D point. In this case, the procedure returns a zero DOF relation. Otherwise, the procedure returns one translational DOF and its range. The reference frame $\mathbf{M}_{ref}$ (see Section 7.3.1) is defined by the axes of the PCA components, with the center in the mean of the point set.

To test if the data can be represented as a two dimensional set of points, a plane is fitted to the data. The principal component with the smallest value is used as an estimate of the plane's normal vector N, with the mean of the point set as point in the plane. Analogous to the line test, this corresponds to a least squares approximation, where the orthogonal distance of the point set to the plane is minimized [Sha98]. The mean square error of the point set to the plane is determined as

$$MSE = \sum_{i=1}^{M} (N \cdot (p_i - P))^2 \tag{7.8}$$

where N is the normal vector to the plane, and P is a point on the plane. If the MSE is below ϵ, the point set is regarded as planar. In this case, the point set is rotated such that the least squares plane is the xy plane. This is accomplished by multiplying each point p_i with the matrix

$$\mathbf{M}_{plane} = \begin{pmatrix} 1 - \frac{a^2}{c+1} & -\frac{ab}{c+1} & -a & 0 \\ -\frac{ab}{c+1} & 1 - \frac{b^2}{c+1} & -b & 0 \\ a & b & c & 0 \\ 0 & 0 & 0 & 1 \end{pmatrix} \tag{7.9}$$

where (a, b, c) are the components or direction cosines of N. The procedure then performs 2D fitting routines on the transformed point set to find the most appropriate geometric shape. In case the data cannot be accurately represented by one or two dimensional variables, the data is considered to be volumetric.

2D Fitting Routines

If the point set lies in a plane, 2D fitting routines are performed. The point set is rotated such that its least squares plane corresponds to the xy plane using Equation 7.9. Next, two 2D fitting routines are performed: an annulus and a rectangle fit.

The rectangle fit is implemented as an optimization routine over one rotational variable θ around the z-axis, rotating the coordinate system in which the point set is expressed and minimizing the rectangle defined by the x and y-range of the data. The downhill simplex method is used for optimization (see also Chapter 4). During each function evaluation that is performed by the simplex method, the x and y-range of the point set in the rotated frame estimate $\mathbf{M}_{rect} = \mathbf{R}_z(\theta)$ is calculated. The area of the rectangle with ranges x_r and y_r is minimized, such that the objective function J can be written as

$$J(\theta) = x_r y_r \tag{7.10}$$

where x_r, y_r are functions from θ.

To obtain an initial estimate of θ, as needed by the simplex method, the principal components are used as axes of the initial pose. These axes are rotated into the xy plane using Equation 7.9. The PCA components generally give a good initial estimate of the pose of the rectangle. Only when the width and height of the rectangle are identical, and assuming uniformly distributed data, the obtained axes pass through the corners of the rectangle. This situation is illustrated in Figure 7.6. In case the width and height of the rectangle differ, the

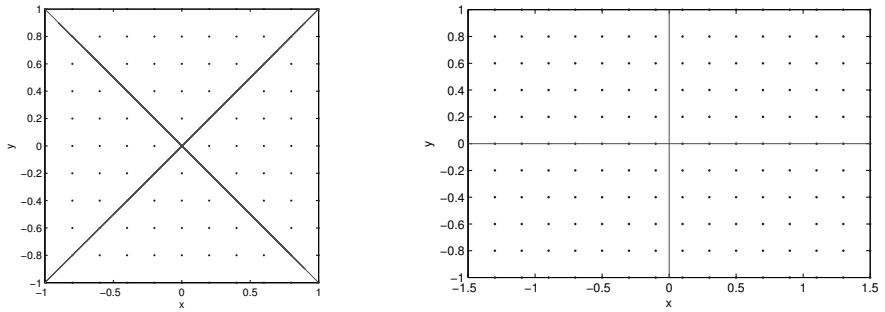

(a) (b)

Figure 7.6: The PCA components of two uniform point sets. (a) The PCA components of a uniform square point set give axes through its corners, (b) The PCA components of a uniform rectangular point set give the desired axes.

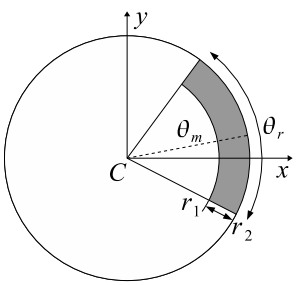

Figure 7.7: An annulus with minimum and maximum radii r_1 and r_2, rotation range θ_r, and center C.

axes obtained by the PCA are reasonably accurate. As is illustrated in the figure, the maximally allowed rotation of the initial estimate is 45 degrees, which defines the initial size of the simplex.

The obtained solution $\mathbf{R}_z(\theta)$ is rotated back from the xy plane using the transpose of $\mathbf{M}_{plane}$ as defined in Equation 7.9, to form the reference frame $\mathbf{M}_{ref}$. The x and y ranges are returned as DOFs.

The annulus fit is also implemented as a simplex optimization routine. An annulus is defined as the region lying between two concentric circles (see Figure 7.7). It is fully described by its center C, the inner radius r_1, the outer radius r_2, and the rotation range θ_r. This geometric shape corresponds to a rotational DOF, followed by a translational DOF. Using the center of the annulus as optimization variable, the remaining parameters can be determined as follows. The inner radius r_1 and outer radius r_2 are determined by calculating the minimum and maximum distances of the point set to the center. The rotation range θ_r is determined by expressing the point set in polar coordinates, and calculating the angle each point makes with the x-axis. These angles are sorted to obtain $\theta_i, i = 1, \cdots, N$, such that θ_r can be calculated as

$$\theta_r = 2\pi - \max(2\pi - \theta_{max} + \theta_{min}, \max_i(\theta_{i+1} - \theta_i)) \tag{7.11}$$

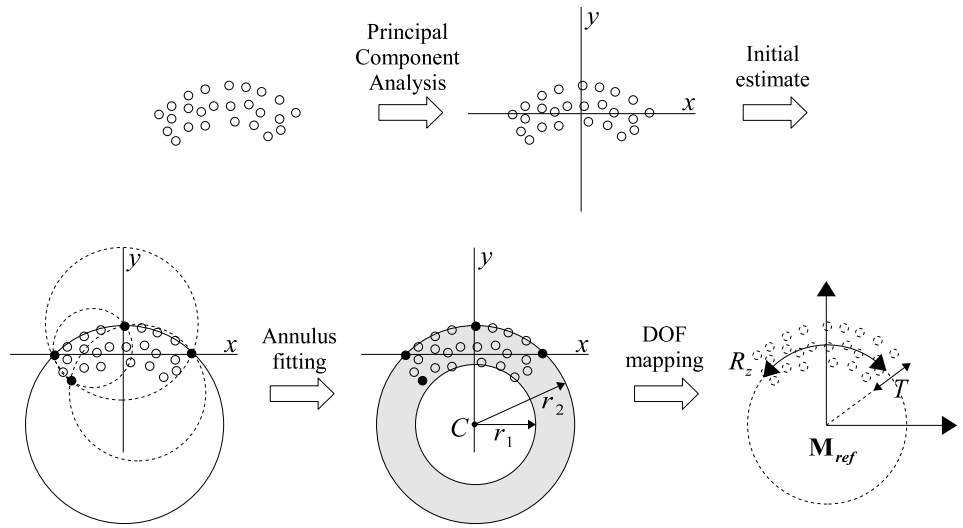

Figure 7.8: Obtaining the DOFs of a moving marker. First, a PCA is performed to obtain the axes corresponding to the largest variability in the data. Next, the markers with minimal and maximal x and y values are determined, and circle estimates are created through each combination of three markers. An annulus fitting routines is used to obtain a final estimate of the parameters of the geometric figure the marker describes. Finally, the annulus parameters are mapped to a DOF model with one translation and one rotation.

The objective function J is defined as the area of this region, which is minimized as

$$J(C) = \int_{r_1}^{r_2} r \int_{\theta_1}^{\theta_2} d\theta dr = \frac{1}{2}(\theta_2 - \theta_1)(r_2 - r_1)^2 = \frac{1}{2}\theta_r(r_2 - r_1)^2 \tag{7.12}$$

where r_1, r_2, θ_r are functions from C.

The complete procedure for fitting an annulus to motion data and mapping the parameters of the annulus to a DOF model is outlined in Figure 7.8. First, the point set is expressed in the coordinate system obtained from the principal component analysis. Next, an initial estimate for the center C of the annulus is obtained. The minimal and maximal value of the x and y components of each marker location is determined, yielding 4 coordinates. Three of these coordinates should lie close to the circle with outer radius r_2 (see Figure 7.8). Since a circle can be defined by 3 non-collinear coordinates, each combination of 3 points (x_1, y_1), (x_2, y_2), (x_3, y_3), is selected to calculate an estimate of the circle center (x_c, y_c).

The fitting routines are applied four times, using each combination of 3 points to provide an initial estimate of the circle center C. The solution with the minimal area A is selected. The parameters of the resulting annulus are mapped to a DOF model, with a rotational DOF of range $\theta_r = \theta_2 - \theta_1$, and a translational DOF in the range $[r_1, r_2]$. The reference frame $\mathbf{M}_{ref} = \mathbf{M}_{plane}^T \mathbf{R}_z(\theta_m)\mathbf{T}(C)$, where $\mathbf{R}_z(\alpha)$ represents a rotation matrix around the z-axis, θ_m is the midway angle of the rotation range θ_r, and $\mathbf{T}(C)$ a translation matrix.

3D Fitting Routines

The 3D fitting routines are executed when the point set lies within a volume. In this case, a sphere, cylinder, and a box fit are performed.

The box fit is a trivial extension of the rectangle fit. It is implemented using the simplex method, optimizing three rotation angles α, β, γ that define the pose of the box.

$$\mathbf{M}_{box} = \mathbf{R}_x(\alpha)\mathbf{R}_y(\beta)\mathbf{R}_z(\gamma) = \begin{bmatrix} 1 & 0 & 0 \\ 0 & \cos\alpha & -\sin\alpha \\ 0 & \sin\alpha & \cos\alpha \end{bmatrix} \begin{bmatrix} \cos\beta & 0 & \sin\beta \\ 0 & 0 & 1 \\ -\sin\beta & 0 & \cos\beta \end{bmatrix} \begin{bmatrix} \cos\gamma & -\sin\gamma & 0 \\ \sin\gamma & \cos\gamma & 0 \\ 0 & 0 & 1 \end{bmatrix} \tag{7.13}$$

During each function evaluation, the x, y, and z ranges of the point set expressed in $\mathbf{M}_{box}$ are determined. The objective function to be minimized is defined as the area of the resulting volume $x_r y_r z_r$. The three principal components are used as initial estimates to define the axes of $\mathbf{M}_{box}$. The final solution gives the reference frame $\mathbf{M}_{ref}$.

Note that the minimum enclosing box and rectangle can also be found using the rotating calipers method [Tou83, O'R85]. The rotating calipers method is based on the observation that one side of a minimal rectangle must coincide with one edge of the convex hull of the point set it contains. Therefore, only the orientations given by the edges of the convex hull have to be considered. This can be extended to three dimensions to find the minimum enclosing box. However, the PCA generally finds an accurate initial estimate of minimum enclosing rectangles and boxes, such that the optimization procedures are efficient and provide a common framework for all fitting routines.

The cylinder and sphere fitting routines are standard least squares routines. The optimization parameters of the cylinder fit are a point on the cylinder axis C, the direction of the axis D, and the radius r. As discussed in [Sha98], the Levenberg-Marquardt algorithm can be used as unconstrained optimization procedure to minimize the objective function

$$J(D, C, r) = \sum_{i=1}^{N} (|D \times (p_i - C)| - r)^2 \tag{7.14}$$

A reasonable initial estimate for the cylinder axis can be obtained from the principal components. The least squares fitting procedure is performed using each principal component as an estimate of the cylinder axis, and the center of the data as point on the axis. The solution that gives the lowest value of the objective function in Equation 7.14 is selected. The cylinder corresponds to a translational DOF, followed by a rotational DOF. The reference frame $\mathbf{M}_{ref}$ is given by the coordinate system with the z-axis aligned with the cylinder axis, and the x-axis such that the angles that the data points make with the z-axis is symmetric around zero. Similarly, the position of $\mathbf{M}_{ref}$ is chosen such that the translations of the data points, as obtained by projecting them onto the cylinder axis, are symmetric around zero.

The sphere fit is performed by optimization of its center C and its radius r. The objective function to be minimized is given by

$$J(C, r) = \sum_{i=1}^{N} (|p_i - C| - r)^2 \tag{7.15}$$

Analogous to the annulus fit, the initial estimate for C and r are provided by expressing the point set in the coordinate system defined by the principal components. Next, the minimum

and maximum values of the x, y, and z components are determined, giving 6 coordinates. Each combination of 4 points is used to calculate an estimate of C and r, which is used to perform the least squares optimization. The solution with the lowest value of Equation 7.15 is selected. Next, the azimuth and elevation range in which the point set lies is optimized. This is achieved by optimizing the elevation axis, expressed as two angles α, β, to minimize the objective function

$$J(\alpha, \beta) = (\theta_2 - \theta_1)(\cos\phi_1 - \cos\phi_2)r^2 \tag{7.16}$$

where $\theta_1, \theta_2, \phi_1, \phi_2, r$ are functions from α, β.

7.3.3 Skeleton Estimation

The fitting routines described in the previous section provide a method to determine the DOF relation between a single marker and a reference coordinate system. By defining a local coordinate system in a single marker location that moves according to its DOF, the DOF relation between single markers can be determined. The basis of skeleton estimation is to repeatedly execute the fitting techniques to find all possible DOF relations between each pair of segments. These DOF relations are used to determine the 'best' skeleton structure of the composite interaction device. This structure is optimized to contain those DOF relations between segments that describe the structure most compactly. The skeleton structure is found by calculating a minimum spanning tree (MST), where the fitting results of segment pairs are compared to determine which DOF relation is to be considered more optimal than another.

The calculation of the MST is accomplished by an adaptation of Prim's minimum spanning tree (MST) algorithm, as outlined in Algorithm 1. The procedure determines the model graph $G = (V, P, D, \Psi)$ as defined in Section 7.3.1.

The method works as follows. First, all data points are assigned to segments using the marker identifiers obtained from frame-to-frame correspondence. Algorithm 1 then slowly grows a minimum spanning tree that describes the hierarchical skeleton structure and DOF relations of the segments of the device. It starts from a single segment and adds new DOF relations that link the partial model tree to a new segment outside of the tree.

Algorithm 1 BUILD_TREE($G(V, P, D, \Psi)$)

```
Q ← V
for all u ∈ Q do
    D_u ← NIL
end for
P_0 ← NIL
while Q ≠ ∅ do
    u ← EXTRACT_MIN(Q)
    for all v ∈ Q do
        d ← FIND_DOF_RELATION(v, u)
        if SIMPLER_DOF_RELATION(d, D_v) then
            P_v ← u
            D_v ← d
        end if
    end for
end while
```

The routine FIND_DOF_RELATION(v, u) determines the DOF relation between segments v and u in the graph. The data points p_{v_i} of segment v are expressed in the local coordinate system of segment u, using

$$\mathbf{M}_{u_{local}} = \mathbf{M}_{u_{ref}}\mathbf{M}_{u_{dof}}^{-1}\mathbf{M}_{u_{ref}}^{-1} \tag{7.17}$$

$$p'_{v_i} = \mathbf{M}_{u_{local}}^{-1} p_{v_i} \qquad i = 1, \cdots, N \tag{7.18}$$

where $\mathbf{M}_{u_{dof}}$ is the transformation matrix formed by the DOF parameters of node u, and $\mathbf{M}_{u_{local}}$ is the local coordinate system of u. Next, the geometric fitting routines outlined in Figure 7.5 are applied to p'_{v_i} to determine a DOF relation. This relation d is checked by the function SIMPLER_DOF_RELATION(v, u), which compares d to the DOF relation already assigned to vertex v, D_v. If the new DOF relation is considered more optimal, the parent of v is set to u and its DOF relation D_v is updated. A DOF relation is considered more optimal than another under the following conditions:

1. The geometric shape has lower dimension, or
2. The geometric shape provides a tighter fit with the point set if the dimensions are identical (i.e. the model describes the point set better).

To construct the matrix $\mathbf{M}_{dof}$ in Equation 7.17, the data points p_i are expressed in the reference coordinate system, $p'_i = \mathbf{M}_{ref}^{-1} p_i$. In case of a DOF relation with azimuth, elevation, radius (AER) parameters, $\mathbf{M}_{dof}$ is formed as

$$r = |p'_i| \tag{7.19}$$

$$\alpha = \tan^{-1}\left(\frac{p_i.y'}{p_i.x'}\right) \tag{7.20}$$

$$\epsilon = \cos^{-1}\left(\frac{p_i.z'}{|p'_i|}\right) \tag{7.21}$$

$$\mathbf{M}_{dof} = \mathbf{R}_z(\alpha)\mathbf{R}_y(\epsilon)\mathbf{T}_z(r) \tag{7.22}$$

where $\mathbf{R}_y$ and $\mathbf{R}_z$ represent the rotation matrices around the y and z axes, and $\mathbf{T}_z$ represents the translation matrix in the z direction. Note that the spherical coordinates of a data point are directly interpreted as DOF parameters. In case of a translational DOF, $\mathbf{M}_{dof} = \mathbf{T}(p'_i)$, where the cartesian coordinates of a data point are interpreted as DOF parameters. In case of a cylindrical DOF, $\mathbf{M}_{dof}$ is written as

$$t = p_i.z' \tag{7.23}$$

$$\alpha = \tan^{-1}\left(\frac{p_i.y'}{p_i.x'}\right) \tag{7.24}$$

$$\mathbf{M}_{dof} = \mathbf{T}_z(t)\mathbf{R}_z(\alpha) \tag{7.25}$$

Note that Algorithm 1 always finds the tree of lowest cost as defined by these conditions. Each vertex pair is examined for DOF relations, making the cost of the method $O(N^2 \log_2(N))$, where $N = |V|$. A convenient property of Prim's MST method is that a tree is maintained at each step of the procedure. Therefore, local coordinate systems need not be recalculated each iteration, but can be propagated directly to a segment's children.

Figure 7.9 gives an example of the results of skeleton estimation. Consider three segments v_i, for which the structure must be examined. The first segment is a reference segment,

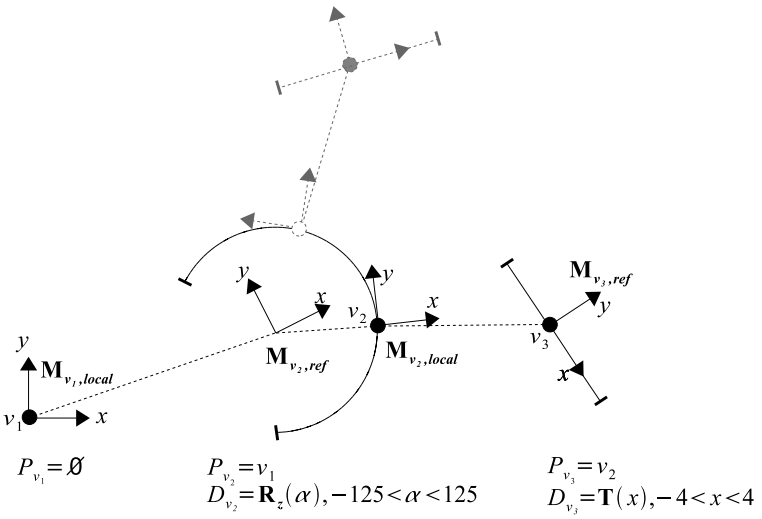

Figure 7.9: An example of skeleton estimation. The model consists of three segments, where segment v_1 is a reference segment. Segment v_2 has one rotational DOF D_{v_2} with respect to its parent $P_{v_2} = v_1$. Segment v_3 has one translational DOF D_{v_3} relative to its parent $P_{v_3} = v_2$.

for which a full coordinate system has been obtained by the rigid body model estimation techniques. Skeleton estimation proceeds by examining all (node, parent) relations (v_2, v_1), (v_3, v_1), (v_2, v_3), and (v_3, v_2). The resulting structure is (v_2, v_1), (v_3, v_2), such that v_2 has one rotational DOF relative to v_1 and v_3 has one translational DOF relative to v_2. Other structures are suboptimal. Consider for instance a structure that includes the relation (v_3, v_1). Expressing the point set of segment v_3 in $\mathbf{M}_{v_1,local}$ results in a complex two-dimensional figure, that cannot be expressed in one variable. In contrast, expressing the point set of v_2 in $\mathbf{M}_{v_1,local}$ results in a circle arc, which can be represented by one rotational DOF.

7.3.4 Handling Noise

The model estimation techniques presented in this chapter are sensitive to noise and outliers in the data. To remove outliers from the data, a simple clustering technique is used. Since each marker trajectory is a time series, the position of a marker at time t is close to the position at time $t + \Delta t$, where $\frac{1}{\Delta t}$ represents the frame rate at which data is recorded. As a result, data points that are further than a certain threshold distance from the rest of the time series are removed. Since during model estimation motion is slow and smooth, this threshold can be chosen small.

An alternative approach would be to use a RANSAC [FB81] algorithm. RANSAC chooses random sets of points to which the fitting methods are applied, until a fit metric is within a given tolerance. This has the advantage of making the model estimation method very robust against noise and outliers. The disadvantage is that model estimation takes longer.

Other techniques to make the model estimation techniques more robust are to apply filtering and prediction techniques to compensate for noise and latency (see Chapter 6). Another

approach would be to use weighted fitting routines, where data points are given a measure of importance based on various metrics, e.g. blob size, distance from the epipolar lines, and local density.

7.4 Model-based Object Tracking

Given labeled 3D marker locations, model-based object tracking proceeds in three steps.

- *Rigid body tracking*
  The segments that consist of three or more markers are identified. These segments define the initial reference frames used to identify single marker segments. They are tracked using the rigid body tracking techniques described in Chapter 4.
- *Single marker segment tracking*
  The skeleton structure and DOF model are used to identify single marker segments.
- *Occlusion handling*
  The situation where the parent of a segment is lost due to occlusion is dealt with. In these cases, the children of the lost segment cannot be found by using the DOF relations in the skeleton structure.

7.4.1 Single Marker Segment Tracking

The goal of tracking the single markers segments is to determine the values of their degrees of freedom with respect to their parents. These DOFs can be coupled to application parameters, which a user needs to manipulate in order to perform a complex interaction task.

The DOFs of each segment are determined by using the reference coordinate systems obtained from rigid body tracking and the model information. The model defines the skeleton structure and the DOF relations and ranges of the single marker segments. An exhaustive search is performed that matches markers to model segments, and prunes the search space using a backtracking approach. The resulting procedure is outlined in Algorithm 2.

The procedure TEST_DOF(S, p) is called for each unidentified marker p and each segment S for which a reference coordinate system has been found. A stack σ is maintained,

Algorithm 2 TEST_DOF(S, p)

```
σ.PUSH(S, p)
if DOFMATCH(S, p) then
  S.m ← p
  UPDATEBEST()
  for all S ∈ CHILDREN(S) do
    for all p ∈ P do
      TEST_DOF(S, p)
    end for
  end for
else
  σ.POP()
end if
```

which holds the matches between segments and markers. When the procedure is called, the stack is updated, and DOFMATCH(S, p) is called to check if the current point can be expressed by the DOF model of segment S. The point p is expressed in the reference frame $\mathbf{M}_{ref}$ of S, and its DOF parameters are calculated according to the model. If the parameters are within the ranges of the DOF parameters in the model, the best match is updated by calling UPDATEBEST(), and the child segments of S are examined. If there is no match, the algorithm backtracks by popping the stack σ. Note that Algorithm 2 is a simple extension of a depth first search to include a backtracking step.

The procedure finds a maximum length match between markers and model segments. It exploits the hierarchy in the model for efficient DOF testing. Since it maintains a tree, the local coordinate systems of identified segments can be stored and used in subsequent segments. The model allows for information propagation during tracking. As relations between markers and reference frames are determined, this information is used to construct new reference frames to identify new segments. However, when a segment is lost, the procedure fails to find its child segments. In the next section, the techniques used to make the tracker robust to occluding segments are discussed.

7.4.2 Occlusion Handling

The previous sections have described methods to track segments with three or more points, and how this information is used to construct reference coordinate systems and to identify segments with single markers. The techniques for tracking three or more points require sufficient points to unambiguously construct a coordinate system, but do not require all points of the segment to be visible. However, when a single marker segment is occluded, all its child segments cannot be identified. The DOFs of these segments are defined relative to the local coordinate system of the occluded segment. To address this problem, the DOF relations between all segments are stored in the model, next to the DOF relations that are part of the skeleton structure. The skeleton relations are used for the tracking procedure described in Section 7.4.1. In case some segments are determined to be occluded and unidentified markers are present after this procedure, the remaining relations are used to identify single marker segments relative to other parent segments.

In general, only the 3D location of segments with an occluded parent can be determined. Only when a parent segment is completely redundant, i.e., when an unambiguous relation of its child segments with other parents was correctly found, the DOF parameters of the child segments and of the lost parent segment can be determined. As such, extra redundancy can be introduced to the interaction device. The advantage is that the device is better suited to handle partial occlusion.

7.5 Results and Discussion

The model-based optical tracking and automatic model estimation techniques have been implemented and evaluated in the PSS. For the following tests, a two-camera setup was used.

7.5.1 Model Estimation

Figures 7.10 and 7.11 show the results of model estimation for two composite interaction devices. The figures depict the devices, along with the model points as determined by the

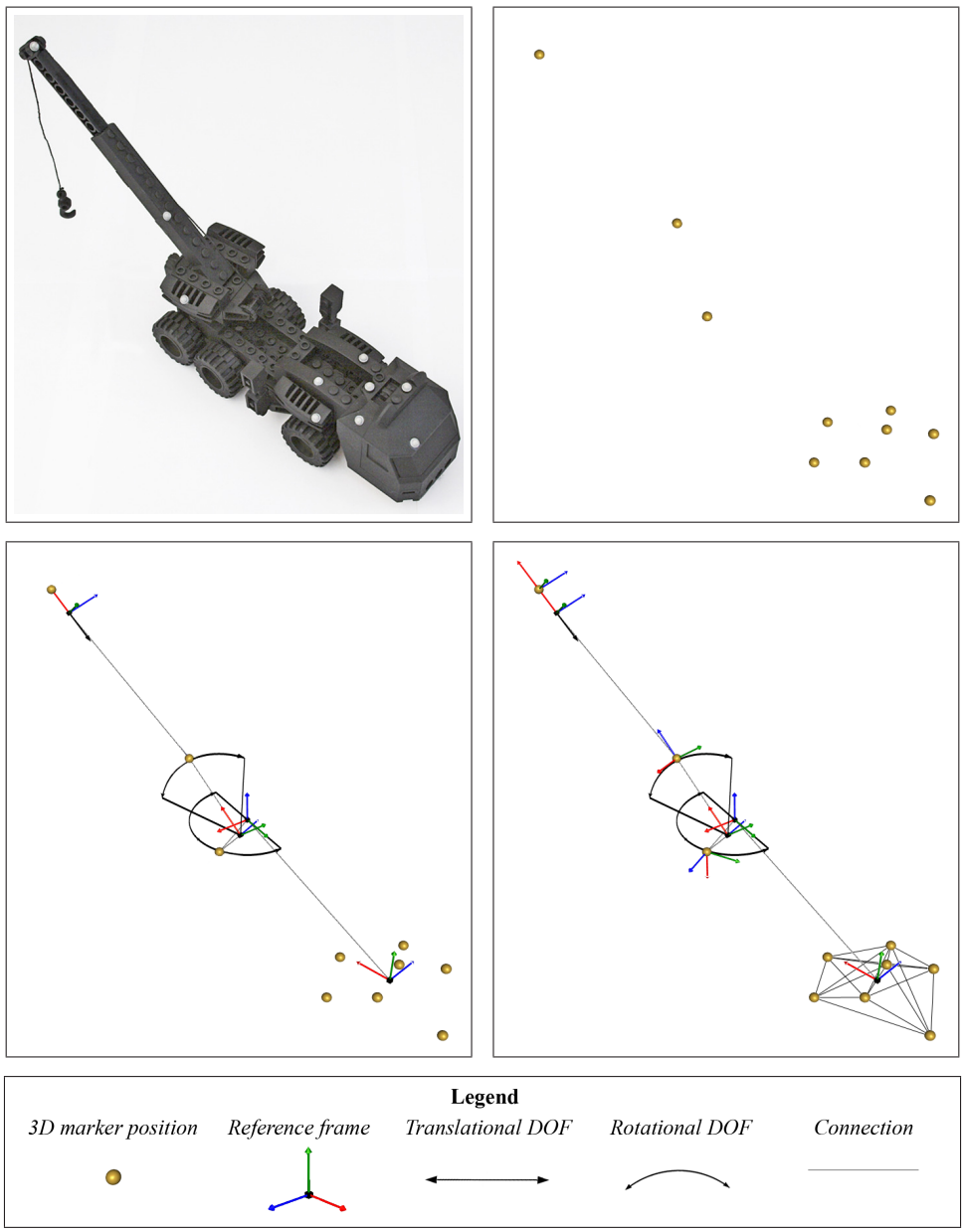

Figure 7.10: Model estimation results of a composite interaction device. At the top, a crane is depicted, along with the model points. At the bottom left, the complete model is illustrated with the skeleton structure, reference coordinate systems, model points, and DOF relations and ranges. The bottom right shows the complete model including local coordinate systems at the marker locations.

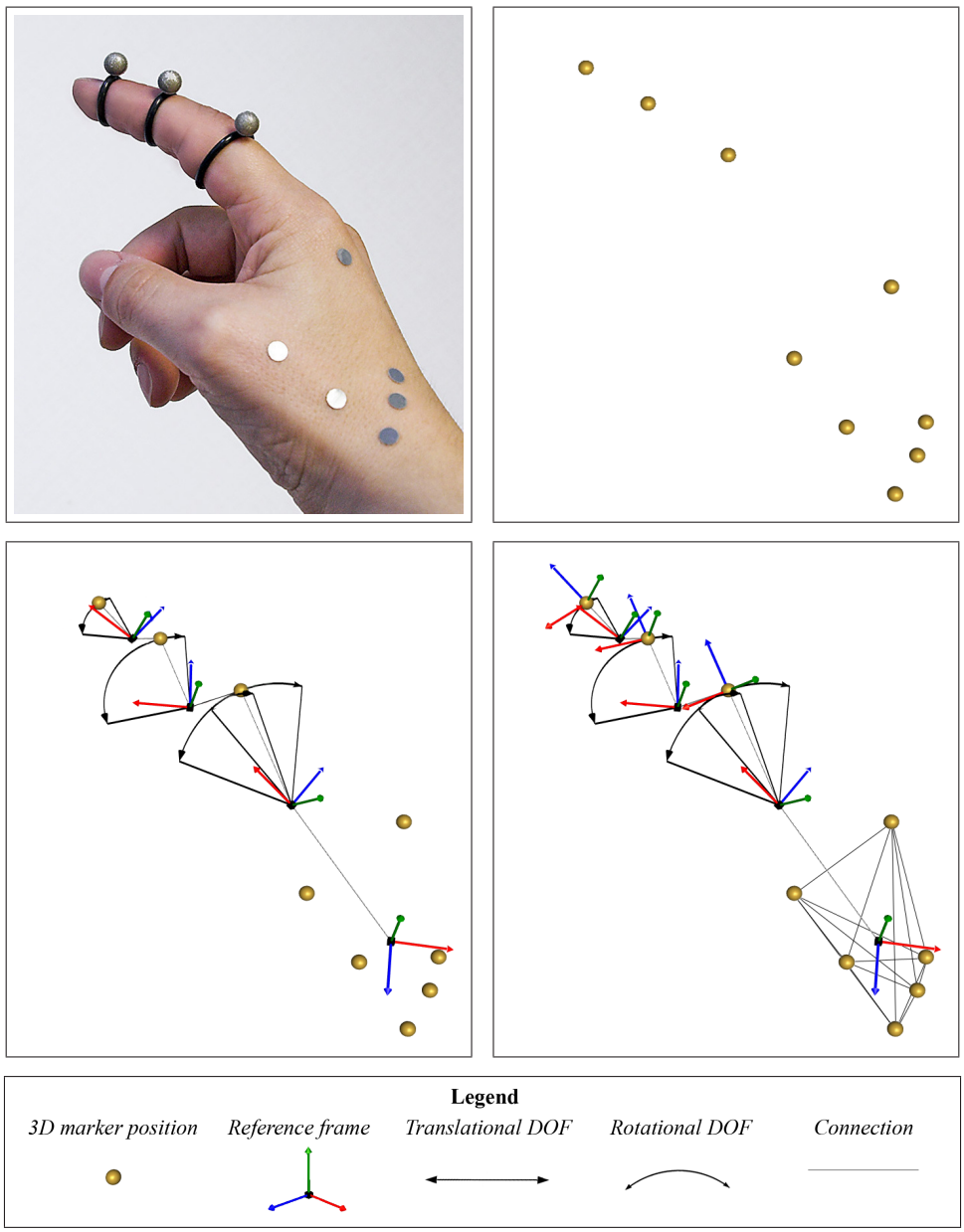

Figure 7.11: Model estimation results of a composite interaction device. At the top, a finger is depicted, along with the model points. At the bottom left, the complete model is illustrated with the skeleton structure, reference coordinate systems, model points, and DOF relations and ranges. The bottom right shows the complete model including local coordinate systems at the marker locations.

	Crane				*Finger*			
seg.	model	param	range		model	param	range	
1	AER	a	-90.3	90.3	AER	a	-19.3	19.3
		e	90	90		e	34.8	115.0
		r	2.46	2.58		r	3.55	3.55
2	AER	a	-40.6	40.6	AER	a	-2.4	2.4
		e	90	90		e	4.6	108.5
		r	3.98	4.16		r	2.34	2.34
3	Trans	x	-1.29	1.29	AER	a	-1.56	1.56
		y	0	0		e	63.6	129.6
		z	0	0		r	1.43	1.43

Table 7.2: DOF ranges of the device segments of Figures 7.10 and 7.11, where rotational DOFs are given in degrees, and translational DOFs in cm.

automatic model estimation procedure. The lower parts of the figures show the complete models, including reference coordinate systems and DOF relations and ranges, and the models with the local coordinate systems at the marker locations, as defined by the DOF relations. Table 7.2 lists the relevant DOF parameters corresponding to the models in Figure 7.10. Both devices were moved in front of the cameras over a period of about one minute (3397 frames for the crane, and 3162 frames for the hand). The developer should take care to sweep through the DOF ranges, so that the system has enough data to recognize the underlying geometric shapes. After the developer has shown the system all DOFs in the device, skeleton estimation is performed. This procedure took less than 30 seconds for the examples in Figures 7.10 and 7.11. The DOF parameters listed in Table 7.2 were verified by hand, and by applying the obtained model in the tracking system.

Note that these devices represent simple examples, illustrating some of the DOFs the system can handle. For instance, an assumption of the finger example is that the thumb is not moved, so that the reference frame is kept rigid. In a practical situation, one could attach a rigid structure to the hand or glove. In Chapter 8, the model estimation and tracking techniques for composite interaction devices are applied in a real world scenario. A configurable interaction device is developed and applied in various VR applications.

The 3D marker locations that are reported by the tracking system of the PSS contain measurement noise, which is included in the model estimation procedure. Since this noise is encountered in practice during tracking, it is advantageous that this noise is modeled. However, noise is propagated as more segments are connected during the model estimation procedure. Obtained DOF relations between single markers and reference coordinate systems are used to construct new coordinate systems. A subsequent marker expressed in this coordinate system contains a combination of its own noise and the noise in the coordinate system. As an example, the radius range of the first single marker segment of the crane in Figure 7.10 is about 1.1 mm (which ideally should be 0). Its child segment has a radius range of 1.8 mm, which is a combination of its own noise and the noise of its parent segment. Clearly, long chains of segments are more difficult to train, as the tolerances of the fitting routines would have to be set to prohibitively high values. However, the noise can be reduced by using a weighted fitting strategy, such that more trusted data is more important. For instance, a local density estimate of each data point can be used as a weight factor.

Another possibility to increase the accuracy of the model is to use more cameras. A very minimal setup with only two cameras was used, where the noise in a single 3D point was

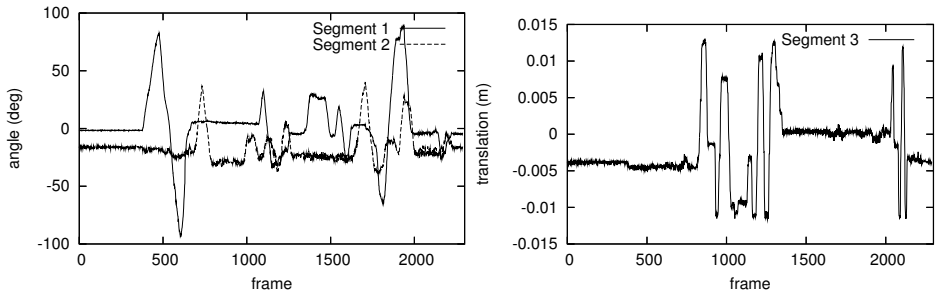

Figure 7.12: The DOFs of the crane model, as determined by the tracking system during a 39-second motion data set. (Top) The rotational DOFs of the crane's base and arm. (Bottom) The translational DOF of the crane's arm extension.

determined to have a maximum value of about 2 mm. More cameras or larger markers would provide more accurate 3D point measurements. One could also use more markers on a single segment higher up a chain. Each segment for which a full reference frame can be determined effectively resets the noise propagation in a chain.

Note that this system only finds DOF relations between single marker segments and a reference coordinate system. When an interaction device contains multiple segments with three or more points, the DOF relation between two coordinate systems also needs to be determined. To support DOF relations between coordinate systems, the work of Hornung et al. [HSDK05] could easily be incorporated, extending their approach to provide a higher level DOF description. The skeleton estimation and tracking procedures would remain the same.

The motion data sets to obtain the models of Figures 7.10 and 7.11 were both about a minute in length. Model estimation completes in less than a minute. The time required for calculating a model depends on the structure of the device, the complexity of the fitting routines, and the complexity of the skeleton estimation procedure, which is $O(N^2 \log_2(N))$ with N the number of segments. Clearly, for larger data sets computation time increases rapidly. However, the model estimation procedure is a post processing procedure, which is fully automated.

7.5.2 Model-based Object Tracking

The model of the crane as acquired from the model estimation procedure (see Figure 7.10) was used as input to the model-based tracking system. Figure 7.12 depicts the DOFs of each segment for a data sequence of 2360 frames, which is about 39 seconds. In this sequence, each segment was manipulated with varying speeds. The tracking system identified all segments and their DOFs correctly in 97.16% of the data sequence. The figure shows the rotational DOF of the base of the crane and the rotational DOF of the arm. On the right, the translational DOF of the arm's extension is shown. The system maintains a frame rate of 60 Hz throughout the tracking sequence, which is constrained by the speed of the cameras.

A problem may occur during tracking when invalid markers, or markers from other devices, come within the range of a DOF relation between two segments. Since the tracker tries to maximize the number of matches between markers and segments, the system often rejects these stray markers. However, if a stray marker comes within the DOF range of a segment

without children, it is uncertain which marker is the correct one. In these cases, the tracking system could use history information to determine the best match.

7.6 Conclusion

In this chapter, a model-based optical tracking and automatic model estimation system was presented. The system supports composite interaction devices, which consist of several segments connected in a tree structure. Segments can have combinations of translational and rotational degrees of freedom with respect to a parent segment. The system requires only one segment to contain three or more markers, such that a full coordinate system can be determined and the tracking system can be kept fast and efficient. Other segments may contain only one marker. This allows for small interaction devices, without the need for large numbers of markers on each moving segment. Moreover, when larger numbers of markers are used, the model automatically includes this extra redundancy, allowing for more occlusion during tracking.

The model provides a high level DOF description between segments, along with the ranges of these DOFs and the skeleton structure. No pre-defined models are required. The tracking system uses the model estimate to recognize the device in a backtracking approach. The tracking method supports partial occlusions.

Model estimation is based on estimating the DOF relation between a marker and a coordinate system. When such a relation has been found, the system determines a local coordinate system in the marker according to the DOFs. However, noise may get propagated throughout a branch of connected segments. More research can be done to investigate noise reduction techniques. For instance, a local density estimate could be used as an importance measure of a data sample.

Chapter 8

A Configurable Interaction Device

In Chapters 3 and 4, techniques were developed and evaluated for optical tracking and automatic model estimation of rigid interaction devices. In Chapter 6 filtering and prediction techniques were analyzed, which can be used to reduce noise and latency problems. The developed tracking techniques were extended in Chapter 7 to handle composite interaction devices. In this chapter, all these techniques are combined in an optically tracked configurable interaction device. The aim of the device is to allow an interface developer to rapidly construct new devices, of which the spatial structure can match the structure of the task at hand. The device is tested in a number of application scenarios.

8.1 Introduction

Interaction in a virtual environment is often a complicated task. Designing effective interaction techniques is especially difficult when a user has to manipulate many parameters to complete a task. There have been various approaches to designing input devices for such high dimensional input tasks. One approach is to use a device with a relatively small number of degrees of freedom (DOFs) that can be put into different modes, for instance by using extra buttons or menu selections. Such mode switching may interrupt the task flow and present an extra cognitive load on the user [JS92]. Another option is to use multiple devices and assign different subtasks to each of them. In this case, mode switching is implicit in the selection of a device, and may present the same interruption of task flow. One could also construct a single device specific for a particular application or interaction task. This way, a user has direct control over all required DOFs. However, constructing a new device from scratch for each interaction task is inefficient and impractical.

An approach to relieve these limitations would be to construct flexible interfaces, which can be reconfigured for specific interaction tasks. One way to achieve this is to create interfaces that can easily be changed in software, for instance by using 2D widget interfaces attached to handheld props [CW99, KL04].

In this chapter, another approach is explored: the development and application of a configurable input device, which can easily be configured specifically for a required interaction task. The aim of the device is to meet the objectives as defined in Chapter 1:

- A user should be able to manipulate a large number of application parameters with a single, compact device.
- A developer should be able to structure the device such that it reflects the parameters of the interaction task at hand.
- A developer should be able to rapidly develop new interaction techniques and test new

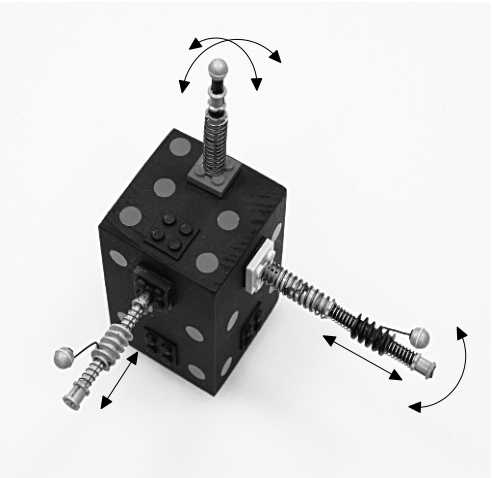

Figure 8.1: An example device configuration with three actuators.

configurations.

- The device should be optically tracked, resulting in a compact, light, wireless, low-cost, and unobtrusive interaction device.
- Two-handed interaction and proprioception should be exploited.

The developed configurable interaction device (CID) is based on two components: the base object and the actuators. Each configuration of CID consists of a base object, which defines a (six DOF) frame of reference. The base object has a number of connection points, to which actuators can be attached. Actuators define interaction relative to the base object. They can have various combinations of translational and rotational degrees of freedom. For instance, an actuator can be a slider, having one translational DOF, or a joystick, having two rotational DOFs. An actuator may consist of several linked segments, incorporating multiple joints. Interaction is performed by positioning and orienting the base object and by manipulating the actuators.

An example configuration of CID is shown in Figure 8.1. The base object is a box, to which three actuators are attached. The actuator on the top has two rotational DOFs, corresponding to a joystick. The left actuator has one translational DOF, while the right actuator has one rotational and one translational DOF.

CID is optically tracked. This allows CID to be low-cost, compact, light weight, wireless, and unobtrusive. The tracking system is described in Chapter 7. It needs to identify at least three markers on the base object to be able to unambiguously determine a frame of reference, whereas actuators can have as little as one marker. This results in configurations that are small enough for comfortable interaction. The system can automatically obtain a hierarchical model of a new configuration of CID by the model estimation procedure described in Chapter 7. During this procedure, a developer simply moves the device in front of the cameras, manipulating each actuator such that the system can determine the DOFs and DOF ranges of each actuator.

The configurable interaction device was tested in three application scenarios. The first is

a modeling application, which enables a user to quickly design new object shapes by manipulating a set of control points. The second is a scientific visualization application, used for the manipulation and exploration of a volume rendering of a human head. The third application enables a user to create animations of a 3D virtual representation of a human skeleton.

This chapter is organized as follows. In Section 8.2, related work is reviewed. Section 8.3 describes the configurable interaction device in detail. In Section 8.5, the flexibility of CID is illustrated using three device configurations in different application scenarios. Section 8.6 provides a discussion of the results. Finally, in Section 8.7 conclusions are given.

8.2 Related Work

Relatively little work has been done on interaction devices that enable a user to manipulate a large number of degrees of freedom in a single device. Most previous work on devices for complex interaction tasks uses multiple props. For instance, Hinckley et al. [HPGK94] proposed two handed interaction for neurosurgical visualization using several props. Balakrishnan et al. [BFKS99] presented a single, application specific device for curve and surface manipulation. It is based on a bend and twist sensitive strip.

Ayers et al. [AZ96] presented a rapid prototyping system for physical interaction devices. The system allows quick assembly of interaction hardware based on snapping Lego® parts together. However, the system is limited to three types of sensors. Fitzmaurice et al. [FIB95] presented a software and hardware framework for graspable user interfaces. The framework allows for rapid development of interfaces for complex interaction tasks.

Various researchers have proposed the use of 2D widget interfaces attached to handheld props [CW99, KL04]. Subramanian et al. [SAM03] evaluated the use of hybrid 2D and 3D interfaces. An experiment was conducted that requires users to navigate an intersection plane through a solid 3D model, in order to locate a disc hidden inside the body of the model. They found that the combination of a 3D and a 2D prop, along with the possibility of constraining the DOFs, allowed users to complete the task faster than using only a 2D or 3D interface.

The configurable interaction device presented in this chapter shares ideas with the Cubic Mouse, which was presented by Fröhlich et al. [FP00]. The Cubic Mouse is a handheld device, designed for complex interaction tasks. It allows for direct manipulation of a relatively large number of parameters. The device is depicted in Figure 1.3(b). It consists of a cubic base, with three orthogonal rods passing through it. Virtual objects can be translated and rotated relative to the pose of the cube by manipulating the rods. It is mostly used for scientific data visualization, where the cube controls the pose of a 3D model, and the rods are used to move slicing planes through the data set using position control techniques.

Simon et al. [SF03] introduced the YoYo, a handheld interaction device that combines elastic force input and isotonic input. The device is depicted in Figure 1.3(c). It consists of a cylindric base, with two rings on each side that can be moved relative to the base. The rings are used as elastic six DOF force sensors. The device enables a user to directly control a coordinate system using the cylindric base, and two additional coordinate systems using elastic force input.

This chapter complements previous work by introducing a configurable interaction device, rather than a fixed device suited for a specific type of application. A developer can rapidly design and evaluate new interaction devices. Moreover, the device allows for a direct relation between the structure of the device and the parameters of the interaction task.

Figure 8.2: Base objects of CID

8.3 CID Construction

The main goal of CID is to allow a developer to rapidly design and evaluate new interaction devices that provide natural and intuitive interfaces for complex interaction tasks. To accomplish this, the structure of the perceptual space should mirror that of the control space [JS92]. This implies that if a user perceives attributes as related, the structure of the device should reflect this, allowing the user to manipulate the attributes in parallel. The structure of the device should reflect the application parameters. Moreover, the device should enable a user to manipulate integral and separable dimensions effectively.

To be able to define a frame of reference in which interaction is performed, the device is built from two components: a base object, which defines a six DOF coordinate system, and actuators, which define interaction relative to the base object. Different actuators can be used for manipulating separable dimensions. CID can be configured by selecting a base object and attaching the desired actuators to it.

A prototype of CID was made using off the shelf components. Wooden geometric shapes function as base objects. Each base object has a set of connection points, to which actuators can be attached. A developer can choose from a set of prefabricated base objects, such as shown in Figure 8.2.

Actuators are constructed out of Lego® parts. An actuator can have various combinations of DOFs, and can consist of several linked segments, incorporating multiple joints. Figure 8.3 shows four example actuators:

- A slider with one translational DOF, using springs to hold it in a return position.
- A joystick with two rotational DOFs, using a universal joint and a spring to hold it in a return position.
- An actuator with one rotational DOF followed by a translational DOF, using a rotational joint and springs for the return position.
- An actuator consisting of two segments, one with a rotational DOF, followed by a segment with one rotational DOF.

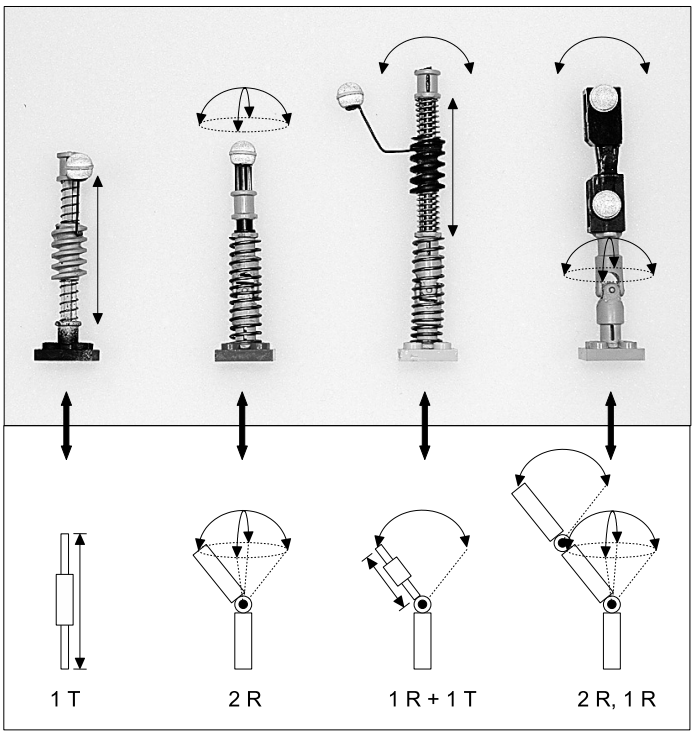

Figure 8.3: Four examples of actuators: a slider with one translational DOF, a joystick with two rotational DOFs, an actuator with one translational and one rotational DOF, and a multi-segment actuator with two rotational DOFs followed by an additional rotational DOF.

CID is tracked using a model-based optical tracking system. The tracker needs to determine the pose of the base object and the DOF values of the actuators, and send them to the application. The system requires that a base object contains three or more (non-collinear) markers, such that a frame of reference can be determined. Figure 8.2 shows these markers as orange circles on the wooden objects. Actuators can have one or more markers per segment, which are shown in Figure 8.3 as silver spheres. Since the tracking system only needs a single marker for an actuator, CID can be kept compact.

8.4 Parameter Mapping

The tracking system developed in Chapter 7 sends the pose of the base object and the degrees of freedom of each actuator directly to the virtual reality application. As a result, the mapping between device DOFs and application parameters has to be hard coded into an application. Consequently, during the development and evaluation of different interaction techniques, the application needs to be repeatedly adjusted. This makes the development cycle a time-consuming and inefficient process.

The flexibility of CID can be improved by adding a step between the tracker and the application, which maps device DOFs to one-dimensional application variables. This way, a

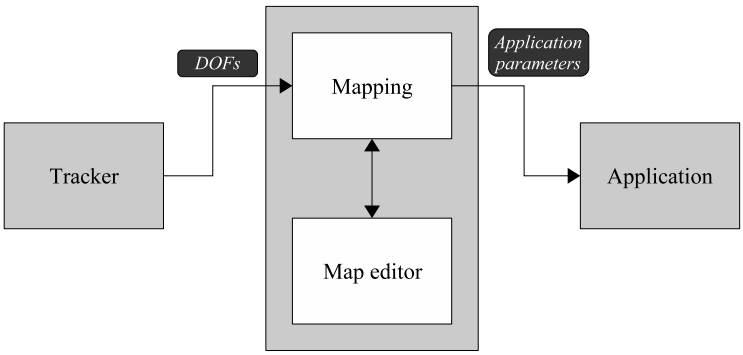

Figure 8.4: Generic mapping of device DOFs to application parameters.

developer is able to adjust various factors that influence the interaction with an actuator, such as its sensitivity, threshold, offset, and filtering parameters, and whether it is position or rate controlled. The effects of changes in the mappings on the interaction can be directly studied in the application.

A generic mapping is introduced between the application and tracker, as illustrated in Figure 8.4. The system consists of four components.

- A *map daemon* continuously monitors the tracker and application, and maps incoming tracker events to application variables. The tracker and application register at the map daemon at startup.
- A *tracker* transmits a list of device parameters to the map daemon upon registration. The parameters describe the type, the range, and the name of each DOF.
- An *application* sends a list of variables to the map daemon that can be manipulated by user interaction. The map daemon then continuously observes the tracker events, maps them to application variables, and sends these on to the application.
- A *map editor* is used to create connections between application variables and device DOFs.

An implementation of the map editor is depicted in Figure 8.5. The figure shows the mapping that was used for the scientific visualization application described in Section 8.5.2. The pose of the base object is considered a special case, and can only be connected to an application variable that represents a 4×4 transformation matrix. All other mappings are used to transform the value of a device DOF d_k at time k to an application variable p_k. A mapping is described by the following parameters:

- *Gaussian filter*
  A Gaussian filter with the specified odd-sized kernel size is applied to the device DOF d_k, resulting in the estimated device DOF $\hat{d}_k$. The filter is described in Chapter 6 by Equations 6.11 and 6.12.
- *Input Parameter*
  The input parameter defines how the estimated DOF value $\hat{d}_k$ is used in the mapping

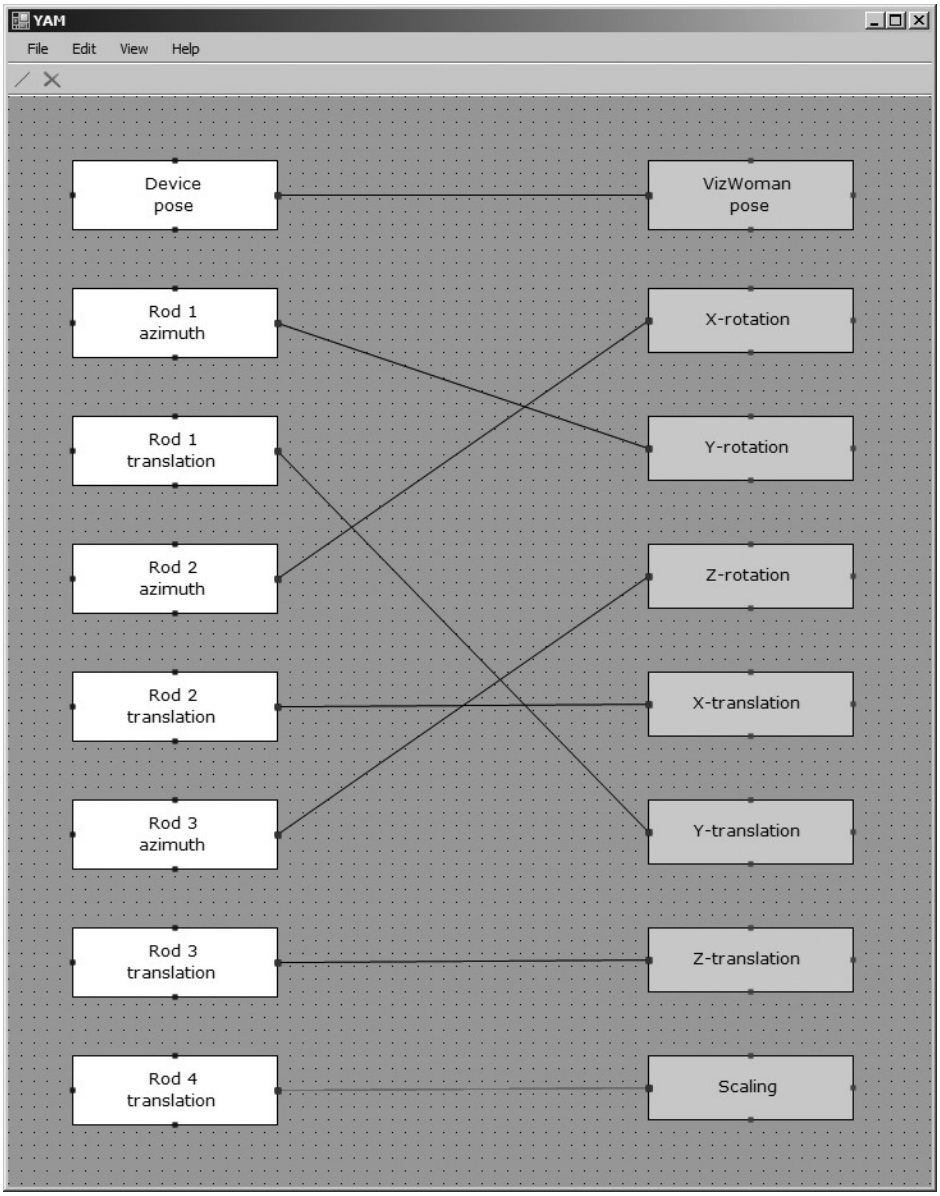

Figure 8.5: An editor that can be used to map device DOFs to application parameters.

function. The input parameter can be set directly to the DOF value $\hat{d}_k$, or to the difference between the current and last DOF estimates $\hat{d}_k$ and $\hat{d}_{k-1}$. In case the DOF is a rotation, the angular difference is used. As such, the input parameter v_k is defined by

$$v_k = \begin{cases} \hat{d}_k & \text{DOF value} \\ \hat{d}_k - \hat{d}_{k-1} & \text{positional DOF difference} \\ \Theta(\hat{d}_k - \hat{d}_{k-1}) & \text{angular DOF difference} \end{cases}$$

where the function $\Theta(\Delta\theta)$ is used to normalize the angular difference to the range $[-pi, pi)$:

$$\Theta(\Delta\theta) = \begin{cases} \Delta\theta & -\pi \leq \Delta\theta < \pi \\ \Delta\theta + 2\pi & \Delta\theta < -\pi \\ \Delta\theta - 2\pi & \Delta\theta \geq \pi \end{cases}$$

- *Target range*
  A scaling function $S(v, r)$ is defined as a linear mapping of the input range $v = [x_1, x_2]$ to the target range $r = [r_1, r_2]$. The function is applied to the input v_k, resulting in a scaled value s_k which is given by

$$s_k = S(v_k, r) = (v_k - x_1)\frac{r_2 - r_1}{x_2 - x_1} + r_1 \tag{8.1}$$

- *Threshold*
  A threshold function $T(v, \epsilon)$ is defined that returns v if $|v| > \epsilon$ and v otherwise. The function is applied to the scaled value s_k, resulting in

$$t_k = T(s_k, \epsilon) = \begin{cases} 0 & |s_k| \leq \epsilon \\ s_k & |s_k| > \epsilon \end{cases}$$

  Changes in a (scaled) DOF that fall below ϵ are not considered as input changes. As such, a dead zone is introduced in which manipulations of the device DOFs do not generate application events. This can be used to reduce unintended operations within the application due to noise in the DOF estimates.

- *Quantization*
  A continuous value can be mapped to a discrete range by specifying a quantization value q. For instance, a rotation between 0 and 360 degrees can be mapped to a discrete interval of integers in the range of 0 to 10 by setting the quantization value to 36. A quantization function $Q(v, q)$ is used to round the value t_k to its nearest discrete value, using

$$q_k = Q(t_k, q) = q\lfloor\frac{t_k + 0.5}{q}\rfloor \tag{8.2}$$

  Alternatively, the quantization function can be set to round to the lower or upper discrete value.

- *Control type*
  This parameter describes the type of control mechanism by which an object's position or orientation is changed. The choices are direct or incremental control. Generally, direct is used for position control scenarios, which refers to the case where a user can

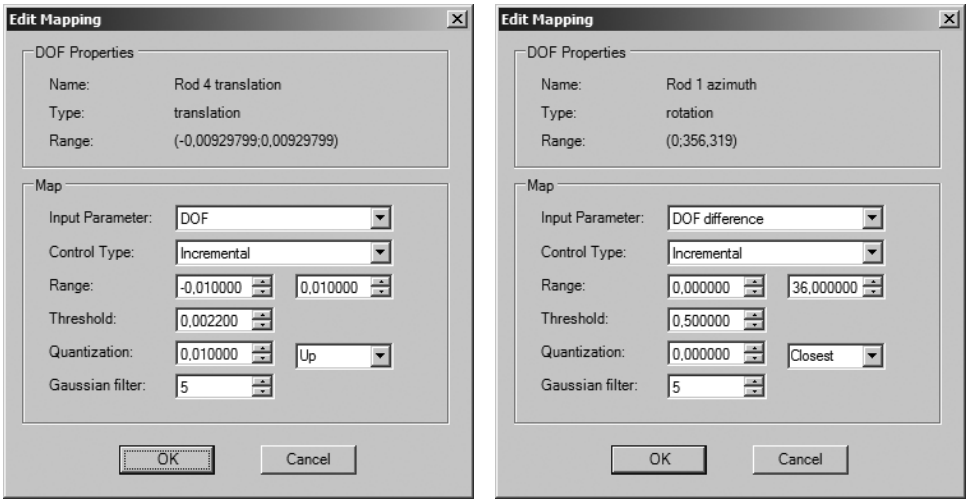

(a) (b)

Figure 8.6: Mapping editor. (a) The mapping parameters for a rate controlled translational DOF to a scaling value, (b) The mapping parameters that couples a rotational DOF to an application variable, such that actuator rotations result in ten times slower rotations in the application.

control an object's position or orientation directly. For rate control, the control type is set to incremental. Rate control maps the user's input to the velocity of the object movement. The control type defines a function

$$C(q_k, q_{k-1}) = \begin{cases} q_k & \text{direct control} \\ q_k + q_{k-1} & \text{incremental control} \end{cases}$$

The complete mapping that transforms the value of the DOF d_k at time k to the application variable p_k is given by

$$p_k = C(Q(T(S(v_k, r), \epsilon), q), p_{k-1}) \tag{8.3}$$

When a user edits a connection between a device DOF and application variable, a dialog with the mapping parameters is presented as shown in Figure 8.6. The figure illustrates two mappings that are used in the application discussed in Section 8.5.2. Figure 8.6(a) depicts the dialog used for editing a rate controlled translational DOF to a scaling parameter, whereas Figure 8.6(b) shows the mapping of a rotational DOF to an application variable that is 10 times less sensitive, using the angular difference as input parameter and incremental control.

Adjusting the parameters of the mapping function provides a convenient way to quickly change the way an application responds to tracker data, while allowing the most common type of mappings to be applied. To support more types of mappings, the system could be extended with a function parser. This would allow a developer to create any one-to-one mapping between device DOFs and application variables. The disadvantage of such an approach is that adjusting mappings becomes more complex. Another possible extension is to allow multiple device DOFs to be mapped to a single application variable and vice versa.

8.5 Applications

CID was evaluated in the PSS, using a tracking setup with four cameras. The device was tested in three application scenarios, each requiring a different configuration. The first is a simple modeling application, which enables a user to create surfaces of revolution. The second is a scientific visualization application, which is used for data exploration and manipulation of a volume rendering of a CT scan. The third application is an animation package. In this application, CID is configured to resemble a human body. By manipulating the actuators of the configuration, the limbs of a model of a human skeleton can be moved into a desired pose. A smooth animation can be created by defining key frames that describe a collection of skeleton poses.

In all applications, the base object is used to define a coordinate system, which is coupled to a virtual object or scene. This basically enables a user to hold an object in his non-dominant hand, while the dominant hand performs the interaction on the object by manipulating the actuators. This type of two-handed interaction exploits proprioception [Gui87].

8.5.1 Modeling

The first application is a modeling application, which allows a user to create surfaces of revolution (see Figure 8.7(a)). A surface of revolution is a surface generated by rotating a two-dimensional curve about an axis. The curve is described by a number of control points. The shape of the object can be altered by selecting and moving control points.

CID is configured as illustrated in Figure 8.7(b). The base object is a 55×55×55 mm cube, which defines the coordinate system of the surface of revolution, allowing a user to hold the surface of revolution in his hands.

At the top of the cube, an actuator is attached which has one translational DOF. This slider is used to select the active control point. Pushing and pulling the slider selects the next or previous control point. The slider can be pushed and pulled relative to the cube over 1.9 cm. To ensure no unintended selections occur, a dead zone was defined in which the slider is inactive. The threshold value for this dead zone was set to 3 mm.

At the right side of the cube, an actuator with one rotational DOF followed by a translational DOF is attached. The rotational DOF of this actuator allows the user to move the control point up and down with respect to the object's axis, whereas the translational DOF is used to move the control point from and towards the axis. The actuator is held in a return position by springs. The angular range is 116 degrees, whereas the translation range is 1.3 cm. The interaction on the control point is rate-controlled, meaning that the speed of movement of the control point depends on the deviation of the actuator from its reference position. Analogous to the actuator used for control point selection, a dead zone was included for robustness.

Figure 8.7(c) depicts the model obtained by the device training procedure. The model shows the 3D marker locations on the base object, along with the DOFs and DOF ranges of the actuators.

8.5.2 Manipulation and Data Exploration

A scientific visualization application was created, enabling data exploration and manipulation. A user is presented with a volume rendering of a Computed Tomography (CT) scan of a human head (see Figure 8.8(a)). Three orthogonal slicing planes can be manipulated to cut

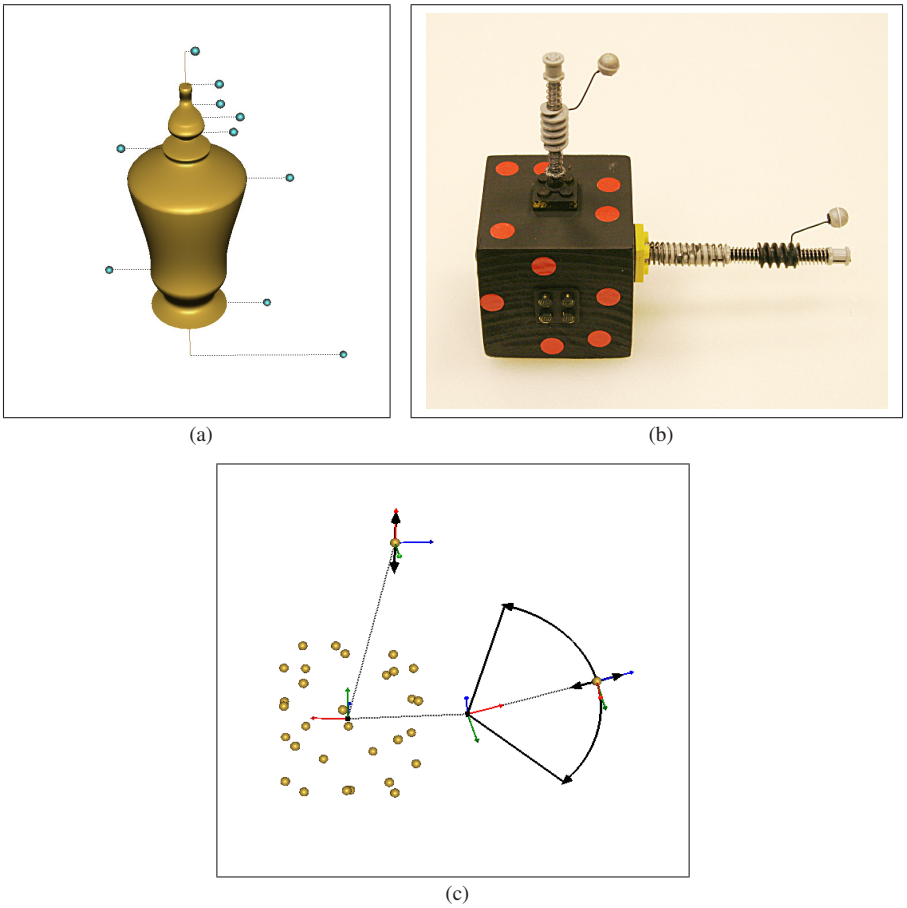

Figure 8.7: (a) A modeling application. (b) CID's configuration, consisting of a cube and two actuators controlling the shape of the virtual model. (c) The model of the configuration, as acquired by the device training procedure.

through the data set along the main axes. Slicing a data set is a basic and frequently used task in scientific visualization for data exploration. Additionally, the user is able to zoom in/out of the data set, and the data set can be rotated with respect to the slicing planes.

CID is configured as depicted in Figure 8.8(b). The base object is a 7×7×7 cm truncated cube. This base object is coupled to the virtual data set of the CT scan, such that the data set can be viewed from every angle.

Three sides of the interaction device are equipped with actuators having one rotational DOF and one translational DOF along the rotation axis. The translational components allow the user to move the slicing planes along the principal axes that are defined by the truncated cube. The rotational component allows for rotation of the data set around these principal axes.

The degree to which a user is able to bring a data set closer to him for closer inspection is limited in the PSS. Therefore, an extra actuator with one translational DOF is attached to one

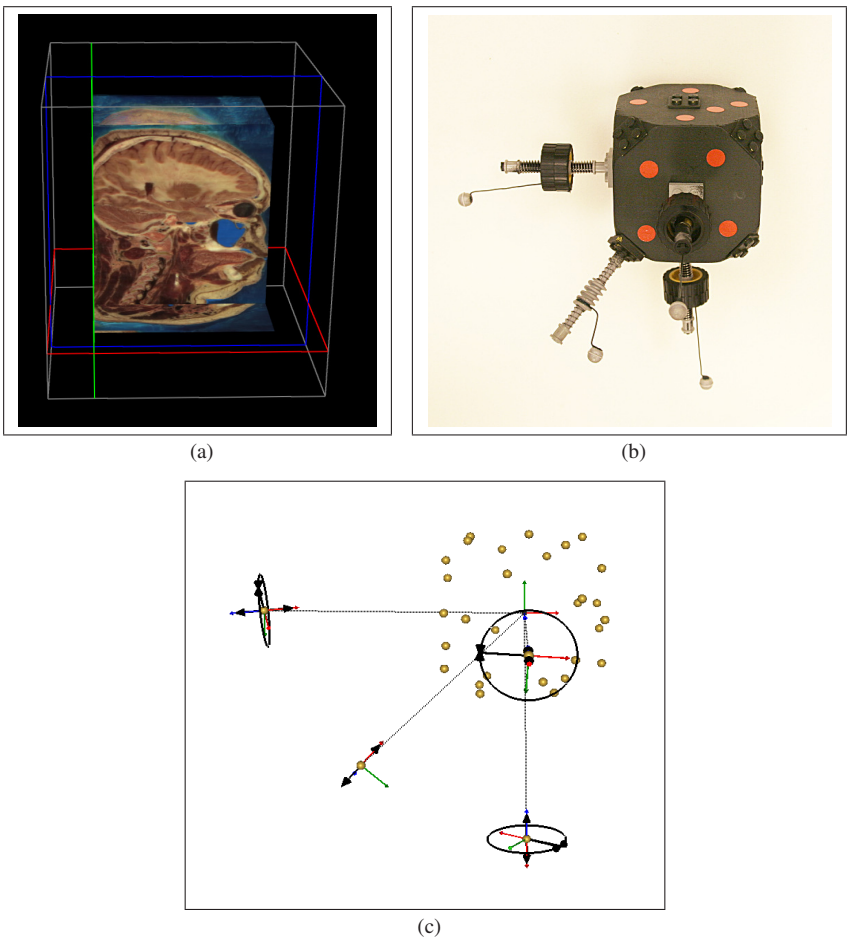

Figure 8.8: (a) A scientific visualization application for manipulation and data exploration. (b) CID's configuration, consisting of a truncated cube and 4 actuators. Three actuators control three orthogonal slicing planes, whereas the one at the corner controls the zoom factor. (c) The model of the configuration, as acquired by the device training procedure.

of the corners of the truncated cube to allow for scaling. Pulling the slider out scales the data set up, while pushing the slider in scales it down. The mapping parameters of this actuator are illustrated in Figure 8.6(a).

All translational actuators are held in a return position by springs. Note that this configuration resembles the cubic mouse [FP00], which also allows for a natural mapping between the DOFs of the interaction device (the translational component of three orthogonal rods) and application parameters (the position of the slicing planes).

The rotational components of the actuators that are used to rotate the data set relative to the cutting planes have a range of 360 degrees. The mapping between actuator rotation and data set rotation is set 10:1, enabling fine adjustments to the rotations. It was found that a mapping of 1:1 is too direct for pleasant interaction, since already a relatively small motion

of an actuator results in a large rotation of the data set. The mapping parameters of one of the rotational actuators is depicted in Figure 8.6(b).

The translational components of the actuators coupled to the slicing planes have ranges of approximately 1.8 cm, with a dead zone of 3 mm. If the actuators are pushed in or pulled out beyond the dead zone, the associated slicing plane starts to move in the appropriate direction at a constant speed.

The actuators used to translate the slicing planes are held in a return position by springs. By removing the springs, position control could be used, instead of rate control. Although in general position control is preferable [JHWB78, KTES87], the interaction range using position control depends directly on the size of the interaction device. In contrast, rate control has no limit on the range of interaction. As such, the configuration can be kept small.

The actuator that controls zooming also has a translation range of 1.8 cm and a dead zone of 3 mm, with a constant speed rate-control interaction.

Figure 8.8(c) shows the model of CID's configuration obtained by the training procedure, illustrating the base object and actuator DOFs and DOF ranges.

8.5.3 Animation

An application was created which enables a user to create character animations. In this application, a configuration of CID is coupled to a virtual model of the human skeleton. When actuators on the device are manipulated, the graphical representation is updated accordingly. Figure 8.9(a) shows a screenshot of the animation application.

CID is configured as follows. The base object is cylindrical, with five connection points (see Figure 8.9(b)). On the top side, an actuator with one rotational DOF is attached. This actuator is used to control the head of the virtual model. Its rotation range is 360 degrees, which is directly mapped onto the orientation of the virtual head.

On each side of the cylinder, actuators are attached to control the arms of the skeleton. These actuators consist of two segments. The first segment has a joint with two rotational DOFs, to which a segment is attached with one rotational DOF. These correspond to the shoulder and elbow joints of the skeleton. The rotation range of the shoulder joint is about 80 degrees, rotating away from the body, and 160 degrees in the other direction. The elbow joint has a range of about 190 degrees.

The actuators at the bottom of the cylinder are constructed similarly to the actuators controlling the arms. They consist of two segments, with two rotational DOFs followed by one rotational DOF. They are used to control the upper and lower legs. The first segment has a range of approximately 185 degrees in the walking direction, and about 60 degrees in the other direction. The second segment has a rotation range of 180 degrees. The result of the model training procedure is illustrated in Figure 8.9(c).

To create an animation, a user manipulates the actuators to put the head, arms and legs in the desired position. The cylinder is coupled to the skeleton's torso. When the pose of the virtual skeleton is satisfactory, a key frame can be added to the animation. The user can continue adding key frames, or at any time start the animation. If a new key frame did not provide the intended result, it can be removed again. The system creates an animation by using spline quaternion interpolation techniques to preserve continuity between key frames (see [Sho85]).

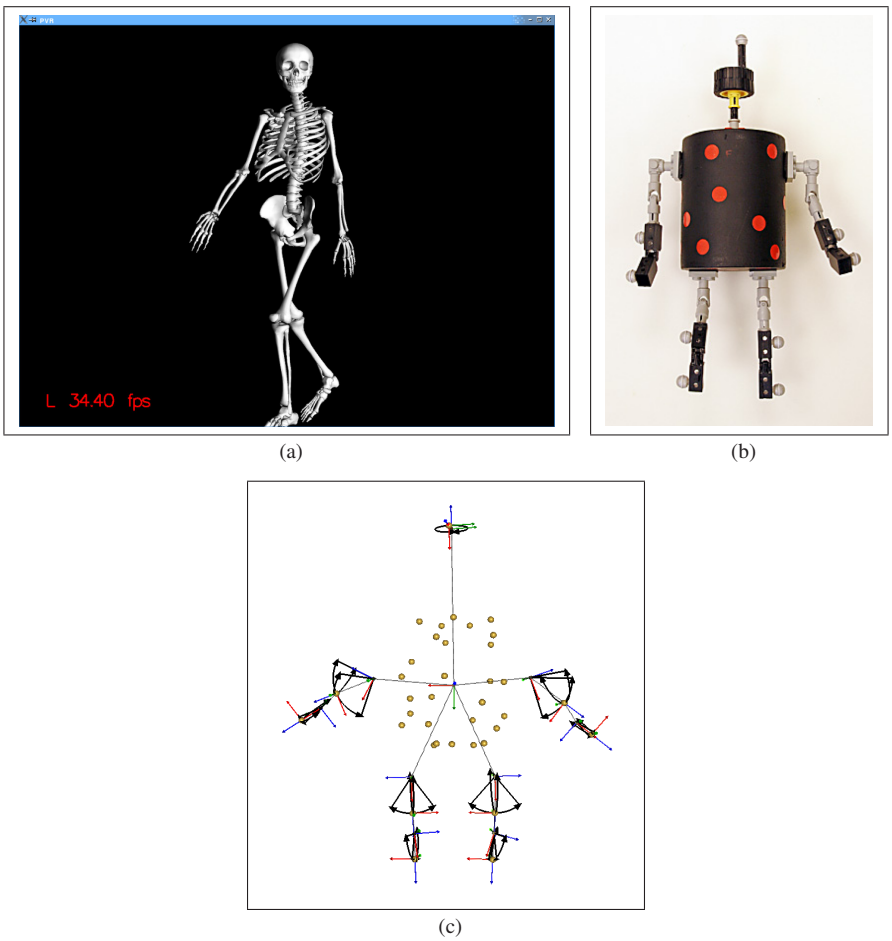

Figure 8.9: (a) A frame of an animation. (b) CID's configuration, consisting of a cylinder and 5 actuators. One actuator controls the head of the virtual model of the human skeleton, while the others control its arms and legs. (c) The model of the configuration, as acquired by the device training step.

8.6 Discussion

CID is an optically tracked configurable interaction device. It was designed to provide an intuitive interface for a variety of complex interaction tasks. Due to CID's configurability, it enables a developer to rapidly construct new configurations to experiment with new interaction techniques and devices. The device was tested in a modeling, manipulation and data exploration, and animation application. In these application, the structure of the device reflects the application parameters, allowing for overlap between the perception/cognition space and the motor space (see Chapter 1).

During use of CID it was noticed that users generally do not need to see CID while manipulating it. This suggests that proprioception can be used to manipulate the device.

Even when the device has many actuators with various translational and rotational DOFs, such as for instance the configuration of Figure 8.8, users were observed to reach for the correct actuator during their trials.

The base object and actuators of CID are optically tracked, which has a few consequences. First, it requires line-of-sight to operate. Due to the design of the device and by using a tracking setup with four cameras, occlusion turned out to have little influence in the modeling and data exploration applications. However, the configuration used for the animation application is more complex. The markers are very close to the actuators, and the configuration consists of 5 actuators featuring 9 segments in total. Due to this complexity, some occlusion issues are present. This problem could be alleviated by using more than one marker on each actuator segment, or by using more cameras. Another possibility would be to determine a more optimal camera placement. This could be done by developing a model of the environment that describes the camera placement and parameters, the tracking volume, the device, and marker occlusion. This model could be used in an optimization procedure to determine the optimal placement for a given number of cameras.

The second consequence of optical tracking, and a property of any tracking technology, is that measurement noise is introduced. Obviously, when a user does not manipulate an actuator, the application should not perform the associated action. To minimize noise effects, actuators have a dead zone. If the change in tracker value is below a certain threshold, this change is regarded as noise and no action is taken. Furthermore, a simple low pass LTI filter operating on the actuator DOFs was included. The dead zone and filter parameters can be adjusted using the map editor presented in Section 8.4.

A third consequence of optical tracking is that it may introduce tracking errors when a marker lies in the same line of view as another marker, causing their blobs to merge in the camera image. The resulting 2D position of the resulting blob is then slightly shifted, resulting in an erroneous 3D marker position. If this marker position falls within the DOF range of an actuator, unintended actions may occur in the application. This effect can occur quite frequently if a single marker segment is located in front of a surface of the base object. The problem can be solved by incorporating confidence metrics in the markers positions, based on for instance the epipolar distance between blobs in two camera images, and by rejecting invalid blobs by shape analysis.

The configuration of CID is currently limited to structures with a base object to which actuators are attached. Since the tracking system can handle complete tree structures, the flexibility of CID can be increased by enabling a developer to attach actuators to each other, instead of only to the base object.

More work is needed to evaluate the usefulness of CID compared to other solutions for flexible, reconfigurable interfaces. For instance, CID could be compared to 2D widget interfaces attached to handheld props [CW99, KL04]. However, it may prove difficult to control for instance a virtual character effectively using 2D widgets. The power of CID could be further demonstrated and evaluated by extending the animation application in Section 8.5.3 to a real-world animation application, providing all degrees of freedom animators require.

8.7 Conclusion

In this chapter, CID was presented, an optically tracked configurable interaction device. The device is tracked using the model-based optical tracking system presented in the previous chapters. CID enables users to manipulate a large number of application parameters with

a single, compact device. A developer is enabled to rapidly construct new configurations to experiment with new interaction techniques and devices. The idea of CID is that the structure of a configuration of CID can directly reflect the application parameters, resulting in an intuitive interface.

The device consists of a six DOF base object, to which actuators can be attached. The base object defines the frame of reference for the interaction performed by manipulating the actuators. The flexibility of the concept was illustrated in a number of application scenarios.

Chapter 9

Spatial Input Device Structure

The previous chapter presented CID, an optically tracked configurable interaction device. In this chapter, CID is used to study the effects of different spatial interface structures used to perform a 3D interaction task, with respect to aspects like task performance, intuitiveness, and comfort.

9.1 Introduction

High dimensional 3D interaction tasks require the manipulation of a large number of spatial input parameters. Input devices for such tasks can be constructed such that their spatial structure reflects the task parameters. This enables a user to perform operations on a virtual object in the same frame of reference as this object, and allows for the physical action and the perceived motion of the virtual object to match. As such, somatosensory cues that a user receives during device manipulation, as well as a users expectations, can be made consistent with visual cues from the virtual environment. Intuitively, such a match between the spatial device structure and the task at hand would seem to allow for more natural and direct interaction. However, the exact effects of such a direct match between the spatial device structure and 3D interaction task parameters using two-handed interaction techniques on aspects like task performance, intuitiveness, and user comfort, are yet unknown.

The goal of the research in this chapter is to study the effects of input device structure for high dimensional interaction tasks on user performance. Two factors are investigated: the relation between the frame of reference of a user's actions and the frame of reference of the virtual object being manipulated, and the relation between the type of motion a user performs with the input device and the resulting type of motion of the virtual object. The hypothesis is that input devices should be structured such that the motion type and frame of reference of a user's physical action matches the motion type and frame of reference of the virtual object being manipulated. This may allow users to manipulate the device more effectively and to predict the results of their actions in the virtual environment more accurately.

A user study was performed in which subjects performed a high dimensional interaction task using four different spatial input device structures. The task entails docking a data set and translating a virtual object over an axis in the same frame of reference as the data set, where the structure of the interface reflects this task to different degrees. First, the action subjects need to perform to translate the object is either a translation or a rotation. Second, the action is performed in the same frame of reference of the virtual object, or in a fixed, separately located, frame of reference.

For each interface structure, the device manipulation time was measured. Additionally, the number of times subjects erroneously moved the virtual object away from the target was measured. Furthermore, users were asked to fill in a questionnaire in order to get subjective

ratings on intuitiveness and comfort. The different device structures were constructed using CID (see Chapter 8).

This chapter is organized as follows. In Section 9.2, related work is reviewed. Section 9.3 describes the test setup and method. In Section 9.4, the results of the user study are given. Section 9.5 provides a discussion of the results. Finally, in Section 9.6 conclusions are given.

9.2 Related Work

Guiard [Gui87] presented a model that describes the relation between the dominant and non-dominant hand in bimanual manipulation tasks. The non-dominant hand can provide a frame of reference for manipulations of the dominant hand. Furthermore, Guiard found that the sequence of motion is usually from non-dominant to dominant hand, and that the action of the non-dominant hand is coarser than that of the dominant hand.

Garner [Gar74] presented a theory of perceptual structure of visual information. Visual information is characterized by an integral structure, if its attributes can be perceptually combined to form a unitary whole. For instance, the 2D position and size of an object have an integral structure. On the other hand, visual information is characterized by a separable structure if the attributes have perceptually independent dimensions, e.g. the 2D position and color of an object.

Jacob et al. [JS92, JSM+94] extended Garner's theory to interaction tasks. They reasoned that the attributes of objects in multi-dimensional spaces can have different perceptual structures, that affect how a user perceives an object. As a result, interaction movements in an integral space should be Euclidean, whereas movements in a separable space should be city-block. They hypothesized that the control structure of an input device should match the perceptual structure of the interaction task. An experiment was conducted in which subjects performed two tasks with different perceptual structures. Two input devices were used that exhibit the corresponding control structures, an integral 3D tracker and a separable mouse using a mode switch. The results showed that performance is better when using the 3D tracker to position a cube and change its size, whereas the mouse results in better performance to position a cube and change its brightness.

Wang et al. [WMSB98] noted that the theory of Garner originally only dealt with intrinsic properties of an object, such as size and color. They argued that Jacob et al. did not address that location and size of an object are extrinsic properties. Due to the complexity of the human visual system, the perceptual structure of an object may not match the structure of interaction movement of an object. They conducted an experiment that had subjects dock a cube in different visual feedback conditions. Experimental results showed that object translation and orientation have a parallel, interdependent structure that is generally independent of visual feedback conditions. This implies that haptic and kinesthetic information plays a strong role in object manipulation.

Kabbash et al. [KBS94] studied four techniques for performing a compound drawing and color selection task. They argue that techniques where the action of the dominant hand depends on the non-dominant hand would result in better performance. Results showed that using an appropriately designed two-handed technique, subjects performed better than in the single hand case.

To compensate for the lack of haptic feedback during virtual object manipulation, Mine et al. [MBS97] proposed exploiting proprioception. They introduced and evaluated various interaction techniques that exploit proprioception. Results showed proprioception can greatly

enhance 3D interaction.

Balakrishnan et al. [BH99a] explored how the match between input space of the hands and output space of a graphical display influences two-handed input performance. They found that the Guiard's model of human bimanual action applies to visual as well as kinesthetic feedback. Vision was found the dominant feedback channel as it can overcome significant limitations in kinesthetic reference.

Wang et al. [WM99] studied the effects of input device, cursor and virtual object size on 3D manipulation tasks. A user experiment was performed in which subjects had to match the location and angle of a cursor cube to that of a target cube as fast and accurate as possible. Results showed that matching the size of the input device and cursor decreases task completion time, whereas matching cursor and target object size increases accuracy.

Ware et al. [WA04] investigated the effect of rotating the frame of reference of an input device with respect to the frame of the virtual object being rotated. They found that at large angles of mismatch, manipulation times were four to five times longer. However, smaller angles of mismatch have a relatively modest impact on performance.

Stimulus-response (S-R) compatibility plays an important role in the design of 3D interfaces. Spatial and directional S-R compatibility in bimanual 3D interaction tasks has received relatively little attention. Broadbent and Gregory studied spatial S-R compatibility by asking participants to respond to a left or right visual stimulus by pressing a left or right key [BG62]. Left to left and right to right stimulus-response relations were found to be more effective than left to right and vice versa.

Worringham and Beringer [WB89, WB98] performed various studies on directional S-R compatibility. They found that physical controls with implicit directional cues, such as joysticks and rotary knobs, have effects on responses towards particular directions, depending on operator orientation.

Previous work has studied several factors relating to how real-world knowledge and passive feedback factors as kinesthesia and proprioception influence human performance of 3D manipulation tasks. However, studies on spatial and directional S-R compatibility have been performed primarily using two-dimensional interfaces. Several studies suggest that it is difficult to determine what the most compatible S-R configuration will be among several user interface alternatives [Tla04, VP03]. Therefore, the effects of different levels of S-R compatibility in bimanual 3D interaction tasks are uncertain. Additionally, the most S-R compatible configuration may not result in the most comfortable interface. In this chapter, the focus is on the relation between the frame of reference and type of human action and the corresponding frame of reference and motion type of the virtual object being manipulated, in the context of bimanual 3D spatial manipulation tasks. Interfaces where the motion type and frame of reference of a user's physical action matches the motion type and frame of reference of the virtual object being manipulated are expected to be more S-R compatible.

9.3 Method

A group of subjects was asked to perform a task using different device structures for bimanual manipulation. Four device structures were evaluated, where the user's actions and the observed changes in the virtual environment have different levels of consistency. In the following sections, the test setup, the task and device configurations, and the test procedure is discussed.

9.3.1 Test Environment

The experiments were performed using the Personal Space Station (PSS) [ML02, PST], as described in Chapter 1. For the experiments in this chapter, the PSS was equipped with four progressive scan CCD-cameras with wide-angle lenses (with a focal length of 3.6 mm). The interaction volume is approximately 50×50×50 cm. The cameras operate at 60 Hz.

The display of the PSS consists of a 22" Iiyama monitor, operating at a refresh rate of 60 Hz and a resolution of 1280×1024 pixels. The reflected image is perceived by the user at a depth of about 50 cm. Two iBot FireWire IEEE 1394 cameras are used for head tracking, using the method as described by Mulder et al. [MJR03].

The PSS can be turned into an augmented reality system by using a semi-transparent mirror. However, the experiments were performed using an opaque mirror. As a consequence, subjects were not able to see the device they were manipulating, relying on somatosensory cues as proprioception and kinesthesis for device manipulation, rather than on visual cues.

9.3.2 Task Description

Subjects were asked to perform a task using different configurations of CID. An application displayed a volume rendering of a Computed Tomography (CT) scan of a human head, as illustrated in Figure 9.1. An orthogonal slicing plane can be translated through the data set. Slicing a data set is a basic and frequently used task in scientific visualization. The task involves docking the volume rendering into a target cube, and placing the slicing plane in a target position. The slicing plane is defined relative to the frame of reference of the volume rendering. The pose of the volume rendering and the position of the slicing plane can be controlled using different configurations of CID.

9.3.3 Device Configurations

Subjects executed the task using four configurations of CID. Each configuration is aimed at two-handed interaction, and uses a cube as base object for CID. The cube allows the user to control the position and orientation of the volume rendering. The size of the data set was approximately 7×7×7 cm, which is identical to the size of the cube. The four configurations differ in the way the user is able to translate the slicing plane. Each configuration is described in detail below.

DT: Dial on table

The dial on table (DT) configuration allows a user to translate the slicing plane through the data set by rotating a dial (see Figure 9.2). The dial is attached to the table, at a fixed position and orientation in the workspace. This corresponds to a common interaction scenario, where a user is enabled to manipulate application attributes using a toolbox with widgets. A rotation of 360 degrees of the dial translates the slicing plane through the data set over a distance that equals the size of the cube. It is expected that this configuration represents the least direct form of interaction. First, the type of physical motion required to move the slicing plane (a rotation) does not match the motion of the virtual object (a translation). Second, the frame of reference in which the physical action is performed (the table) does not match the frame of reference in which the operation on the virtual object is performed (the frame of reference of the slicing plane).

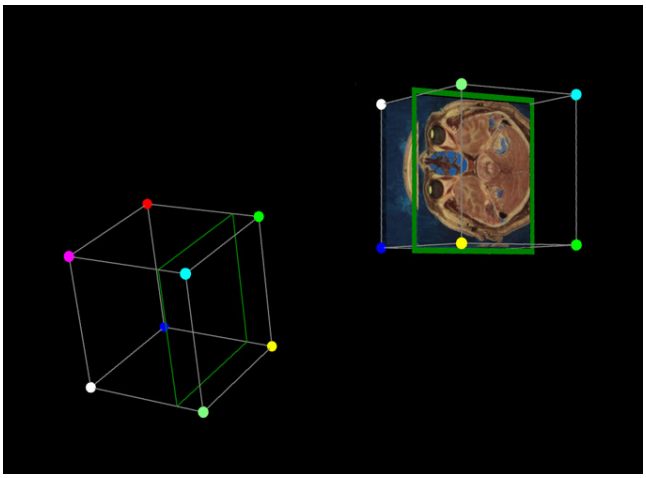

Figure 9.1: The docking application. A user can control the position and orientation of a volume rendering of a CT scan. A slicing plane can be translated through the data. The task is to dock the volume rendering and position the slicing plane onto the target on the left.

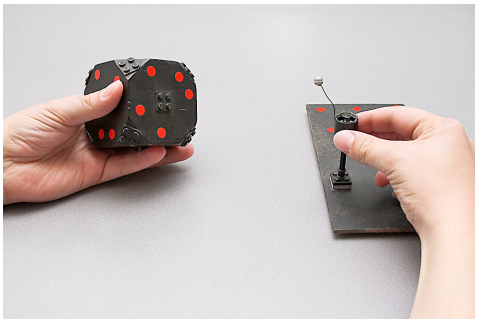

Dial on table (DT)

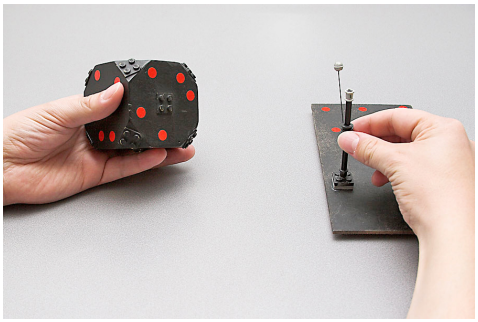

Slider on table (ST)

Dial on cube (DC)

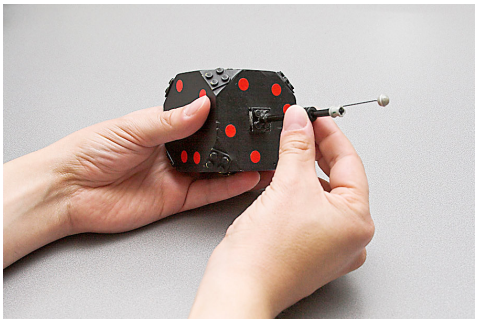

Slider on cube (SC)

Figure 9.2: Interface configurations. The cube controls the position and orientation of the volume rendering as shown in Figure 9.1. The configurations differ in two ways: the type of actuator that is used to translate the slicing plane (dial or slider) and the frame of reference of the actuator (same frame of reference as the data set or fixed).

ST: Slider on table

The slider on table (ST) configuration allows a user to translate the slicing plane using a slider. The slider is position controlled, and its length is approximately the size of the cube. Position control is generally accepted to result in higher human performance than rate control [JRM+80]. Analogous to the DT configuration, the slider is placed on the table, at a fixed location in the workspace. This configuration is expected to represent more direct interaction than the DT configuration, since the physical motion required to move the slicing plane is a translation.

DC: Dial on cube

The dial on cube (DC) configuration allows a user to translate the slicing plane using a dial. The dial is placed on the cube that is used to control the pose of the volume rendering. Therefore, the coordinate system of the dial matches the frame of reference of the cube. As a result, the frame of reference in which the physical action is performed matches the frame of reference in which the operation on the virtual object is performed. The relation between rotation direction and slicing plane movement was chosen similar as in case of a screwdriver: rotating clock-wise moves the slicing plane "into" the data set. Using the screwdriver metaphor, it is expected that the dial has implicit directional cues for virtual object translation along the rotation axis.

SC: Slider on cube

The slider on cube (SC) configuration allows a user to translate the slicing plane using a slider. Analogous to the DC configuration, the slider is placed on the cube that is used to control the pose of the volume rendering. The position of the slider directly corresponds to the position of the slicing plane. This configuration is expected to result in the most direct interaction scenario, where both the type and the frame of reference of the physical motion matches the resulting motion of the virtual objects.

Hypotheses

From the previous sections, the following hypotheses are defined:

- The configuration in which the type and the frame of reference of the physical motion matches that of the virtual objects is the most S-R compatible. As a result, the slider on cube configuration is expected to result in the best performance.
- The configuration in which both the type and frame of reference of the physical motion does not match that of the virtual objects is the least S-R compatible. As such, the dial on table configuration is expected to result in lowest performance.
- The configuration in which only the motion type of the physical motion matches that of the virtual object is more S-R compatible than the configuration where only the frame of reference matches.

9.3.4 Procedure

Subjects performed multiple trials with all four configurations. Each trial involved docking a data set onto a target cube, and placing a slicing plane at a target position. Before the

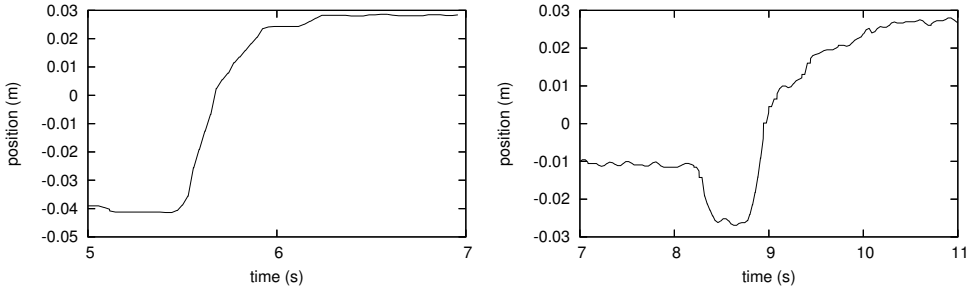

Figure 9.3: Trajectory examples of moving the slicing plane. (a) A user moved the slicing plane directly to a target location. (b) A user first moved the slicing plane in an unintended direction, and then corrected the mistake.

experiment, subjects were made aware of the limitations of the tracking system, and were instructed to use the handles on the actuators to prevent them from grabbing the markers.

Before commencing with the experiment, subjects were verbally instructed and were given four training trials for each configuration of CID. Next, subjects performed the task 30 times for each configuration, resulting in 120 recorded trials. The total time subjects took to complete the experiment was approximately an hour.

After completing the trials for all configurations, subjects were asked to fill in a questionnaire for subjective ratings. After accessing the subjects' prior experience with virtual reality and the PSS, they were asked to give each of the four configurations ratings for overall impression, comfort, and intuitiveness.

9.3.5 Performance Metrics

Each trial, the time was measured that subjects took to manipulate an actuator. This manipulation time was obtained by filtering and differentiating the tracking data. Each subject performed 30 trials for each of the four configurations, resulting in $14 \times 30 = 420$ measurements of slicing plane manipulation time per configuration.

To check the effect of different configurations on the ability of a user to perform the docking task, the total task completion time was also measured. Different interface structures may affect the user's ability to perform the docking task.

A third performance metric is the chance that a user starts movement of the slicing plane in the opposite direction of the position of the target. This metric is estimated by measuring the number of trials that users start movement in the opposite direction. It is expected that in less direct interaction scenarios, users cannot predict the outcome of their actions. For instance, in the slider on cube configuration, users are expected to make less manipulation errors than in the case of a dial on table configuration.

Figure 9.3 shows two example trajectories of the slicing plane. On the left, a user moves the slicing plane directly in the direction of the target position. The trajectory on the right shows a typical example of a user initially manipulating the actuator such that the slicing plane erroneously moves in the opposite direction of the target position. After observing the unintended movement, the user moves the slicing plane in the correct direction. Interface configurations that have a significantly lower chance of these manipulation errors are expected to perform better and be more intuitive.

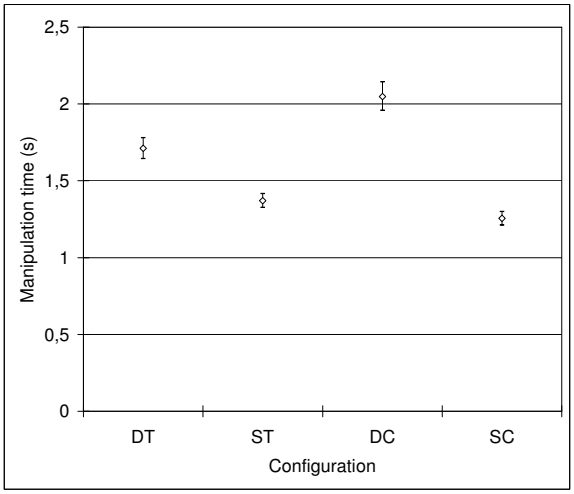

Figure 9.4: Slicing plane manipulation times with 95% confidence intervals.

	Dial		Slider	
	Mean	95%	Mean	95%
Table	1.71	0.08	1.37	0.05
Cube	2.04	0.09	1.25	0.04

Table 9.1: Slicing plane manipulation times with 95% confidence intervals.

9.4 Results

Fourteen right-handed subjects participated (1 female and 13 males). All subjects were used to working with computers. Seven subjects had little to no prior experience working in the PSS, and six had moderate to much experience. All subjects reported to have good to excellent depth perception during the trials.

9.4.1 Slicing Plane Manipulation Time

Statistical analysis of the slicing plane manipulation time T_s showed that the logarithm of time could be approximated well by a Gaussian distribution. The t-distribution was used to determine a 95% confidence interval for the average $\log T_s$, giving the estimated range of values which is likely to include $\log T_s$ [DS98]. The average values and confidence intervals were mapped back to duration time to allow for easier interpretation of the results. Figure 9.4 summarizes the results. The vertical lines define the ranges of the 95% confidence intervals. Table 9.1 summarizes the results of the manipulation times. The figure and table suggest that the dial configurations perform worse than the slider configurations, and that the slider on cube configuration performs best.

An analysis of variance (ANOVA) was performed on $\log T_s$, and a highly significant effect was found for device structure on slicing plane manipulation time ($F(3,1676) = 129.5$, $p < 0.01$). The dial on table configuration performs significantly worse than the slider on table configuration ($F(1,838) = 72.2$, $p < 0.01$). Similarly, the dial on cube configuration

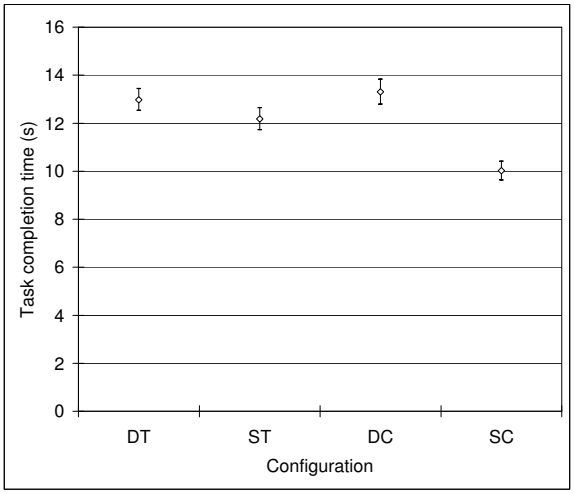

Figure 9.5: Total task completion times with 95% confidence intervals.

performs significantly worse than the slider on cube (F(1,838) = 288.8, $p < 0.01$) configuration. The slider on table configuration perform significantly worse than the slider on cube configuration (F(1,838) = 13.2, $p < 0.01$). Interestingly, the dial on table configuration performs significantly better than the dial on cube configuration (F(1,838) = 35.3, $p < 0.01$). These results are discussed in more detail in Section 9.5.

9.4.2 Total Task Completion Time

The total task completion time T_t is analyzed in the same way as the slicing plane manipulation time. A 95% confidence interval for the average $\log T_t$ was determined to give the estimated range of values which is likely to include $\log T_t$. The results, mapped back to duration time, are summarized in Figure 9.5.

An analysis of variance (ANOVA) was performed on $\log T_t$, and a significant effect was found for device structure on total task completion time (F(3,1676) = 45.5, $p < 0.01$). The dial on table configuration performs significantly worse than the slider on table configuration (F(1,838) = 10.53, $p < 0.01$). No significant effect was found between the dial on table and dial on cube configurations (F(1,838) = 0.88, $p > 0.1$). The slider on cube configuration performs significantly better than the dial on cube (F(1,838) = 95.0, $p < 0.01$), slider on table (F(1,838) = 50.6, $p < 0.01$), and dial on table (F(1,838) = 103.7, $p < 0.01$) configurations. Comparing these results with the slicing plane manipulation times, there is no significant statistical evidence to assume users are extra hampered in performing the task in either the cube configurations or the table configurations.

9.4.3 Manipulation Error Chances

The 95% confidence intervals for samples from the Binomial distribution were calculated for the chance of manipulation errors [YMS03]. Figure 9.6 summarizes the results. The figure suggests that the error chance is lowest in the slider on cube configuration. To test if the error chance of the configurations corresponds to 0.5, a binomial test is performed. If the error

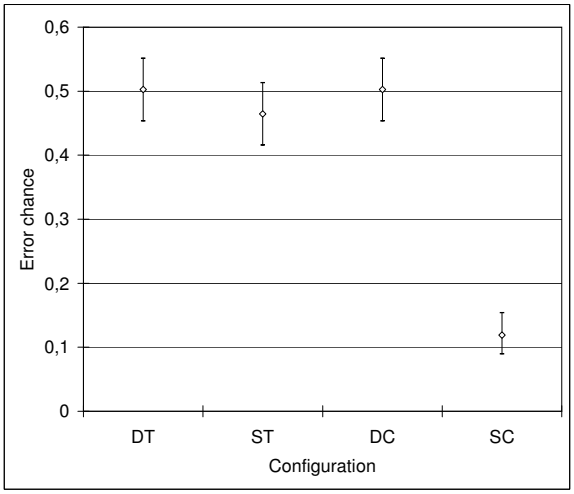

Figure 9.6: Error chances of unintended initial slicing plane movements in the opposite direction of the target.

	Dial		Slider	
	Avg	p-value	Avg	p-value
Table	0.50	0.96	0.46	0.16
Cube	0.50	0.96	0.12	0*

Table 9.2: Estimated error chance with two-tailed p-values. Statistical significance is indicated by *.

chance is 0.5, it is completely random whether an actuator is initially moved in the direction of the target position or not. In this case, a user cannot accurately predict the effect on the virtual environment of manipulating an input device.

The method of small p-values is used to calculate the two-tailed p-value [YMS03]. This value indicates the statistical significance associated with testing whether the error chance is different from 0.5. With a confidence interval of 95%, $p < 0.05$ indicates statistical significance. The results are summarized in Table 9.2. From the table can be derived that the error chance is only significantly different from 0.5 for the slider on cube configuration ($p \approx 0$). This suggests that in the other configurations, the chance of moving in the right direction may be 0.5. Only in the slider on cube configuration, the chance of moving in the correct direction is significantly lower (95% confidence interval $= [0.089, 0.154]$).

9.4.4 Subjective Ratings and Observations

The results of the subjective ratings are depicted in Figure 9.7. The graph shows the average grades subjects gave overall, for comfort, and for intuitiveness. Most subjects have a preference for the sliders on cube configuration, giving an average overall rating of 7.4. The dials on cube configuration scored lowest, with 5.6. Subjects found the slider on cube configuration most intuitive (8.0), while the slider on table configuration was rated most comfortable (6.9).

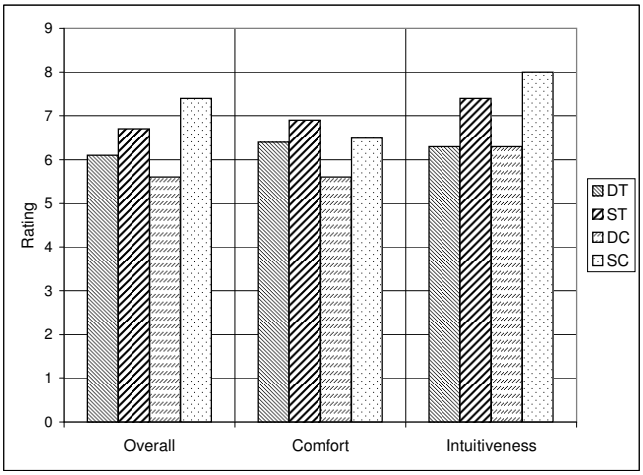

Figure 9.7: Average subject ratings on overall impression, comfort, and intuitiveness of operating the device structure.

It was found that 9 out of 14 subjects reported to prefer the slider on cube configuration, followed by 4 for the slider on table configuration and 2 for the dial on table configuration. When asked further, most subjects that did not rate the sliders on cube configuration the overall best indicated that the slider on cube configuration was indeed more intuitive, but that they regarded comfort more important than intuitiveness.

Various subjects reported that manipulating the input device felt more comfortable in the table configurations. They stated that docking the data set was more difficult in the actuator on cube configurations, because the cube was more obtrusive to handle with an actuator attached to it. Furthermore, it was observed that in the actuator on cube configurations, subjects have difficulties performing the task when the target is oriented such that the actuator has to be manipulated on the left side of the base object. This resulted in subjects passing CID over from their non-dominant to their dominant hand, and manipulating the actuator with their non-dominant hand. Some subjects insisted on manipulating the actuator with their dominant hand like in other situations, resulting in crossing of hands to manipulate the actuator on the left side. As a result, subjects lost accuracy and speed while manipulating the actuator. Some subjects reported slightly more tracking issues, caused by occlusion of the markers by the hands.

All subjects were found to perform the docking of the data set and the positioning of the slicing plane serially. This indicates that the pose of the data set and the position of the slicing plane are perceived as independent attributes.

In the table configurations, some subjects docked the data set with two hands and then searched for the actuators on the table. Others held the data set in the non-dominant hand and held the dominant hand on the actuator all the time. The latter group of subjects generally had more prior VR experience.

9.5 Discussion

9.5.1 Motion Type

Figure 9.4 shows that manipulation times of the slider configurations are both lower than the dial configurations. Taking the difference of $\log T$ between the slider on table and dial on table configurations, the logarithm of the ratio between the manipulation times of the configurations is obtained. Taking the exponential, it is found that on average, the dial on table configuration is 1.25 times slower than the slider on table configuration. A similar analysis reveals that the dial on cube configuration is 1.63 times slower than the slider on cube configuration. This indicates that rotating a dial to move a slicing plane results in a 1.25 to 1.63 times lower S-R compatibility than translating a slider. As such, it may be advantageous to match the type of a user's action to the corresponding observed virtual object motion.

The manipulation error chances and the binomial test summarized in Table 9.2 suggest that subjects do not know which way to rotate the dial to move the slicing plane to a given location, even if the dial is placed in the correct frame of reference. This indicates that merely matching the frames of reference of a user's action and the virtual object is not sufficient. In this case, visual and somatosensory cues of the user's action and the perceived effect in the virtual environment are not in agreement.

Although there is not enough evidence to support the claim that the error chance is 0.5 in the slider on table configuration (with a two-tailed p-value of 0.16), some subjects stated that they could feel if the slider was up or down, and could use this information to move the slicing plane in the correct direction during the next trial.

The slider on table configuration is the most intuitive with respect to slicing plane movement, with a two-tailed $p < 0.05$ and a 95% confidence interval of the error chance of $[0.089, 0.154]$.

9.5.2 Frame of Reference

The slider on cube configuration has significantly lower manipulation times, with times of 73% of the dial on table configuration, 61% of the dial on cube configuration, and 88% of the slider on table configuration. This suggests that this configuration is the most S-R compatible. Therefore, it is desirable to match the frames of reference of a user's action and of the corresponding observed virtual object. However, the dial configurations do not show similar results. On the contrary, the dial on cube configuration performs 1.2 times slower than the dial on table configuration. This may be explained by Fitt's law [Fit54, FP64]. Fitt's law describes the time taken to acquire a visual target using a manual input device. It can be described as

$$T = C_1 + C_2 + D \tag{9.1}$$

where D represents the index of difficulty of the task, which depends in the distance to the center of the target and the target width, and where C_1 and C_2 are experimentally determined constants. The quantity $1/C_2$ is called the index of performance. Previous work suggests that especially for relatively small distances and small targets, the index of performance is larger for the dominant hand than for the non-dominant hand [Flo75, KMB93]. In the cube configurations, subjects were sometimes forced to either operate the dial with the non-dominant hand, or to cross hands to operate the dial (see Section 9.4.4). Therefore, task performance is decreased in cases where the actuator is on the opposite side of the user's dominant hand.

Additionally, subjects could not profit from the benefits of having the dial in the same frame of reference as the observed motion of the slicing plane, as the motion types did not match. This is supported by Figure 9.6, which indicates that the manipulation error chance is around 0.5 for both dial configurations. However, the error chance of the slider on cube configuration is significantly lower. This indicates that the slider on cube configuration enables subjects best to predict the outcome of their manipulations, resulting in more natural and intuitive interaction.

9.5.3 Intuitiveness versus Comfort

The subjective ratings (see Figure 9.7) show that subjects generally find the slider on cube configuration most intuitive, followed by the slider on table configuration. However, subjects rated the slider on table configuration better in terms of comfort. This indicates that there is a tradeoff between intuitiveness and comfort in designing spatial input devices. The slider on cube configuration allows for more direct and natural interaction, but is less comfortable and therefore more tiring than the table variant. However, it may be possible to reduce this gap in comfort. The most important reason subjects gave for their comfort ratings is the fact that the actuator on the base object hampers the user somewhat during the docking of the data set. However, results indicate that this does not have a significant performance impact. Furthermore, many applications do not require the repeated docking of an object, but simply use an input device to allow a user to view a data set from different angles. Furthermore, the ergonomics of CID could be improved and the size of the actuators reduced to increase comfort.

9.5.4 Design Principles

The design principles for the slicing plane positioning task can be summarized as follows:

- Human performance increases when a device is structured such that both the motion type and frame of reference of a user's physical action match the motion type and frame of reference of the virtual object being manipulated.
- It may be more comfortable and beneficial for task performance if users are able to manipulate the actuator with their dominant hand.
- For tasks that require much manipulation of the base object of CID, the slider on table configuration may be a good alternative to increase user comfort, at the expense of lower human performance.

9.6 Conclusion

In this chapter, the effects were studied of matching the spatial structure of an input device to a 3D interaction task on aspects like effectiveness, intuitiveness, and comfort. A user study was performed using CID, an optically tracked configurable interaction device. This device allows for rapid development and evaluation of different device structures. Subjects were asked to perform a task in which they had to dock a data set to a target position and orientation, and position a slicing plane through this data set. The slicing plane was positioned along an axis that was defined in the frame of reference of the data set.

The device was structured in four different ways, varying the frame of reference and type of the physical action that needs to be performed. The frame of reference of the device used for translating the slicing plane through the data set was either identical to the frame of reference of the data set, or was kept at a fixed, separately located, frame of reference. The type of action was varied by using either a slider or a dial to translate the slicing plane. Subjects could control the position and orientation of the data set in each configuration using a cube-shaped object.

Results show that the structure of a device influences S-R compatibility. It can be advantageous to structure a device such that both motion type and frame of reference of a user's action match the frame of reference and type of motion of the virtual object being manipulated. It was found that matching only the frame of reference may degrade performance, since users do not have enough information to efficiently position the slicing plane using a dial. This is expected to be true for other motion types as well.

An interesting result is that users generally found the device structures with the widget at a fixed location more comfortable to manipulate. However, the use of a slider attached to a cube was generally found to be most intuitive. More research can be done to study this effect further.

It was also found that users perform the docking of the data set and the positioning of the slicing plane serially. This indicates that these attributes are perceived as separable. Further research can be done to test whether these results hold for integral tasks. However, Wang et al. [WMSB98] found that 3D positioning and orientation only partially exhibit a parallel relation. More work is needed to determine whether users are capable of perceptually combining more than six dimensions and manipulating these simultaneously.

Chapter 10

Conclusion

Three-dimensional interaction between a user and a virtual environment is a powerful concept to manipulate, study, and communicate spatial information. Two aspects play a crucial role in determining the effectiveness of this interaction process. The first is the display system, which is used to convey information from the virtual environment to the user. The second is the input system, which steers the computational processes that control the display. The research presented in this thesis focussed on the input side of 3D interaction. The research objective was formulated as:

> The development and application of configurable input devices for direct 3D interaction in near-field virtual environments using optical tracking.

The concepts and techniques presented in this thesis have been implemented and evaluated in the Personal Space Station, the virtual environment developed at CWI.

In the next section, the contributions of this thesis and the developed concepts and techniques are summarized. In Section 10.2, suggestions for valuable extensions and future work are given.

10.1 Contributions

Optical Motion Tracking

A number of lessons were learned during the development and evaluation of the optical tracking techniques used for the configurable interaction device:

- The selection of the best tracking technique depends on the requirements as defined in Chapter 1, and on which of these requirements are considered most important for a given virtual environment.

  The tracking technique based on finding subgraph isomorphisms of point features in three-dimensional space is accurate and has low latency. Furthermore, it is better suited to handle partial occlusion than related pattern-based approaches, since any combination of a predetermined minimum amount of points is sufficient to recognize the device. It allows objects of arbitrary shape to be tracked and enables a developer to rapidly construct new devices.

  The tracking system that uses projection invariant properties of line pencils is also accurate and has low latency, and is more robust against partial occlusion and small camera calibration errors. However, the construction of new interaction devices is more difficult than the subgraph tracker that uses point features, and the shape of interaction devices is limited since line pencils are required to be applied to planar surfaces.

- Filtering and prediction strategies provide an effective means for reducing tracker inaccuracies caused by noise and latency. However, more complex does not always equal better. For the motion models used in this thesis, a linear time-invariant filter extended with a simple prediction step based on the motion model was shown to be competitive to more complex filtering strategies, in case the sampling frequency is sufficiently high (i.e. larger than 30 Hz).

- The automatic model estimation technique for rigid interaction devices, which is based on using frame-to-frame correspondence to maintain a graph of points that correspond to the same rigid object, is a powerful tool for the construction of new interaction devices. It enables a developer to equip an object with markers, move it around in front of the cameras, and use the object as interaction device in the virtual environment. The method supports partial occlusion of the marker sets.

- Composite interaction devices consist of several segments connected in a tree structure. Segments can have combinations of translational and rotational degrees of freedom with respect to a parent segment. Such devices can efficiently be tracked by searching a root segment with the subgraph tracking method, and using a backtracking method to match model segments to single markers.

  The model estimation procedure based on estimating the DOF relation between a moving marker and a coordinate system provides a convenient way to construct composite objects and apply them as interaction devices in the virtual environment. It would be a tedious and error-prone job to construct a composite object and manually measure a model that describes the DOFs and DOF ranges of each segment.

Configurable Interaction Devices

The optical tracking techniques for composite devices have been used to construct an optically tracked configurable interaction device (CID). CID was shown to enable a user to manipulate a large number of application parameters with a single, compact device. A developer can rapidly construct new configurations to experiment with new interaction techniques and devices. The structure of a configuration of CID can directly reflect the application parameters, resulting in an intuitive interface.

In Chapter 8, the flexibility of CID was demonstrated in a number of application scenarios, using different interface configurations. The applications range from modeling, scientific data exploration, and interactive animation. CID allows for the creation of a large number of new device configurations, specifically tuned to a given application. Furthermore, the developed tracking techniques allow for automatic model estimation of new device configurations and for robust estimation of all degrees of freedom of CID.

Spatial Device Structure

CID proved to be a valuable tool for studying the effects of different interface structures on factors as task performance, intuitiveness, and comfort. It was found that the structure of a device for a 3D spatial object manipulation task influences stimulus-response compatibility. This may indicate that the structure of an interaction device should reflect the spatial parameters of the interaction task at hand. In this case, stimulus-response compatibility is maximized, which should result in a more direct and intuitive interface.

10.2 Future Work

Optical Tracking

The tracking techniques presented in this thesis take a next step towards the ideal tracking method, i.e., the method that satisfies all requirements listed in Chapter 1. The tracking technique based on finding subgraph isomorphisms of point features in 3D allows for objects of arbitrary shape to be tracked, and allows for rapid development of new devices. On the other hand, the tracking method that uses projection invariant properties of line pencils is more robust against partial occlusion, while the development of new devices is more difficult and the shape of devices is restricted. Future work should focus on the development of new tracking methods that combine the best qualities of these methods.

More extensive models can be developed, using more mathematical rigor. These models can be used for analytical evaluations of new tracking methods. This results in more accurate evaluations of tracking methods, providing a means of proving why one method performs better than another in a given virtual environment, tracking setup, and application. Additionally, such models could possibly be used to predict the usefulness of a given tracking approach, before the approach is realized in practice.

The model estimation procedure for rigid interaction devices as presented in this thesis could be extended to support faster and more erratic motions during model estimation. This could be achieved by falling back on the subgraph tracking method in case of loss of frame-to-frame correspondence. When a part of the (incomplete) device model has been identified by the tracking method, the normal model estimation procedure can be resumed. A useful and challenging extension to the model estimation procedure for composite interaction devices is to support partial occlusion of the marker sets.

Filtering and prediction techniques could benefit from more accurate models to describe hand motion characteristics in a virtual environment. Such models can be used to create synthetic signals that act as a performance benchmark for filter and prediction performance evaluation, as well as to develop more accurate filtering and prediction strategies. Other interesting areas for future work are adaptive and multi-modal filtering, including the development of a motion model that exploits high level interaction information. For example, the motion model can be adapted to the task a user performs, exploiting knowledge about the expected motion speed, direction, and orientation changes.

In this thesis, tracking techniques were developed for determining the 3D position and orientation of interaction devices. Next, the techniques were extended to support composite interaction devices, allowing for more degrees of freedom in a single device. The next step would be to develop tracking methods for deformable objects. Deformable interaction devices would open up new perspectives for complex 3D interaction tasks. For instance, deformable interaction devices could enable a user to model a virtual object by simple pushing and pulling operations on the surface of the device, enabling a user to "mould" a virtual object into a desired shape. An interesting option for the development of a tracking system for deformable objects would be to exploit the projection invariant property of graph topology [SRL06].

Configurable Interaction Devices

The research in this thesis has resulted in a framework for the development and application of new interaction devices for high dimensional input. The next step would be to extend the

framework to allow for:

- Efficient design and development of interaction devices. This includes the development of tools to aid the developer in the design and construction of the interaction devices, as well as to apply the device in the virtual environment using the optical tracking system.
- Effective development of interaction techniques. This involves the mapping of the degrees of freedom of the device to the parameters of the interaction task, as well as the development of the visual (or possibly multi-modal) feedback associated with manipulations of the interaction device.
- Evaluation of interaction devices and techniques. This involves the development of tools to aid the developer to rapidly set up user experiments and evaluate new interaction devices and techniques, subject to a set of predefined parameters.

CID allows for efficient design and development of interaction devices. The map editor presented in Chapter 8, which allows a developer to adjust the mapping of the degrees of freedom of the device and the parameters of the interaction task in real-time, takes the first step to a framework that allows for efficient development of interaction techniques. The further development of this framework, including an intuitive user interface to develop and test new configurations of CID, would allow for the development of new interaction devices by people who are not computer scientists or tracking experts.

It would be interesting to study if CID can be applied successfully to other application areas and other virtual environments. Possible application areas include entertainment, modeling, construction, training, simulation, and scientific visualization areas such as geology, biology, and medicine. The applications of CID and the underlying optical tracking techniques developed in this thesis have been applied and evaluated in the Personal Space Station. However, the concepts and techniques presented in this thesis could also be applied to other types of virtual environments, such as workbenches and CAVE systems. Spatially immersive environments as the CAVE often only provide remote interaction by using simple pointing devices. CID could enable more direct spatial interaction in such environments, opening up new interaction perspectives.

Spatial Device Structure

CID can be used to perform more studies to test the driving vision of this thesis under more circumstances. Although the user study in Chapter 9 indicates that spatial and directional S-R compatibility plays an important role in human performance, this may not be true in all cases. For instance, human beings are capable of learning new skills and efficiently operate interfaces that are seemingly counter-intuitive. However, experimental evidence suggests that the effects of S-R compatibility can never be fully "trained away" [VP03]. As a result, even the most experienced users still benefit from compatible mappings between stimuli and responses. More work is needed to evaluate how much more effective an S-R compatible interface is compared to an interface with a less compatible mapping, especially if significant training is allowed.

Another interesting area for further research is to evaluate how many degrees of freedom should be included in an interaction device for a given interaction task. Some 2D interfaces use large control panels that allow for the adjustment of many parameters. Similarly, graphical interfaces often have a large number of options and settings that can be selected. Even

though the latter example may be operated with a single desktop mouse, these examples show that interfaces with many degrees of freedom not necessarily become too complex for use. It seems that human beings are very capable of focussing their attention to a specific part of an interface. However, evidence suggests that the number of parameters that can be manipulated simultaneously is more limited. For instance, Wang et al. [WMSB98] found that 3D positioning and orientation are only partially performed in parallel. It would be interesting to determine how many input dimensions users are capable of perceptually combining and manipulating in parallel.

An interesting result of the study in Chapter 9 is that the most intuitive interface not necessarily results in the most comfortable interface. For the experiments performed in Chapter 9, some users preferred a toolbox type of interface over the more intuitive interface, as the hands could rest more on the table. This leads to the question: "Can an interface be designed such that both intuitiveness and comfort are maximized?". The answer to this question, along with the development of a framework that developers could use to construct interfaces that are both intuitive and comfortable, would be a significant contribution to the field of virtual reality. It would enable developers to create truly natural interfaces that can be operated with minimum effort and for prolonged periods of time.

References

[AB94] R. Azuma and G. Bishop. Improving static and dynamic registration in a see-through HMD. In *Proceedings of SIGGRAPH'94*, pages 197–204. 1994.

[AF98] M. J. Atallah and S. Fox, editors. *Algorithms and Theory of Computation Handbook*. CRC Press, Inc., Boca Raton, FL, USA, 1998. ISBN 0849326494. Produced By-Suzanne Lassandro.

[ÅM95] K. Åström and L. Morin. Random cross ratios. In *Proc. 9th Scand. Conf. on Image Anal.*, pages 1053–1061. 1995.

[AMGC02] S. Arulampalam, S. Maskell, N. Gordon, and T. Clapp. A tutorial on particle filters for on-line non-linear/non-gaussian bayesian tracking. *IEEE Transactions on Signal Processing*, 50(2):174–188, February 2002.

[AZ96] M. Ayers and R. C. Zeleznik. The lego interface toolkit. In *ACM Symposium on User Interface Software and Technology*, pages 97–98. 1996.

[Azu95] R. Azuma. *Predictive Tracking for Augmented Reality*. Ph.D. thesis, University of North Carolina at Chapel Hill, 1995.

[BC93] B. Bell and F. Cathey. The iterated kalman filter update as a gauss-newton method. *IEEE Transactions on Automatic Control*, 38(2):294–297, 1993.

[BFKS99] R. Balakrishnan, G. Fitzmaurice, G. Kurtenbach, and K. Singh. Exploring interactive curve and surface manipulation using a bend and twist sensitive input strip. In *SI3D '99: Proceedings of the 1999 symposium on Interactive 3D graphics*, pages 111–118. ACM Press, New York, NY, USA, 1999.

[BG62] D. E. Broadbent and M. Gregory. Donders' b- and c- reactions and S-R compatibility. *Journal of Experimental Psychology 63*, pages 575–578, 1962.

[BH99a] R. Balakrishnan and K. Hinckley. The role of kinesthetic reference frames in two-handed input performance. In *Proceedings of the 12th annual ACM symposium on User interface software and technology*, pages 171–178. 1999.

[BH99b] D. Bowman and L. Hodges. Formalizing the design, evaluation, and application of interaction techniques for immersive virtual environments. *The Journal of Visual Languages and Computing*, 10(1):37–53, February 1999.

[BJH01] D. A. Bowman, D. B. Johnson, and L. F. Hodges. Testbed evaluation of virtual environment interaction techniques. *Presence: Teleoperators and Virtual Environments*, 10(1):75–95, February 2001.

[BKLP01] D. A. Bowman, E. Kruijff, J. J. LaViola Jr, and I. Poupyrev. An introduction to 3D user interface design. *Presence: Teleoperators and Virtual Environments*, 10(1):96–108, February 2001.

[BM92] P. J. Besl and N. D. McKay. A method for registration of 3-D shapes. *IEEE Transactions on Pattern Analysis and Machine Intelligence*, 14(2):239–256, 1992.

[Bro99] F. P. Brooks Jr. What's real about virtual reality? *IEEE Computer Graphics and Applications*, 19(6):16–27, 1999.

[BSF88] Y. Bar-Shalom and T. E. Fortmann. *Tracking and Data Association*. Academic Press, 1988.

[BT80] S. Barnard and W. Thompson. Disparity analysis of images. *IEEE Trans. Pattern Anal. Machine Intell*, pages 333–340, 1980.

[BT98] S. Birchfield and C. Tomasi. Depth discontinuities by pixel-to-pixel stereo. In *Proceedings of the Sixth IEEE International Conference on Computer Vision*, pages 1073–1080. 1998.

[CFSV04] L. P. Cordella, P. Foggia, C. Sansone, and M. Vento. A (sub)graph isomorphism algorithm for matching large graphs. *IEEE Trans. Pattern Anal. Mach. Intell.*, 26(10):1367–1372, 2004.

[CH99] S. Christy and R. Horaud. Iterative pose computation from line correspondences. *Computer Vision and Image Understanding*, 73(1):137–144, January 1999.

[Che91] H. Chen. Pose determination from line-to-plane correspondences: existence condition and closed-form solutions. *IEEE Transactions on pattern analysis and machine intelligence*, 13(6):530–541, June 1991.

[Chv83] Q. V. Chvatal. *Linear Programming*. W. H. Freeman and Co., 1983.

[CMR90] S. Card, J. Mackinlay, and G. Robertson. The design space of input devices. In *Proceedings of CHI*, pages 117–124. 1990.

[CNHV99] L. Chai, K. Nguyen, B. Hoff, and T. Vincent. An adaptive estimator for registration in augmented reality. In *Proc. of 2nd IEEE/ACM Int'l Workshop on Augmented Reality (IWAR '99)*. October 1999.

[CNX] 3DConnexion, http://www.3dconnexion.com/.

[CS00] J-X. Chai and H-Y. Shum. Parallel projections for stereo reconstruction. In *Proceedings of the IEEE Conference on Computer Vision and Pattern Recognition*, volume 2, pages 493–500. 2000.

[CTCG95] T. Cootes, C. Taylor, D. Cooper, and J. Graham. Active shape models - their training and application. *Computer Vision and Image Understanding*, 61(1):38–59, 1995.

[CW99] S. Coquillart and G. Wesche. The virtual palette and the virtual remote control panel: A device and an interaction paradigm for the responsive workbench((tm)). In *VR '99: Proceedings of the IEEE Virtual Reality Conference*, pages 13–17. IEEE Computer Society, Washington, DC, USA, 1999.

[DGK01] A. Doucet, N. J. Gordon, and V. Krishnamurthy. Particle filters for state estimation of jump markov linear systems. *IEEE Transactions on Signal Processing*, 49(3):613–624, 2001.

[DH72] R. O. Duda and P. E. Hart. Use of the hough transformation to detect lines and curves in pictures. *Communications of the ACM*, 15(1):11–15, 1972.

[Dor99] K. Dorfmüller. Robust tracking for augmented reality using retroreflective markers. *Computers and Graphics*, 23(6):795–800, 1999.

[Dou98] A. Doucet. On sequential monte carlo methods for bayesian filtering. Technical report, University of Cambride, UK, Department of Engineering, 1998.

[DS98] N. R. Draper and H. Smith. *Applied Regression Analysis*. John Wiley & Sons, third edition, 1998.

[ET98] S. Emura and S. Tachi. Multisensor integrated prediction for virtual reality. *Presence: Teleoperators and Virtual Environments*, 7(4):410–422, August 1998.

[EYAE99] S. R. Ellis, M. J. Young, B. D. Adelstein, and S. M. Ehrlich. Discrimination of changes of latency during voluntary hand movement of virtual objects. In *Proceedings of the Human Factors and Ergonomics Society*. 1999.

[FB81] M. A. Fischler and R. C. Bolles. Random sample consensus: a paradigm for model fitting with applications to image analysis and automated cartography. *Commun. ACM*, 24(6):381–395, 1981.

[Fia05] M. Fiala. ARTag, a fiducial marker system using digital techniques. In *CVPR '05: Proceedings of the 2005 IEEE Computer Society Conference on Computer Vision and Pattern Recognition (CVPR'05) - Volume 2*, pages 590–596. IEEE Computer Society, Washington, DC, USA, 2005.

[FIB95] G. W. Fitzmaurice, H. Ishii, and W. Buxton. Bricks: laying the foundations for graspable user interfaces. In *CHI '95: Proceedings of the SIGCHI conference on Human factors in computing systems*, pages 442–449. ACM Press/Addison-Wesley Publishing Co., New York, NY, USA, 1995.

[Fit54] P. M. Fitts. The information capacity of the human motor system in controlling the amplitude of movement. *Journal of Experimental Psychology*, 47:381–391, 1954.

[Flo75] K. Flowers. Handedness and controlled movement. *British Journal of Psychology*, 66:39–52, 1975.

[FP64] P. M. Fitts and J. R. Peterson. Information capacity of discrete motor responses. *Journal of Experimental Psychology*, 67:103–112, 1964.

[FP00] B. Fröhlich and J. Plate. The cubic mouse: A new device for 3D input. In *Proc. ACM CHI 2000*, pages 526–531. ACM Press, New York, 2000.

[FP02] D. A. Forsyth and J. Ponce. *Computer Vision: A Modern Approach*. Prentice Hall, 2002. ISBN 0130851981.

[FS53] P. M. Fitts and C. M. Seeger. S-R compatibility: Spatial characteristics of stimulus and response codes. *Journal of Experimental Psychology*, 46:199–210, 1953.

[Gar74] W. Garner. *The Processing of Information and Structure*. Wiley, New York, 1974.

[GSS93] N. J. Gordon, D. J. Salmond, and A. F. M. Smith. Novel approach to nonlinear/non-gaussian bayesian state estimation. In *IEEE Proceedings on Radar and Signal Processing*, volume 140, pages 107–113. 1993.

[Gui87] Y. Guiard. Assymetric division of labor in skilled bimanual action: The kinematic chain as a model. *Journal of Motor Behavior*, 19:486–517, 1987.

[HHN86] E. L. Hutchins, J. D. Hollan, and D. A. Norman. Direct manipulation interfaces. In D. A. Norman and S. W. Draper, editors, *User Centered System Design: New Perspectives on Human-Computer Interaction*, pages 87–124. Erlbaum, Hillsdale, NJ, 1986.

[Hor87] B. K. P. Horn. Closed-form solution of absolute orientation using unit quaternions. *Journal of the Optical Society of America, A*, 4(4):629–642, 1987.

[HPGK94] K. Hinckley, R. Pausch, J. C. Goble, and N. F. Kassell. Passive real-world interface props for neurosurgical visualization. In *CHI '94: Proceedings of the SIGCHI conference on Human factors in computing systems*, pages 452–458. ACM Press, New York, NY, USA, 1994.

[HS97] J. Heikkilä and O. Silvén. A four-step camera calibration procedure with implicit image correction. *Computer Vision and Pattern Recognition*, pages 1106–1113, 1997.

[HSDK05] A. Hornung, S. Sar-Dessai, and L. Kobbelt. Self-calibrating optical motion tracking for articulated bodies. In *Proceedings of the IEEE Virtual Reality Conference*, pages 75–82. 2005.

[HUHF03] L. Herda, R. Urtasun, A. Hanson, and P. Fua. Automatic determination of joint limits using quaternion field boundaries. *International Journal for Robotis Research*, 22(6):419–436, 2003.

[HV00] W. Hoff and T. Vincent. Analysis of head pose accuracy in augmented reality. *IEEE Transactions on Visualization and Computer Graphics*, 6(4):319–334, 2000. ISSN 1077-2626. doi:http://dx.doi.org/10.1109/2945.895877.

[IB98] M. Isard and A. Blake. Condensation - conditional density propagation for visual tracking. *Int. J. Computer Vision*, 29:5–28, 1998.

[JHWB78] R. J. Jagacinski, E. J. Hartzell, S. Ward, and K. Bishop. Fitts' law as a function of system dynamics and target uncertainty. *Journal of Motor Behavior*, 10:123–131, 1978.

[Jol02] I. T. Jolliffe. *Principal Component Analysis*. Springer; 2nd edition, 2002.

[JRM+80] R. J. Jagacinski, D. W. Repperger, M. S. Moran, S. L. Ward, and B. Class. Fitts' law and the microstructure of rapid discrete movements. *Journal of Experimental Psychology: Human Perception and Performance*, 6(2):309–320, 1980.

[JS92] R. J. K. Jacob and L. E. Sibert. The perceptual structure of multidimensional input device selection. In *CHI '92: Proceedings of the SIGCHI conference on Human factors in computing systems*, pages 211–218. ACM Press, New York, NY, USA, 1992.

[JSM+94] R. J. K. Jacob, L. E. Sibert, D. C. McFarlane, M. Preston, and J. R. Mullen. Integrality and separability of input devices. *ACM Transactions on Computer-Human Interaction*, 1(1):3–26, 1994.

[JU97] S. J. Julier and J. K. Uhlmann. A new extension of the kalman filter to nonlinear systems. *Int. Symp. Aerospace/Defense Sensing, Simulation and Controls*, 1997.

[KB99] H. Kato and M. Billinghurst. Marker tracking and HMD calibration for a video-based augmented reality conferencing system. In *IWAR '99: Proceedings of the 2nd IEEE and ACM International Workshop on Augmented Reality*, pages 85–94. IEEE Computer Society, Washington, DC, USA, 1999.

[KBS94] P. Kabbash, W. Buxton, and A. Sellen. Two-handed input in a compound task. In *CHI '94: Conference companion on Human factors in computing systems*. 1994.

[KHYN02] K. Kurihara, S. Hoshino, K. Yamane, and Y. Nakamura. Optical motion capture system with pan-tilt camera tracking and realtime data processing. In *Proc. of IEEE International Conference on Robotics and Automation(ICRA2002)*, volume 2, pages 1241–1248. May 2002.

[KL04] A. J. F. Kok and R. van Liere. Co-location and tactile feedback for 2d widget manipulation. In *Proceedings of the IEEE Virtual Reality Conference 2004*. March 2004.

[KMB93] P. Kabbash, I. S. MacKenzie, and W. Buxton. Human performance using computer input devices in the preferred and non-preferred hands. In *Proceedings of InterCHI '93*, pages 474–481. 1993.

[KTES87] W. S. Kim, F. Tendick, S. R. Ellis, and L. W. Stark. A comparison of position and rate control for telemanipulation with consideration of manipulator system dynamics. *IEEE Journal of Robotics and Automation*, 3:426–436, 1987.

[Lau01] M. Laurent. Matrix completion problems. *Matrix completion problems. The Encyclopedia of Optimization*, 3:221–229, 2001.

[LaV03] J. J. LaViola Jr. A comparison of unscented and extended kalman filtering for estimating quaternion motion. In *Proc. 2003 Am. Control Conf.*, pages 2435–2440. June 2003.

[LF05] V. Lepetit and P. Fua. Monocular model-based 3D tracking of rigid objects: A survey. *Foundations and Trends in Computer Graphics and Vision*, 1(1):1–89, 2005.

[LM03] R. van Liere and J. D. Mulder. Optical tracking using projective invariant marker pattern properties. *Proceedings of the IEEE Virtual Reality 2003 Conference*, pages 191–198, 2003.

[LPN+06] C. Liu, W. Pei, S. Niyokindi, J. C. Song, and L. D. Wang. Micro stereo matching based on wavelet transform and projective invariance. *Seventh International Symposium on Measurement Technology and Intelligent Instruments*, 17(3):565–571, 2006.

[LR03] R. van Liere and A. van Rhijn. Search space reduction in optical tracking. In *Proceedings of the workshop on Virtual environments 2003*, pages 207–214. ACM Press, 2003.

[LR04] R. van Liere and A. van Rhijn. An experimental comparison of three optical trackers for model based pose determination in virtual reality. In *Proceedings of the Eurographics Symposium on Virtual Environments*, pages 25–34. June 2004.

[LS00a] J. Lasenby and A. Stevenson. Using geometric algebra for optical motion capture. *Geometric algebra: a geometric approach to computer vision, neural and quantum computing, robotics and engineering*, pages 147–169, 2000.

[LS00b] J. Lee and S. Y. Shin. General construction of time-domain filters for orientation data. *IEEE Transaction on Visualization and Computer Graphics*, 8:119–128, 2000.

[LSW88] Y. Lamdan, J. T. Schwartz, and H. J. Wolfson. On recognition of 3-D objects from 2-D images. In *Proceedings of IEEE Int. Conf. on Robotics and Automation*, pages 1407–1413. 1988.

[May79] P. S. Maybeck. *Stochastic Models, Estimation and Control, Volume 1*. Academic Press, 1979.

[May95] S. J. Maybank. Probabilistic analysis of the application of the cross ratio to model based vision: Misclassification. *Intl. J. of Computer Vision*, 14:199–210, 1995.

[MBS97] M. R. Mine, F. P. Brooks Jr, and C. H. Séquin. Moving objects in space: Exploiting proprioception in virtual-environment interaction. In *SIGGRAPH 97 Conference Proceedings*, pages 19–26. 1997.

[MDFW00] R. Merwe, A. Doucet, N. Freitas, and E. Wan. The unscented particle filter. Technical Report CUED/F-INFENG/TR380, Cambridge University, Engineering Department, August 2000, 2000.

[Mei71] D. Meister. *Human Factors: Theory and Practice*. Wiley-Interscience, 1971.

[MFDW01] R. van der Merwe, N. de Freitas, A. Doucet, and E. Wan. The unscented particle filter. In *Advances in Neural Information Processing Systems 13*. November 2001.

[Min93] M. R. Mine. Characterization of end-to-end delays in head-mounted display systems. Technical Report TR93-001, UNC Chapel Hill, Computer Science, 1993.

[MJR03] J. D. Mulder, J. Jansen, and A. van Rhijn. An affordable optical head tracking system for desktop VR/AR systems. In J. Deisinger and A. Kunz, editors, *Proceedings of the Workshop on Virtual Environments 2003*, pages 215–223. 2003.

[MKM90] D. Mendlovic, N. Konforti, and E. Marom. Shift and projection invariant pattern recognition using logarithmic harmonics. *Appl. Opt.*, 29:4784–4789, 1990.

[ML02] J. D. Mulder and R. van Liere. The personal space station: Bringing interaction within reach. In S. Richer, P. Richard, and B. Taravel, editors, *Proceedings of the Virtual Reality International Conference, VRIC 2002*, pages 73–81. 2002.

[MLR98] P. Meer, R. Lenz, and S. Ramakrishna. Efficient invariant representations. *IJCV*, 26(2):137–152, 1998.

[MN00] S. Mills and K. Novins. Motion segmentation in long image sequences. In *Proceedings of the British Machine Vision Conference (BMVC2000)*, pages 162–171. 2000.

[MRWB03] M. Meehan, S. Razzaque, M. Whitton, and F. P. Brooks Jr. Effect of latency on presence in stressful virtual environments. In *Proceedings of the IEEE Virtual Reality Conference*, pages 141–148. 2003.

[NM65] J. A. Nelder and R. Mead. A simplex method for function minimization. *Comput. J.*, 7:308–313, 1965.

[OBBH00] J. F. O'Brien, R. E. Bodenheimer, G. J. Brostow, and J. K. Hodgins. Automatic joint parameter estimation from magnetic motion capture data. In *Proc. Graphics Interface*, pages 53–60. 2000.

[O'R85] J. O'Rourke. Finding minimal enclosing boxes. *International Journal of Computer and Information Sciences*, 14(3):183–199, 1985.

[Pil97] M. Pilu. A direct method for stereo correspondence based on singular value decomposition. In *Proc. IEEE International Conference of Computer Vision and Pattern Recognition*, pages 261–266. 1997.

[PMF85] S. B. Pollard, J. E. Mayhew, and G. P. Frisby. PMF: A stereo correspondence algorithm using a disparity gradient limit. *Perception*, 14:449–470, 1985.

[PS99] M. K. Pitt and N. Shepard. Filtering via simulation: Auxiliary particle filters. *Journal of the American Statistical Association*, 94(446):590–599, 1999.

[PST] Personal Space Technologies, http://www.personalspacetechnologies.com/.

[QL99] L. Quan and Z. Lan. Linear N-point camera pose determination. *IEEE Trans. Pattern Anal. Mach. Intell.*, 21(8):774–780, 1999.

[RDB00] J. P. Rolland, L. D. Davis, and Y. Baillot. A survey of tracking technology for virtual environments. In Barfield and Caudell, editors, *Fundamentals of Wearable Computers and Augmented Reality*, pages 67–112. Mahwah, NJ, 2000.

[Rey03] O. Reynhout. *Improving optical tracking for the Personal Space Station*. Master's thesis, Technische Universiteit Eindhoven, 2003.

[RL02] M. Ringer and J. Lasenby. A procedure for automatically estimating model parameters in optical motion capture. In *British Machine Vision Conference*, pages 747–756. 2002.

[RLM05] A. van Rhijn, R. van Liere, and J. D. Mulder. An analysis of orientation prediction and filtering methods for VR/AR. In *Proceedings of the IEEE Virtual Reality Conference 2005*, pages 67–74. March 2005.

[RM04] A. van Rhijn and J. D. Mulder. Optical tracking using line pencil fiducials. In *Proceedings of the Eurographics Symposium on Virtual Environments 2004*, pages 35–44. 2004.

[RM05] A. van Rhijn and J. D. Mulder. Optical tracking and calibration of tangible interaction devices. In *Proceedings of the Immersive Projection Technology and Virtual Environments Workshop 2005*, pages 41–50. 2005.

[RM06a] A. van Rhijn and J. D. Mulder. CID: An optically tracked configurable interaction device. In *Proceedings of Laval Virtual International Conference on Virtual Reality 2006*. 2006.

[RM06b] A. van Rhijn and J. D. Mulder. Optical tracking and automatic model estimation of composite interaction devices. In *Proceedings of the IEEE Virtual Reality Conference 2006*, pages 135–142. Alexandria, Virginia, USA, 2006.

[RM06c] A. van Rhijn and J. D. Mulder. Spatial input device structure and bimanual object manipulation in virtual environments. In *Accepted for publication at the ACM Symposium on Virtual Reality Software and Technology*. 2006.

[RPF01] M. Ribo, A. Pinz, and A. Fuhrmann. A new optical tracking system for virtual and augmented reality applications. In *Proceedings of the IEEE Instrumentation and Measurement Technical Conference*, volume 3, pages 1932–1936. Budapest, Hungary, 2001.

[SAM03] S. Subramanian, D. Aliakseyeu, and J-B. Martens. Empirical evaluation of performance in hybrid 3d and 2d interfaces. In *Proceedings of Interact 2003*, pages 916–919. September 2003.

[SCTM95] P. Sozou, T. Cootes, C. Taylor, and E. Di Mauro. Non-linear point distribution modelling using a multi-layer perceptron. *British Machine Vision Conference (BMVC'95)*, pages 107–116, 1995.

[SF03] A. Simon and B. Fröhlich. The YoYo: A handheld device combining elastic and isotonic input. In *Proc. of INTERACT 2003*, pages 303–310. 2003.

[Sha98] C. M. Shakarji. Least-squares fitting algorithms of the NIST algorithm testing system. *Journal of Research of the National Institute of Standards and Technology*, 103(6):633–641, 1998.

[Sho85] K. Shoemake. Animating rotation with quaternion curves. *Computer Graphics*, 19:245–254, 1985.

[SLH91] G. Scott and H. Longuet-Higgins. An algorithm for associating the features of two patterns. In *Proc. Royal Society London*, volume B244, pages 21–26. 1991.

[Smi95] S. M. Smith. ASSET-2: Real-time motion segmentation and shape tracking. In *Proc. 5th Int. Conf. on Computer Vision*, pages 237–244. 1995.

[SPB+98] M. Silaghi, R. Plaenkers, R. Boulic, P. Fua, and D. Thalmann. Local and global skeleton fitting techniques for optical motion capture. *Lecture Notes in Computer Science*, 1537:26–40, 1998.

[SRL06] F. A. Smit, A. van Rhijn, and R. van Liere. A topology projection invariant optical tracker. In *Proceedings of the Eurographics Symposium on Virtual Environments 2006*, pages 63–70. Lisbon, Portugal, May 2006.

[SS02] D. Scharstein and R. Szeliski. A taxonomy and evaluation of dense two-frame stereo correspondence algorithms. *Int. J. Comput. Vision*, 47(1-3):7–42, 2002.

[Sug94] A. Sugimoto. Geometric invariant of noncoplanar lines in a single view. *Proc. 12th IAPR Int. Conf. on Pattern Recognition (ICPR'94)*, 10:190–195, 1994.

[Sut65] I. Sutherland. The ultimate display. In *Information Processing 1965: Proceedings of IFIP Congress 65*, pages 506–508. 1965.

[SW01] T. Schank and D. Wagner. Finding, counting and listing all triangles in large graphs, an experimental study. Technical Report TR-043, DELIS, 2001.

[Tla04] M. Tlauka. Display-control compatibility: The relationship between performance and judgments of performance. *Ergonomics*, 47(3):281–295, 2004.

[Tou83] G. T. Toussaint. Solving geometric problems with the rotating calipers. In *Proc. IEEE MELECON'83*. Athens, Greece, 1983.

[Tsa86] R. Y. Tsai. An efficient and accurate camera calibration technique for 3D machine vision. In *Proceedings of IEEE Conference on Computer Vision and Pattern Recognition*, pages 364–374. 1986.

[Van94] D. VanArsdale. Homogeneous transformation matrices for computer graphics. *Computers and Graphics*, 18(2):177–191, 1994.

[VIC] Vicon, http://www.vicon.com/.

[VP03] K. L. Vu and R. W. Proctor. Naïve and experienced judgments of stimulus-response compatibility: Implications for interface design. *Ergonomics*, 46(1):169–187, 2003.

[VY86] A. Verri and A. Yuille. Perspective projection invariants. Technical Report AIM-832, Massachusetts Institute of Technology, 1986.

[WA04] C. Ware and R. Arsenault. Frames of reference in virtual object rotation. In *Proceedings of the 1st Symposium on Applied perception in graphics and visualization*. 2004.

[WB89] C. J. Worringham and D. B. Beringer. Operator orientation and compatibility in visual-motor task performance. *Ergonomics*, 32(1):387–399, 1989.

[WB98] C. J. Worringham and D. B. Beringer. Directional stimulus-response compatibility: A test of three alternative principles. *Ergonomics*, 41(6):864–880, 1998.

[WF02] G. Welch and E. Foxlin. Motion tracking: No silver bullet, but a respectable arsenal. *IEEE Computer Graphics and Applications*, 22(6):24–38, November/December 2002.

[Wie49] N. Wiener. *Extrapolation, Interpolation and Smoothing of Stationary Time Series with Engineering Applications*. New York, Wiley, 1949.

[WM99] Y. Wang and C. L. MacKenzie. Object manipulation in virtual environments: relative size matters. In *Proceedings of the SIGCHI conference on Human factors in computing systems: the CHI is the limit*, pages 48–55. 1999.

[WMSB98] Y. Wang, C. L. MacKenzie, V. A. Summers, and K. S. Booth. The structure of object transportation and orientation in human-computer interaction. In *CHI '98: Proceedings of the SIGCHI conference on Human factors in computing systems*, pages 312–319. ACM Press/Addison-Wesley Publishing Co., New York, NY, USA, 1998.

[WO00] J. Wu and M. Ouhyoung. On latency compensation and its effects on head-motion trajectories in virtual environments. *The visual computer*, 16(2):79–90, 2000.

[XSE] Xsens Motion Technologies, http://www.xsens.com/.

[YMS03] D. Yates, D. S. Moore, and D. S. Starnes. *The Practice of Statistics*. W. H.Freeman and Co Ltd, second edition, 2003. ISBN 0716783428.

[YP84] A. L. Yuille and T. Poggio. A generalized ordering constraint for stereo correspondence. *A.I. Laboratory Memo 777*, 1984.

[YP06] J. Yan and M. Pollefeys. Automatic kinematic chain building from feature trajectories of articulated objects. In *Proceedings of the IEEE Conf. on Computer Vision and Pattern Recognition*. 2006.

[ZF92] Z. Zhang and O. D. Faugeras. Three-dimensional motion computation and object segmentation in a long sequence of stereo frames. *Int. J. Comput. Vision*, 7(3):211–241, 1992.

[ZH03] V. B. Zordan and N. C. van der Horst. Mapping optical motion capture data to skeletal motion using a physical model. In *Proceedings of the 2003 ACM SIGGRAPH/Eurographics symposium on Computer animation*, pages 245–250. 2003.

[Zha98] S. Zhai. User performance in relation to 3D input device design. *ACM SIGGRAPH Computer Graphics*, 32(4):50–54, 1998.

[Zha00] Z. Zhang. A flexible new technique for camera calibration. *IEEE Transactions on Pattern Analysis and Machine Intelligence*, 22(11):1330–1334, 2000.

[Zha02] Z. Zhang. Camera calibration with one-dimensional objects. *Proceedings of the European Conference on Computer Vision*, 4:161–174, 2002.

[ZM93] S. Zhai and P. Milgram. Human performance evaluation of manipulation schemes in virtual environments. In *Proceedings of the IEEE Virtual Reality Annual International Symposium*, pages 155–171. 1993.

Summary

Three-dimensional interaction with virtual objects is one of the aspects that needs to be addressed in order to increase the usability and usefulness of virtual reality. Human beings have difficulties understanding 3D spatial relationships and manipulating 3D user interfaces, which require the control of multiple degrees of freedom simultaneously. Conventional interaction paradigms known from the desktop computer, such as the use of interaction devices as the mouse and keyboard, may be insufficient or even inappropriate for 3D spatial interaction tasks.

The aim of the research in this thesis is to develop the technology required to improve 3D user interaction. This can be accomplished by allowing interaction devices to be constructed such that their use is apparent from their structure, and by enabling efficient development of new input devices for 3D interaction.

The driving vision in this thesis is that for effective and natural direct 3D interaction the structure of an interaction device should be specifically tuned to the interaction task. Two aspects play an important role in this vision. First, interaction devices should be structured such that interaction techniques are as direct and transparent as possible. Interaction techniques define the mapping between interaction task parameters and the degrees of freedom of interaction devices. Second, the underlying technology should enable developers to rapidly construct and evaluate new interaction devices.

The thesis is organized as follows. In Chapter 2, a review of the optical tracking field is given. The tracking pipeline is discussed, existing methods are reviewed, and improvement opportunities are identified.

In Chapters 3 and 4 the focus is on the development of optical tracking techniques of rigid objects. The goal of the tracking method presented in Chapter 3 is to reduce the occlusion problem. The method exploits projection invariant properties of line pencil markers, and the fact that line features only need to be partially visible.

In Chapter 4, the aim is to develop a tracking system that supports devices of arbitrary shapes, and allows for rapid development of new interaction devices. The method is based on subgraph isomorphism to identify point clouds. To support the development of new devices in the virtual environment an automatic model estimation method is used.

Chapter 5 provides an analysis of three optical tracking systems based on different principles. The first system is based on an optimization procedure that matches the 3D device model points to the 2D data points that are detected in the camera images. The other systems are the tracking methods as discussed in Chapters 3 and 4.

In Chapter 6 an analysis of various filtering and prediction methods is given. These techniques can be used to make the tracking system more robust against noise, and to reduce the latency problem.

Chapter 7 focusses on optical tracking of composite input devices, i.e., input devices

that consist of multiple rigid parts that can have combinations of rotational and translational degrees of freedom with respect to each other. Techniques are developed to automatically generate a 3D model of a segmented input device from motion data, and to use this model to track the device.

In Chapter 8, the presented techniques are combined to create a configurable input device, which supports direct and natural co-located interaction. In this chapter, the goal of the thesis is realized. The device can be configured such that its structure reflects the parameters of the interaction task.

In Chapter 9, the configurable interaction device is used to study the influence of spatial device structure with respect to the interaction task at hand. The driving vision of this thesis, that the spatial structure of an interaction device should match that of the task, is analyzed and evaluated by performing a user study.

The concepts and techniques developed in this thesis allow researchers to rapidly construct and apply new interaction devices for 3D interaction in virtual environments. Devices can be constructed such that their spatial structure reflects the 3D parameters of the interaction task at hand. The interaction technique then becomes a transparent one-to-one mapping that directly mediates the functions of the device to the task. The developed configurable interaction devices can be used to construct intuitive spatial interfaces, and allow researchers to rapidly evaluate new device configurations and to efficiently perform studies on the relation between the spatial structure of devices and the interaction task.

Samenvatting

Drie-dimensionale interactie met virtuele objecten is een van de aspecten die aangepakt moet worden om de bruikbaarheid en de toepasbaarheid van virtual reality te vergroten. Gebruikers hebben moeite om 3D ruimtelijke relaties te begrijpen en om 3D user interfaces te manipuleren, waarbij meerdere vrijheidsgraden gelijktijdig gecontroleerd moeten worden. Conventionele interactie concepten die bekend zijn van de desktop computer, zoals het gebruik van invoerapparaten zoals de muis en het toetsenbord, kunnen ontoereikend of zelfs onbruikbaar zijn voor 3D ruimtelijke interactie taken.

Het doel van het onderzoek in dit proefschrift is het ontwikkelen van de technologie die nodig is om 3D gebruikersinteractie te verbeteren. Dit kan worden bereikt door het bieden van de mogelijkheid om invoerapparaten zo te construeren dat het gebruik duidelijk is uit de structuur, en door efficiënte ontwikkeling van nieuwe invoerapparaten voor 3D interactie.

De visie, die het onderzoek in dit proefschrift stuurt, is dat voor effectieve en directe 3D interactie de structuur van een invoerapparaat specifiek moet worden afgestemd op de interactie taak. Twee aspecten spelen een belangrijke rol bij deze visie. Ten eerste zouden invoerapparaten zo moeten worden gestructureerd dat interactie technieken zo direct en transparant mogelijk zijn. Interactie technieken definiëren de transformatie van de vrijheidsgraden van invoerapparaten naar de parameters van een interactie taak. Ten tweede zou de achterliggende techniek ontwikkelaars in staat moeten stellen om snel en effectief nieuwe invoerapparaten te construeren en evalueren.

Dit proefschrift is als volgt ingedeeld. In hoofdstuk 2 wordt een overzicht gegeven van het veld van optische tracking. De problematiek wordt gedefinieerd, bestaande methodes worden besproken, en mogelijkheden ter verbetering geïdentificeerd.

Het doel van hoofdstukken 3 en 4 is om optische tracking technieken te ontwikkelen voor rigide objecten. De technieken gepresenteerd in hoofdstuk 3 hebben tot doel het occlusie probleem te verminderen. De methode gebruikt projectie invariante eigenschappen van waaiers van lijnen, en het feit dat lijnsegmenten slechts gedeeltelijk zichtbaar hoeven te zijn.

In hoofdstuk 4 wordt een tracking systeem ontwikkeld dat willekeurige vormen van invoerapparaten ondersteunt, en dat de mogelijkheid biedt om snel nieuwe invoerapparaten te ontwikkelen. De methode is gebaseerd op deelgraaf isomorphisme om puntenwolken te identificeren. Om de ontwikkeling van nieuwe invoerapparaten voor een virtuele omgeving mogelijk te maken wordt een automatische model schattingsmethode gebruikt.

Hoofdstuk 5 geeft een analyse van drie optische tracking systemen die op verschillende principes zijn gebaseerd. Het eerste systeem is gebaseerd op een optimalisatie methode, die de relatie tussen 3D modelpunten en de gedetecteerde 2D datapunten afleidt. De andere systemen zijn de tracking methodes die in hoofdstukken 3 en 4 zijn geïntroduceerd.

In hoofdstuk 6 wordt een analyse gemaakt van verscheidene filterings- en voorspellings-

methoden. Deze technieken kunnen worden gebruikt om het systeem robuuster te maken tegen ruis en om het latency probleem te verminderen.

Hoofdstuk 7 richt zich op optische tracking van samengestelde invoerapparaten. Dit zijn apparaten die uit verscheidene rigide gedeeltes bestaan, die combinaties van rotatie en translatie vrijheidsgraden ten opzichte van elkaar kunnen hebben. Technieken worden gepresenteerd voor het automatisch genereren van een 3D model van een samengesteld invoerapparaat uit bewegingsdata, en voor het gebruik van dit model voor de tracking van het apparaat.

In hoofdstuk 8 worden de gepresenteerde technieken gecombineerd om een configureerbaar invoerapparaat te ontwerpen, dat tot doel heeft om directe en natuurlijke interactie mogelijk te maken. In dit hoofdstuk wordt het doel van het proefschrift verwezenlijkt. Het apparaat kan zo worden geconfigureerd, dat de structuur de parameters van de interactie taak afspiegelt.

In hoofdstuk 9 wordt het configureerbare invoerapparaat gebruikt in een gebruikersstudie. De studie heeft tot doel om de invloed van de ruimtelijke structuur van invoerapparaten in relatie tot de interactie taak te bestuderen. De visie van dit proefschrift, dat de ruimtelijke structuur van een invoerapparaat de structuur van de taak moet afspiegelen, wordt geanalyseerd en geëvalueerd door een gebruikersstudie.

De concepten en technieken die in dit proefschrift ontwikkeld zijn stellen onderzoekers in staat om nieuwe invoerapparaten te construeren en toe te passen in virtuele omgevingen. Apparaten kunnen zo worden geconstrueerd dat de ruimtelijke structuur de 3D parameters van de interactie taak reflecteert. De interactie techniek wordt zo een 1-op-1 relatie tussen apparaat en taak. De ontwikkelde configureerbare invoerapparaten kunnen worden gebruikt om ruimtelijke interfaces te ontwerpen. Ze stellen onderzoekers tevens in staat om snel nieuwe apparaat configuraties te evalueren en studies te doen naar de relatie tussen de ruimtelijke structuur van een apparaat en de taak parameters.

Curriculum Vitae

Arjen van Rhijn was born in April 1976 in Diemen, the Netherlands. In June 1994 he received his Gymnasium diploma in eight courses at the Prisma College in Utrecht. The same year he started studying Electrical Engineering at the Delft University of Technology (TU Delft), where he received his Master of Science degree in March 2001. His graduation project was performed under the supervision of dr.ir. N.P. van der Meijs, and involved developing techniques for automatic generation of schematics of extracted transistor level circuits. After his graduation he worked at the Philips Research Laboratories for Cimsolutions as a software engineer for analog circuit simulation. In March 2002, he joined the Visualization and 3D User Interfaces theme of the Center for Mathematics and Computer Science (CWI). There he performed the Ph.D. research that is described in this thesis, under the supervision of dr. J.D. Mulder, prof.dr.ir. R. van Liere, and prof.dr.ir. J.J. van Wijk.